UNIVERSITY OF READING

Department of Meteorology

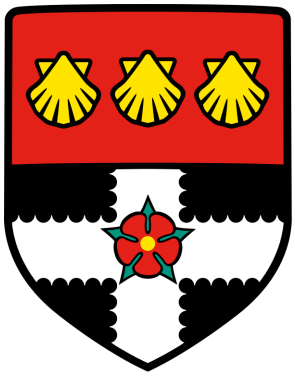

Improving the Treatment of Vegetation Canopy Architecture in Radiative Transfer Schemes

Renato Kerches Braghiere

A thesis submitted for the degree of Doctor of Philosophy

September 2017

Declaration

I confirm that this is my own work and the use of all material from other sources has been properly and fully acknowledged.

Renato Kerches Braghiere

"Science cannot solve the ultimate mystery of nature. And that is because, in the last analysis, we ourselves are part of nature and therefore part of the mystery that we are trying to solve."

– Max Planck

Where is Science Going?, trans. James Murphy (1933), Epilogue, **217**.

Abstract

Addressing the impact of vegetation architecture on the treatment of shortwave radiation in land surface models (LSMs) is important for accurate weather forecast and climate predictions. The study of the carbon budget is also impacted by vegetation architecture because shortwave radiation is used by plants to photosynthesise. Three pieces of research are presented in this thesis: the implementation and evaluation of different parameterisations of vegetation architecture in a commonly used radiative transfer scheme; analysis of the impact of Sun zenith angular variability on vegetation structural parameters including the effect that these parameters have on Gross Primary Productivity (GPP) at site level; and a study on how the simulation of global carbon assimilation is impacted when considering vegetation architecture with satellite derived data sets.

Neglecting canopy heterogeneity in radiative transfer schemes leads to significant uncertainties in shortwave radiation absorption and reflectance. The best agreement between detailed 3D radiative transfer schemes and a parameterised 1D version that accounts for vegetation architecture heterogeneity is given when considering zenith angular variability of the parameters. The major impacts on shortwave radiation distribution along the vertical axis are found at the bottom layers of the canopy, which absorbs more radiation when structure is considered. Further impacts on photosynthesis are evaluated at site level with digital hemispherical photography and eddy covariance measurements, and at global level with satellite data and global modelling. Impacts on GPP are dependent on the vertical distribution of the photosynthesis limiting regimes and the variation of the structural parameters with Sun zenith angle is more important over sites with denser foliage than sites with sparser foliage. At global level, prediction of GPP increases by 5.53 ± 1.02 PgC.yr^{-1} when considering canopy structure, with a strong signal in the tropics.

This work establishes the importance of considering vegetation canopy architecture in land surface modelling and predicts that current values of global GPP might be underestimated by LSMs.

Acknowledgements

Firstly, I would like to thank my supervisors, Tristan Quaife and Emily Black, who gave me the opportunity of taking on such an exciting PhD and the chance to discuss science every other day. They have provided continual support and guidance over the past four years. Secondly, I must thank my monitoring committee members, Pier Luigi Vidale and Sue Grimmond, who have helped substantially to keep my work on track. I also would like thank people who have shared data, models, and insights with me along my PhD, and in one way or another made this work possible. Thanks to Tristan Quaife for sharing the modified two-stream scheme; Jean-Luc Widlowski for sharing the RAMI4PILPS reference data; Youngryel Ryu, Martin De Kauwe, and Ewan Pinnington for sharing digital hemispherical photographs; Qi Chen and Dennis Baldocchi for sharing tree positioning data for Tonzi Ranch; and Liming He and Jing Chen for sharing the global map of clumping index. Thanks to members of the Meteorology department, especially the PhD students, who have made Reading a great place to be over the past years. In addition to this, Javier Amezcua for reading the thesis. Thanks to my first office mates in Harry Pitt 179 for making me feel very welcome to this rainy country. A big thanks to my colleagues in Lyle 5, who have provided assistance with coding, JULES, *Python*, and UNIX in general. Thanks to the members of the land surface group, who have made Monday afternoons a bit more interesting. I also would like to thank my 'Brazilian family abroad', Letícia Guimarães, Rachel Peterson, and Flávia Pinheiro, who have made me feel a bit less '*saudade*' from Brazil. I would like to thank my parents and family for their support and encouragement with my education and helping me get where I am now. Special thanks to my grandmother Nilza Kerches. I could not let Vlad Bezrodnny out of this, because he has being there along the way since Norway, and stopped me giving up when I had reached the limit of my sanity. A massive hug to my friends in Berlin and Trieste, who have shared so many academic and life experiences with me. And to the British people, you guys are very kind and polite. Last but not least, this PhD was supported by the Science without Borders Program grant number 9549-13-7, financed by CAPES Brazilian Federal Agency for Support and Evaluation of Graduate Education within the Ministry of Education of Brazil.

Contents

List of Figures

List of Tables

List of Acronyms

Acronym	Definition
AIC	Akaike Information Criterion
AR	Assessment Report
BIC	Bayesian Information Criterion
BOREAS	Boreal Ecosystem-Atmosphere Study
BRDF	Bidirectional Reectance Distribution Function
BVOCs	Biogenic Volatile Organic Compounds
CI	Confidence Interval
CLM4CN	Community Land Model for Carbon Nitrogen
CMIP	Coupled Model Intercomparison Project
CPU	Central Processing Unit
DBH	Diameter at breast height
DGVMs	Dynamic Global Vegetation Models
ECMWF	European Centre for Medium Range Weather Prediction
ENSO	El Niño Southern Oscillation
ESU	Elementary Sampling Units
fAPAR	fraction of Absorbed PAR
FAVD	Foliage Area Volume Density
FIFE	The First ISLSCP Field Experiment
FLUXNET	FLUX NETwork
GCM	Global Climate Model
GCP	Global Carbon Project
GPCC	Global Precipitation Climatology Centre
GPP	Gross Primary Productivity
IGBP	International Geosphere-Biosphere Programme
IPCC	Intergovernmental Panel on Climate Change
ISLSCP	International Satellite Land Surface Climatology Project
ISO	Isotropic
JULES	Joint UK Land Environment Simulator
LAI	Leaf Area Index

LBA	The Large-Scale Biosphere-Atmosphere Experiment in Amazonia
LiDAR	Light Detection and Ranging
LSM	Land Surface Model
LUC	Land Use Changes
LUE	Light Use Efficiency
LUT	Lookup Table
MISR	Multi-angle Imaging SpectroRadiometer
MODIS	Moderate Resolution Imaging Spectroradiometer
MOSES	Met Office Surface Exchange Scheme
MSD	Mean Squared Deviation
MTE	Model Tree Ensemble
N	Nitrogen
NEE	Net Ecosystem Exchange
NEON	National Ecological Observatory Network
NIR	Near Infra-Red
NPP	Net Primary Production
NSA	Northern Study Area
OA	Old Aspen
OBS	Old Black Spruce
OJP	Old Jack Pine
ORCHIDEE	ORganizing Carbon and Hydrology in Dynamic EcosystEms model
PAI	Plant Area Index
PAR	Photosynthetically Active Radiation
PFT	Plant Functional Type
POLDER	POLarization and Directionality of the Earth's Reflectances
RGB	Red Green Blue colour model
RMSE	Root-Mean-Squared-Error
RNA	Research Natural Area
RT	Radiative transfer
SSA	Southern Study Area
STD	Standard Deviation of the product error
SZA	Sun Zenith Angle

TIR	Thermal Infra-Red
TOA	Top of the Atmosphere
TOC	Top of the Canopy
TRIFFID	Top-down Representation of Interactive Foliage and Flora Including Dynamics
VPD	Vapour Pressure Deficit

List of Mathematical Notation

Symbol	Definition	Units
α	Maximum quantum efficiency of photosynthesis	mol.CO_2 mol^{-1}.PAR
α_{soil}	Soil albedo	-
α_s	Surface albedo	-
β	Soil moisture availability function	-
β	Upscattering parameters for the diffuse beam	-
β_0	Upscattering parameters for the direct beam	-
δe	Vapour pressure deficit	kPa
λE	Latent heat flux	W.m^{-2}
λ	Latent heat of vaporisation	J.kg^{-1}
μ	Cosine of the Sun zenith angle	-
ω	Leaf scattering coefficient	-
$\Omega(\theta)$	Clumping index	-
$\overline{\mu}$	Average inverse diffuse optical depth per unit leaf area	-
Φ	Crown porosity	-
Ψ_l	Leaf water potential	kPa
ρ_{leaf}	Leaf reflectance	-
σ	Stefan-Boltzmann constant	5.67×10^{-8} W.m^{-2}.K^{-4}
τ_{leaf}	Leaf transmittance	-
θ	Sun zenith angle	$^\circ$
θ_l	Leaf normal zenith angle	$^\circ$
ε	Surface emissivity	-
Γ	CO_2 compensation point of respiration	Pa
$\zeta(\mu)$	Structure factor	-
A	Absorptance	-
A_n	Net CO_2 assimilation	μmol.CO_2.m^{-2}.s^{-1}
b	Minimum value of leaf conductance	mmol.m^{-2}.s^{-1}
c_s	CO_2 concentration at the leaf surface	ppm
D	Tree crown diameter	m
E	Evaporation	mm
e^*	Saturated vapour pressure at surface	hPa

E_{FF}	Fossil fuel emission	$\mathrm{GtC.yr^{-1}}$
E_{LUC}	Land-use change emission	$\mathrm{GtC.yr^{-1}}$
e_r	Vapour pressure of the first layer of free atmosphere	hPa
F	Chemical energy of photosynthesis/respiration	$\mathrm{W.m^{-2}}$
$FAVD$	Foliage area volume density	$\mathrm{m^{-1}}$
f_c	Fraction of vegetation cover	-
G	Soil heat flux	$\mathrm{W.m^{-2}}$
$G(\mu)$	Foliage area orientation function	-
G_{ATM}	Growth rate of atmospheric CO_2 concentration	$\mathrm{GtC.yr^{-1}}$
g_s	Leaf conductance	$\mathrm{mmol.m^{-2}.s^{-1}}$
GPP	Gross Primary Productivity	$\mu\mathrm{mol.CO_2.m^{-2}.s^{-1}}$
H	Sensible heat flux	$\mathrm{W.m^{-2}}$
h_s	Relative humidity at the leaf surface	%
I	Vegetation water interception	mm
I_c	Incident irradiance at soil	$\mathrm{W.m^{-2}}$
I_o	Incident irradiance at TOC	$\mathrm{W.m^{-2}}$
k	Light extinction coefficient	-
L	Cumulative LAI	$\mathrm{m^2.m^{-2}}$
$L^{\downarrow}$	Downward longwave radiation	$\mathrm{W.m^{-2}}$
$L^{\uparrow}$	Upward longwave radiation	$\mathrm{W.m^{-2}}$
LAI	Leaf Area Index	$\mathrm{m^2.m^{-2}}$
L_T	Total vertical LAI	$\mathrm{m^2.m^{-2}}$
N	Number of tree crowns within an area	-
NEE	Net Ecosystem Exchange	$\mu\mathrm{mol.CO_2.m^{-2}.s^{-1}}$
NPP	Net Primary Production	$\mu\mathrm{mol.CO_2.m^{-2}.s^{-1}}$
O_a	Partial pressure of atmospheric oxygen	Pa
p	Atmospheric pressure	hPa
P	Precipitation	mm
R	Reflectance	-
R_{drain}	Soil infiltration	mm
R_{surf}	Surface runoff	mm
r_a	Aerodynamic resistance	$\mathrm{s.m^{-1}}$

R_A	Autotrophic respiration	μmol.CO_2.m^{-2}.s^{-1}
r_c	Canopy resistance	s.m^{-1}
R_H	Heterotrophic respiration	μmol.CO_2.m^{-2}.s^{-1}
R_n	Net radiation	W.m^{-2}
S	Water storage term in soil	mm
$S^{\downarrow}$	Downward shortwave radiation	W.m^{-2}
$S^{\uparrow}$	Upward shortwave radiation	W.m^{-2}
S_{LAND}	Land surface uptake of CO_2	GtC.yr^{-1}
S_{OCEAN}	Ocean uptake of CO_2	GtC.yr^{-1}
T	Air temperature	K
T	Transmittance	-
T_s	Surface temperature	K
T_r	Temperature of the first layer of free atmosphere	K
z_0	Surface roughness length	m
c_i	Leaf internal carbon dioxide partial pressure	Pa
dL_c	Leaf area increment	m^2.m^{-2}
f_{sun}	Fraction of sunlit leaves	-
K_c	Michaelis-Menten parameters for CO_2	Pa
K_o	Michaelis-Menten parameters for O_2	Pa
P_{gap}	Direct transmittance	-
V_{cmax}	The maximum rate of carboxylation of Rubisco	mol.CO_2.m^{-2}.s^{-1}
W	Gross photosynthesis rate	μmol.CO_2.m^{-2}.s^{-1}
W_c	Carbon limiting rate of photosynthesis	μmol.CO_2.m^{-2}.s^{-1}
W_e	Export limiting rate of photosynthesis	μmol.CO_2.m^{-2}.s^{-1}
W_l	Light limiting rate of photosynthesis	μmol.CO_2.m^{-2}.s^{-1}
W_p	Smooth minimum of Farquhar limiting regimes	μmol.CO_2.m^{-2}.s^{-1}

Chapter 1:

The Land Surface in the Climate System

1.1 Introduction

This chapter introduces the surface energy balance (Section 1.2.1) and the terrestrial carbon cycle (Section 1.2.2) in order to determine their importance to the Earth system and to establish the research territory of this thesis. Section 1.3 describes the chronological evolution of LSMs and the main scientific steps towards a more accurate understanding and representation of land surface processes in a modelling perspective. Section 1.4 summarises the broad impact of vegetation canopy heterogeneity on the vegetation-soil-atmosphere continuum and it indicates important processes that are still not represented in LSMs. Section 1.6 relates the research territory and niche, and presents the research questions to be addressed by this thesis.

1.2 Overview of the land surface

The Earth system behaves as a single, self-regulating system comprised of physical, chemical, biological, and human components (Pronk, 2002). In order to understand the interactions between those components, natural scientists have done a lot of work on creating and improving Earth system models. Even though humanity has always been under the influence of the weather for several reasons, (e.g., agriculture, natural catastrophes, among others) until the 19^{th} century the weather forecast was based on empirical rules with

limited understanding of physical mechanisms. The advent of new theories based on pre-existing laws of mass continuity, conservation of momentum, and the first and second laws of thermodynamics allowed the prediction of the state of the atmosphere in the future through numerical methods (Lynch, 2008).

Regional mathematical models of weather forecast were soon extended to the entire globe, in order to evaluate the behaviour of the atmosphere as a whole. The first type of general circulation models could realistically depict patterns in the troposphere, however it was the appearance of new knowledge related to other areas of the Earth system, such as the oceans, sea ice, soil, and vegetation, and the concomitant increasing computational power that led the scientific community to the development of more realistic coupled models, the so-called global climate models (GCMs).

GCMs are currently used for understanding the present, and predicting the future, climate. Furthermore, offline implementations of particular components of the Earth system allow researchers to understand and predict the interaction between climate and ecosystems, which are directly related to food production, plant and animal species distribution on planet Earth, and ultimately have an impact on human life itself.

Usually GCMs include information about how radiation, water and momentum are transferred between the land surface and the atmosphere, and these values are calculated by mathematical schemes referred to as land surface models (LSMs). Therefore, LSMs are important for understanding land-surface-atmosphere dynamics and interactions, and climate-carbon feedbacks (Loew et al., 2014; Prentice et al., 2015). LSMs started from simple, idealised, models of the soil-vegetation-atmosphere interface and developed into highly complex models, after years of scientific research in radiative transfer, plant physiology, and hydrology, as well as an increase in data availability due to largescale *in situ* fieldwork and the advance of satellite era (Sellers, 1997).

Among LSMs, there is no consensus on important aspects of the radiative balance or carbon cycle in a future climate (Friedlingstein et al., 2006; Sitch et al., 2008). For instance, differences in surface albedo due to land use change exert a heterogeneous climate forcing; however, there is still a large spread of estimates owing to different assumptions for the albedo of natural and managed surfaces, and a low agreement on the sign of the net change in global mean temperature, resulted from land use change (Myhre et al., 2013). Also lately, several studies have suggested a hiatus on atmospheric CO_2 growth rate due

to increased vegetation carbon uptake (Keenan et al., 2016; Zhu et al., 2016), an effect often attributed to as "the greening of the Earth" (Myneni et al., 1997; Pan et al., 2011), and although the detection of 'greening' is based mainly on observed satellite data, the attribution to various drivers is often based on modelling.

The relevance and realism of several approximations and their potential implications for the range of projections of the future climate have been discussed elsewhere, as far as it concerns land surface modelling (Van Bodegom et al., 2012; Loew et al., 2014), because it is well known that even though LSMs became more complex in the last decades (Prentice et al., 2015), they still misrepresent a large number of biogeophysical processes or parameterisations of sub-grid features that directly impact the Earth radiative and carbon balances (Ciais et al., 2013), The land surface is heterogeneous at spatial scales and LSMs cannot explicitly resolve sub-grid features for the purposes of large-scale modelling, and so parameterisations can be used to address highly non-linear processes in a computationally efficient way (Prentice et al., 2015).

1.2.1 The surface energy balance

Despite the central role of the global energy balance in the climate system, such as the general circulation of the atmosphere and oceans produced by the spatial and temporal radiative imbalances (Hartmann et al., 2013), substantial uncertainties exist in the quantification of its different components and its representation in climate models. Uncertainties in the components of the surface radiation budget are thus generally large and partly related to the partitioning of solar radiation between the atmosphere and surface, including vegetation and soil, as well as the determination of the thermal energy exchanges at the surface/atmosphere interface (Wild et al., 2013).

The Sun irradiates shortwave radiation that can be either absorbed, reflected, or transmitted to the Earth's surface. Given an amount of shortwave radiation ($S^{\downarrow}$) reaching the surface, part of it is reflected back into the atmosphere ($S^{\uparrow}$) depending on the surface albedo (α_s). The balance between incident and reflected shortwave radiation, and incident longwave radiation from the atmosphere ($L^{\downarrow}$) with the outgoing longwave radiation emitted by the Earth's surface ($L^{\uparrow}$) is referred to as net radiation (R_n) (Pitman, 2003):

$$R_n = S^{\downarrow} - S^{\uparrow} + L^{\downarrow} - L^{\uparrow} = S^{\downarrow}(1 - \alpha_s) + L^{\downarrow} - \varepsilon\sigma T_s^4 \tag{1.1}$$

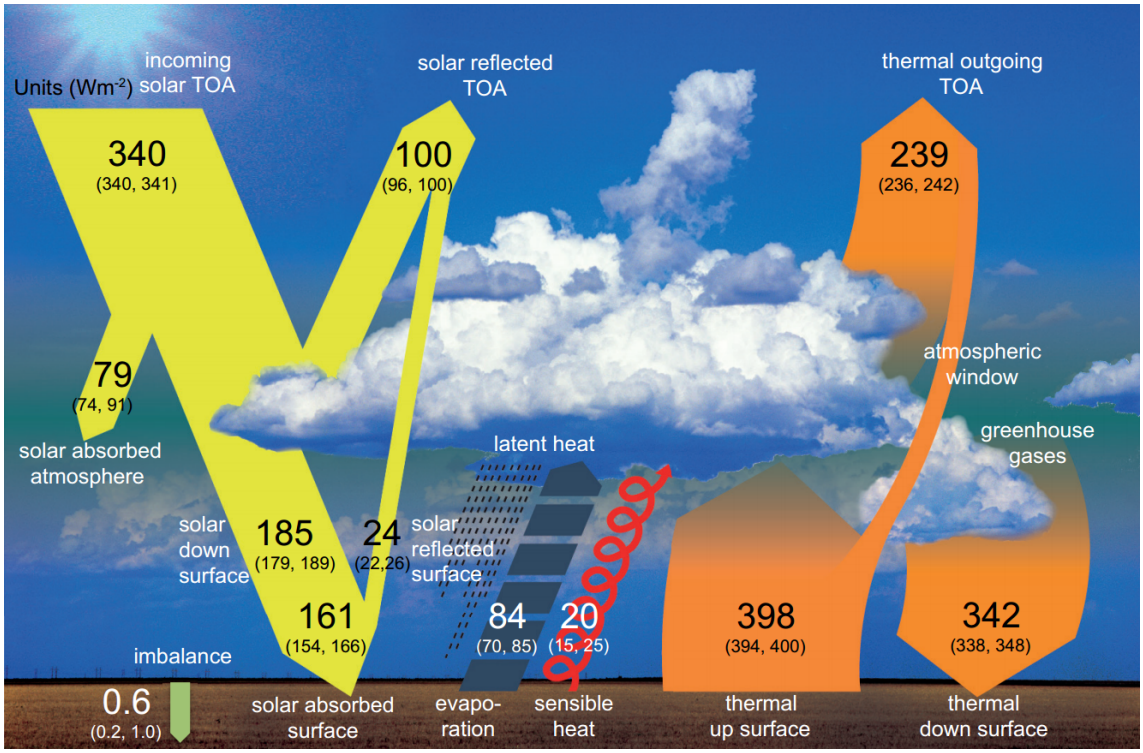

Figure 1.1: Schematic diagram of the global mean energy balance of the Earth. Numbers indicate best estimates for the magnitudes of the globally averaged energy balance components together with their uncertainty ranges, representing present day climate conditions at the beginning of the 21^{st} century. Units W.m^{-2}. Figure taken from Wild et al. (2013).

where ε is the surface emissivity, the Stefan-Boltzmann constant is $\sigma = 5.67 \times 10^{-8}$ W.m^{-2}.K^{-4}, and T_s is the surface temperature in kelvin. An estimate of the radiation budget at Earth's surface is shown in Figure 1.1.

Assuming a global mean surface albedo of 0.13, from the best estimate of 185 W.m^{-2} of incident solar energy at the Earth's surface, 24 W.m^{-2} is reflected. The value of 0.13 corresponds to the multi-model mean albedo of the CMIP5 models used in Wild et al. (2013), and it presents similar values found in previous studies of the surface energy balance, as well as estimates in the reanalyses from the European Centre for Medium Range Weather Prediction (ECMWF) ERA Interim (0.127) and ERA 40 (0.125) (Wild et al., 2013). For the longwave radiation terms, 342 W.m^{-2} corresponds to the incident radiation, and 398 W.m^{-2} is the emitted. Applying these values to Eq. 1.1 gives an average net radiation at the surface equals to 105 W.m^{-2}.

In radiative terms, the Earth's surface has a positive net value and this energy is partitioned by the land surface between sensible heat ($H = 20$ W.m^{-2}), and latent heat

fluxes (λE = 84 W.m^{-2}), plus the soil heat flux (G = 0.6 W.m^{-2}). There is also some chemical energy (F) placed by plant ecosystems when they photosynthesise and released when they respire; however, this chemical energy is usually neglected as it amounts to negligible parts of the absorbed fraction (Sellers et al., 1992):

$$R_n = H + \lambda E + G + F \tag{1.2}$$

Impacts in surface albedo can affect net radiation, and therefore sensible and latent heat fluxes. Although surface albedo naturally varies with seasonal changes in vegetation, rain and snowfall, and Sun zenith angle variability throughout the day and the year, surface albedo can also be directly impacted by human activies such as land use changes (LUC) or natural causes such as wild fires, or indirectly via "the greening of the Earth" or sea level rise. Appropriately determining surface albedo is therefore an important challenge to be addressed in order to accurately perform weather and climate modelling, since an impact on surface albedo can impact surface fluxes of heat and water, and therefore, surface temperature and precipitation.

LSMs usually require values of $S^{\downarrow}$ and $L^{\downarrow}$ to be prescribed and calculate the energy balance by determining α_s and T$_s$. α_s is determined by the radiative transfer scheme in LSMs that work by partitioning the shortwave radiation in different components (see Eq. 1.7) in a simplified way. A number of biogeophysical sub-grid features are not directly represented by LSMs, which may affect the predictions of α_s, and ultimately impact the energy balance. Section 1.4 describes one of these sub-grid biogeophysical features that are not directly resolved in LSMs, and Chapter 4 addresses the impacts that have on surface albedo.

1.2.2 The carbon cycle

The carbon balance of plants

Energy reaching the surface not only impacts the surface energy bugdet but also other biogeochemical cycles dependend on solar radition. The net carbon stored within a terrestrial ecosystem is the difference between carbon uptake during photosynthesis and carbon loss during respiration (Bonan, 2016). The photosynthetic uptake of an individual leaf must

be summed over all canopy to give the Gross Primary Productivity (GPP); plant respiration, or autotrophic respiration (R_A), must be summed over all respiratory tissues in the plant. The difference between carbon losses during maintenance and growth respiration, and carbon assimilation during photosynthesis is referred to as Net Primary Production (NPP).

An ecosystem is not only formed by plants but also other forms of life present in the soil. These microorganisms decompose organic matter and are responsible for carbon losses to the atmosphere, a process called heterotrophic respiration (R_H), together, both forms of respiration (i.e., autotrophic and heterotrophic) comprise the total ecosystem respiration (R_E). The net land-atmosphere carbon flux is referred to as Net Ecosystem Exchange (NEE), which is negative if the ecosystem works as a sink of carbon, and it is positive for a source of carbon to the atmosphere. The carbon balance of an ecosystem is given as follows:

$$NPP - R_H = (GPP - R_A) - R_H = -NEE \tag{1.3}$$

Ecosystems also usually lose carbon by other processes such as wildfire, emission of other trace gases (e.g., BVOCs, methane), and the carbon balance is highly related to other biogeochemical cycles of nutrients such as nitrogen and phosphorus (Figure 1.2).

The global carbon balance

The carbon balance of terrestrial ecosystems is only a portion of the global carbon cycle and it is responsible for roughly 30% uptake of all anthropogenic carbon emissions for the period 2006-2015 (Le Quéré et al., 2016). The global carbon cycle can be interpreted as a series of reservoirs of carbon in the Earth system, which are connected by exchange fluxes of carbon. Since the beginning of the Industrial Era by the 1850s, fossil fuel extraction and their combustion have resulted in the transfer of significant amounts of carbon from deep geological reservoirs into the atmosphere, thus causing an unprecedented, major human-induced perturbation in the carbon cycle (Ciais et al., 2013).

A schematic of the global carbon cycle is shown in Figure 1.3, where the arrows represent emission from the components of the CO_2 budget: (1) fossil fuel combustion and oxidation, and cement production (E_{FF}) and (2) the emissions resulting from deliberate human activities on land leading to land-use change (E_{LUC}), as well as their partitioning among (3) the growth rate of atmospheric CO_2 concentration (G_{ATM}), and the uptake of

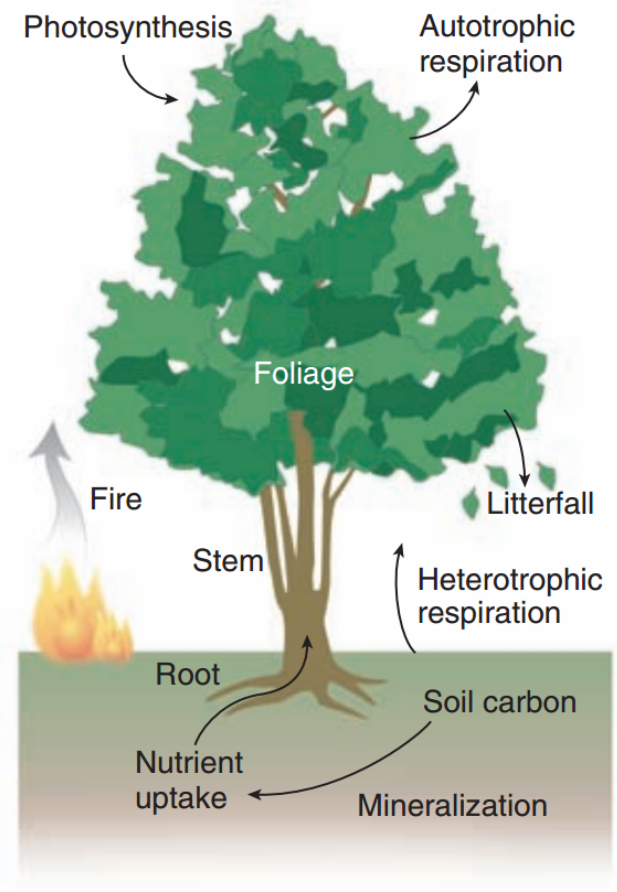

Figure 1.2: Schematic representation of the ecosystem carbon cycle. Figure taken from Bonan (2008).

CO_2 by the "CO_2 sinks" in (4) the ocean (S_{OCEAN}) and (5) on land (S_{LAND}), all given in GtC.yr^{-1}. Uncertainties reported as ± 68% confidence interval (CI) updated from Le Quéré et al. (2009) to the International Geosphere-Biosphere Programme (IGBP) for the Global Carbon Project (GCP). The global emissions and their partitioning among the atmosphere, ocean, and land are in balance following:

$$E_{FF} + E_{LUC} = G_{ATM} + S_{OCEAN} + S_{LAND} \tag{1.4}$$

1.3 Land surface models

LSMs consist of the application and development of computational models that should either, explicitly or implicitly, represent those processes that influence the weather and the climate in their respective relevant time scales (Pitman, 2003). Since their first appearance

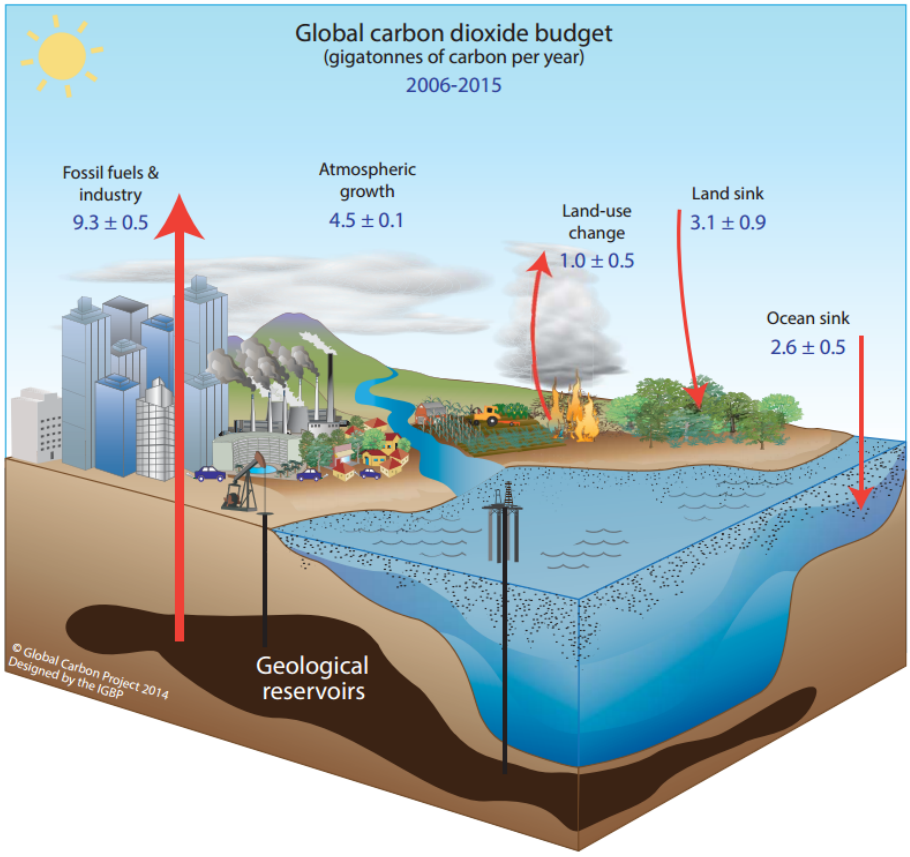

Figure 1.3: Schematic representation of the overall perturbation of the global carbon cycle caused by anthropogenic activities, averaged globally for the decade 2006-2015. Figure taken from Le Quéré et al. (2016).

in the late 1960s and 1970s, LSMs have evolved fast as knowledge increased about diversity and complexity of the Earth system interactions and feedbacks (Prentice et al., 2015), and they are being currently required to perform new and more accurate functions. The next sections briefly review the evolution of land surface modelling and identify current features and processes that are still misrepresented in LSMs.

1.3.1 First-generation models: Manabe bucket scheme

The first generation of LSMs is known as the 'Manabe bucket scheme' (Sellers, 1997; Pitman, 2003; Prentice et al., 2015) because it was firstly implemented by Manabe (1969), and the soil was prescribed as a 'bucket' regarding water holding capacity, which was given as a constant value throughout the globe. All precipitation was turned into surface runoff after the the soil saturation point was reached, and evaporation was limited by the soil water content, air humidity at the surface, and at the free atmosphere. Besides the water

balance in those primitive models, the energy balance was given by Eq. 1.1 and Eq. 1.2 combined, with energy fluxes simply proportionally related to differences in temperature and humidity between the surface and the atmosphere analogously following the Ohm's law with terms G and F equal zero in Eq. 1.2. Figure 1.4 shows a schematic representation of the first-generation bucket scheme taken from Sellers (1997).

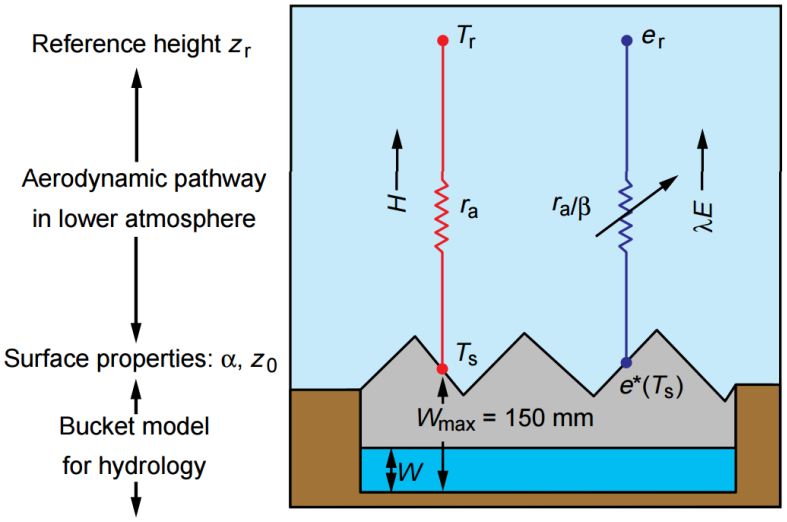

Figure 1.4: Schematic representation of first-generation LSM often referred to as 'Manabe bucket scheme'. T_r is the air temperature within the first layer of the free atmosphere, e_r is the vapour pressure within the first layer of the free atmosphere, r_a is the aerodynamic resistance, T_s is the surface temperature, $e^*(T_s)$ is the saturated vapour pressure at surface temperature, W is the level of moisture in the soil. Figure taken from Sellers (1997).

In early LSMs net radiation is divided into two main components, sensible heat flux, which is related to the surface temperature (T_s) and the air temperature within the first layer of the free atmosphere (T_r), and latent heat flux, which is related to the saturated vapour pressure at surface temperature ($e^*(T_s)$) and the vapour pressure within the first layer of the free atmosphere (e_r). Both fluxes flow between the surface-atmosphere interface following the Ohm's law, where the fluxes are proportional to the aerodynamic resistance (r_a), which is inversely related to the logarithm of the surface roughness length (z_0) and wind speed. In the case of latent heat flux, r_a is regulated by the soil moisture availability function β ($0 \leq \beta \leq 1$), where 0 indicates an empty 'bucket', while 1 indicates the opposite.

In the first-generation LSMs, surface albedo (α in Figure 1.4) and z_0 are prescribed variables. In reality, it is well known the impact that α_s has on the energy balance, as well as z_0 has on fluxes of mass and energy. Surfaces around Earth are significantly different

in terms of albedo and roughness, so the errors associated with assumptions made by this first-generation LSMs were quite significant. Still the first scheme initiated by Manabe (1969) started a significant development on the description and understanding of many land surface related processes that were never before researched or applied.

1.3.2 Second-generation models: two layers scheme

The second generation of LSMs is often referred to as the 'two layers scheme' because in these LSMs the surface can be divided into two separate layers: first, a radiative active vegetation represented as a single bulk layer that interacts with radiation, blocking part of the radiation and allowing the other part to reach the ground; and second, a soil layer divided into two different layers, where a novel method for simulating temperature conductance and moisture propagation throughout the soil was introduced by Deardorff (1978) in the late 1970s and represented a very important development in land surface modelling (Pitman, 2003).

New forms of representing the land-atmosphere interactions were added into second-generation LSMs including: different radiative treatment between soil and vegetation in different spectral bands, because leaves and soil interact differently with distinct parts of the electromagnetic spectrum (Dickinson, 1983; Sellers, 1985); momentum transfer was parameterised as a function of the vegetation roughness length affecting energy and water fluxes (Sellers, 1997); water interception by the vegetation was accounted for, once it can affect evapotranspiration, ground and sensible heat fluxes, as well as soil moisture availability; but perhaps the consideration of plants as a responsive live element with biogeophysical characteristics determining how the atmosphere interacts with the land surface was the most significant scientific upgrade in second-generation LSMs. Although when first biogeophysical LSMs were being formulated in the early 1980s, the climate scientific community did not yet recognised the models relating photosynthesis-stomatal conductance link, or the further impact that could have on surface fluxes represented in GCMs (Sellers, 1997).

Figure 1.5 shows a schematic representation of the second-generation LSMs with separated vegetation up-layer and a underneath layer representing the soil. Water flows from the plants to the atmosphere modulated by a canopy resistance (r_c) (Monteith and Unsworth, 1990b), which is related to the inverse of the leaf stomatal conductance (g_s)

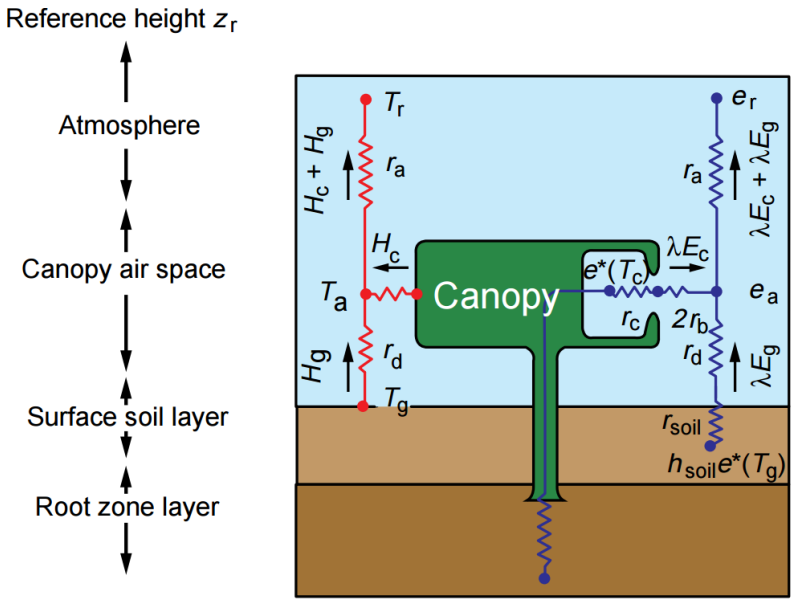

Figure 1.5: Schematic representation of the second-generation LSMs often referred to as 'two layers scheme'. Taken from Sellers (1997).

to the exchange of water vapour from the interior of the leaves to the canopy air outside the plants. Leaf stomatal conductance was first described by the empirical work of Jarvis (1976), and it is related to air temperature (T), vapour pressure deficit (δe), leaf water potential (Ψ_l), and light intensity (PAR) following Equation 1.5:

$$g_s = g_s(PAR)[f(\delta e)f(T)f(\Psi_l)] \tag{1.5}$$

where $g_s(PAR)$ is the unstressed light regulated stomatal conductance and the other functions ($f(x)$) are related to other environmental stress factors described by their respective variables replaced by x (Sellers, 1997).

Modelling canopy conductance empirically is a really important advance of the second-generation LSMs because it takes into account the vegetation as a responsive live element that interacts with environmental conditions. This description takes into account environmental conditions such as air humidity, and plant conditions, such as how light intensity impacts stomatal conductance by controlling stomata opening. Although, this new representation was a significant advance in determining canopy transpiration, stomatal conductance was not providing further information about photosynthesis and other ecosystems metabolic processes.

1.3.3 Third-generation models: the 'greening' of LSMs

The third-generation LSMs is often referred to as the 'greening phase' because carbon started to be considered in these LSMs through knowledge acquired from the plant physiology community (Pitman, 2003). LSMs went through significant advances when the work of Farquhar et al. (1980) was firstly implemented in the late 1980s with further developments in the early 1990s describing leaf photosynthesis as being rate-limited by (i) the amount of the carboxylating enzyme Rubisco and its cycle time (W_c), both mostly controlled by the leaf internal concentration of CO_2, (ii) the efficiency of leaves in absorbing intercepted light (W_l), mostly controlled by the total PAR absorbed by chlorophyll in the leaf, and (iii) the capacity of the leaf to transport and utilise the products of photosynthesis (W_e), mostly controlled by temperature. More details on the Farquhar model are given in Section 3.5.

The linkage between photosynthesis and water availability is often referred to as the "plant's dilemma" (Grill and Ziegler, 1998) because the stomata work to maximise the efficiency of plant water use. In the third-generation LSMs, the "dilemma" was represented via a semi-mechanistic model of leaf photosynthesis, instead of purely empirical like in Equation 1.5, integrating models of stomatal conductance and photosynthesis based on how stomata are believed to function (Figure 1.6a) following the work of Ball (1988) and Collatz et al. (1991):

$$g_s = m\frac{A_n}{c_s}h_s p + b \tag{1.6}$$

where m is an empirical coefficient from observations, A_n is the net CO_2 assimilation, c_s is the CO_2 concentration at the leaf surface, h_s is the relative humidity at the leaf surface, p is the atmospheric pressure, and b is the minimum value of leaf conductance (g_s) described in more detail in Sellers (1997).

A reduction on the total number of parameters needed for calculating net CO_2 assimilation and leaf stomatal conductance represents a step forward from the second-generation LSMs (Figure 1.6b), at the same time that simplifies their relation. Only three parameters (V_{cmax}, m, and b) are used in the calculation of A_n and g_s, where the main parameters derived from observations defining carbon assimilation is V_{cmax}, which is directly related to leaf nitrogen content and it describes the maximum catalytic capacity of the leaf's photosynthetic machinery (Sellers, 1997).

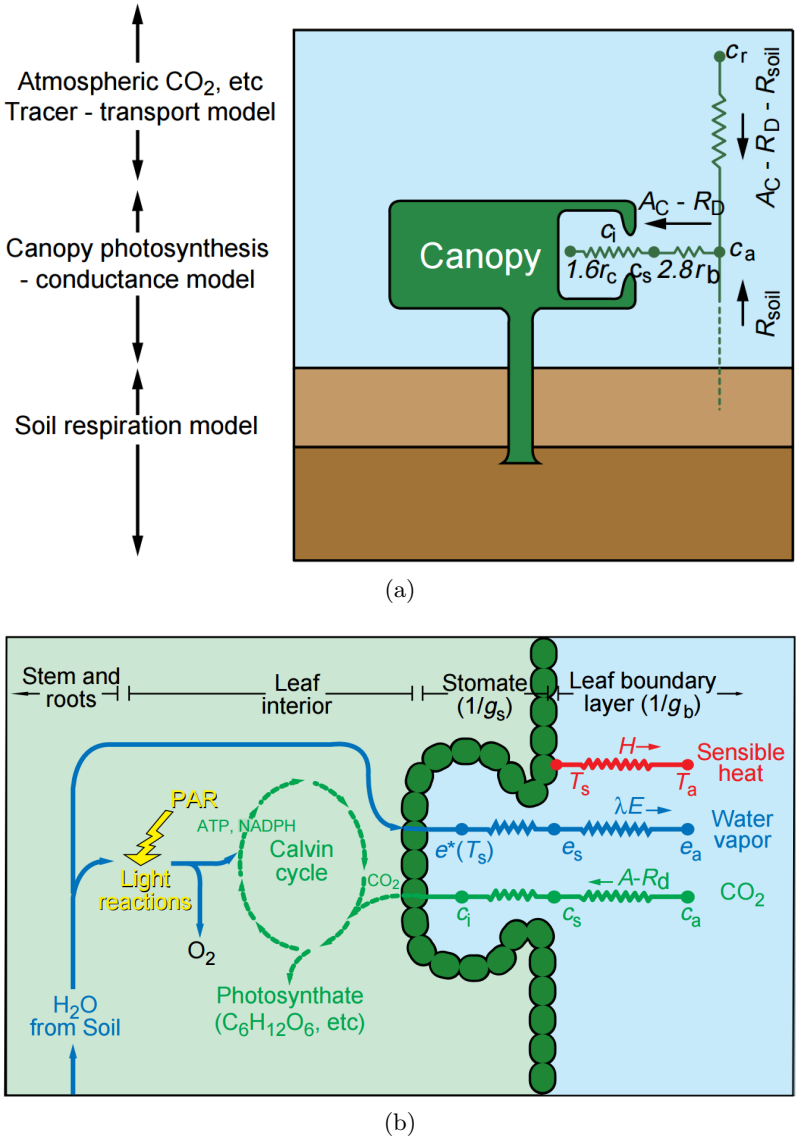

Figure 1.6: Schematic representation of third-generation LSMs often referred to as the 'greening' phase of LSMs. **(a.)** A carbon flux pathway is added to the energy flux pathway shown in Figure 1.5, and; **(b.)** Schematic of carbon and water exchange in a leaf as conceptualised in a combined photosynthesis-conductance model. Figure taken from Sellers (1997).

The complete equation set can be solved to yield mutually consistent values of leaf photosynthesis and transpiration (Sellers, 1997; Pitman, 2003), which makes the third-generation LSMs present advantages over their predecessors including: (i) a more realistic biological link between photosynthesis and stomatal conductance models in order to perform coupled calculations of fluxes of energy, water, and carbon; (ii) fewer empirical parameters are required to perform the calculations, since the processes are described in a more mechanistic way; and (iii) LSMs can respond directly to fluctuations in atmospheric

CO_2 concentrations in a more realistic way, therefore third-generation LSMs are more suitable for climate change related studies (Sellers, 1997).

1.4 Impacts of vegetation canopy architecture on LSMs

Vegetation canopy architecture, or structure, plays an important role in the partitioning of incident solar radiation, photosynthesis, transpiration, and momentum fluxes (Nilson, 1971; Goudriaan, 1977; Norman and Welles, 1983; Sellers, 1997; Pinty et al., 2006; Kobayashi et al., 2012; Loew et al., 2014; Dutta et al., 2017). Canopy structure may be thought of as the amount and organisation of aboveground plant material, which might include size, shape, orientation, and positional distribution of various plant organs such as leaves, stems, branches, flowers, and fruits (Norman and Campbell, 1989).

Plant canopies can be structurally diverse due to unique spatial patterns that different species adopt for intercepting light and an even diversity of plant species which occupies a natural community (Atwell et al., 1999). Although it is clear that vegetation architectural features might be due to adaptive evolutionary reasons, such as hydraulic constraints, maximise reproduction, maximise light capture and carbon gain (Pearcy et al., 2005), the nature of structural organisation driving land plant evolution has been an enigma for over 200 years (Jill Harrison, 2017).

The term structure is broad and not-limited to individual plants, while the level of complexity usually increases from uniform stands to heterogeneous plant comunities. In particular in this thesis, vegetation canopy structure is interpreted as the spatial separation of individual leaves or whole plants, i.e., the 'gaps' in between and/or within the vegetation, with regions where radiation, water or wind travel without interacting with plant material, and remaining regions where these environmental elements directly interact with some parts of the canopy.

Canopy heterogeneous structure can affect the land surface fluxes with the atmosphere in four main different fronts: (1) radiation, (2) carbon, (3) water, and (4) momentum. The following subsections describe how canopy architecture can affect each one these fluxes in LSMs.

1.4.1 Radiation

The first major impact of canopy architecture is on light distribution within plant canopies, where the impacts can be numerous as: on photosynthesis, stomatal conductance, energy balance, and leaf temperature in a short-term response but also related to delayed responses, such as nitrogen and nutrients distribution throughout the canopy and the variability in architecture itself. As discussed in Section 1.2.1, changes in surface albedo can change the surface energy balance. The spectral shortwave radiation interacts with the vegetation canopy following the energy conservation law according to Equation 1.7, which describes the shortwave radiation partitioning in a determined wavelength, or narrow waveband, in a vegetation canopy as:

$$A + R + T \cdot (1 - \alpha_{soil}) = 1.0 \tag{1.7}$$

where A is absorptance, R is reflectance or the surface/canopy albedo (α_s) in a specific radiation waveband, T is the total transmittance, and α_{soil} is the soil albedo underneath the vegetation canopy, i.e., once energy is not emitted in this part of the electromagnetic spectrum, the energy can be either absorbed, refelected, or transmitted.

The explicit representation of 3D canopy architecture in GCMs is not possible yet because of computational efficiency and limitation of available known parameters; however, some studies (Yang et al., 2001; Yang and Friedl, 2003) have performed some evaluations of 3D canopy architecture on shortwave radiation partitioning and their main findings indicate a decrease in canopy absorptance, and an increase in canopy reflectance and total transmittance. There is a systematic bias resulting from the lack of this process representation in LSMs.

1.4.2 Carbon

Canopy architecture affects how shortwave radiation is intercepted by the vegetation and, consequently, influences canopy photosynthesis (Sarlikioti et al., 2011). The consideration of vegetation structure on the way that shortwave radiation propagates through the canopy influences the local environment, such as changes in leaf temperature, for example, and it can impact physiological processes on the regulatory aspects of photosynthetic carbon metabolism, playing an important role in the dynamic responses of CO_2 assimilation, as

well as it has an impact on the ecology of understory plants (Porcar-Castell and Palmroth, 2012).

Current LSMs (e.g., JULES (Clark et al., 2011), CLM4CN (Lawrence et al., 2011), ORCHIDEE (Krinner et al., 2005)) deal with plant canopies as they were a 1D turbid medium, therefore they often do not consider horizontal structural variability in plant communities, such as the presence of 'gaps' in the canopy. Considering 'gaps' is critical in the lower parts of dense canopies, where light is a limiting factor of photosynthesis and diffuse radiation becomes the dominant source of energy of bottom layers (Roden and Pearcy, 1993). In addition, areas located at very high latitudes, where incident sunlight comes from steep angles, are often light-limited.

Heterogeneous canopy architecture can make the variability of the spatial light environment highly dynamical, which could lead to a significant impact on photosynthesis in parts of the canopy with limited light availability, such as the bottom of dense canopies, such as tropical forests, for example. Analysis of δ13C of biomass reveals that the annual contribution of carbon fixed during episodes of direct radiation reaching the canopy floor can be close to 50% for certain understory species (Pearcy and Pfitsch, 1991), and not considering canopy gaps in LSMs could lead to an underestimation of photosynthesis.

Photosynthesis is the biological mechanism responsible for gross productivity in plants, but ecosystems also lose carbon via respiration (Eq. 1.3). Respiration is highly related to temperature, and differences in the radiative environment description in LSMs can impact leaf and canopy temperatures, that ultimately can impact canopy respiration, by affecting both, autotrophic and heterotrophic respiration.

It is also important to remember that carbon fluxes can be passively affected by canopy architecture via turbulent fluxes. Both transport and production processes result in spatial variation of carbon within tree canopies, especially along vertical transects in dense forest stands (Godin et al., 2005), and more details are given in Section 1.4.4.

1.4.3 Water

Precipitation (P) can be either intercepted by vegetation (I), which can either evaporates (E_c), or drips to the soil underneath. Precipitation can also reach the soil surface directly, that combined with the drip from intercepted water, can either evaporates (E_s), infiltrates the soil (R_{drain}) or run across the soil surface (R_{surf}). The evaporation term (E) has

another component over vegetated areas, related to the transpiration by the plants (E_t). Part of precipitation remains in the soil as a storage term (S) and changes in soil moisture storage (ΔS) take part in the water balance according to Equation 1.8:

$$P = E - I - R - \Delta S = E_c + E_s + E_t - I - R_{surf} - R_{drain} - \Delta S \tag{1.8}$$

Water that reaches the soil surface may drain through the soil or may evaporate from the surface. Drained water can also be taken up by the plants roots and evapotranspired back to the atmosphere. Soil moisture impacts many processes in LSMs, and although only a small portion of the total water is stored in the soil, it is important for photosynthesis and fresh water storage (Pitman, 2003). Note that the water balance has the evaporation component, E (kg.m^{-2}.s^{-2}), which is linked to the surface energy balance through latent heat flux, λE (W.m^{-2}), where λ (J.kg^{-1}) is the latent heat of vaporisation.

LSMs used in the last CMIP5 (Anav et al., 2013) make use of a one-dimensional description of the water balance given the canopy structure under the assumption of horizontal homogeneity, usually dependent on surface types, and variables like the 'vegetation canopy water holding capacity' through the interception of precipitation, which depends on the amount of vegetated material. The balance between soil water flux and evapotranspiration is affected by the spatial distribution of vegetation, roots depth, soil properties, as well as the evaporation of intercepted water, among other things. This three-dimensional impact of vegetation structure on the water balance can impact the surface energy balance and a number of other processes linked to atmosphere-biosphere interactions.

Rainfall interception by plants involves similar processes to those involved in radiation interception related to plant heterogeneous architecture, as well as direct rain troughfall and stemflow induce spatial variability of rainfall water at the ground surface, which can impact soil moisture. Furthermore, rainfall interception can be impacted by vegetation canopy heterogeneity and influence the water partitioning at canopy scales (Godin et al., 2005). Some detailed rainfall interception models have been tested using 3D virtual plants, such as the DROP model (Bussiere et al., 2002), or Monte Carlo like approaches (Saint-Jean et al., 2004), and these authors were able to demonstrate a significant impact of vegetation structure on water partitioning.

1.4.4 Momentum

Plant canopies are not smooth surfaces and they generate turbulence, which enhances the exchange of energy and mass. Thus, appropriately describing the aerodynamic resistance of the surface is important to determine atmosphere-biosphere exchanges (Pitman, 2003). The aerodynamic resistance is a function of friction properties of the land surface, including the logarithm of the surface roughness length for momentum (z_0), but it is also dependent upon environmental characteristics of the air flow, such as wind speed, for example. Considering that turbulence structure depends on the interaction between plant canopy architecture and atmospheric boundary layer dynamics, several models provide a 1D description of the wind field given canopy structure under the assumptions of horizontal homogeneity, neutrality, and steady state conditions (Marcolla et al., 2003); and perhaps the major limitation in the application of turbulence closure models to plant canopies is the quantitative description of plant architectural features determining the aerodynamics and the momentum absorption.

In current LSMs, the description of canopy structure for the application of turbulence closure models is based on vertical profiles of leaf area density and drag coefficient, which are sometimes proportional to canopy height only, and which often overestimate the variability of the drag coefficient among different canopies (Marcolla et al., 2003). Few authors (Marcolla et al., 2003; Yang and Friedl, 2003) attempted to parameterise canopy 3D architectural effects on turbulence in a comparative way to the effects of canopy structure on shortwave radiation partitioning, and these studies were able to generate model improvements for vertical wind profiles and sensible heat flux.

A more recent study (Seidl et al., 2014) used 3D plant canopy heterogeneity to simulate wind disturbance impacts on forest landscapes finding that neglecting structural and spatial heterogeneity resulted in underestimated forest damage. Another study performed in laboratory (Bai et al., 2015) demonstrated that 3D canopy geometry impacts air flow within the canopy, and the authors were able to establish a significant link between canopy heterogeneity and turbulence.

1.5 Discussion

The evolution of LSMs from their early development until the addition of realistic biological features linking photosynthesis and water fluxes has being described by several authors (Sellers, 1997; Pitman, 2003; Prentice et al., 2015) as one of the major factors of increased confidence in future climate predictions; however, there are still several physical based processes missing or poorly represented in current LSMs.

According to the IPCC Fifth Assessment Report (AR) some important poorly represented or missing processes in current LSMs are: (i) LSMs are still at their early stages in dealing with transfer of radiation, water and heat, which are still treated very simply (Ciais et al., 2013; Prentice et al., 2015); (ii) nutrient dynamics are taken into account only by a small number of LSMs despite the fact it is well established that nutrient constrains photosynthesis once nitrogen deposition can enhance carbon assimilation (LeBauer and Treseder, 2008), as well as phosphorus dynamics (Goll et al., 2012); (iii) many key processes relevant to decomposition of carbon are missing in LSMs (Todd-Brown et al., 2012), particularly for permafrost carbon and for carbon in boreal and tropical wetlands and peatlands; (iv) the negative effects of elevated tropospheric ozone on GPP have not been taken into account by most currently used LSMs (Sitch et al., 2007), and; (v) LSMs, in general, do not explicitly take into account the various forms of disturbances or ecosystem dynamics (e.g, migration, fire, logging, harvesting, insect outbreaks), and the resulting variation in forest age and structure, which is known to affect the net carbon exchange (Kurz et al., 2008; Higgins and Harte, 2012; Hardiman et al., 2013; Ciais et al., 2013).

Among all the space for improvement in land surface modelling, more physically accurate ways to calculate transfer of radiation, water, and heat are fundamental to increase the understanding of land surface physical based processes. Most LSMs make unrealistic assumptions to treat the transfer of energy and mass between the land surface and the atmosphere, mainly because of lack of computational power to deal with such level of detail over large areas for long periods of time, lack of knowledge of all parameters involved in the calculations, and lack of theoretical description in large scales of all the processes related to biosphere-atmosphere exchanges.

In Le Quéré et al. (2016) most uncertainties in the global carbon cycle are allocated to S_{LAND} (see Eq. 1.4) because of processes that are poorly represented or understood in LSMs. S_{LAND} is often estimated as the residual term in the global carbon budget, and in

order to verify its consistency, S_{LAND} is usually compared to LSM simulations. Throughout the last decades the LSMs mean value of carbon assimilation presents an average to high correlation with S_{LAND} ($r = 0.68$, $0.50 < r < 0.78$ for individual models); however, the LSMs did not contribute to reduce the uncertainties associated with the terrestrial CO_2 sink in comparison to the residual budget (Le Quéré et al., 2016). This result indicates that LSMs are still lacking of important processes needed to reduce uncertainties in future climate scenarios, even though the LSMs ensemble mean and the residual method values are within their respective range of uncertainties.

1.6 Direction of the thesis

The general aim of this thesis is to explore the impact of vegetation architecture heterogeneity at the sub-grid scale (not directly resolved in LSMs) on the transfer of shortwave radiation in the vegetation-soil-atmosphere continuum, treated in a very simplified way in GCMs (Ciais et al., 2013) and currently used to make important predictions about radiative forcing and carbon assimilation.

LSMs use incoming shortwave radiation among other physical data to diagnose relevant variables for weather forecast and climate predictions. More about the primary impact of shortwave radiation on the land surface can be found in Section 1.2.1. The two-stream scheme (Sellers, 1985) is a 1D radiative transfer scheme commonly used in LSMs, which does not account for vegetation 3D structural influences on radiation partitioning, because it treats the vegetation canopy as a homogeneous volume with randomly distributed leaves and constant radiative properties related to absorption and scattering of light. Section 1.4.1 describes how canopy architecture impacts light distribution within plant canopies, and a detailed description of the two-stream scheme can be found in Section 2.2.3.

Highly detailed canopy radiative transfer schemes have been developed (Wang and Jarvis, 1990; Ni et al., 1999; Gastellu-Etchegorry, 2008; Duursma and Medlyn, 2012), but they are too computationally expensive to be employed in large-scale studies over long time periods (Song et al., 2009) in GCMs. In order to account for architectural effects of vegetation on shortwave radiation partitioning, some studies (Kucharik et al., 1999; Pinty et al., 2006; Ni-Meister et al., 2010) attempted to develop efficient parameterisation

schemes in radiative transfer schemes of LSMs by modulating the optical depth of the vegetation canopy through the addition of an effective variable so-called 'clumping index' (Nilson, 1971). The clumping index was firstly introduced as a constant value, but few other authors (Pinty et al., 2006; Ryu et al., 2010) described the dependence of clumping index on Sun zenith angle. More details on the clumping index are given in Section 2.4.1.

The importance of considering a clumping index that varies with Sun zenith angle is not a concensus in the literature but it is relevant in the context of biogeophysical modelling, because it can affect surface albedo and land photosynthesis. Moreover, more radiometric data have been collected over the past decades associated with biogeophysical responses of the land surface, such as the derivation of GPP through eddy covariance and flux partitioning techniques. More data, together with the development of new methodologies and models, present a scientific opportunity to further explore the impact of clumping index parameterisation schemes on photosynthesis.

The specific research questions of this PhD are:

1. By using a 'clumping index', is it possible to make the 1D two-stream scheme match the shortwave radiation partitioning (means absorptance/reflectance/transmittance) of more complex models that explicitly account for 3D structural variability of vegetation canopies?

2. To what extent is it possible to retrieve the required parameters of a clumping index that varies with Sun zenith angle from digital hemispherical photographs?

3. What are the impacts of clumping on photosynthesis calculated by the Farquhar model at site and global levels?

This thesis is divided into seven chapters, where Chapter 1 was used to explore the wider context of the land surface in the climate system with focus on the energy and carbon balances, a description of the major contributions to the development of LSMs, and a description of how canopy structure may impact radiation partitioning and other land surface related processes.

Chapter 2 describes the radiative transfer theory and the impacts of different radiative transfer schemes on the energy budget and the carbon cycle. It also describes the concept of clumping index as an approach to considering canopy structure in 1D radiative transfer schemes. Chapter 2 identifies gaps in the literature related to a clumping index that varies

with Sun zenith angle, and its acquisition in the field. In the same chapter there is also a brief section of studies using *in situ* measurements to derive vegetation structural related parameters.

Chapter 3 describes the radiative transfer models used in this thesis, the co-limitation photosynthesis model proposed by Farquhar et al. (1980), and the study sites and data collected in each of them.

Chapter 4 investigates the impacts of vegetation canopy structure on shortwave radiation partitioning through the evaluation of different parameterisation schemes in the two-stream scheme over different canopy scenes.

Chapter 5 explores observational methods to derive and compute vegetation structural parameters. First, it describes and evaluates different treatments of digital hemispherical photographs in order to estimate the direct transmittance for each one of the study sites. Second, it compares the values obtained through observations with results from a 3D model for two sites where structural LiDAR data was also available. Third, it statistically compares the measured direct transmittance with the fitted direct transmittance for two different 'clumping indices', in order to determine whether the dependency of vegetation structure on Sun zenith angle matters for the correct determination of the impact of canopy structural variability on shortwave radiation partitioning and carbon fluxes at site level.

Chapter 6 is used to evaluate the impact of vegetation canopy structure on shortwave radiation partitioning through an experiment performed for the entire globe with a modified version of the JULES land surface model (Best et al., 2011; Clark et al., 2011) including structural data derived from remote sensing. The new version of the land surface model is also used to better understand the spatial distribution of the Farquhar co-limiting regimes of photosynthesis over the world, and to determine the impact of vegetation structure on global carbon assimilation.

Finally, Chapter 7 summarises the main findings of the thesis and points out remaining open questions that were not addressed by this work, but could be further developed in the future.

Chapter 2:

Vegetation Canopy Architecture Heterogeneity in RT Schemes

2.1 Introduction

The main goals of this chapter are: first, to describe the general field of radiative transfer in LSMs and second, to identify places where improvements could be made in this area. To this end, this chapter critically evaluates the parameterisation schemes proposed by different authors to account for vegetation canopy structural heterogeneity on the shortwave radiation partitioning by radiative transfer schemes.

Section 2.2 establishes the research territory of vegetation radiative transfer representations in LSMs by describing the main theories and approaches. Section 2.3 explores the application of this research territory through the review of the impact of canopy architecture representation in LSMs on carbon assimilation. Section 2.4 compares approaches to parameterise canopy structure in radiative transfer schemes, and it summarises the pros and cons of various schemes. Section 2.5 discusses ways to assess radiative transfer schemes and parameterisations, as well as ways to observe radiative transfer related variables.

2.2 Vegetation radiative transfer schemes in LSMs

Regarding land surface-atmosphere interactions, the most important processes to be represented in LSMs are: (i) shortwave radiative transfer, (ii) sensible and latent heat fluxes between the land surface and the atmosphere, and (iii) momentum transfer between the

lower atmosphere and the land surface due to wind deceleration caused by friction (Sellers, 1997).

Radiative transfer in vegetation canopies determines the energy going into the land surface. Also, the partitioning of solar radiation between various compartments of the surface constitutes an important process to further quantify and understand the role of vegetation in distributing energy, which drives related biogeophysical processes, such as photosynthesis, evapotranspiration, changes in leaf and soil temperature, and snowmelt (Alton et al., 2007; Widlowski et al., 2011).

Shortwave solar radiation can be absorbed or scattered by the vegetation canopy as a result of the interaction of photons travelling through a medium mostly comprised of foliage, bounded by a radiative participating surface at the bottom and a radiative participating atmosphere at the top. The next sub-sections introduce important variables related to the radiative transfer theory, and radiative transfer schemes of different complexities.

2.2.1 Basic principles: LAI and extinction coefficient

The portion of radiation that goes through a vegetation canopy is mostly determined by the amount of vegetated material within the canopy. Defined as: "the one-sided leaf area per unit ground area" (Watson, 1937), the leaf area index (LAI) links canopy structure, i.e., the amount of vegetated material spatially distributed throughout the canopy, and function of ecosystems for several reasons:

1. LAI influences the radiative balance of LSMs. It is used to calculate the amount of intercepted Photosynthetically Active Radiation (PAR, 400-700 nm) by leaves, which is directly related to the amount of CO_2 assimilation through photosynthesis (Norman, 1982; De Pury and Farquhar, 1997); it is related to the amount of reflected shortwave radiation by the surface (Ni and Woodcock, 2000; Anderson et al., 2005), which has an impact on the energy balance; and finally, it affects canopy transmittance, which impacts soil temperature and the timing of snowmelt (Hardy et al., 1997);

2. LAI impacts rainfall interception (Aston, 1979), hence soil evaporation (Schulze et al., 1994; Kelliher et al., 1995), and canopy evapotranspiration (Leuning et al., 1995; Baldocchi et al., 2002), which has implications on ecosystem hydrological dy-

namics;

3. LAI affects momentum exchanges between the surface and the atmosphere. LAI decreases wind speed due to surface friction impacting energy and mass exchanges on the land surface-atmosphere interface (Albertson et al., 2001).

Appropriately determining and understanding LAI is fundamental to accurately determine most of the biogeophysical processes represented in LSMs. Different plant functional types (PFTs) are often characterised by different amounts and ranges of LAI, leaf biomass, and leaf area density (Asner et al., 2003). Some studies (Woodward, 1987; Scheffer et al., 2005) also suggested that LAI can be strongly related to nutrient cycles and water balance at site level. However, LAI does not provide sufficient information to estimate shortwave radiation partitioning within vegetation canopies because leaves can present different angular orientation in nature. Therefore, other variables are necessary to determine the path length of shortwave radiation through the vegetation canopy.

The extinction coefficient (k) can be equated to the ratio between the shadow cast by a leaf on the horizontal and the leaf area (Monteith and Unsworth, 1990a), and it is used to attenuate shortwave radiation propagation in vegetation canopies. Several approaches have been proposed to understand and compute the extinction coefficient, especially regarding leaf angle distribution (Ross, 1981), and the effect that leaf angle can have on radiation path length through the canopy (Wang et al., 2007). The extinction coefficient is considered as the fraction of hemi-surface leaf area that is projected onto the horizontal from a particular zenith angle (θ).

In real canopies, leaves are described by a statistical distribution of a range of elevation and azimuth angles. The leaf orientation function is derived using solid angle geometry (Ross, 1981; Myneni et al., 1989). In the radiative transfer literature, a commonly used assumption is that foliage angular distribution is random, or often referred to as 'spherical', and $k = 0.5$ is usually assigned to describe the projection coefficient for objects of any shape (Chen et al., 1997).

2.2.2 Beer's law

Monsi and Saeki (1953) were the first authors to propose a radiative transfer scheme to estimate the attenuation of the incident radiation through a vegetation canopy by a

method called the "big-leaf approach", so-called because it treats vegetation as a single body of vegetated material. The method follows essentially the Beer-Bourguer-Lambert's law, as described below:

$$I_c = I_o \exp(-k.LAI) \tag{2.1}$$

where I_c is the incident irradiance at the soil surface beneath the vegetation canopy, I_o is the incident irradiance at the top of the vegetation canopy (TOC), k is the light extinction coefficient, and LAI is the leaf area index, which includes leaves and woody components, and because of that, it is sometimes referred to as Plant Area Index (PAI).

The main assumption made when using the Beer's law is that shortwave radiation passes through a vegetation medium containing infinitesimal radiative active particles, that can either absorb or scatter radiation, and these particles are assumed to be uniformly distributed throughout the turbid medium (Figure 2.1). However, the assumption made in Eq. 2.1 is a simplification because plant stands are composed of clumped groups of leaves, with a particular angular distribution (Sinclair, 2006).

Because of its theoretical simplicity and computational efficiency, Beer's law has been commonly used in LSMs, however, it does not account for the loss of scattered radiation (Wang, 2003). Radiative scattering processes are fundamental to accurately determine the Earth's surface albedo, which is a basic control factor for the surface energy budget (Dickinson, 1983).

2.2.3 The two-stream scheme

To account for the effects of multiple scattering by air molecules, aerosols, and cloud particles, the two-stream scheme is a radiative transfer scheme commonly used in numerical weather prediction and climate modelling. In the two-stream scheme, the radiation field is divided into the direct solar beam, plus the diffuse solar radiation (i.e., radiation scattered at least once), and in two directions, downward and upward. The angular distribution of scattered radiation is not computed in any further detail, which means that they are effectively isotropic (Räisäenen, 2002).

Meador and Weaver (1980) introduced a new method of the two-stream scheme after reviewing some variant forms of the two-stream scheme applied to the radiative transfer in the atmosphere. Not many years after that Dickinson (1983) expanded the two-stream

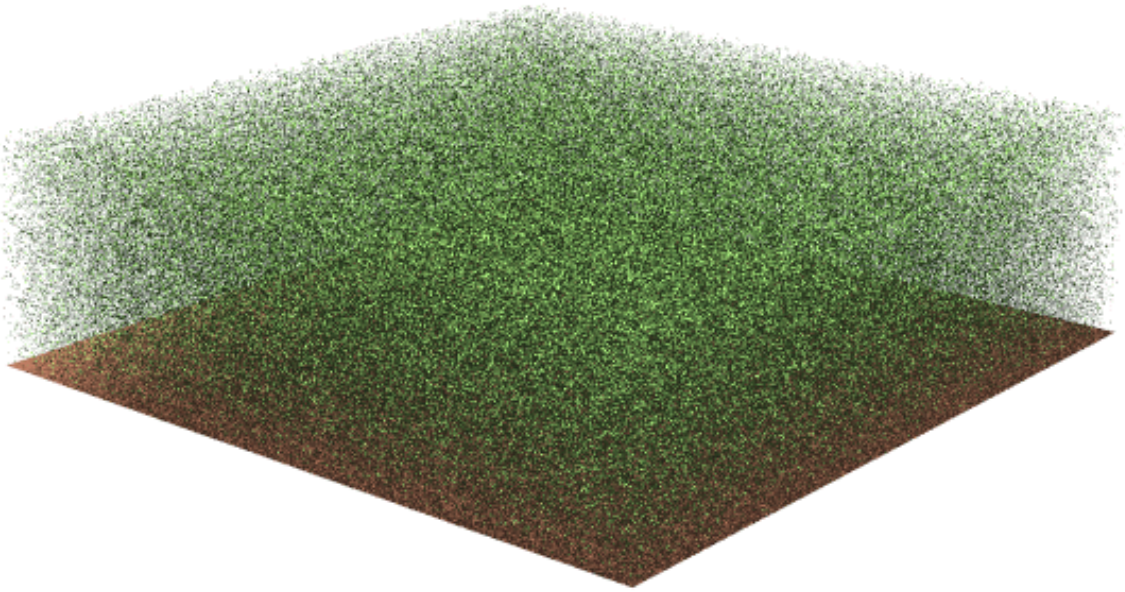

Figure 2.1: Structurally homogeneous canopy scenario with infinitesimally small (turbid) foliage representations. Figure taken from Widlowski et al. (2007).

scheme to be applied in vegetation canopies, and therefore it became suitable for LSM applications. However, it was the study of Sellers (1985) that split the two-stream scheme in two separate shortwave wavebands, PAR and NIR, to calculate values of hemispheric canopy reflectance and make comparisons with observations of surface albedo.

The two-stream scheme assumes that the optical properties of leaves are identical in both sides, upper and lower. The two-stream scheme is given by the following equations, as described in Sellers (1985):

$$\begin{aligned} -\overline{\mu}(dI^{\uparrow})/dL + [1-(1-\beta)\omega]I^{\uparrow} - \omega\beta I^{\downarrow} &= \omega\overline{\mu}K\beta_0 \exp(-KL), \\ -\overline{\mu}(dI^{\downarrow})/dL + [1-(1-\beta)\omega]I^{\downarrow} - \omega\beta I^{\uparrow} &= \omega\overline{\mu}K(1-\beta_0) \exp(-KL) \end{aligned} \tag{2.2}$$

where $I^{\uparrow}$ and $I^{\downarrow}$ are the upward and downward diffuse radiative fluxes normalised by the incident flux respectively, μ is the cosine of the Sun zenith angle, or the incident beam, K is the optical depth of direct beam per unit leaf area and it is often equal to $G(\mu)/\mu$, where $G(\mu)$ is the projected area of leaf elements in the direction $cos^{-1}\mu$, $\overline{\mu}$ is the average inverse diffuse optical depth per unit leaf area, and it is equal to $\int_0^1 [\mu'/G(\mu')]d\mu'$, μ' is the direction of scattered flux, ω is the scattering coefficient and is given by $\rho_{leaf} + \tau_{leaf}$, the leaf reflectance and transmittance respectively, and L is the cumulative LAI. β and β_0 are

upscattering parameters for the diffuse and direct beams, respectively (see Sellers (1985) for details).

In order to obtain an exact solution for Equations 2.2 it is necessary to specify appropriate boundary conditions (Sellers, 1985). In the case of direct radiation, the top boundary condition is $I^{\downarrow} = 0$ for L = 0, and the bottom boundary condition is $I^{\uparrow} = \rho_s[I^{\downarrow} + \exp(-kL)]$ for $L = L_T$, where ρ_s is the soil reflectance and L_T is the total vertical LAI. The corresponding solution of Equations 2.2 yields are:

$$\begin{aligned} I^{\uparrow} &= \frac{h_1 \exp(-KL)}{\sigma} + h_2 \exp(-hL) + h_3 \exp(hL), \\ I^{\downarrow} &= \frac{h_4 \exp(-KL)}{\sigma} + h_5 \exp(-hL) + h_6 \exp(hL) \end{aligned} \tag{2.3}$$

In the case of diffuse radiation, the top boundary condition is $I^{\downarrow} = 1$ for L = 0, and the bottom boundary condition is $I^{\uparrow} = \rho_s I^{\downarrow}$ for $L = L_T$. Therefore, the corresponding solution is given as:

$$\begin{aligned} I^{\uparrow} &= h_7 \exp(-hL) + h_8 \exp(hL), \\ I^{\downarrow} &= h_9 \exp(-hL) + h_{10} \exp(hL) \end{aligned} \tag{2.4}$$

where coefficients such as σ and h_1 to h_{10} can be found in Sellers (1985). Note that there is an error in the expression for h_4 in the appendix of Sellers (1985). The correct expression can be found in Sellers et al. (1996).

2.2.4 3D radiative transfer schemes

For most natural woody vegetation such as conifers and savannahs, the spatial distribution of individual tree crowns creates clear spaces where beam radiation propagates without interference of vegetation elements, and because of that the two-stream scheme results in large deviations from the actual amounts of absorbed and reflected radiation (Pinty et al., 2006; Ni-Meister et al., 2010; Kobayashi et al., 2012; Loew et al., 2014).

For detailed computation of radiation fields within heterogeneous vegetation canopies, radiative transfer schemes can use different complexities to approach the problem. The two-stream scheme was adapted by Dai et al. (2004) to account for sunfleck penetration in order to better simulate the impacts of clearings on shortwave radiation partitioning, and a description of its methodology is presented in Section 3.2.1. Other more complex approaches can be used, such as MAESPA (Wang and Jarvis, 1990; Duursma and Medlyn,

2012), which treats vegetation canopy heterogeneity by setting individual tree crowns within the stand, or through a geometrical optical approach like in the GORT model (Li et al., 1995), which statistically distributes individual trees within the stand and accounts for multiple scattering with foliage clumped within tree crowns. A number of other more complex 3D radiative transfer schemes are based on Monte Carlo simulation of photon transport, such as the FLIGHT model (North, 1996; Disney et al., 2000), the DART model (Gastellu-Etchegorry et al., 1996, 2004), and the raytran model (Govaerts and Verstraete, 1998). However, these 3D radiative transfer models cannot be directly used in LSMs due to their computational expense (Yang et al., 2001), and high number of required vegetation structural parameters (Loew et al., 2014). The 3D models MAESPA and GORT used in this thesis are described in Section 3.2.2 and Section 3.2.3, respectively.

2.3 Impacts of using different radiative transfer schemes

The amount of absorbed radiation obtained with the Beer's law overestimates the values calculated with the two-stream scheme (Wang, 2003). As previously discussed, the Beer's law does not consider any order of scattering, which implies that by using this method, any interaction between the downward beam radiation and elements of the vegetation canopy is assumed to be either absorbed or transmitted.

On the other hand, the two-stream scheme considers all orders of scattering, which means that part of the downward beam radiation after interaction with the vegetation canopy is scattered to an isotropic diffuse form. The upward scattered radiation not absorbed by the vegetation canopy is the sum between the contribution of scattered radiation by the vegetation and the one scattered by the background soil. The scattered radiation by the background soil can be absorbed by the vegetation canopy, transmitted upwards without any further interaction, or scattered again.

In a sensitivity analysis performed by Alton et al. (2007) using measured meteorological and flux data for three different ecosystems (boreal, tropical, and temperate forests), the differences between measured and simulated GPP were evaluated for different radiative transfer schemes available in the JULES (Joint UK Land Environment Simulator) model (Best et al., 2011; Clark et al., 2011).

Figure 2.2 shows differences in GPP between the two-stream approximation with sun-

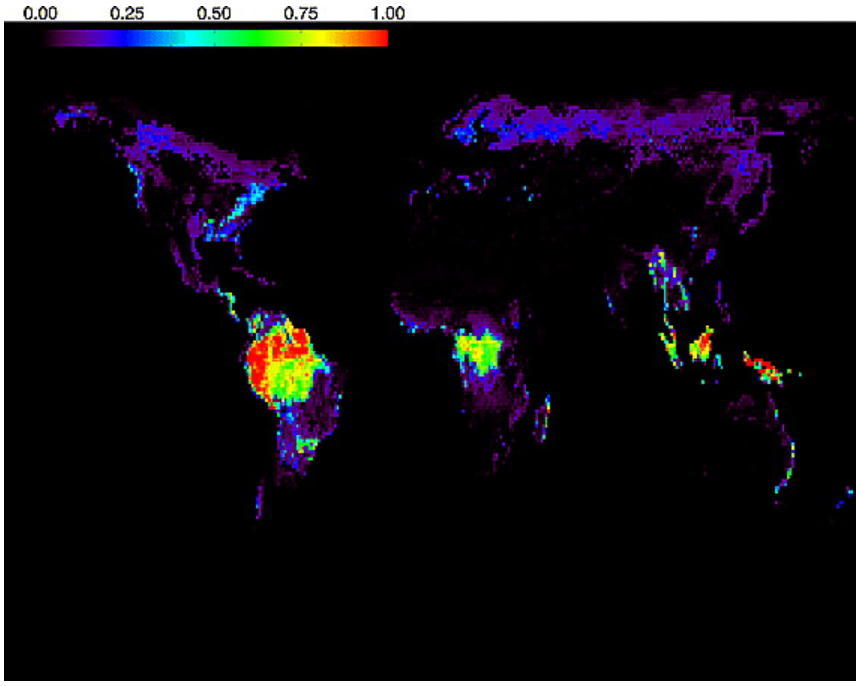

Figure 2.2: Beer's law and the two-stream schemes difference in GPP ($kg.m^{-2}.yr^{-1}$) predicted by JULES. The colour table is scaled from 0.0 (black) to 1.0 $kg.m^{-2}.yr^{-1}$ (red). Figure taken from Alton et al. (2007).

fleck penetration and Beer's law (see Section 1.2.2 for a general description of GPP). The authors obtained values for global GPP derived with Beer's law and with the two-stream approximation equal to 131 $PgC.yr^{-1}$ and 129 $PgC.yr^{-1}$, respectively. The authors also pointed out that the major differences were founded in regions with higher mean LAI. For example, GPP predicted by the Beer's law in the tropics was up to 25% higher than the equivalent estimates from the two-stream approximation.

Further developments of the two-stream approach, which was used in this comparison exercise, include a multilayer approach with a sunlit and shaded leaves parameterisation and a nitrogen profile decreasing vertically through the canopy, as well as inhibition of leaf respiration in light (Mercado et al., 2007). The differentiation between sunlit and shaded leaves, or the so-called 'sunfleck penetration' parameterisation scheme (Dai et al., 2004) was an attempt to account for direct light penetration into the vegetation canopy, and it usually gives a better agreement with observed data in comparison to the Beer's law. The positive results obtained with the sunfleck penetration parameterisation scheme is also an indicator of the importance of considering vegetation 'gaps' when calculating photosynthesis.

Mercado et al. (2007) tested the improved vertical multilayer vegetation canopy model against data derived from eddy covariance measurements for a tropical site in South America. The authors found a more realistic response of modelled photosynthesis and water fluxes to the implementation of a multilayer two-stream scheme, mainly because of a more realistic representation of light vertical propagation in the vegetation canopy.

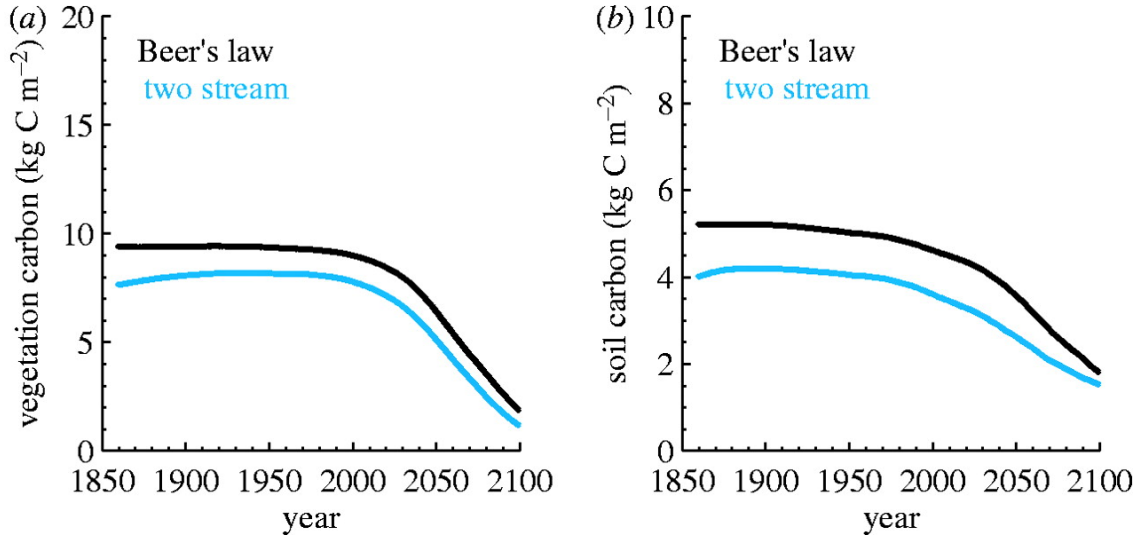

Figure 2.3: Changes in **(a.)** vegetation and **(b.)** soil carbon pools for the Amazon region using climate change patterns derived from a simulation described in Cox et al. (2000). The black curve corresponds to the Beer's law version and the blue curve to the two-stream scheme. Figure taken from Huntingford et al. (2008).

Another study based on the evaluation of differences between radiative transfer schemes present in LSMs can be found in Huntingford et al. (2008). The authors performed a sensitivity study between Beer's law and a modified version of the two-stream approximation with sunfleck penetration (Jogireddy et al., 2006; Mercado et al., 2007) in order to quantify uncertainties in predictions of the Amazon "dieback" hypothesis (Cox et al., 2000).

The Amazon dieback scenario was found as a result of a large-scale GCM simulation in which the Amazon forest interacted with a changing global climate through the 21^{st} century, and predictions indicated that forests would continue to uptake CO_2 until 2050. After 2050, however, the association of warmer average global temperatures and localised water stress would cause a "dieback" of the Amazon forest, which would change its carbon sink nature to a source of carbon to the atmosphere. Although in Cox et al. (2000) the authors made assumptions of a pessimistic global warming scenario, where temperature changes over Amazon were at the upper limits of uncertainty related to climate change

and the Amazon forest was represented as a single PFT, i.e., broadleaf trees.

Huntingford et al. (2008) used the MOSES model (Cox et al., 1999) to calculate the effects of using different radiative transfer methodologies on stomatal conductance, its impact on photosynthesis and evaporation, and finally on modelled vegetation and soil carbon over the Amazon rainforest from 1850 to 2100. Shortwave radiation partitioning was calculated in two distinct wavebands, PAR and NIR, for direct and diffuse radiation separately throughout a vertical multilayer vegetation canopy.

The authors explained that modelled photosynthesis usually saturates for high amounts of solar radiation, with a 'flat' response on GPP, whereas observations show that GPP changes to varying light levels throughout the entire day. The modified radiative transfer scheme simulated higher GPP, lower NPP, and therefore lower carbon pools in vegetation and soil relative to the original Beer's law (Figure 2.3).

Huntingford et al. (2008) also identified that the improved treatment of shortwave radiation absorptance have a little impact on the original 'Amazon dieback' result obtained with the standard radiation scheme. However, the future simulations of vegetation and soil carbon seemed to be approximately 25% smaller when using the two-stream approximation instead of using the Beer's law.

The study of Huntingford et al. (2008) noted a negative impact on carbon storage when using a more "transparent" vegetation canopy to solar radiation by including: (i) spectral properties of the vegetation canopy and background soil (e.g., leaf reflectance, transmittance, and background soil albedo), (ii) differences in the nature of light (e.g., different mathematical formulation for direct and diffuse light), and (iii) an irregularly illuminated canopy (e.g., different mathematical formulation for sunlit and shaded leaves).

These two comparative studies were focused on testing different radiative transfer schemes broadly used in LSMs, and their results indicated a strong evidence that simulated carbon assimilation and balance are sensitive to the radiative transfer scheme used in the simulations. They also noted that these impacts are important to improve the understanding of complex radiative transfer phenomenon, and to reduce uncertainties in LSMs predictability of diagnostic variables that will impact climate predictions. These two studies exemplify how impacting the radiative transfer scheme assumptions can be on other parts of LSM, such as the carbon cycle, for example. Therefore, non-considering vegetation canopy architecture heterogeneity by the two-stream scheme might result in

inaccurate calculations of the carbon balance.

The next section introduces the work of authors who have proposed ways to parameterise vegetation canopy structural heterogeneity using 1D radiative transfer schemes.

2.4 Considering vegetation canopy structure in radiative transfer schemes

Structure has a systematic effect on grid scale radiative fluxes and GPP. There is thus a need to parameterise structure in LSMs. Several authors (Kucharik et al., 1999; Pinty et al., 2006; Ni-Meister et al., 2010) attempted to address canopy spatial heterogeneity in a simple way to be directly used in LSMs. Their attempt to produce something relatively 'simple' is mainly due to computational efficiency and availability of input parameters.

In Yang et al. (2001) a complex 3D radiative transfer model was tested against the two-stream approximation and results indicated that a factor of roughly 50 times more CPU time was required for the complex model, depending on the vertical resolution used. The authors concluded that the inclusion of a complex 3D model with such an elevated CPU demand in LSMs was not plausible.

Some studies attempted to address the impact that vegetation canopy architecture could have on radiation propagation (Nilson, 1971; Chen et al., 1997; Kucharik et al., 1999; Pinty et al., 2006; Ni-Meister et al., 2010; Kobayashi et al., 2012); however, a lack of observational data led to inaccuracies in specifying model parameters, such as between and within-crown gaps, needle-to-shoot clumping, and forest stand density. The aims of large scale experiments, such as FIFE (Hall and Sellers, 1995), BOREAS (Sellers, 1997), LBA (Keller et al., 2004) were to improve and validate parameterisations, and also to enhance methods for deriving parameters from fieldwork observations.

The following sections describe the theory for parameterising canopy structure in radiative transfer schemes, evaluate proposed parameterisations pointing out their pros and cons, and discuss possible ways to address these problems in this thesis.

2.4.1 Foliage clumping

In both radiative transfer schemes discussed previously (Beer's law vs. the two-stream scheme), the vegetation is represented as a 1D turbid medium. Even though efforts have been made in order to consider canopy gaps in radiative transfer schemes, such as the sunlit/shaded leaves parameterisation developed by Mercado et al. (2007), their treatment of different properties of incident light (diffuse-shaded vs. direct-sunlit) in vegetation canopies does not consider vegetation structure explicitly, and it only makes use of LAI, leaf angle distribution, and spectral properties related to different PFTs.

For most natural forest stands, such as the tropical forest, deciduous forest, conifer forests, savannahs, and shrublands, various sizes of gaps exist between tree crowns. The term 'gaps' is used here in the sense of 'openness', i.e., canopy openings, which light goes through without being intercepted. Thus, using a 1D radiative transfer scheme can result in errors when estimating shortwave radiation partitioning, such as absorption or surface albedo.

More complex 3D radiative transfer models and observations of canopy gaps indicate that architectural heterogeneous distribution of vegetation and foliage can significantly affect the vertical shortwave radiation profile in many plant canopies, such as needleleaf forest and woody savannahs, or in any type of forest canopies that are not completely homogeneous (Nilson, 1971; Kucharik et al., 1999; Yang et al., 2001; Jonckheere et al., 2004; Chen et al., 2008; Ni-Meister et al., 2010). Vegetation architecture has been shown to be important for accurate calculation of the vegetation energy balance (Anderson et al., 2005), surface albedo (Ni and Woodcock, 2000), absorbed PAR (Chen et al., 2008), and photosynthesis (Law et al., 2001b), as well as the timing of snowmelt (Hardy et al., 1997).

In order to characterise the impact of spatial structure of vegetation on the radiation regime, Nilson (1971) introduced a variable called the clumping index ($\Omega(\theta)$) into Beer's law, to describe the plant canopy direct transmittance, or the gap fraction, $P_{gap}(\theta)$:

$$P_{gap}(\theta) = \exp\left(\frac{-G(\theta)LAI\Omega(\theta)}{cos\theta}\right) \tag{2.5}$$

where θ is the Sun zenith angle, and $G(\theta)$ is the projection coefficient of unit foliage area on a plane perpendicular to the view direction (Ross, 1981).

When $\Omega(\theta) = 1$, there is no clumping and leaves are considered to be randomly dis-

tributed. When $\Omega(\theta) < 1$, direct transmittance is enhanced by clumping, which is usually the case in most clumped vegetation canopies. Although, it is also possible to find cases in nature where $\Omega(\theta) > 1$, which means that direct transmittance decreases with clumping effects. The cases where $\Omega(\theta)$ exceeds 1 are associated with vegetation canopies exhibiting a significant amount of woody elements, which contribute to the interception of shortwave radiation (Pinty et al., 2006).

The clumping index defines the spatial distribution of leaves (Norman and Jarvis, 1974) and trees, and it can be quantified based on gap size distribution measured by instruments like ceptometres (Leblanc et al., 2002) or digital hemispherical cameras (Chen and Cihlar, 1995; Leblanc et al., 2005).

Some of the main difficulties in correctly determining and evaluating the clumping index in forests include the mathematical methods to derive the parameters from direct transmittance data, the range of view zenith angles in which the data was collected, and how clumping index may or may not vary with zenith angle depending on the evaluated site (Ryu et al., 2010). Several authors have shown the variance of foliage clumping index with zenith angle (Andrieu and Sinoquet, 1993; Chen, 1996; Kucharik et al., 1999; Chen et al., 2008), and this variance may be important for spatial values of $\Omega(\theta)$. The underlying mechanism of clumping index varying with Sun zenith angles remains unclear (Ryu et al., 2010).

Previous studies (Chen, 1996; Kucharik et al., 1999) reported that clumping index increases with Sun zenith angle; however, in a more recent study, Ryu et al. (2010) found the opposite behaviour of clumping index decreasing with Sun zenith angle when analysing data collected in a spatially heterogeneous woody savannah in California. Ryu et al. (2010) suggested that the radiation path length through a woody savannah decreases with Sun zenith angle because the vegetation canopy is vertically prolonged and horizontally dense. Large gaps are decomposed into smaller ones when the radiation path length is longer, which is a similar case to a random gap size distribution. The authors also suggested that the angular dependence of clumping index was controlled by tree distribution at ecosystem scale over a heterogeneous woody savannah ecosystem, and that it might be an unique characteristic specific to this type of ecosystems.

Some authors attempted to formulate simplified modelling approaches to resolve vegetation clumping at several levels of organisation in order to address one major difficulty

associated with radiative transfer in forest canopies. A number of these parameterisation schemes are described in Chapter 3 and further evaluated in Chapter 4, and their main results are summarised in the next subsections.

2.4.2 Semi-empirical and analytical derivations of clumping

Kucharik et al. (1999) used a set of semi-empirical equations to estimate clumping index for five different forest types: jack pine (OJP), black spruce (OBS), aspen (OA), oak, and sugar maple, over two different regions of the BOREAS sites Southern Study site (SSA) and Northern Study site (NSA). The results are presented by dashed lines in Figure 2.4 and the best fit to data for each forest site is represented by solid lines. The range of clumping index obtained in Kucharik et al. (1999) was from approximately 0.37, for minimum Sun zenith angle ($\theta = 0°$), with convergence to $\Omega(\theta) = 1.0$ for maximum Sun zenith angle ($\theta = 90°$). Kucharik et al. (1999) showed the value of clumping index increasing with Sun zenith angle for all evaluated sites in this study.

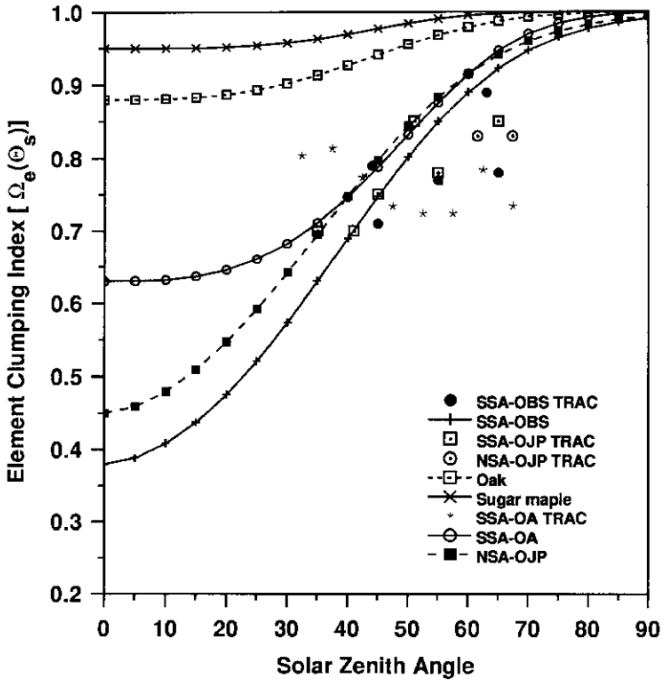

Figure 2.4: Results of general solution of $\Omega(\theta)$ calculated for five forest species, where solid lines represent the best fit to data for each forest. Figure taken from Kucharik et al. (1999).

It is also possible to distinguish between three groups of clumping index: a highly varying clumping index observed for black pine and jack spruce, both needle-leaved species;

a medium varying clumping index for aspen; and a low varying clumping index for oak and sugar maple; the last three tree species are broad-leaved. The semi-empirical relation underestimated the best-fit clumping index for jack pine over all Sun zenith angles, and overestimated the best-fit clumping index for aspen for Sun zenith angles higher than 20°. For the other cases, the adjusted values presented a fair agreement with measured clumping index.

Ni-Meister et al. (2010) developed an analytical expression and compared the solutions for clumping index with the ones calculated by the full GORT model (Li et al., 1995). To evaluate the difference in clumping index estimated by the analytical and complete versions of the GORT model, Figure 2.5 compares the two approaches for a number of plots in Harvard forest (Barford et al., 2001). Most input parameters in GORT were obtained based on allometric equations, except for diameter at breast height (DBH) and tree height that were directly measured *in situ* (Ni-Meister et al., 2010). Changes in clumping index with different structure parameters have shown comparable results for both versions of the GORT model, the analytical versus the complete model.

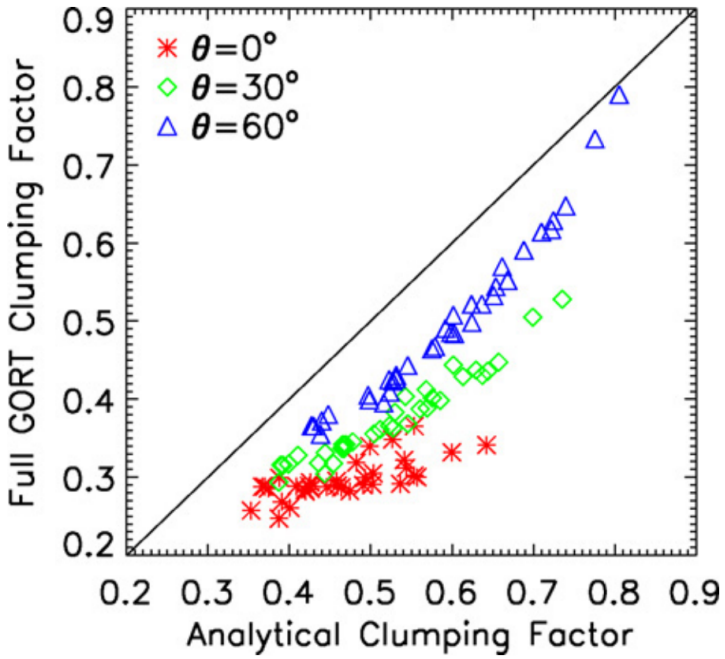

Figure 2.5: Comparison of clumping index calculated with both versions of the GORT model (analytical vs. complete) for a number of plots in Harvard Forest. Figure taken from Ni-Meister et al. (2010).

The clumping index derived from the analytical GORT is usually larger than the one

derived from the complete version of GORT because even though both assume a random distribution of tree crowns, which leads to over clumping, the former assumes that tree crowns do not overlap. This difference between both clumping indices (analytical vs. full GORT) becomes smaller at larger Sun zenith angles (Ni-Meister et al., 2010).

Differently than Kucharik et al. (1999), which used observed data, Ni-Meister et al. (2010) evaluated their analytical clumping index in relation to a more complex 3D radiative transfer model. This exercise allowed the authors to build a perfectly controlled experimental scenario in a modelling context, and to evaluate changes in clumping index with different structure parameters such as foliage density, tree density, horizontal crown radius, and vertical/horizontal crown radius ratio. Their results show agreement with the previous parameterisation and their conclusion is that clumping index increased with Sun zenith angle for all evaluated scenarios, independently of canopy structure. In their modelling experiment, clumping index increased with tree density and vertical/horizontal crown radius ratio, which indicates that over dense vegetation canopies or in the presence of tall trees, the shortwave radiation transfer can be approximated to the random case, i.e., $\Omega(\theta) = 1$.

Their second main finding related to canopy structure is that clumping index decreased with horizontal crown radius and foliage density. By increasing horizontal crown radius and keeping all the other variables constant (i.e., tree density, foliage density, and vertical/horizontal crown radius ratio), there is an increase in number and size of within-crown gaps, which turns the vegetation canopy into a more spatially heterogeneous, or more "gappy" canopy as a whole. On the other hand, by increasing foliage density, there is a decrease in within-crown gaps, which makes the canopy less heterogeneous but increases the ratio between-crown gaps/total gaps. Ryu et al. (2010) indicated a relation between canopy cover and between-crown gaps/total gaps ratio as being inversely proportional, i.e., if a vegetation canopy presents a relatively high value of between-crown gaps/total gaps ratio, it is equivalent to say that the canopy is sparser, with lower tree density (see Figure 2.6).

2.4.3 Empirical derivations of clumping

Quantifying and understanding canopy structure in remote sensing derived products is relevant because these data can be used in LSMs, and such data are needed for GCMs

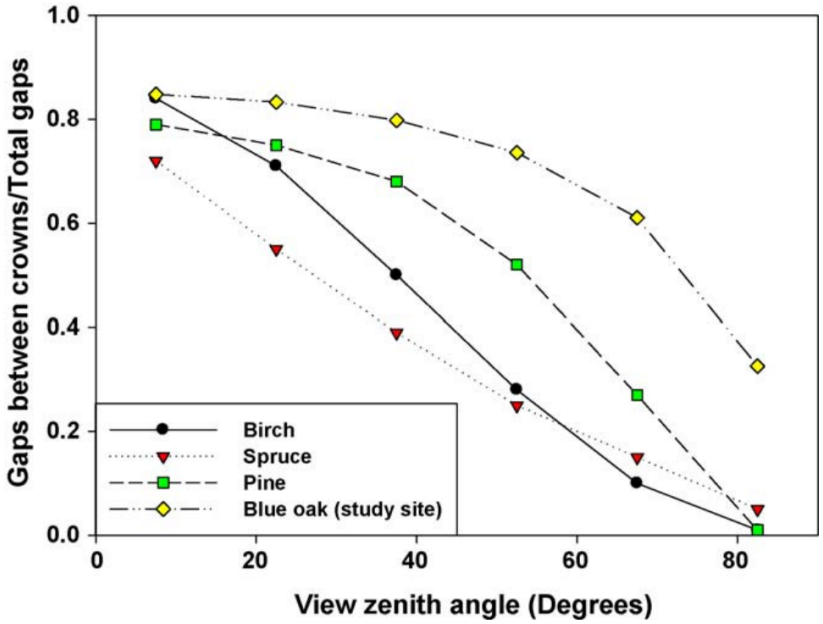

Figure 2.6: Between-crown gaps to total gaps ratio for different tree species simulated by Nilson 's model (Nilson, 1999). Canopy cover was 0.80, 0.90, 0.74 and 0.47 for birch, spruce, pine and blue oak, respectively. Figure taken from Ryu et al. (2010).

ancillaries. The main relevance of Earth observation data is its global coverage. In order to derive variables that describe the properties of the land surface from satellite data, such as fAPAR (Gobron et al., 1999), LAI (Myneni et al., 2002), and surface albedo (Schaaf et al., 2002), algorithms have been developed to relate radiometric satellite observations to land surface properties.

There is a need to develop methodologies for utilising such data directly into LSMs. However, the direct implementation of satellite derived variables into LSMs is not straightforward because of the different nature of these two distinct platforms. For instance, the radiative transfer scheme used to generate MODIS (Moderate Resolution Imaging Spectroradiometer) derived LAI product is based on a radiative transfer 3D model, but the commonly used radiative transfer scheme in LSMs is the two-stream scheme, which is a 1D model; therefore, these two algorithms work in different dimensions and make different assumptions about the nature of radiation propagation.

The effects of complex vegetation canopy architecture have to be represented by radiative transfer formulations, but generally these formulations are too simplified, for instance when they assume that leaf angular distribution is random (Pinty et al., 2006). A number of authors (Knyazikhin et al., 1998; Widlowski et al., 2001; Pinty et al., 2006) indicated

that in order to accurately derive the appropriate shortwave radiation partitioning, 3D radiative transfer models should be used instead of simpler 1D models to account for heterogeneous vegetation architectural impacts on radiation propagation.

Pinty et al. (2004) developed a parameterisation scheme based on the use of an "effective variable", which is defined as a parameter that modulates the optical depth of a 1D canopy to appropriately estimate the radiation partitioning at the satellite pixel resolution in order to improve the radiation partitioning by 1D radiative transfer schemes and force them to behave as 3D radiative radiative transfer schemes (Pinty et al., 2006). Pinty et al. (2004) demonstrated that this principle can be applied to any variable used in a radiative transfer scheme.

Pinty et al. (2006) showed a relation between true and effective LAI (Figure 2.7) for coniferous forest based on modelled cases from Widlowski et al. (2004). The effective LAI was estimated using the methodology described in Pinty et al. (2004) and the values of direct transmittance were obtained using a ray tracing Monte Carlo model (Govaerts and Verstraete, 1998). The authors found that values of effective LAI should be smaller in 1D radiative transfer schemes than the true LAI by a factor between 0.3 for low tree density canopies to 0.8 for high tree density canopies.

This parameterisation scheme referred to as the "structure factor", firstly described in Pinty et al. (2004), and further discussed and evaluated in Pinty et al. (2006), can be interpreted as being analogous to the clumping index, although with an extra parameter that accounts for zenith angular variations, and where both parameters can be freely determined at the same time in order to modulate LAI to appropriately describe the shortwave radiation path length in accordance to a structurally heterogeneous vegetation canopy.

In order to parameterise the canopy spatial variability of LAI into 1D radiative transfer schemes, there is a need to add extra information to account for 3D induced effects on radiation partitioning (Pinty et al., 2006). Effective variables can be estimated by inverting a 1D radiative transfer scheme against solutions for the radiative transfer equations generated by a more complex 3D radiative transfer scheme, or directly from observations.

Pinty et al. (2006) confirmed that the structure factor parameterisation is "a very robust approach since it guarantees accurate simulations" for all components of the radiative partitioning (absorptance, reflectance, and transmittance) when using effective variables,

and "it does not require an explicit description and understanding of the complex phenomena arising from the presence of heterogeneous vegetation architecture".

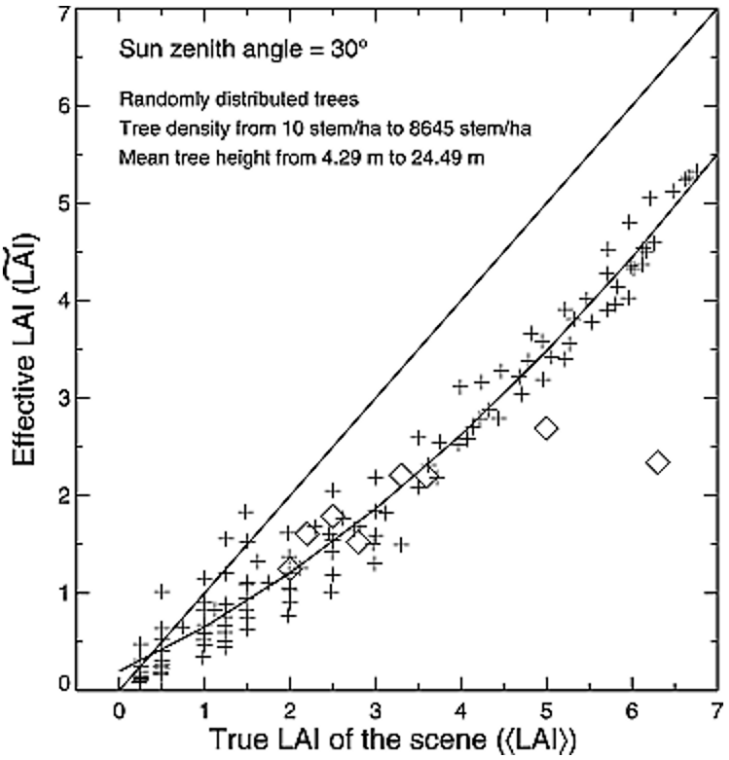

Figure 2.7: Simulated relation between true and effective LAI values over coniferous forests taken from Widlowski et al. (2004). Field measured (diamonds) values were taken from the BOREAS experiment. Figure taken from Pinty et al. (2006).

2.4.4 Summary

Between the three mentioned parameterisation schemes, i.e., Kucharik et al. (1999); Ni-Meister et al. (2010); Pinty et al. (2006), the one proposed by Pinty et al. (2006) presents a relative 'self-sufficiency', because it does not require any previous knowledge about vegetation structure, and because of that, it can be applied to any vegetation canopy, although each one of the previously discussed parameterisation schemes present pros and cons that will be further explored in Chapter 4.

In the scheme described by Kucharik et al. (1999), it is necessary to know the number of stems within a predetermined ground area, the crown diameter, and the ratio of crown depth to crown diameter. Besides that, Kucharik's relation for determining clumping index is a semi-empirical equation adjusted for a specific set of data collected in boreal forests during the BOREAS experiment, and its applicability cannot necessarily be extended to

other PFTs.

In Ni-Meister et al. (2010) the relation for clumping index is based on an analytical expression, which is determined using knowledge about stem density, crown radius, and LAI. Besides that, the generalised equation for spheres does not depend on Sun zenith angle (see Eq. 3.16), which might introduce errors as previously discussed. In these terms, an empirical derivation of clumping would benefit from the freedom of previously determined parameters, since there is no need for having any type description about canopy structure, whereas the parameters are minimised against reference values, either observed or modelled terms of the radiative transfer balance. Further investigations need to be performed in order to address the parameter's variability over different areas, as well as different spectral and structural properties. This research area has been surprisingly neglected until recently (Loew et al., 2014), and the need for the development of physically consistent radiative transfer schemes in LSMs has been highlighted by recent studies (Widlowski et al., 2011; Ciais et al., 2013).

In summary Kucharik et al. (1999) derived an expression for clumping index based on fieldwork observations for a limited study area in the boreal forest, while Ni-Meister et al. (2010) derived an analytical solution for clumping index based on more complex 3D radiative transfer models; although, both studies lack of more testing and validation. Finally, Pinty et al. (2006) proposed an approach that does not need information about the vegetation canopy structure itself, although this parameterisation scheme needs to be minimised against reference data either from 3D radiative transfer models or observed data.

This thesis presents a validation study between the parameterisation schemes previously mentioned and further explores the applicability of the clumping index in radiative transfer schemes in the two-stream scheme (Chapter 4), as well as further evaluates the possible impacts that could have on local and global carbon assimilation (Chapter 5 and Chapter 6, respectively).

2.5 Assessment and observations of vegetation canopy structure representations

It is important to assess the uncertainties in current radiative transfer schemes and its possible impacts on energy and carbon fluxes in the land surface-atmosphere interface. Therefore, it is necessary to assess the consistency and accuracy of radiative transfer schemes in LSMs (Loew et al., 2014).

It has always been a challenge to test radiative transfer model performance. Usually to do so, such type of assessment requires physically consistent and highly accurate 3D radiative transfer models to work as a reference (Kobayashi et al., 2012). For example, radiative transfer models have been tested in model intercomparisons approaches (Pinty et al., 2001, 2004; Widlowski et al., 2007, 2011, 2013), or with different sources of observed data sets, such as bidirectional reflectance (North, 1996) and measurements of direct transmittance (Wang and Jarvis, 1990; Law et al., 2001b; Kobayashi et al., 2012), for example.

Radiative transfer scheme intercomparisons decrease uncertainties related to an incomplete knowledge of the (i) "structural, spectral, and illumination-related characteristics of the canopy target", and (ii) "the uncertainties introduced into the reference solution by calibration, sampling, and upscaling errors" (Widlowski et al., 2011), which is not completely possible when comparing computer simulations against observations performed *in situ*.

Experiments like the RAMI4PILPS (Widlowski et al., 2011) allow an assessment of the implications of the use of particular canopy radiative transfer schemes on the radiative balance, and it is important when decisions on further development of LSMs needs to be made with limited computational and data resources (Loew et al., 2014).

In order to evaluate a parameterisation scheme in radiative transfer schemes in LSMs, it is therefore necessary to address and assess, at least two major points regarding the potentialities and applicability of their formulation (Widlowski et al., 2011):

1. to address how capable a parameterisation scheme is at reproducing canopy radiative transfer formulations based on more complex and accurate state-of-the-art 3D radiative transfer models, in order to simulate consistently: canopy absorptance, reflectance, and transmittance of idealised reference cases; and to assess at which

conditions the canopy radiative transfer schemes with their parameterisations might lead to major biases in the radiative balance estimates.

2. to compare the parameterisation scheme with observed data, or at least, to propose applicable methods for acquisition and validation of the parameterisation scheme, and its direct or indirect impacts with the observable world, locally and globally.

2.5.1 Local validation studies

Several observational studies have improved the understanding of exchanges of energy, water and carbon between the atmosphere and the land-surface, and their controlling processes of the physical climate system. An example of these large field campaigns later used to evaluate parameterisations is the BOREAS experiment. The primary goal of BOREAS was to acquire data needed to improve climate model predictions of global change effects, particularly focused on temperature and precipitation differences associated to global warming, as well as giving a better description of atmosphere-biosphere interaction processes (Sellers, 1997).

One of the many new discoveries emerged from BOREAS data sets was made by Chen et al. (1997), who found that the LAI-2000, an optical method to estimate LAI, underestimated the destructive sample estimates of LAI, because its algorithm assumed a spatially random distribution of leaves as a function of canopy gap fraction. This finding confirmed the importance of vegetation canopy structure in boreal forests and highlighted the difficulties with ground characterisation of biophysical variables. Another important novel measuring approach with BOREAS was the combination of a large number of measurements (hemispherical photograph, stand mapping, destructive sampling, and modelling), in order to characterise the canopy architecture in boreal forests (Fournier et al., 1997). Stand level field data acquisition is important to input tree-based 3D radiative transfer models, which can fill theoretical gaps between 1D models and actual ecosystems (Widlowski et al., 2011).

One way to acquire information about clumping index without the spatial and temporal satellite limitations is by using optical field instruments, particularly digital hemispherical photographs (DHPs). Photographs can provide a large number of advantages on the process of acquiring direct transmittance data in multiple directions, such as the permanent record and spatial discrimination of vegetated material positioning, important for the cal-

culation of vegetation clumping (Gonsamo and Pellikka, 2009). In the particular case of the structure factor (see Section 3.3.4), that accounts for zenith variations of clumping index, digital hemispherical photographs are more suitable than satellite measurements, because a complete zenith profile can be derived from one single photograph of the upper hemisphere.

Other large-scale experiments were conducted in different regions and scales, for example, the First ISLSCP (International Satellite Land Surface Climatology Project) Field Experiment (FIFE) project conducted in the Konza Prairie in Kansas, USA, from 1987 to 1989, within 15 $\times$ 15 km area of grassland (Hall and Sellers, 1995); or the Large-Scale Biosphere-Atmosphere Experiment in Amazonia (LBA) conducted from 1995 to 2005 with sparse research areas all over the Amazon region, focused on carbon storage, nutrient dynamics, and trace gas fluxes for the tropical rainforest. A more recent example is the National Ecological Observatory Network (NEON) is the first continental scale ecological observatory with remote sensing of vegetation canopy structure (Kampe, 2010). NEON provides a robust material to develop land surface studies relating 3D canopy structure and atmosphere-biosphere exchanges of mass and energy. Few other studies have used data from airborne-LiDAR (Chen et al., 2008; Kobayashi et al., 2012), which estimates the distribution of vegetation canopies, providing high-resolution mapping of vegetation structure, tree height, vegetation cover, as well as sub-canopy topography, but they are still very temporal and spatially limited.

2.5.2 Large scale satellite products

Satellite observations can estimate biogeophysical parameters over large areas; however, the resolution of these variables are limited to the satellite pixels, which are not directly comparable to measurements acquired *in situ*. In the case of clumping index, Chen et al. (2005) used the bidirectional reflectance distribution function (BRDF) of vegetated land surfaces to extract vegetation structural information globally, using multiangular data from the POLDER instrument. A global clumping index map was derived using a geometrical optical model; however, the clumping index map presented by the authors presents a number of limitations, such as low spatial resolution, the impact of topographic effects, and a lack of evaluation with field measurements. Later on, further studies from the same research group improved and validated the global clumping index map with *in situ*

observations (Pisek et al., 2010).

Using BRDF data, He et al. (2012) derived a global clumping index map at 500 m resolution from MODIS, however, the MODIS-derived clumping index map was found to be consistently lower than available ground data and with no zenith angular dependency, because the authors derived the minimum value of clumping index following Nilson (1971). Although, He et al. (2012) highlights the dependence of clumping index on zenith angle and land cover type, especially related to the shape of tree crowns.

Following the same research questions and deriving a clumping index map from MISR data (Pisek and Oliphant, 2013), Pisek et al. (2015) developed a comparison study between all available satellite based clumping index products and *in situ* observations. Among their main conclusions, the authors pointed out that the MODIS clumping index map (He et al., 2012) with its spatial resolution at 500 m compared to 6 km from POLDER might be more suitable for distinguishing between different PFTs within a grid-scale and, therefore, more applicable to be used in LSMs after rescaling to their spatial resolution. Pisek et al. (2015) found that correct land cover information is crucial for retrieving accurate clumping index values. More details on the satellite derived clumping index map and its applicability will be given in Chapter 6.

2.6 Addressing the research questions

In summary, it is clear the growth of interest of the research community in developing, testing, and applying methods to address canopy vegetation structure in a feasible way affecting the shortwave radiation partitioning, especially to be directly used in LSMs, and to allow improvements in weather forecast and climate predictions with GCMs. However, further evaluations have to be addressed in previously proposed parameterisation schemes, especially regarding their ability to reproduce more complex models results, and actually reproduce what can be observed in the real world. Furthermore, the indirect impacts of parameterisations on applicable knowledge improvements is necessary and it opens a new horizon to be scientifically explored.

This thesis is divided into: (i) a purely modelling phase with radiative transfer schemes and structural parameterisation schemes in order to address the first research question of this thesis, and (ii) a mixed phase with land surface modelling and observational data sets

of shortwave radiation partitioning and carbon fluxes, in order to address the second and third research questions of this thesis.

The modelling phase compares the parameterisation schemes presented in Section 2.4 with a detailed description of methodology, models, and data sets presented in Chapter 3. The mixed phase makes use of different validation methods and, local and large scale data sets introduced in Section 2.5. A new method for deriving a clumping index from DHPs is presented and evaluated, and a global evaluation of the impact of canopy structure on carbon assimilation is developed through the implementation of a global clumping index product introduced in Section 2.5.2.

Chapter 3:

Models, Data, and Methods

3.1 Introduction

This chapter describes the models, study sites, and methodologies used in this thesis to address the research questions. The first sections are related to the radiative transfer models and the parameterisation schemes of vegetation canopy heterogeneity that are used in Chapter 4. The next sections describe the photosynthesis model in JULES and summarise the model setups for the experiments performed with the land surface model along the thesis; it also describes the flux tower sites used in Chapter 5. The final sections of this chapter are used to describe the global experiment setups, data, and methodology.

3.2 Radiative transfer schemes

3.2.1 The two-stream scheme in JULES

The two-stream scheme used in this thesis was directly extracted from the JULES model (Best et al., 2011; Clark et al., 2011). The JULES model is the UK community LSM designed to be interfaced with the UK Met Office Unified Model (Walters et al., 2014) by predicting fluxes of heat, water, and carbon between the land surface and the atmosphere. It originated from the Met Office Surface Exchange Scheme (MOSES) (Cox et al., 1999) and it includes the TRIFFID (Top-down Representation of Interactive Foliage and Flora Including Dynamics) dynamic vegetation model (Cox, 2001). Much of the physical basis of JULES is common to other land surface models and a detailed technical description of the full JULES can be found in Best et al. (2011) and Clark et al. (2011).

JULES uses a default number of 10 vertical layers in the canopy with equally distributed LAI to calculate the radiative transfer in the canopy following an adaptation of the two-stream scheme described in Mercado et al. (2007). The spectral properties of leaves are prescribed by PFTs following a lookup table (LUT) methodology and are given by leaf reflectance (ρ_{leaf}) and transmittance (τ_{leaf}) in the PAR and NIR spectral wavebands separately. The canopy leaf angle distribution can be prescribed as being either spherical, or horizontal in JULES but throughout this thesis the spherical approximation was used, where $G(\mu) = 0.5$. The amount of absorbed incident radiation at each layer is therefore determined by Sun zenith angle, incident direct and diffuse radiation at the top of the canopy, scattering properties of leaves, and the canopy extinction coefficient.

Another advance in JULES to the calculation of shortwave radiation absorption within vegetation canopies was the consideration of penetration of sunflecks (can_rad_mod = 5), which corresponds to the direct component of the direct beam radiation because eliminates the scattering component (Clark et al., 2011). The term associated with sunflecks is not included in the original formulation of the two-stream scheme. The radiative components are separated into direct radiation, scattered radiation from the direct beam, and diffuse radiation as first described in Dai et al. (2004), and implemented by Mercado et al. (2007). Sunlit leaves are assumed to absorb direct and diffuse radiation, while shaded leaves absorb only diffuse radiation. The fraction of sunlit leaves (f_{sun}) is defined as:

$$f_{sun} = e^{\frac{-G(\mu)}{\mu} \cdot dLAI} \tag{3.1}$$

where $G(\mu)$ is the G-function (Ross, 1981), μ is the cosine of Sun zenith angle, and LAI is the total leaf area index.

JULES calculates the fraction of sunlit leaves for each canopy layer (i), with leaf area increment dL_c, as well as the fraction of absorbed direct beam radiation, fraction of scattered direct beam, and fraction of absorbed diffuse radiation as described in Clark et al. (2011). In individual canopy layers, the fraction of incident radiation absorbed by sunlit and shaded leaves, separately, depends on the fraction of incident diffuse shortwave radiation at the top of the canopy. Therefore, appropriately estimating the fraction of diffuse radiation when using can_rad_mod = 5 in JULES is important because it impacts GPP.

3.2.2 MAESPA: a 3D tree-based model

MAESPA is a model of forest canopy radiation absorption, photosynthesis, and water balance that originated in the early 1970s, with major contribution published in Norman and Jarvis (1974, 1975) where the authors measured and characterised non-randomness in forest canopy structure. An application of the originally named MAESTRO (Wang and Jarvis, 1990) was a detailed investigation of the importance of crown shape, leaf area, leaf area distribution, and leaf inclination angles for crown radiation interception and photosynthesis. Later on, Medlyn (1998) used MAESTRO to incorporate standard formulations of leaf gas exchange models and to investigate physiological basis of light use efficiency (LUE). Duursma and Medlyn (2012) expanded the model by including water balance and plant hydraulics routines, largely based on the SPA model (Williams et al., 1996).

The MAESPA model (Wang and Jarvis, 1990; Medlyn, 2004; Medlyn et al., 2007; Duursma and Medlyn, 2012) represents a forest canopy as an array of tree crowns, with specified tree dimension and positioning. The vegetation canopy is composed of individual tree crowns described by a basic shape (e.g., ellipsoids, cylinders, and cones), crown length, height to crown base, and width in both horizontal directions. Radiation calculations can be performed only for a set of target crowns, specified by the user to save time, or for all trees if wanted (Wang and Jarvis, 1990). The distribution of leaf area within the target crown can be specified per individual tree, or for the whole stand, as well as the leaf angle distribution.

The target tree crown is divided into grid points, and the penetrating radiation at each grid point is calculated for three separate wavebands (PAR, NIR, and TIR) based on shading within and between crowns, Sun zenith and azimuth angles, and the fractions of direct and diffuse radiation. Direct, diffuse, and scattered radiation are considered separately. Radiation scattering is obtained following the methodology in Norman (1979) and the leaf area index of a single tree crown is assumed to be distributed randomly within the crown (Wang and Jarvis, 1990), although other distributions (e.g., beta distribution in the vertical only, or vertical and horizontal directions) can be specified by the user. At each grid point, leaves are separated into sunlit and shaded following the scheme described in Norman (1993). The MAESPA model has been applied to a number of study sites with different plant species (e.g, *Picea sitchensis*, *Pinus radiata*, *Betula pendula*, *Pinus taeda*)

by different authors (Wang and Jarvis, 1990; Mcmurtrie and Wang, 1993; Wang et al., 1998) for the study of energy and carbon fluxes (Medlyn, 2004).

In Chapter 4 the MAESPA model is used to calculate canopy shortwave radiation partitioning. It is used as the reference model of absorptance in Section 4.2.

3.2.3 GORT: a geometric optical radiative transfer model

The GORT model was developed to describe the shortwave radiation partitioning over vegetation canopies with spatial heterogeneous structure at the forest stand scale (Ni-Meister et al., 2010). GORT uses theory from radiative transfer and geometric optics to treat vegetation canopies as trees with ellipsoidal crowns, randomly distributed over space. Shortwave radiation passes through the tree crowns and interact with leaves that can either absorb or reflect radiation. Multiple scattering is calculated within and between tree crowns, as well as between a soil surface underneath and the vegetation canopy. GORT was extended by Ni et al. (1997) to include the vertical profile of canopy gap probability.

In Chapter 4 the GORT model is used to calculate canopy shortwave radiation partitioning. It is also used as the reference model for reflectance in Section 4.2. GORT calculates shortwave radiation partitioning for specific wavebands, and for the exercise performed in Chapter 4 the PAR radiation spectrum is centred in 550 nm, and NIR in 850 nm.

3.3 Vegetation canopy architecture parameterisation schemes

The two-stream scheme is used in LSMs because of its simplicity, speed, and suitability to run over large areas. Clumping indices are often used to express the properties of 3D vegetation canopies and to make simpler models analogously simulate the radiation balance of more complex 3D models (Pinty et al., 2004, 2006), as previously discussed in Chapter 2.

The clumping index accounts for all vegetation elements composing the vegetation canopy. The first clumping index was proposed by Nilson (1971) and it is associated with the heterogeneous nature of the canopy volume (Norman and Jarvis, 1974; Chen and Black, 1992; Chen, 1996), often used at the tree resolution, and revisited later on by other authors (Pinty et al., 2004, 2006), who used the same scientific proposition to

account for structural heterogeneity of different radiative media at stand scale as a whole. This approach is specifically useful for direct comparison with measurements acquired over areas larger than a single tree, such as data collected in flux tower sites or associated with the use of satellite products.

Few other authors (Kucharik et al., 1999; Pinty et al., 2006; Ni-Meister et al., 2010) attempted to formulate simplified modelling approaches to solve vegetation clumping at several levels of organisation to address the major differences in shortwave radiation partitioning between 1D and 3D radiative transfer schemes over non-homogeneous forest canopies.

The next section describes a modified version of the two-stream scheme for the implementation of four different clumping indices to address vegetation heterogeneity impacts on shortwave radiation partitioning. The following sections also describe each one of the parameterisation schemes used in Chapter 4.

3.3.1 Parameterising vegetation canopy architecture into the two-stream scheme

The clumping index was introduced into the two-stream scheme by modifying three main groups of variables to account for canopy structural effects:

1. the optical depth of direct beam per unit leaf area, K;
2. the average inverse diffuse optical depth per unit leaf area, $\overline{\mu}$; and,
3. the single scattering albedo, $a_s(\mu)$, used to obtain the upscattering parameters for the diffuse and direct beams, β and β_0, respectively.

The modified two-stream equations described in this section make use of the clumping index of Pinty et al. (2006), the so-called structure factor ($\zeta(\mu)$); however, the addition of the other clumping indices (often referred to as $\Omega(\theta)$) is analogous to the structure factor by not considering Sun angular variations on the structure factor, i.e., by making $b = 0$ in Equation 3.14. The structure factor can be included on the optical depth of direct beam per unit leaf area, by modifying K as:

$$K_{Struc}(\theta) = \frac{G(\theta)}{\mu} \cdot \zeta(\mu) \tag{3.2}$$

The same analogy can be applied when calculating the average inverse diffuse optical depth per unit leaf area, $\bar{\mu}$, but obtaining the structure factor for the direction of scattered flux, μ':

$$\overline{\mu_{Struc}} = \int_0^1 \frac{\mu'}{G(\mu') \cdot \zeta(\mu')} d\mu' \tag{3.3}$$

The parameter $\omega\beta$ can be inferred from the analysis of Norman and Jarvis (1975) in the case of a single leaf whose normal is oriented at zenith angle θ_l from the local vertical defined in the upward hemisphere (Pinty et al., 2006):

$$\omega\beta = \frac{1}{2}(\omega + \delta_l \cos^2 \theta_l) \tag{3.4}$$

where $\omega = \rho_{leaf} + \tau_{leaf}$ and $\delta_l = \rho_{leaf} - \tau_{leaf}$. Eq. 3.4 is only valid for a single leaf, and in order to obtain the total contribution of leaves over the canopy, it is necessary to integrate Eq. 3.4 over the appropriate leaf orientation probability distribution, i.e., between 0 and $\pi/2$, because the leaf normal is assumed to be oriented into the upward hemisphere. And when isolating β, it is possible to obtain the generic diffuse upscatter parameter:

$$\beta = \frac{1}{2\omega}\left(\omega + \delta_l \int_0^{\pi/2} \cos^2 \theta_l g'(\theta_l) \sin \theta_l d\theta_l\right) \tag{3.5}$$

where $\sin \theta_l$ is introduced for normalisation requirement of the probability distribution function.

If the two-stream scheme equations are solved when $\omega \to 0$, i.e., single scatter approximation and semi-infinite canopy, the upward diffuse flux at the top of the canopy may be taken as equal to the single scattering albedo ($a_s(\mu)$). The equation for the direct upscatter parameter, β_0, is

$$\beta_0 = \frac{1 + \overline{\mu}K}{\omega\overline{\mu}K} a_s(\mu) \tag{3.6}$$

And $a_s(\mu)$ is given by,

$$a_s(\mu) = \frac{\omega}{2} \int_0^1 \frac{\mu' G(\mu)}{\mu G(\mu') + \mu' G(\mu)} d\mu' \tag{3.7}$$

The equation above is only valid when assuming isotropic scattering for the leaf elements, which makes the scattering phase function independent of the angle of the incident beam (Dickinson, 1983; Sellers, 1985).

The addition of the structure factor into the single scattering albedo formulation results in,

$$a_s(\mu) = \frac{\omega}{2}\int_0^1 \frac{\mu' G(\mu)\zeta(\mu)}{\mu G(\mu')\zeta(\mu') + \mu' G(\mu)\zeta(\mu)} d\mu' \tag{3.8}$$

In this case the formulation for the direct upscatter parameter considering canopy structure is:

$$\beta_0 = \frac{1 + \overline{\mu_{Struc}} K_{Struc}}{\omega \overline{\mu_{Struc}} K_{Struc}} \left[\frac{\omega}{2}\int_0^1 \frac{\mu' G(\mu)\zeta(\mu)}{\mu G(\mu')\zeta(\mu') + \mu' G(\mu)\zeta(\mu)} d\mu' \right] \tag{3.9}$$

The new variables K_{Struc}, $\overline{\mu_{Struc}}$, and the modified upscattering parameters for the diffuse and direct beams, β and β_0, are applied into Eq. 2.2 to modify the two-stream scheme.

3.3.2 The clumping index of Nilson (1971)

To consider the heterogeneous spatial distribution of leaves, Nilson (1971) proposed an adaptation of Beer's law by introducing an additional quantity, Ω, into Eq. 2.5 as described in Section 2.4.1, where the values G(θ)·LAI are modulated by the clumping index and affect the shortwave radiation partitioning of the vegetation canopy as follows:

$$P_{gap}(\theta) = \exp\left(\frac{-G(\theta) LAI \Omega}{cos\theta}\right) \tag{3.10}$$

where θ is the Sun zenith angle, and $G(\theta)$ is the projection coefficient of unit foliage area on a plane perpendicular to the view direction (Ross, 1981), and LAI is the leaf area index. Note that in Eq. 3.10, Ω is not dependent on Sun zenith angle, while in a more generalised formulation as in Eq. 2.5, $\Omega(\theta)$ has a dependence upon the Sun zenith angle.

The impact of this parameter on shortwave radiation partitioning calculated by the modified two-stream is evaluated in Chapter 4 under the reference name **Nilson** clumping index.

3.3.3 The clumping index of Kucharik et al. (1999)

Kucharik et al. (1999) used measurements of LAI and gap fraction made with MVI (Multi-band Vegetation Imager) (Kucharik et al., 1997) obtained during the BOREAS (Sellers, 1997) field campaigns of 1994-1996 to derive a semi-empirical relationship between $\Omega(\theta)$ and solar zenith angle (θ) (see Section 2.4.2).

In this method, two key quantities are needed: (i) the fraction of vegetation cover (f_c), which depends on tree crown diameter (D), and number of tree crowns (N) within a study area (A); and (ii) crown porosity (Φ) defined as the within crowns gap probability, which depends on foliage density, divided by f_c.

Kucharik et al. (1999) used a number of gap probability observations along a transect beneath a vegetation canopy in order to perform the partitioning of the total gap fraction ($f_{gap}, t(0)$) between within-crown gaps ($f_{gap}, c(0)$) and between-crown gaps ($f_{gap}, b(0)$), and to estimate the fraction of ground area covered by the horizontal projection of crown envelopes (f_c). To determine f_c, Kucharik et al. (1999) multiplied the tree density by the silhouette area of a tree crown, given by πR^2, where R is the crown radius in the horizontal direction. $f_{gap}, t(0)$ can be assumed to be equal to $f_{gap}, c(0)$, when f_c is greater than 1, because tree crowns usually overlap one another in the forest stand. $f_{gap}, b(0)$ can be estimated as $1 - f_c$, and $f_{gap}, c(0)$ is therefore approximated by $f_{gap}, t(0) - f_{gap}, b(0)$. When $f_{gap}, c(0) < 0$, the value can be assigned to 0 for practical purposes.

Kucharik et al. (1999) indicated an error of about 0.05 when determining f_c and Φ by using the average observed values of crown radius and tree density, instead of detailed modelling of f_c. $f_{gap}, c(0)$ divided by f_c is defined as crown porosity (Φ), which can be described as the normalised within-crown gap probability. However, the authors indicated that uncertainties arising from parameters calculated from observed values do not impact appropriate estimates of $\Omega(0)$ when using their methodology of gap fraction partitioning.

In order to determine $\Omega(0)$ from observations in a consistent way compared to numerical modelling calculations, Kucharik et al. (1999) used values of all values of Φ and $f_c \geq 0.20$ to obtain a function through a non-linear least-squares fit based on roughly 250 Monte Carlo simulations. For $0.04 \geq f_c \geq 0.30$, a separate fit was performed over the whole modelled data set. A value of $\Omega(0)$ was be determined for sparse canopies with $f_c < 0.20$.

A semi-empirical relation between values of $\Omega(0)$, f_c, and Φ was determined by adjusting ten coefficients simultaneously. Kucharik et al. (1999) highlighted the importance of the angular dependence of clumping index, and characterised it by determining a minimum value of $\Omega(\theta)$ at $\theta = 0°$, and a second value of $\Omega(\theta)$ at $\theta = 90°$. Kucharik et al. (1999) assumed that $\Omega(\theta)$ reaches its maximum value when $\theta = 90°$ (Ω_{max}), and defined

it as:

$$\Omega_{max} = \left(\frac{ND}{\sqrt{A}}\right)^{0.7} \tag{3.11}$$

where N is number of stems within ground area A, and D is crown diameter. If $ND/\sqrt{A} > 1$, then the value of $\Omega_{max} = 1$. The angular dependence of $\Omega(\theta)$ was defined by Kucharik et al. (1999) following the equation:

$$\Omega = \Omega(\theta) = \frac{\Omega_{max}}{[1 + b\exp(-k(\theta)^p)]} \tag{3.12}$$

where k is constant (usually $k = 2.2$), θ is the zenith angle, and b is solved from Eq. 3.12 using a pre-determined value of $\Omega(\theta)$ (e.g., $\theta = 0°$). Kucharik et al. (1999) performed a quantitative comparison of results produced using Eq. 3.12 with the best-fit curves and suggested that a value for p can be approximated by a formula on the form:

$$p = -0.461\chi + 3.8 \tag{3.13}$$

where χ is the ratio of crown depth to crown diameter. Generally, if χ is ≤ 1.0, $p = 3.34$.

The impact of this parameter on shortwave radiation partitioning calculated by the modified two-stream is evaluated in Chapter 4 under the reference name **Kucharik** clumping index.

3.3.4 The clumping index of Pinty et al. (2006)

The clumping index of Pinty et al. (2006), often referred to as the 'structure factor' is define in Section 2.4.3, and is given by:

$$\Omega(\theta) = \zeta(\mu) = a + b \cdot (1 - \mu) \tag{3.14}$$

where μ is the cosine of θ, $a = \zeta(\mu = 1)$ is the parameter corresponding to an overhead Sun, and b the parameter responsible for include the effects of a range of different Sun geometries. In the particular case of an overhead Sun (μ=1), a is also equal to:

$$\zeta(\mu = 1) = -\ln(1 - F_c)\frac{2}{LAI} \tag{3.15}$$

where F_c is the true vegetation cover (accounting for within and between crown gaps) obtained for a black canopy representation ($\rho_{leaf} = \tau_{leaf} = 0.0$) of the total incident radiation minus direct transmittance with an overhead Sun (1 - $P_{gap}(\mu = 1)$). Both parameters are used to account for vegetation canopy heterogeneity and modify the shortwave radiation path length.

Specifically in this thesis, both parameters (a and b) were found by optimisation against the available data, and in order to keep the use of Pinty's parameterisation scheme purely empirical, Eq. 3.15 is not directly implemented. The impact of these parameters following Eq. 3.14 on shortwave radiation partitioning calculated by the modified two-stream is evaluated in Chapter 4 under the reference name **Pinty** clumping index.

3.3.5 The clumping index of Ni-Meister et al. (2010)

Ni-Meister et al. (2010) developed an analytical expression for clumping based on stem density (λ), crown radius (R), and LAI. Only the equation used for spherical crowns is shown; however, the analytical solution for the modified clumping index in Beer's law is expressed as,

$$\Omega = \gamma = \frac{3}{4\tau_0 R}\Big(1 - \frac{1 - (2\tau_0 R + 1)\exp(-2\tau_0 R)}{2\tau_0^2 R^2}\Big) \tag{3.16}$$

where $\tau_0 r = 3GLAI/4\lambda\pi \cdot R^2$ for spherical crowns.

The authors validated the analytical solutions for clumping factor with the ones calculated by the full GORT model and their results are discussed in Section 2.4.2. The impact of this parameter on shortwave radiation partitioning calculated by the modified two-stream is evaluated in Chapter 4 under the reference name **Ni-Meister** clumping index.

3.3.6 Handling vegetation heterogeneity in JULES

Some simpler methods to deal with heterogeneous vegetation canopy cover have been implemented in LSMs (Loew et al., 2014). The vegetation cover approach divides one grid cell in a number of tiles, where each tile has its own characteristics. The possible number of tiles and their parameters depend on each LSMs. JULES has a default number of 5 PFTs and 4 non-PFTs, or 9 different tiles in total.

Suppose a model grid cell with area A, assumed to be completely covered by a certain

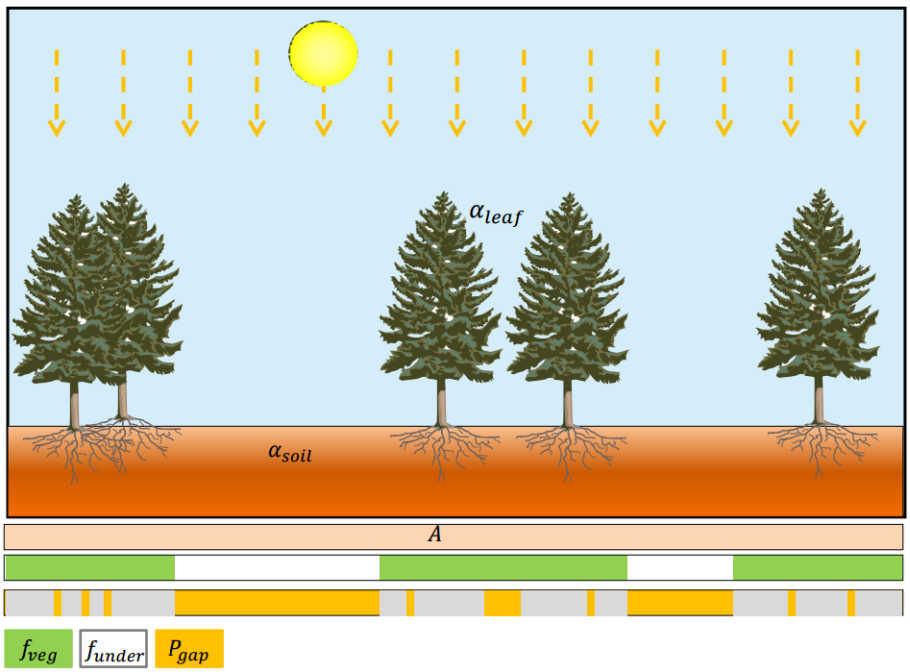

Figure 3.1: Illustration of the difference between vegetation fraction (f_{veg}) and gap probability ($P_{gap}(\theta = 0)$) for a model grid cell. Figure taken from Loew et al. (2014).

vegetation type. In sparse canopies the area A is covered by a dominant vegetation type, usually taller trees, but often presents a second vegetation type, for example, understory vegetation, such as shrubs or grasses, and part of the gridbox without vegetation is assumed to be represented by bare soil. Therefore, the total area A is defined as,

$$A = f_{veg} + f_{under} \tag{3.17}$$

where f_{veg} is the fractional coverage of a vegetation type, and f_{under} corresponds to the soil surface, which is equivalent to f_{under} being the between-crown gaps. The total direct transmittance, or the gap probability with Sun directly above head ($\theta = 0°$) is always greater than or equal to f_{under}. Figure 3.1 shows a representation of a sparse vegetation canopy with f_{veg} being the percentage of the area covered by a single vegetation type, f_{under} is the remaining area, and $P_{gap}(\theta{=}0°)$ as being f_{under} plus the within-crown gap fraction.

In JULES, the total fAPAR of a grid cell ($fAPAR$) is calculated by simply weighting the fAPAR calculated by the radiative transfer scheme by the actual area covered by vegetation as,

$$fAPAR = f_{veg} \cdot fAPAR_{veg} \tag{3.18}$$

where $fAPAR_{veg}$ is the fAPAR directly extracted from the two-stream scheme, which considers the gridbox as being a 1D turbid medium, and $fAPAR$ is the fAPAR of the whole canopy with vegetation and bareground soil. Eq. 3.18 is used to reduce $fAPAR_{veg}$ proportionally to the area only covered by vegetation. And the correspondent canopy albedo (α_s) can be obtained as,

$$\alpha_s = f_{veg} \cdot \alpha_{veg} + f_{under} \cdot \alpha_{soil} \tag{3.19}$$

where α_{veg} is the surface albedo directly extracted from the two-stream scheme and α_{soil} is the soil albedo.

It is important to note that the tile fraction correction affects not only the radiative transfer in LSMs, but other parts of the model related to water and carbon balances as well. This parameterisation scheme is evaluated with other more complex radiative transfer and parameterisation schemes over a number of hypothetical scenarios in Chapter 4, and it is referred to as $\mathbf{Veg_{frac}}$.

3.4 The RAMI4PILPS experiment

The RAMI4PILPS experiment (Widlowski et al., 2011) assessed the implications on radiation partitioning of different canopy radiative transfer schemes in a model intercomparison particularly focused on LSMs. For different heterogeneous canopy scenes tree crowns were approximated by woodless spheres with pre-described size, canopy height, and degree of mutual shading between neighbouring crowns. For each scenario, simulations for different leaf areas and varying soil brightness (Figure 3.2) were performed assuming direct incident radiation for three different Sun zenith angles (27.5°, 60°, and 83.5°), as well as isotropic illumination conditions.

In this thesis, the RAMI4PILPS heterogeneous canopy scenario, referred to as "Open Forest Canopy" is used. Details of the RAMI4PILPS experiments used in this present study are summarised in Table 3.1 and a graphic representation of the experiment setups can be found in Fig. 3.2. Further details of the RAMI4PILPS experiments can be found in Widlowski et al. (2011).

A reference data set of relatively well known uncertainty was provided by a 3D Monte Carlo raytracing model known as raytran (Govaerts and Verstraete, 1998), and a number

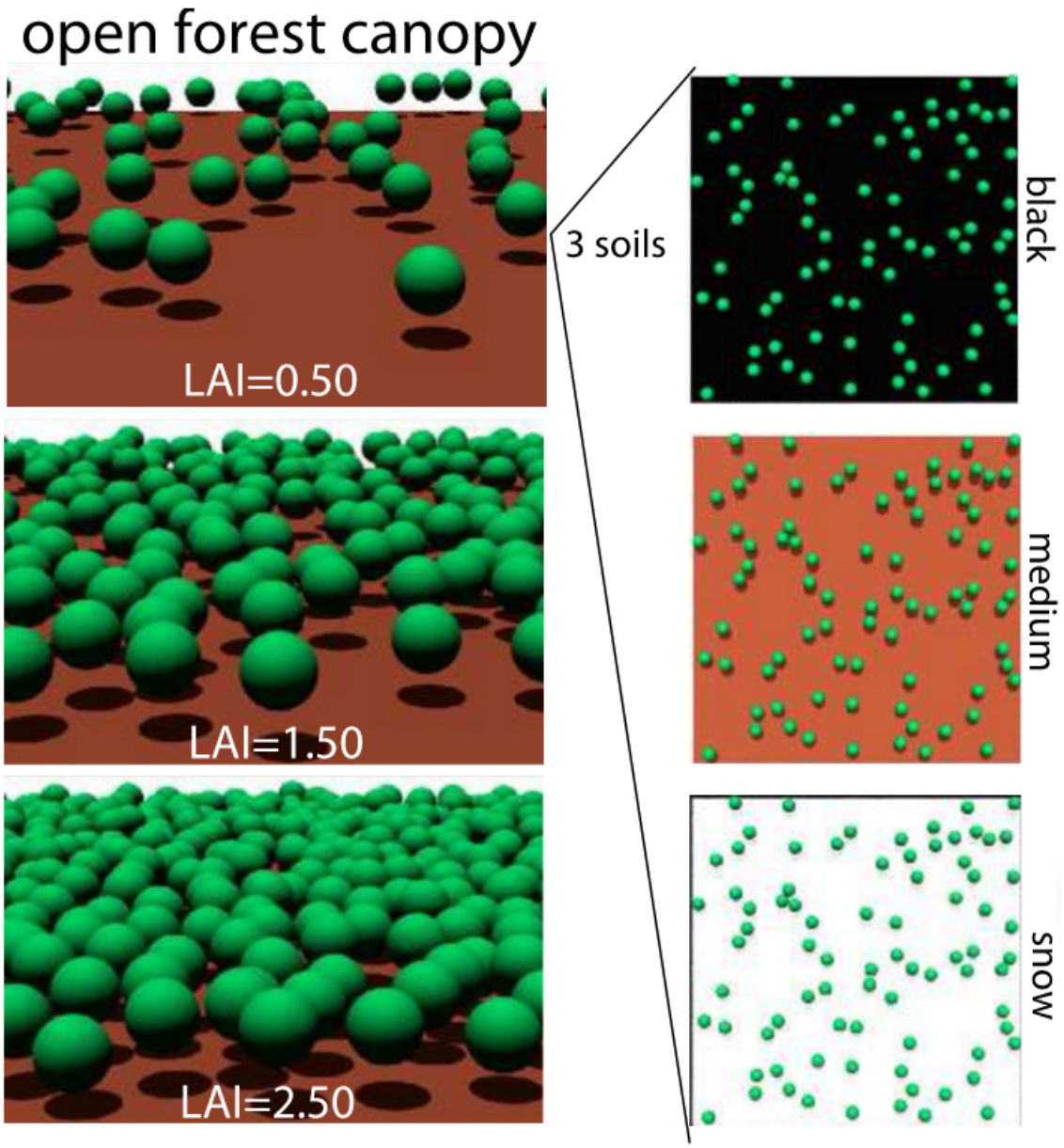

Figure 3.2: Graphical representation of the open forest canopy environments used in RAMI4PILPS. The images on the left represent three different canopy structures and three different background brightness for each canopy density. Figure adapted from Widlowski et al. (2011).

of model simulations was compared against the raytran reference data in the RAMI4PILPS experiments. The ray-tracer code used in the RAMI4PILPS experiment allows the explicit radiation transfer calculations in different heterogeneous canopy scenes by implementing a Monte Carlo approach where "the fate of millions of individual rays are followed as they travel through the computer simulated scene" (Govaerts and Verstraete, 1998). This model is computationally expensive, but implements the most detailed radiation transfer simulations.

Table 3.1: Summary of variables defining structurally heterogeneous scenes (see Widlowski et al. (2011) for details). Different soil albedos are defined as black (BLK), medium (MED), and snow (SNW).

Variable Identification	**Values (Units)**
Leaf Area Index/ canopy	0.50^S, 1.50^M and 2.50^D ($m^2.m^{-2}$)
Leaf Area Index/ sphere	5.0^S, 5.0^M and 5.0^D ($m^2.m^{-2}$)
1 - $P_{gap}(\theta = 0°)$	0.09^S, 0.26^M and 0.434^D
Tree density	12.80^S, 38.24^M and 63.68^D (trees/hectare)
Maximum canopy height	16 m
Minimum sphere centre height	7 m
Maximum sphere centre height	11 m
α_{soil},PAR / α_{soil},NIR	BLK: 0.00/0.00; MED: 0.12/0.21; SNW: 0.96/0.56
Soil scattering law	Lambertian
ρ_{leaf},PAR / ρ_{leaf},NIR	0.0735/0.3912
τ_{leaf},PAR / τ_{leaf},NIR	0.0566/0.4146
Leaf scattering law	Bi-Lambertian
Sun zenith angle	27.5°/60.0°/83.5°/Isotropic(ISO)
Scatterer Normal Distribution	Spherical
Woody area index	0.0 ($m^2.m^{-2}$)

^{S}Sparse vegetation. ^{M}Medium vegetation. ^{D}Dense vegetation.

The raytran model has been compared extensively against field observations (Widlowski et al., 2005), angular measurements (Govaerts and Verstraete, 1995), and against other radiative transfer schemes during RAMI experiments (Pinty et al., 2001, 2004; Widlowski et al., 2007). Raytran performs well when conserving energy and presents a good

match with more complex analytical solutions to within 10^{-4} units of shortwave radiation partitioning terms on average. It was identified as one of six 3D canopy radiative transfer models chosen to participate on the development of a reference data set against which other radiative transfer models could be evaluated (Widlowski et al., 2011). All six 3D Monte Carlo models with less than 1% divergence over hundreds of thousands of model runs have become available for comparison on the RAMI Online Model Checker (`http://romc.jrc.ec.europa.eu/`), a web based facility for benchmarking of canopy reflectance models (Widlowski et al., 2008).

3.5 Modelling photosynthesis: the Farquhar model

Leaf photosynthesis is estimated as the minimum rate of three assimilation regimes as proposed by Farquhar et al. (1980) and modified by Collatz et al. (1991, 1992): (i) the Rubisco-limited rate or **carbon limiting regime** (W_c), (ii) the light-limited rate or **light limiting regime** (W_l), and (iii) the carbon compound export limitation for C3 plants or PEP-carboxylase export limitation for C4 plants, referred to as the electron **transport** or **export limiting regime** (W_e). Further details on the photosynthesis parameterisation in JULES are given in Clark et al. (2011), and the limiting regimes are described in the following equations:

1. Carbon limiting rate:

$$W_c = \begin{cases} V_{cmax}\left(\frac{c_i - \Gamma}{c_i + K_c(1+O_a/K_o)}\right) & \text{for } C_3 \text{ plants} \\ V_{cmax} & \text{for } C_4 \text{ plants} \end{cases} \tag{3.20}$$

   where V_{cmax} (mol CO_2 m^{-2} s^{-1}) is the maximum rate of carboxylation of Rubisco, c_i (Pa) is the leaf internal carbon dioxide partial pressure, Γ (Pa) is the CO_2 compensation point in the absence of mitochondrial respiration, O_a (Pa) is the partial pressure of atmospheric oxygen, and K_c and K_o (Pa) are the Michaelis-Menten parameters for CO_2 and O_2, respectively (Clark et al., 2011).

2. Light limiting rate:

$$W_l = \begin{cases} \alpha \cdot fAPAR \cdot I^{\downarrow}\left(\frac{c_i - \Gamma}{c_i + 2\Gamma}\right) & \text{for } C_3 \text{ plants} \\ \alpha \cdot fAPAR \cdot I^{\downarrow} & \text{for } C_4 \text{ plants} \end{cases} \tag{3.21}$$

where α is the maximum quantum efficiency of photosynthesis (mol CO_2 mol^{-1} PAR), which is regulated by the effect of photorespiration as it is multiplied by the term in brackets to give the effective quantum efficiency in C_3 plants. In the case of C_4 photosynthesis, Γ is close to 0 and the quantum efficiency is independent of intercellular carbon concentration, being equal to its maximum value. fAPAR is given by the two-stream scheme and $I^{\downarrow}$ is the incident PAR at the top of the canopy. fAPAR is calculated separately between sunlit and shaded leaves, therefore the light limiting rate is different between these two types of leaves. The total light limiting rate per layer is the sum between sunlit and shaded W_l weighted by f_{sun} in Equation 3.2.1.

3. Export limiting rate:

$$W_e = \begin{cases} 0.5V_{cmax} & \text{for } C_3 \text{ plants} \\ 2 \times 10^4 V_{cmax} \frac{c_i}{P_*} & \text{for } C_4 \text{ plants} \end{cases} \tag{3.22}$$

where P_* is the surface air pressure (Pa). For C_3 plants W_e is the rate of transport of photosynthetic products from the chloroplast to other parts of the plant, and for C_4 plants it represents the process of the initial carboxylation by PEPCarboxylase.

Two variables that are often used when calculating photosynthesis limiting rates according to the Farquhar et al. (1980) model are independently calculated in JULES, these are: the maximum rate of carboxylation of Rubisco (V_{cmax}) and the CO_2 compensation point in the absence of mitochondrial respiration (Γ), or the photorespiration compensation point. V_{cmax} can be obtained for a range of different temperatures but it is calculated from the maximum rate of carboxylation of the enzyme Rubisco at 25°C (V_{cmax25}) with a PFT-specific optimal range of temperature defined by parameters in JULES, e.g., upper temperature parameter (T_{upp}) and lower temperature parameter (T_{low}) (Clark et al., 2011):

$$V_{cmax} = \frac{V_{cmax25i} Q_{10\_leaf}^{0.1(T_c-25)}}{\left[1 + e^{0.3(T_c - T_{upp})}\right]\left[1 + e^{0.3(T_{low} - T_c)}\right]} \tag{3.23}$$

where T_c is canopy (leaf) temperature and Q_{10_leaf} is a temperature dependent function with default value equals 2. Photosynthetic capacity at each canopy layer is calculated

assuming that the reference value varies as:

$$V_{cmax25i} = \begin{cases} 0.0008 n_0 e^{-k_n(\frac{i}{n})} & \text{for } C_3 \text{ plants} \\ 0.0004 n_0 e^{-k_n(\frac{i}{n})} & \text{for } C_4 \text{ plants} \end{cases} \tag{3.24}$$

where n_0 is the leaf nitrogen concentration at the top of the canopy given in kgN[kgC]$^{-1}$, k_n is a nitrogen profile coefficient estimated to be 0.78 (Clark et al., 2011), but the default value of k_n can be modified when using can_rad_mod = 6 in JULES, i is the canopy layer, and n is the total number of layers with default value equal 10. Γ at any desired partial pressure of atmospheric oxygen is give by:

$$\Gamma = \begin{cases} \frac{O_a}{2\tau} & \text{for } C_3 \text{ plants} \\ 0 & \text{for } C_4 \text{ plants} \end{cases} \tag{3.25}$$

with τ the Rubisco specificity factor[1] for CO_2 relative to O_2, which varies with temperature according to:

$$\tau = 2600 Q_{10\_rs}^{0.1(T_c-25)} \tag{3.26}$$

with Q_{10_rs}=0.57. The Michaelis-Menten parameters are also temperature dependent:

$$\begin{aligned} K_c &= 30 Q_{10\_Kc}^{0.1(T_c-25)} \\ K_o &= 3 \cdot 10^4 Q_{10\_Ko}^{0.1(T_c-25)} \end{aligned} \tag{3.27}$$

with $Q_{10\_Kc} = 2.1$ and $Q_{10\_Ko} = 1.2$.

In JULES, gross photosynthesis rate is calculated from the Farquhar limiting regimes with a set of quadratic equations, which assure a gradual transition from one limitation to another as in:

$$\begin{aligned} \beta_1 W_p^2 - W_p(W_c + W_l) + W_c W_l = 0 \\ \beta_2 W^2 - W(W_p + W_e) + W_p W_e = 0 \end{aligned} \tag{3.28}$$

where W_p is the smooth minimum of W_c and W_l. Finally, W is the gross photosynthesis rate. The smaller root of each quadratic is selected. The values of the co-limitation coefficients are empirically determined (Collatz et al., 1990), in JULES the values β_1 =

[1] According to Galmés et al. (2005) the specificity factor of Rubisco is "a measure of the relative capacities of the enzyme to catalyse carboxylation and oxygenation of ribulose 1,5-bisphosphate and hence to control the relative rates of photosynthetic carbon assimilation and photorespiration".

0.83 and $\beta_2 = 0.93$ are used.

It is important to note that in JULES the radiative transfer scheme follows a multilayer approach for light interception, as previously discussed in Section 2.3, and therefore for photosynthesis as well. The multilayer approach simulates transition between the Farquhar limiting regimes at each canopy layer, resulting in increased carbon limitation towards the top of the canopy and increased light limitation towards the bottom in the canopy (Clark et al., 2011). The diurnal and seasonal cycles also play an important role on the transitioning of carbon limiting regimes. In the middle of the day, bottom canopy layers have photosynthesis usually limited by light but at the beginning and at the end of the day, when the Sun zenith angle is large, all layers present photosynthesis limited by light. This is important for the later discussion of zenith angle impacts on clumping index and GPP in Chapter 5.

3.6 FLUXNET study sites

Flux tower sites make use of sonic anemometers and infrared gas analysers above the vegetation canopy to infer fluxes of energy, water, and carbon between the land surface and the atmosphere. To do so, measures of wind speed in three directional components and gas concentrations are combined through the eddy covariance method, and it is possible to determine the the net flux of CO_2, for example, which is a proxy for the NEE term (excluding storage terms), and that can be later divided into GPP and ecosystem respiration following flux-partitioning algorithms (Reichstein et al., 2005).

A global network of flux tower sites with measurement of energy, water, and carbon fluxes between the land surface and the atmosphere was developed across a range of different ecosystems since the early 1990s, the FLUXNET (Baldocchi et al., 2001). The integration of flux tower data throughout the world is important for the right determination of global carbon and water cycles. Over 500 tower sites are located across the world over a range of study sites with different vegetation types, from tropical to boreal forests, temperate forests in Europe, North America, Asia, as well as grasslands, tundra, crops (Baldocchi et al., 2001). The data is fully available and free of cost from `http://www.fluxnet.ornl.gov/`. The following subsections are used to briefly describe the flux tower study sites used in Chapter 5.

3.6.1 Boreal forests: the BOREAS sites

The BOREAS study areas were defined as:

1. the Northern Study Area (NSA) - with a total of five tower flux sites within 8000 km^2 area over Thompson Manitoba through to Nelson House Manitoba whilst three are used in this present study:

    i. Northern Study Area - Old Black Spruce (NSA-OBS) site: a site containing mostly old black spruce trees, average tree age between 75 and 90 years, average tree height from 9 to 12 meters, and tree density from 1150 to 8700 ha^{-1}.

    ii. Northern Study Area - Old Jack Pine (NSA-OJP) site: a site containing mostly old jack pine trees, average tree age between 50 and 65 years, average tree height from 9 to 13.5 meters, and tree density from 1300 to 3500 ha^{-1}.

    iii. Northern Study Area - Young Jack Pine (NSA-YJP) site: a site containing mostly young jack pine trees, average tree age 25 years, average tree height from 0 to 2.5 meters, and tree density from 5700 to 42,000 ha^{-1}.

2. the Southern Study Area (SSA) - with a total of six tower flux sites within 11170 km^2 area distributed over Prince Albert National Park through to the Candle Lake Saskatchewan whilst four are used in this present study:

    i. Southern Study Area - Old Black Spruce (SSA-OBS) site: a site containing mostly old black spruce trees, average tree age between 0 and 155 years, average tree height from 0 to 10 meters, and tree density from 3700 to 5800 ha^{-1}.

    ii. Southern Study Area - Old Jack Pine (SSA-OJP) site: a site containing mostly old jack pine trees, average tree age between 60 and 75 years, average tree height from 12 to 15 meters, and tree density from 1600 to 4000 ha^{-1}.

    iii. Southern Study Area - Young Jack Pine (SSA-YJP) site: a site containing mostly young jack pine trees, average tree age between 11 and 16 years, average tree height from 4 to 5 meters, and tree density from 4000 to 4100 ha^{-1}.

    iv. Southern Study Area - Old Aspen (SSA-OA) site : a site containing mostly old aspen trees, average tree age 60 years, average tree height 21 meters, and tree density from 900 ha^{-1}.

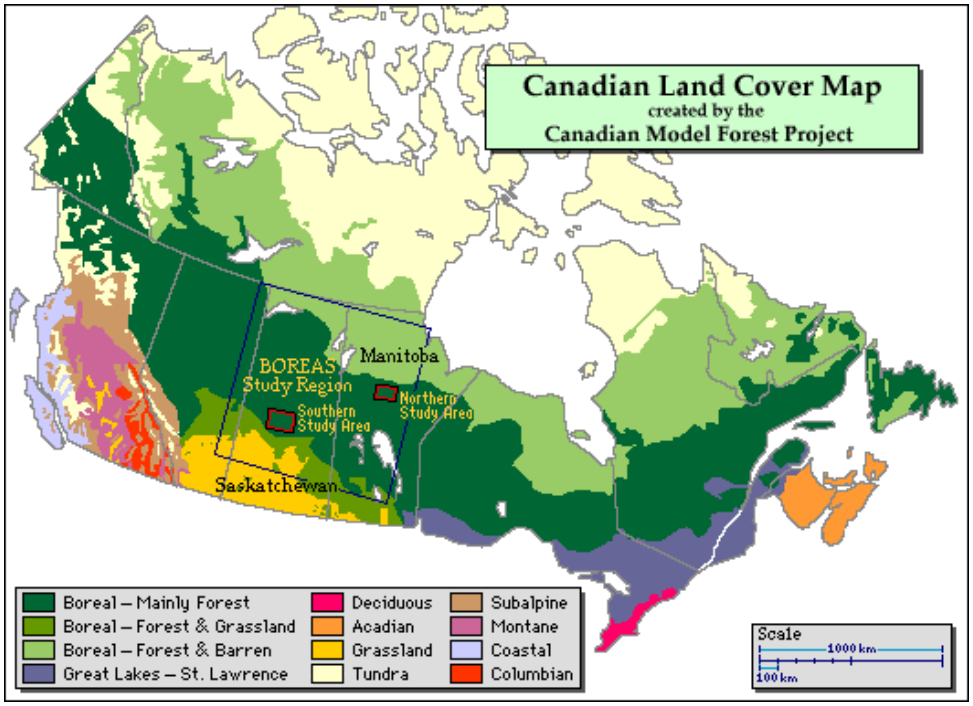

Figure 3.3: Land Cover map of Canada showing the BOREAS Study Region and the Northern and Southern Sites. Figure taken from `https://daac.ornl.gov/BOREAS/bhs/Study_Region.html`

Hemispherical photographs were taken at three heights (0.8, 1.5, and 2.5 m) in separate sample transects for each one of the BOREAS tower flux sites. For all sites photographs were acquired at 10 m intervals along a central axis study mapped plot, except for NSA-YJP, where photographs were acquire in intervals of 5 m. The location of hemispherical photograph sample sites were determined in relation to the main flux tower of each site as follows:

i. NSA-OBS site: the transect was established from 80 to 130 m Southeast of the tower.

ii. NSA-OJP site: the transect was established from 70 to 120 m Southeast of the tower.

iii. NSA-YJP site: the transect was established from 120 to 150 m Southeast of the tower.

iv. SSA-OBS site: the transect was established from 150 to 230 m Southeast of the tower.

v. SSA-OJP site: the transect was established from 130 to 180 m Southeast of the tower.

vi. SSA-YJP site: the transect was established from 30 to 80 m Southeast of the tower.

vii. SSA-OA site : the transect was established from 70 to 120 m Southwest of the tower.

The photographs were digitised at a resolution of 512 (horizontal) x 480 (vertical) x 7 bits using the hemispherical photograph software CANOPY (Rich, 1989, 1990) archived in Kodak PhotoCD format (Chen et al., 1997). The zenith profile of direct transmittance was obtained at 5° zenith angle intervals and separated into five zenith angles from 0 to 75° in order to compare the results obtained with hemispherical photographs and the ones obtained with LAI-2000. The LAI was calculated using the program LAICALC (Rich et al., 1995) following the method of Chen and Black (1991).

3.6.2 Woody-savannah: Tonzi Ranch

The Tonzi Ranch site (US-Ton) is classified as an oak-grass woodland savannah located in the lower foothills of the Sierra Nevada Mountains, California, USA (38.4318°N, 120.9668°W) at 177 m altitude on a flat terrain, under a Mediterranean-type climate with hot, dry summers and mild, rainy winters. This woody savannah site is dominated by blue oak trees (*Quercus douglasii*) with occasional (less than 10%) grey pine trees (*Pinus sabiniana*), and understory mainly composed of grasses (*Brachypodium distachyon*, *Hypochaeris glabra*) (Baldocchi et al., 2004). It presents a sparse vegetation cover of 47%, average tree density of 144 ha^{-1}, with average tree height at 9.4 ± 4.3 m, where trunk height is 1.8 ± 1.3 m, diameter at breast height (DBH) is 0.26 ± 0.11 m, and the average tree crown radius is 2.9 ± 1.4 m (Chen et al., 2008). This flux tower site is part of FLUXNET and AmeriFlux (`http://public.ornl.gov/ameriflux/`) since 2001, and a large number of more detailed information can be found in other studies (Baldocchi et al., 2004; Ma et al., 2007; Chen et al., 2008).

DHPs were acquired from 5^{th} to 7^{th} August, 2008, close to the peak of the growing season, on a 300 m × 300 m sampling plot with the flux tower at the centre, gridded at 30 m × 30 m intervals (Ryu et al., 2010). The extent of the plot corresponds to the scale of spatial heterogeneity as determined through semivariogram analysis performed by Kim et al. (2006).

Direct transmittance was extracted from the DHPs using the CIMES-FISHEYE software (Walter, 2012) for this study and all the others, except for the BOREAS sites. First, the raw photographs were oriented to the geographic North; East and West are inverted on Hemispherical Photographs (East left, West right). Second, the horizon circle of the image had to be identified, and to do so, brightness was increased, and contrast adjusted.

Third, the pixel coordinates of 3 points were clearly defined on the inner border of the circle because their determination is enough to describe the hemisphere of the photograph. The coordinates were used in the software to centre the image and define its circular limit. For the set of DHPs collected at US-Ton, there was no need to repeat this procedure to each image, since the position and diameter did not vary from one image to the next. This was not the case for all study sites (e.g., Harvard forest), and an automated method was created to identify the hemisphere of photographs individually.

Colour digital images are made of pixels, and pixels are made of combinations of primary colours; in this context a image channel is the grayscale image of the same size as a colour image, made of just one of the primary colours. For instance, an image from a standard digital perspective will have a red, a green, and a blue channel, or RGB. A grayscale image has just one channel. The green channel translates best halftones but is not suited for this type of analysis. The red and blue channels offer good contrast separating sky (background) from plants (foreground). And so, the fourth step is to select the blue channel and discard remaining channels.

Fifth, the selection of an appropriate method to calculate a threshold is of concern to hemispherical photography analysis. Some softwares offer several methods to determine automatically a global threshold value derived from the histogram of grey levels of the whole image (Ridler and Calvard, 1978). In fact, there is no perfect thresholding method, therefore, to ensure consistency, it is important to always use the same method for a given set of photographs. It allows repeatability of the process, independent of any user. For Tonzi Ranch and the remaining sites, except for the BOREAS sites the threshold method used was based on Otsu (1979).

3.6.3 Temperate coniferous forest: Oregon sites

The temperate coniferous sites in Oregon are located in a semi-arid climate with annual precipitation between 350 and 880 mm (Law et al., 2001b; Williams et al., 2005; De Kauwe et al., 2011) at the East cost of the United States composed mostly by ponderosa pine (*Pinus ponderosa*) and incense-cedar (*Calocedrus decurrens*) with understory comprised of Manzanita (*Arctostaphylos patula*), and Bitterbush (*Purshia tri-dentata*), and can be characterised by two broad forest age classes:

i. a mature study site (US-Me4) dominated by ponderosa pine with tree age ranging

from 95 to 316 years (Law et al., 2003), with coordinates 44.4992°N, 121.6224°W located within the Metolius Research Natural Area (RNA) and the Metolius river basin (De Kauwe et al., 2011).

ii. an intermediate (US-Me2) site with tree age ranging from 56 to 89 years (Law et al., 2003), also in the presence of ponderosa pine trees that was cleared and allowed to regenerate naturally (Schwarz et al., 2004), with coordinates 44.4524°N, 121.5572°W located in private land that had once been old-growth forest (De Kauwe et al., 2011).

The flux tower sites present a sparse vegetation with relative limited understory foliage partly due to light competition and/or fire, and both sites previously maintained flux towers as part of the FLUXNET, with meteorological and flux measurements recorded since 1999.

De Kauwe et al. (2011) described in detail the methodology used for acquiring the hemispherical photographs over the sites in Oregon, and they are briefly described in here. Digital hemispherical photographs were acquired over three 9 km^2 sub-regions within a 121 km^2 area with relative representativeness of each age class. The 9 km^2 area was then divided into nine 1 km^2 boxes and within each box three Elementary Sampling Units (ESU). Each ESU was randomly located within each 1 km^2 box, in order to reduce the bias and sample the natural heterogeneity of the land surface. In the case of a randomly selected inaccessible ESU, another ESU would be located to a nearby location 100 m away until it was possible to take the photographs. Four extra plots were created at the mature site and an extra one at the intermediate site where defined, resulting in a total of 107 ESU plots across the whole study area.

3.6.4 Mixed Forest: Alice Holt

The Alice Holt forest site (Alice Holt) is classified as a managed deciduous broadleaved plantation woodland, located in the Straits Inclosure, Alice Holt Research Forest, United Kingdom (51.1167 °N, 0.8500 °W) at 80 m altitude on a flat terrain, under a mild temperate, oceanic climate with annual air temperature around 9.6°C and the mean annual precipitation 779 mm (Wilkinson et al., 2012). This managed deciduous broadleaf site is dominated by oak trees (*Quercus robur L.*) with occasional conifers (*Pinus nigra* subsp., *Pinus nigra* Maire., and *P. sylvestris* L.), and understory mainly composed by hazel (*Cory-*

lus avellana L.) and hawthorn (*Crataegus monogyna Jacq.*). This flux tower site has been operating since 1998 as part of FLUXNET, and more detailed information can be found in published studies (Benham et al., 2012; Wilkinson et al., 2012).

Trees are removed from the vegetation canopy in order to reduce competition, and the whole of the stand was thinned in 1995, followed by a thinning at the eastern side in 2007, and then the western side in 2014 (Pinnington et al., 2016), therefore, the Alice Holt study site presents different structural characteristics across the 90 ha area.

DHPs were acquired separately for the three distinct structural areas of the forest (different thinning years, 1995, 2007, and 2014) during an intensive field campaign undertaken on the 15^{th} and 16^{th} August 2015, and further details can be found in Pinnington et al. (2017). In this study, the pictures were considered together in order to characterise the study site as a whole.

3.6.5 Temperate coniferous forest: Harvard Forest Hemlock site

The Harvard Forest Hemlock site (US-Ha2) is classified as a temperate coniferous forest, located in Harvard forest, Massachusetts, USA (42.5393°N, 72.1779°W) at 200 m altitude on a levelled terrain, under a cool, moist temperate climate with air temperature around 20°C in July, and -7°C in January, and mean annual precipitation of 1100 mm. This pristine mixed to evergreen needleleaf forest site is dominated (83%) by eastern hemlock trees (*Tsuga Canadensis* L.) with occasional white pine trees (*Pinus strobus* L.) and few deciduous species, including red maple (*Acer rubrum*), red oak (*Quercus rubra*), and black birch (*Betula lenta*). This flux tower site has been operating since 2000 as part of FLUXNET, and more detailed information can be found in Hadley and Schedlbauer (2002).

Digital hemispherical photographs have been periodically acquired in spring (leaf-off) and summer/autumn (leaf-on) since 2004 with a Nikon 8mm fish-eye lens mounted on a Nikon F3 (non-digital) camera positioned 1-2 m above ground, levelled and oriented over 8 experimental plots in the Simes Tract every 15 m intervals (Ellison, 2005).

Chapter 4:

Parameterising Vegetation Canopy Structure in RT Models

4.1 Introduction

The main goal of this chapter is to investigate the impacts of vegetation canopy structure on shortwave radiation partitioning through a modelling exercise, using different parameterisation schemes in radiative transfer models.

The main research question to be addressed by this chapter is: by using different parameterisation schemes of vegetation canopy structure, is it possible to make the commonly used two-stream approximation (Sellers, 1985) match the shortwave radiation partitioning of more complex 3D radiative transfer models?

First, in Section 4.2 the shortwave radiation partitioning calculated with 3D radiative transfer models is compared with values generated by the two-stream scheme in scenes with constant LAI but differences in vegetation canopy structure only. The main objective of this section is to understand the limitations of using LAI alone to account for structural variability of a vegetation canopy on shortwave radiation partitioning.

Second, in Section 4.3 and Section 4.4 the shortwave radiation partitioning calculated with the two-stream scheme is compared with values generated in the RAMI4PILPS experiment (Widlowski et al., 2011). Also in Section 4.4, the parameters of four structural parameterisation schemes (Nilson, 1971; Kucharik et al., 1999; Pinty et al., 2006; Ni-Meister et al., 2010) are implemented in the two-stream scheme, in order to compare

their shortwave radiation partitioning against more complex radiative transfer models for different zenith angles and illumination conditions.

Finally, in Section 4.5 the vertical profiles of shortwave radiation partitioning generated by different radiative transfer models and parameterisation schemes are compared in order to evaluate their vertical performance through the vegetation canopy for a range of different zenith angles, because LSMs usually calculate photosynthesis based on a vertical multilayer approach.

4.2 How bad is the assumption of a purely 1D turbid medium for heterogeneous canopies?

In order to identify variations in the fraction of absorbed, and reflected PAR (400 - 700 nm) related to canopy structure only, an analysis is conducted based on different canopy structures described in the RAMI4PILPS experiment (Widlowski et al., 2011). For three different vegetation structural representations: i) a sparse canopy, with 80 trees.ha^{-1} and 10% of vegetation cover; ii) a medium canopy, with 239 trees.ha^{-1} and 30% of vegetation cover; and iii) a dense canopy, with 398 trees.ha^{-1} and 50% of vegetation cover; the scene LAI was held constant and equal to 1.5 m^2.m^{-2}. This value of LAI is the same as the medium canopy density in the RAMI4PILPS experiment, where each one of the 239 spheres represented in the 3D Monte Carlo ray-tracing model, raytran, has LAI equal to 5.0 m^2.m^{-2} (see Table 3.1).

The spherical tree crowns represented in all the RAMI4PILPS scenes have the same foliage area volume density (FAVD given in m^{-1}), which can be calculated following the equation bellow (Quaife et al., 2008):

$$FAVD = \frac{3LAI}{\lambda r^2 b 4\pi} \tag{4.1}$$

where LAI is the total scene LAI, λ is tree density per hectare, r and b are the horizontal and vertical tree crown radius, respectively.

The default value of FAVD for all canopy structures in the RAMI4PILPS experiment is equal to 0.75 m^{-1}. However, in the experiment presented here, the sparse case has a larger FAVD, equal to 2.24 m^{-1}, and the dense case has a smaller FAVD, equal to 0.45

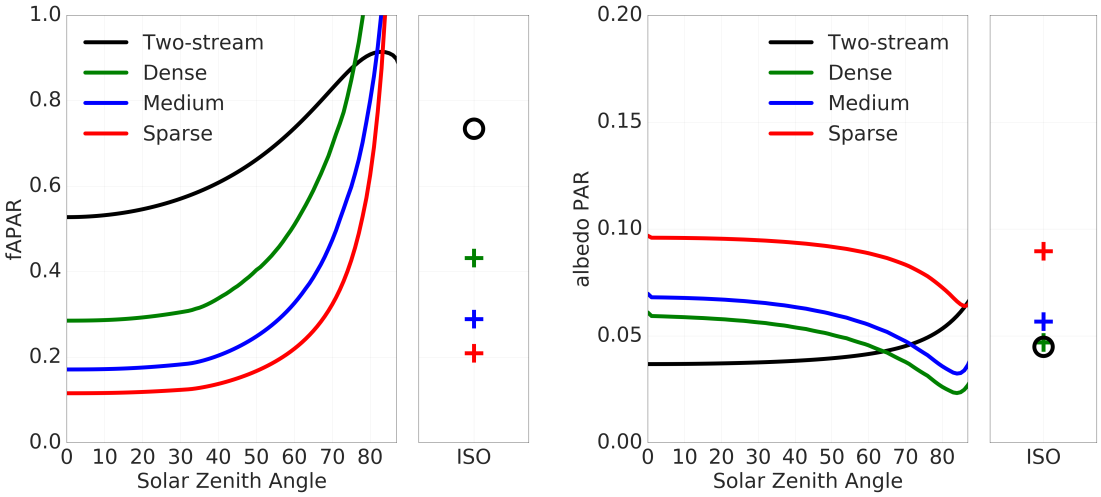

(a) fAPAR (b) albedo PAR

Figure 4.1: Fraction of absorbed and reflected PAR (fAPAR and albedo PAR) respectively, calculated with the two-stream scheme, and other two 3D radiative transfer models **(a.)** MAESPA for absorptance; and **(b.)** GORT for reflectance, over three different vegetation canopy densities with same total scene LAI (1.5 $m^2.m^{-2}$). ISO refers to isotropic radiation.

m^{-1}. This is equivalent to 80 tree crowns with LAI = 14.9 $m^2.m^{-2}$ for the sparse case, and 398 tree crowns with LAI = 3.0 $m^2.m^{-2}$ for the dense case. The FAVD in the sparse case is approximately three times larger than the medium case and, for the dense case, the FAVD is almost half of the medium case. In each case the total scene LAI remains the same.

Modifying FAVD has an effect only on the number of within-crown gaps. In this case, the between-crown gaps were kept as originally defined in the RAMI4PILPS experiment. Note that a different structure in here refers to differences in between-crown gaps only, i.e., the number of tree crowns and the gaps between them define different structural properties.

Three different radiative transfer models were used in this comparison study: i) the two-stream scheme, where the vegetation canopy is treated as a 1D turbid medium (Sellers, 1985), calculating absorptance and reflectance; ii) the 3D tree-based radiative transfer model, MAESPA (Duursma and Medlyn, 2012), calculating vegetation PAR absorptance only; and iii) the 3D geometric optic based radiative transfer model, GORT (Ni et al., 1997), calculating PAR reflectance only. These two 3D models were used to calculate distinct parts of PAR partitioning because of their respective more suitable abilities in

Table 4.1: Bias for model outputs between the two-stream scheme and the MAESPA model for absorptance, and between the two-stream scheme and the GORT model for reflectance in the PAR spectral region (400 - 700 nm). MAESPA and GORT are considered the truth.

		Dense	Medium	Sparse
fAPAR	Bias	-0.177	-0.349	-0.439
albedo PAR	Bias	0.008	0.018	0.049

describing each of the terms within the PAR waveband. MAESPA shows better results in calculating PAR absorption over non-bright backgrounds, while GORT presents a better capacity to represent PAR reflectance.

Figure 4.1 shows the zenith profile of fAPAR and albedo PAR from the two-stream scheme and a more complex model (MAESPA or GORT), for three different canopy structures with same scene LAI. On the right hand side of each plot, with the symbol ISO (isotropic), the totally diffuse radiation case is represented. In terms of absorbed PAR, the two-stream scheme overestimates all the 3D scenarios, except for high zenith angles, for both types of illumination conditions, i.e., direct and diffuse. The dense scene has the closest values for PAR absorptance with an average bias of -0.18. The bias between these two different models decreases with canopy density. For the medium case the bias is -0.35, and the sparse case presents the largest disagreement between the models, with an average bias of -0.44. The results indicate that for a scene with same total LAI but different structural arrangements, the overestimation of the two-stream approach can be as high as 300% for PAR absorptance.

By contrast to canopy absorptance, canopy reflectance is underestimated by the two-stream scheme in comparison to GORT until a Sun zenith angle of approximately 60° for the dense case, 70° for the the medium case, and over the whole zenith profile for the sparse case. The average bias of albedo PAR is up to 0.049 in the sparse case, of the same order of magnitude of the total averaged albedo PAR generated by the two-stream scheme. The differences between the two-stream scheme and the other two 3D radiative transfer models are summarised in Table 4.1.

This experiment performed with three different radiative transfer models indicates that using the scene LAI alone is not sufficient to take into account differences in vegetation canopy structure in order to calculate PAR partitioning into the absorbed and reflected components. It also shows that the diffuse incident light is impacted by vegetation struc-

ture, with overestimation caused by the two-stream scheme regarding absorptance, and underestimation for reflectance. These results are aligned with findings from other studies (Yang et al., 2001; Widlowski et al., 2011; Loew et al., 2014) and they point out limitations caused by the use of the two-stream scheme on the correct estimation of absorbed and reflected PAR over spatially heterogeneous vegetation canopies.

Based on the results presented in this section, it is important to explore mechanisms of making the shortwave radiation partitioning calculated by the two-stream approximation behaves more like complex 3D radiative transfer models in the presence of architectural heterogeneity of the land surface, without losing its original efficiency.

4.3 Evaluating vegetation structural effects in the two-stream scheme: direct transmittance

The next subsections describe and evaluate 4 different clumping indices to address vegetation heterogeneity in the modified version of the two-stream scheme (Section 3.3.1). Evaluations are performed against the RAMI4PILPS (Widlowski et al., 2011) benchmarking exercise. Additionally, two other 3D radiative transfer models, MAESPA and GORT, already used previously are added into the evaluations, in order to determine their abilities and limitations with regards to different spectral and structural properties. Finally, a parameterisation scheme based on the proportion of vegetation cover (Section 3.3.6), commonly used in LSMs to account for vegetation heterogeneity on a grid cell (see Section 3.3.6), is compared with the other approaches as well, in order to evaluated how appropriately LSMs treat shortwave radiation partitioning in the presence of vegetation structure.

4.3.1 Deriving clumping indices coefficients

Two parameterisation schemes were minimised against the RAMI4PILPS reference values: i) the clumping index of Nilson (1971) in Eq. 3.10 and, ii) both structure factor parameters, a and b in Eq. 3.14. The parameters were obtained for each canopy structure through the inversion of the two-stream scheme against direct and diffuse fAPAR and PAR albedo reference values from the RAMI4PILPS experiment. The Nelder-Mead minimisation method (Nelder and Mead, 1964), or 'downhill simplex', was used in the inversion process.

To minimise the structure factor parameters with respect to canopy density, a minimum error evaluation was conducted varying a and b from 0.0 to 1.0 following the equation:

$$RMSE_{ab} = \sqrt{\frac{\sum_{n=1}^{N}(f_{Two-stream} - f_{Reference})^2}{N}} \tag{4.2}$$

where N is number of evaluated cases for each canopy density, a = [0,1], b = [0,1], and $f_{two-stream}$ is the shortwave radiation partitioning term calculated with the two-stream scheme with the structure factor parameterisation for a combination of a's and b's, or in the case of the clumping index, with Ω only; and $f_{Reference}$ is the RAMI4PILPS reference values. The results showed in Figure 4.2 are limited to the PAR waveband, with an intermediate value of background albedo (α_{soil} = 0.12) for the sake of illustration and simplification.

For all the evaluated cases, there is a combination of a and b that gives the minimum error between the 1D and the 3D cases described by a certain area of minimum RMSE (Fig. 4.2). This finding suggests that for a particular forest stand, there is not only a single combination of a's and b's but a number of combinations that modifies the radiative transfer calculations of the two-stream approach, and makes it match the radiation partitioning of more complex 3D models. The elliptical shape represented in dark blue and formed by the minimum error area in Figure 4.2, where the minor axis is given by a range of a's values and the major axis is given by a range of b'values, for all canopy densities, indicates that the range of minimum a's is usually smaller than the range of possible b's, which suggests a stronger effect of a in comparison to b on modulating the radiative fluxes calculated by the two-stream approach.

However, the sparse case seems to be more closely sensitive to the parameters a and b together, as the ellipse that describes the minimum RMSE is inclined towards the y-axis. As canopy density increases, the sensitivity of a starts to increase in relation to b, as it can be noticed by the larger error variation on the x-axis of a. This indicates that for denser canopies, b has a reduced impact due to architectural effects on shortwave radiation partitioning, if compared to a.

The clumping index and structure factor parameters obtained for each canopy density through the inversion of fAPAR and albedo PAR together, over three soil backgrounds at the same time are summarised in Table 4.2:

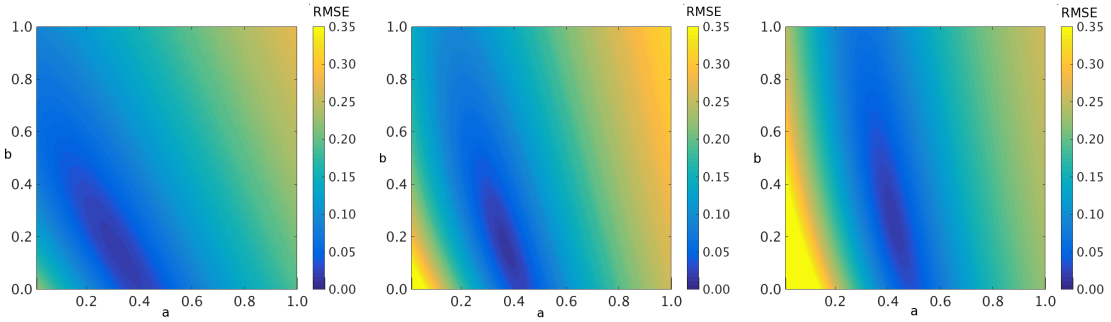

(a) LAI = 0.5 $m^2.m^{-2}$ (b) LAI = 1.5 $m^2.m^{-2}$ (c) LAI = 2.5 $m^2.m^{-2}$

Figure 4.2: Root-Mean-Squared-Error (RMSE) for the two-stream scheme with the structure factor parameterisation and MAESPA for three canopies densities (sparse, medium, and dense).

Table 4.2: Summary of the clumping index (Nilson, 1971) and structure factor coefficients (Pinty et al., 2006) minimised against the RAMI4PILPS reference values for PAR absorptance and reflectance.

RAMI4PILPS scene	Ω	a	b
Sparse	0.424	0.344	0.096
Medium	0.450	0.337	0.256
Dense	0.490	0.418	0.206

Table 4.3: Summary of the clumping index coefficients of Kucharik et al. (1999) (see Eq. 3.12) and Ni-Meister et al. (2010).

RAMI4PILPS scene	Ω_{max}	b	γ
Sparse	0.33	1.44	0.349
Medium	0.70	14.03	0.349
Dense	1.00	3.48	0.349

The remaining clumping indices of Kucharik et al. (1999) and Ni-Meister et al. (2010) follow a set of semi-empirical equations (see Sec. 3.3.3 and Sec. 3.3.5), that were used to estimate the clumping index coefficients for three different canopy sets as in RAMI4PILPS (Table 3.1). All clumping indices are presented by dotted lines in Figure 4.3, and the

clumping index coefficients of Kucharik et al. (1999) and Ni-Meister et al. (2010) are summarised in Table 4.3.

4.3.2 Comparing clumping indices

Direct transmittance was calculated following Eq. 2.5 for each one of the different clumping indices - Ω (Nilson, 1971), $\Omega_e(\theta)$ (Kucharik et al., 1999), $\zeta(\mu)$ (Pinty et al., 2006), and γ (Ni-Meister et al., 2010) (Figure 4.3 right). The 1D case, or Beer's law, was also calculated following Eq. 2.1 which is the equivalent of making $\Omega = 1.0$ in Eq. 2.5.

The 3D tree-based model, MAESPA, was used in the simulations of $P_{gap}(\theta)$ for the RAMI4PILPS scenes, and it was used as the reference model. $P_{gap}(\theta)$ was directly derived from MAESPA by setting a black canopy ($\rho_{leaf} = \tau_{leaf} = 0.0$) with black soil ($\alpha_s = 0.0$) for different structures, and deriving it from fAPAR, as described below,

$$P_{gap}(\theta) = 1.0 - fAPAR(\theta) \tag{4.3}$$

To evaluate the differences between each one of the described parameterisations, the RMSE was calculated following Eq. 4.4,

$$RMSE = \sqrt{\frac{\sum_{\theta=0}^{N}(P_{gap}(\theta)^{\Omega} - P_{gap}(\theta)^{MAESPA})^2}{N}} \tag{4.4}$$

where N = 85 because MAESPA presents numerical instability for very large Sun zenith angles (from 85° to 90°).

The clumping index of Nilson (1971) was also minimised against the RAMI4PILPS reference values of fAPAR and PAR albedo following the Nelder-Mead minimisation method (Nelder and Mead, 1964). This value is a single number, which does not vary with zenith angle, and it is represented as a straight line parallel with the x-axis in Figure 4.3 (left). As represented in Figure 4.3 (right), Nilson's clumping index gives a very good agreement with the calculated $P_{gap}(\theta)$ from the 3D model. The total RMSE from this index is about of 0.15 for the sparse canopy, increasing with canopy density, until up to 0.27 for the dense case (Figure 4.4).

For the sparse canopy, $P_{gap}(\theta)$ obtained with Kucharik's method tends to overestimate the reference values through the range of evaluated solar zenith angles until about 60°.

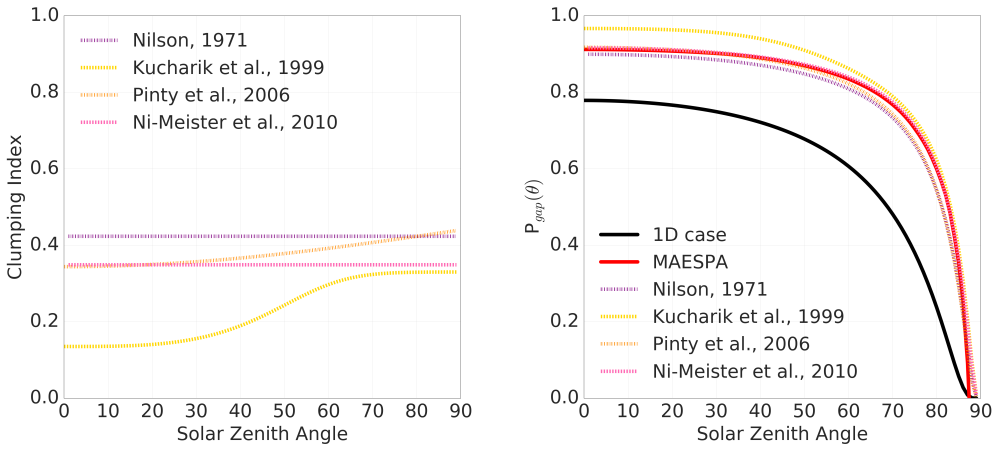

(a) Sparse Canopy

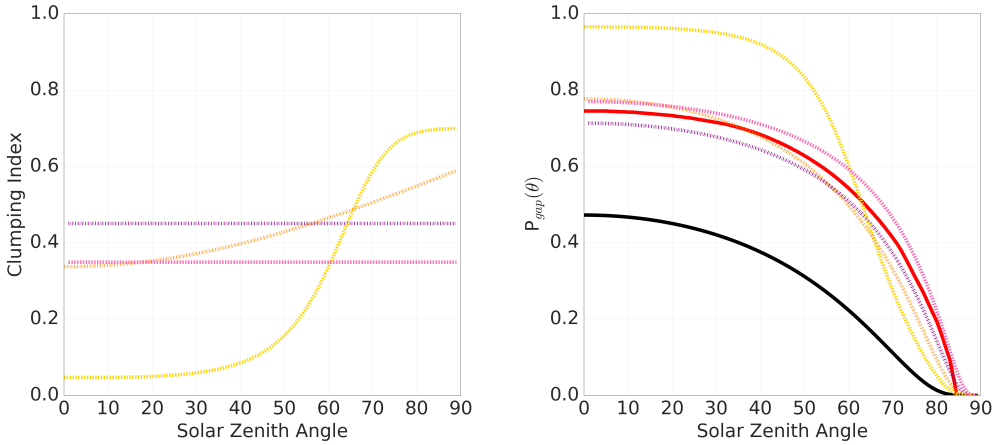

(b) Medium Canopy

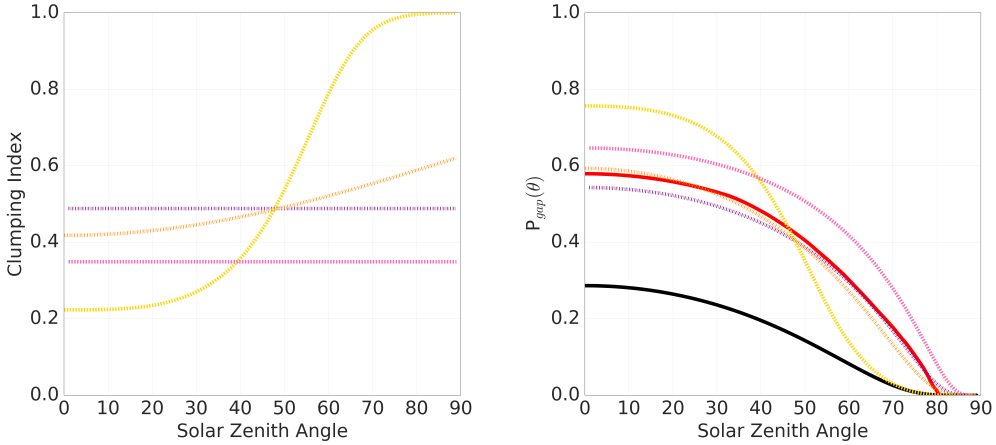

(c) Dense Canopy

Figure 4.3: Comparison between different ways of calculating clumping index and its impact on gap propability.

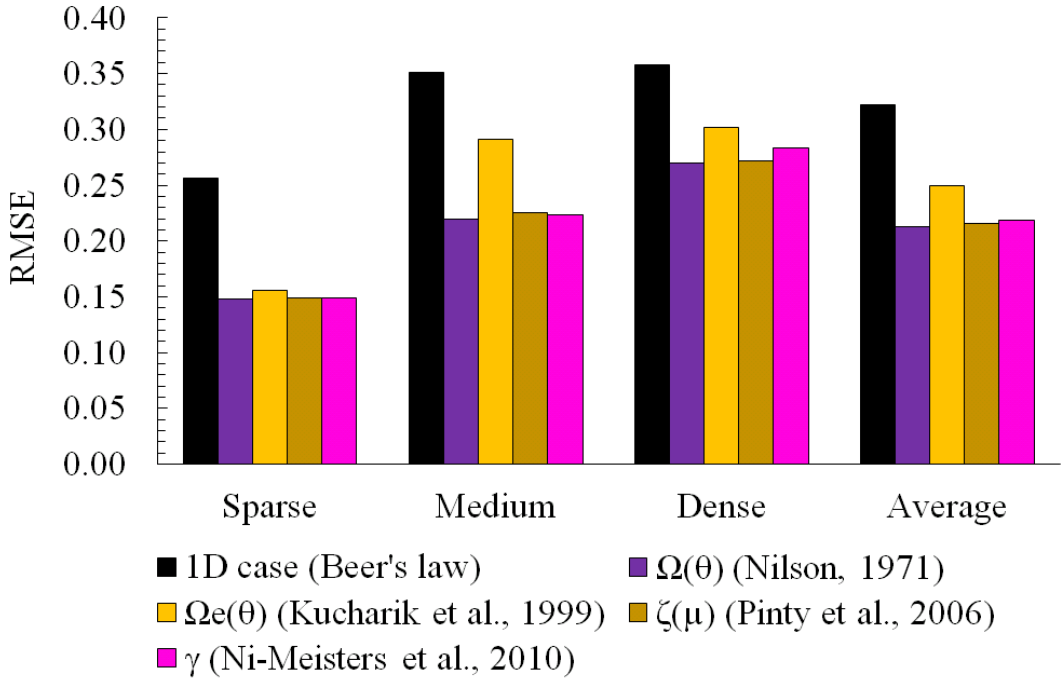

Figure 4.4: RMSE of gap probability generated with three structural parameterisations and MAESPA for three different canopies densities (sparse, medium, and dense) and the average.

For higher solar zenith angles direct transmittance calculated with Kucharik's parameterisation agrees well with the reference values obtained with the 3D model.

Kucharik's parameterisation presents a clumping index always smaller than the other two for the sparse canopy, showing a triple behaviour with a varying zenith angle, i.e., with two asymptotes defined by an empirical relationship. For the sparse case, Figure 4.3 indicates that between the four evaluated parameterisation schemes, the parameterisation scheme presented in Kucharik et al. (1999) shows a slightly larger deviation from the 3D model reference values (≈ 0.15), but still a smaller deviation than the 1D case, which supports the fact that applying the clumping index correction improves direct transmittance estimates.

4.4 Evaluating vegetation structural effects in the two-stream scheme: zenith profile

The performance of the 1D radiative transfer, the two-stream approximation (Sellers, 1985), is tested in this section. Also, in order to evaluate an approach often implemented in GCMs to account for sparse vegetation canopies, a commonly used parameterisation based on the amount of vegetation fraction cover on a model grid cell is also applied, referred as Veg_{frac} (Sec. 3.3.6).

The four different clumping indices described in Section 3.3 were implemented in the modified version of the two-stream scheme, and their ability to calculate shortwave radiation partitioning are compared. These are the clumping indices schemes developed by: 1) Nilson (1971); 2) Kucharik et al. (1999); 3) Pinty et al. (2006), and; 4) Ni-Meister et al. (2010).

The following subsections present the results for absorptance and reflectance separately, over PAR and NIR spectral regions in Figures 4.5, 4.6, 4.7, and 4.8.

4.4.1 Absorptance

The two-stream scheme overestimates the reference values for PAR absorption over all evaluated canopy densities, under both illumination conditions, i.e., direct and diffuse. This behaviour indicates that this scheme is more optically opaque for PAR radiation than the 3D Monte Carlo ray-tracing reference model, particularly due to canopy architectural impacts on radiation propagation. This result is in agreement with the evaluation performed in Section 4.2, where the two-stream scheme overestimates absorption for all different canopy structures generated by the MAESPA model with same total scene LAI.

In the NIR waveband, the two-stream scheme presents a relative good agreement with the reference values for absorption, especially for solar zenith angles equal to 60°, and under a diffuse illumination condition. For other cases, the two-stream scheme overestimates the reference values for smaller solar zenith angles (until approximately 27.5°), and underestimates it for higher solar zenith angles (approximately 83.5°).

MAESPA shows good results in calculating PAR absorption for different vegetation canopy densities. It strongly agrees with the RAMI4PILPS reference values for PAR absorption but only over non-bright surfaces. However, in the presence of snow, MAESPA

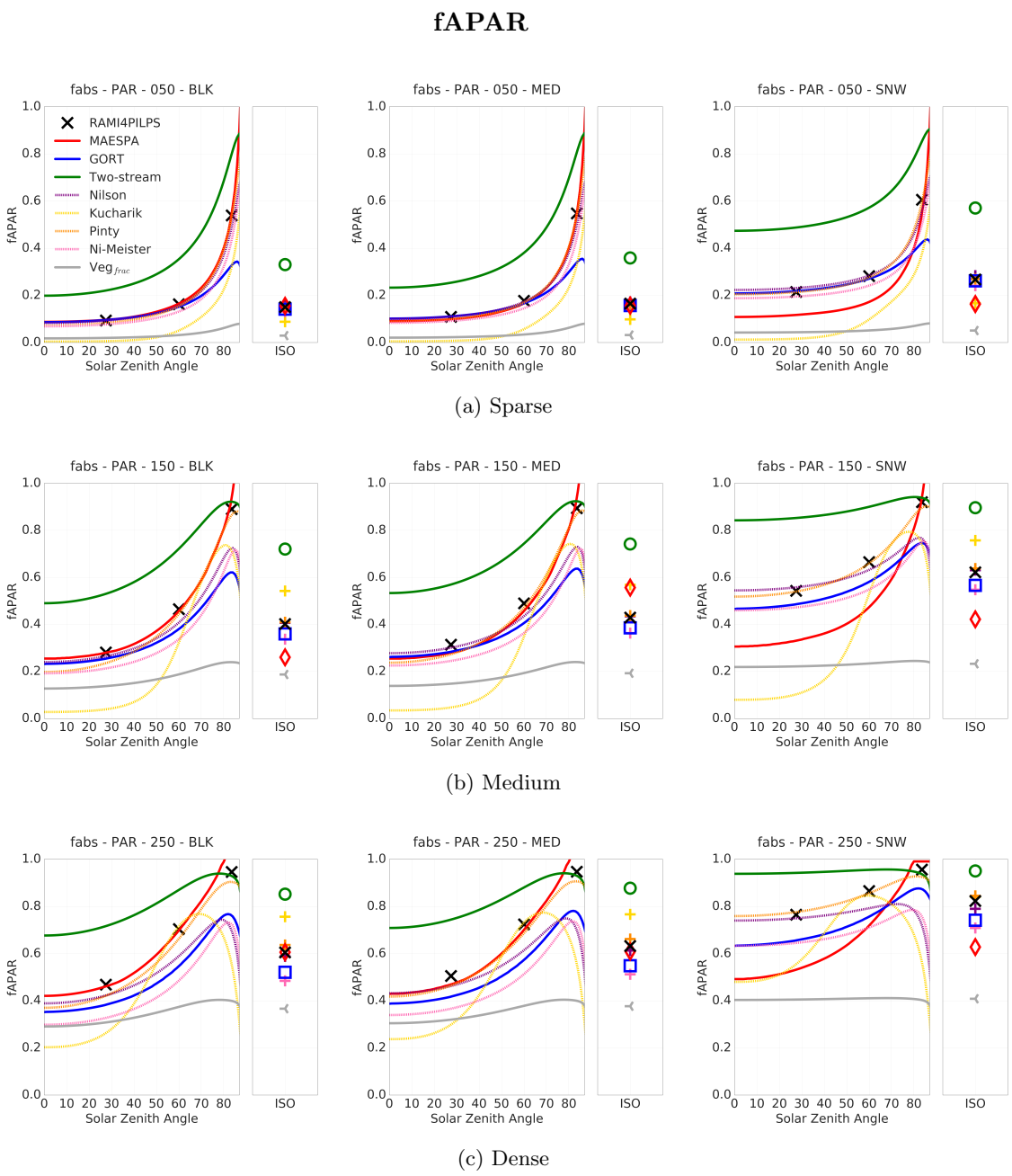

Figure 4.5: Intercomparison of zenith profile of fraction of direct, and diffuse (ISOtropic) absorbed PAR (400-700 nm) calculated with 3 different models (two-stream, MAESPA, and GORT), 4 clumping indices applied into the two-stream scheme (Nilson (1971), Kucharik et al. (1999), Pinty et al. (2006), and Ni-Meister et al. (2010)), a parameterisation scheme commonly used in LSMs based on the vegetation cover of a gridbox (Veg_{frac}), and the RAMI4PILPS reference values obtained with a 3D Monte Carlo ray-tracing model, raytran.

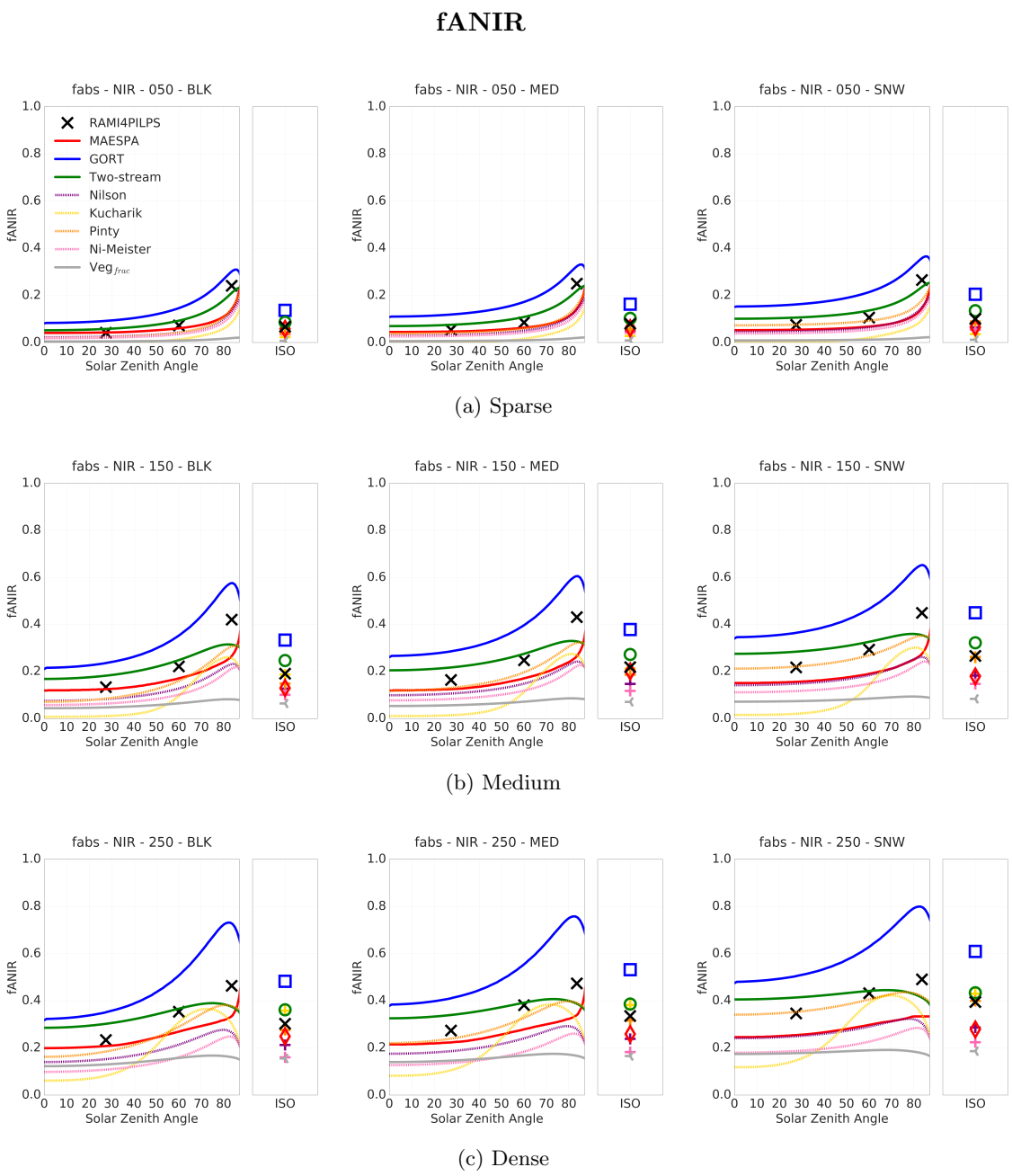

Figure 4.6: Intercomparison of zenith profile of fraction of direct, and diffuse (ISOtropic) absorbed NIR (700-3000 nm) calculated with 3 different models (two-stream, MAESPA, and GORT), 4 clumping indices applied into the two-stream scheme (Nilson (1971), Kucharik et al. (1999), Pinty et al. (2006), and Ni-Meister et al. (2010)), a parameterisation scheme commonly used in LSMs based on the vegetation cover of a gridbox (Veg_{frac}), and the RAMI4PILPS reference values obtained with a 3D Monte Carlo ray-tracing model, raytran.

underestimates PAR absorption in up to 30% over the dense canopy, which demonstrates the limitations of this model in dealing with background reflectance. This lends a degree of confidence to the MAESPA model, which can be used in further intercomparison exercises related to PAR absorption, but its results should be carefully evaluated over highly reflective surfaces. In the NIR spectrum, MAESPA was able to reproduce the shape of the curve associated with absorption but underestimated the reference values by up to 10% in a dense canopy over snow.

The GORT model presented good agreement with the RAMI4PILPS reference values for the sparse case scenario over all soil reflectances for direct illumination. The best agreement with the reference values are found in the solar zenith angle range going from 0° to 60°, in the PAR spectral region. For higher solar zenith angles, GORT underestimates PAR absorption by up to 20% over a black soil background. For diffuse illumination, the GORT model agrees with the reference values. As canopy density increases, PAR absorption generated by the GORT model starts to be underestimated, especially over snow ($\alpha_{soil} = 0.96$), for direct and diffuse illumination conditions. In the NIR waveband, GORT presented a persistent overestimation in absorption for both illumination conditions.

The fraction of vegetation cover, or Veg_{frac} correction, is not able to reproduce the PAR or NIR absorption. It underestimates the total PAR absorption over all evaluated cases. This result is particularly important, because it shows the limited ability of LSMs in correctly estimate PAR absorption used for photosynthesis calculations. Greater discrepancies are associated with higher Sun zenith angles ($> 30°$).

Figure 4.5 indicates that overall the structure factor parameterisation scheme (Pinty et al., 2006) consistently showed a better agreement to the RAMI4PILPS reference values than any other approach under direct (Sun zenith angles from 0 to 90°), and diffuse illumination conditions. It appears to be an accurate tool to derive PAR absorption for all evaluated scenarios, with particular attention to its performance over a brighter background (SNW case). The good agreement with the reference values over snow can be explained by the fact that the minimisation process has been done over all soil brightnesses together, and the different highly scattering behaviour of PAR over snow worked as an 'attractor' for the structure factor parameters.

In the PAR region, the clumping index of Nilson (1971) shows a good agreement with the reference values over the sparse case scenario, and for small Sun zenith angles ($< 30°$),

but, as canopy density increases, and for higher Sun zenith angles ($> 30°$), the clumping index of Nilson (1971) is not able to reproduce the complete behaviour of more complex models for absorption, which indicates that by considering a clumping index that varies with Sun zenith angle as in Pinty et al. (2006), the modified two-stream scheme can match the results of 3D models more accurately.

The main difference between the clumping indices of Pinty et al. (2006) and Ni-Meister et al. (2010) is also related to the inclusion of angular variability. Figure 4.3 shows that for the sparse and medium cases, both clumping indices are basically the same until approximately a solar zenith angle of 25°; after that value, the structure factor based on Pinty et al. (2006) increases with Sun zenith angle. For the dense case, the structure factor is about 5% lager than the clumping index of Ni-Meister et al. (2010) at the beginning of the zenith angular range.

For the sparse case, the differences between Pinty and Ni-Meister's schemes are roughly limited to a small curvature between 60° and 80°. As it can be seen in Figure 4.3, the P_{gap} calculated through both methods agreed quite well for most zenith angles, and present a RMSE = 0.15. Therefore, for the sparse case, the consideration of a clumping index that varies with Sun zenith angle is not crucial to determine absolute values, or the curvature shape of PAR absorption with Sun zenith angle. The remaining parameterisation scheme of Kucharik et al. (1999) underestimates the values of PAR, and NIR absorption, while it overestimates direct transmittance (Fig. 4.3).

The larger discrepancies between the three parameterisation schemes, however, appears when evaluating the medium and dense scenarios. While the Ni-Meister's scheme underestimates the reference values for all evaluated scenes, the most prominent differences are related to higher Sun zenith angles. Nevertheless, these differences are not observed when evaluating Pinty's scheme, because the structure factor varies with Sun zenith angle.

Kucharik's parameterisation scheme has a different behaviour if compared with the other two, and presents a particular good agreement with the reference values for intermediate zenith angles, around 60°. It is important to highlight that this specific parameterisation scheme was derived from observed data from boreal forests, which usually have non-spherical crowns, unlike the RAMI4PILPS canopies; and often presents needle-to-shoot clumping as well, which is not accounted for in this exercise.

4.4.2 Reflectance

For PAR reflectance, the two-stream scheme underestimates the reference values over the majority of the evaluated canopy densities, under both illumination conditions as well, except over black soil albedo (Fig. 4.7). In this particular case, the two-stream scheme reflects more PAR radiation than the 3D models, because photons do not interact with the underneath black soil as much as in the 3D models. Moreover, the two-stream scheme is not able to obtain the correct decaying shape of reflectance with zenith angle over most scenes. In the NIR spectral region, the two-stream scheme tends to overestimate the reference values over the black and medium soil albedos but it shows a relative good agreement over a highly reflective soil.

MAESPA does not show as good agreement as for absorption with the reference values. Over black soil, MAESPA overestimates PAR reflectance for all evaluated cases, especially over the sparse case. Over medium reflective soil, MAESPA behaves closely to the two-stream scheme over the medium and dense canopies, but it shows opposite behaviour than all the other radiative approaches over the sparse case for medium and snow background reflectances; i.e., PAR reflectance remains constant or decreases with Sun zenith angle for most of radiative transfer schemes, while for MAESPA, canopy PAR albedo increases with solar zenith angle (Fig. 4.7a). Over snow, MAESPA underestimates PAR canopy albedo over all evaluated scenarios. MAESPA is not able to reproduce the behaviour of PAR canopy albedo with Sun zenith angle either. MAESPA does not deal with soil reflectance in an accurate manner. This result was already highlighted by its behaviour over a highly reflective soil when looking at absorption.

It is important to note that canopy reflectance is not a direct output variable from the MAESPA model. MAESPA was modified and canopy reflectance was extracted from the model exclusively to make the radiative transfer scheme intercomparison exercise possible to be performed in this chapter. In other terms, MAESPA was never designed to perform accurate calculations of canopy reflectance based on energy balance.

For PAR reflectance, GORT underestimates the reference values over black soil for all the evaluated canopy densities. For the medium soil albedo, GORT is the model which agrees most with the reference values, especially over the medium canopy density. GORT was able to characterise exactly the decay of PAR reflectance following the solar zenith angle curve. Over snow, however, GORT tends to overestimate PAR reflectance,

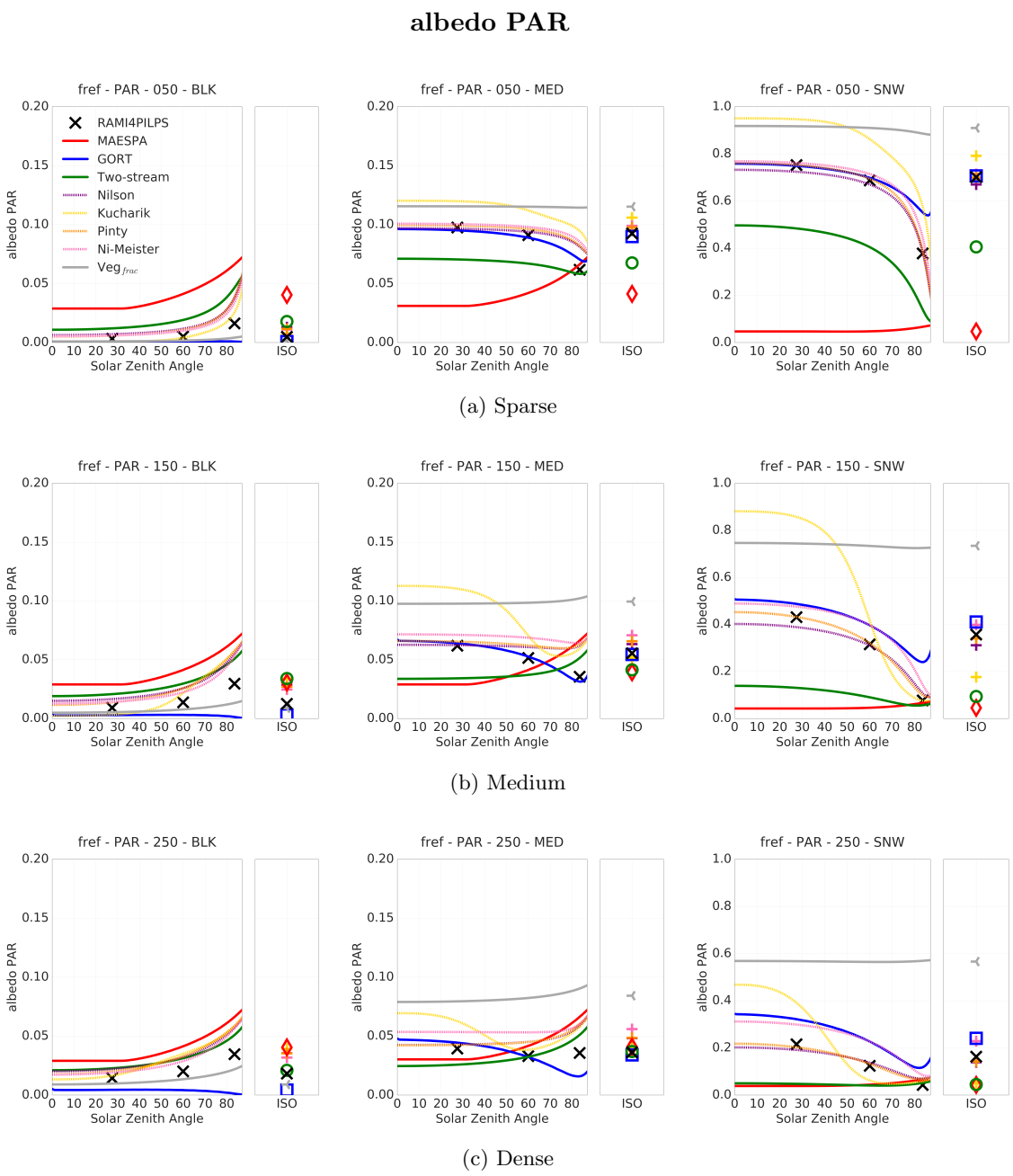

Figure 4.7: Intercomparison of zenith profile of fraction of direct, and diffuse (ISO) reflected PAR (400-700 nm) calculated with 3 different models (two-stream, MAESPA, and GORT), 4 clumping indices applied into the two-stream scheme (Nilson (1971), Kucharik et al. (1999), Pinty et al. (2006), and Ni-Meister et al. (2010)), a parameterisation scheme commonly used in LSMs based on the vegetation cover of a gridbox (Veg_{frac}), and the RAMI4PILPS reference values obtained with a 3D Monte Carlo ray-tracing model, raytran.

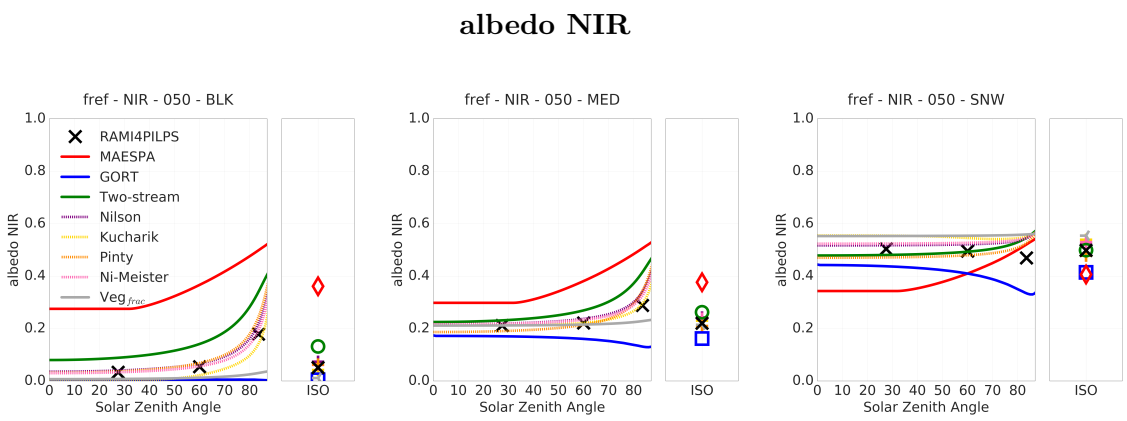

(a) Sparse

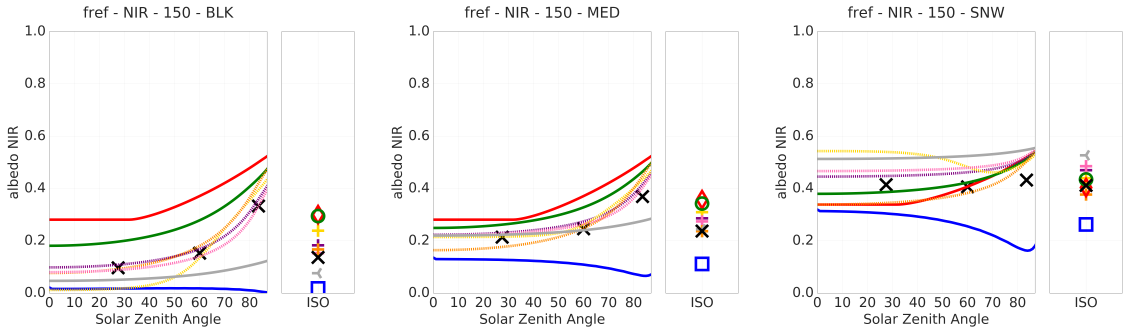

(b) Medium

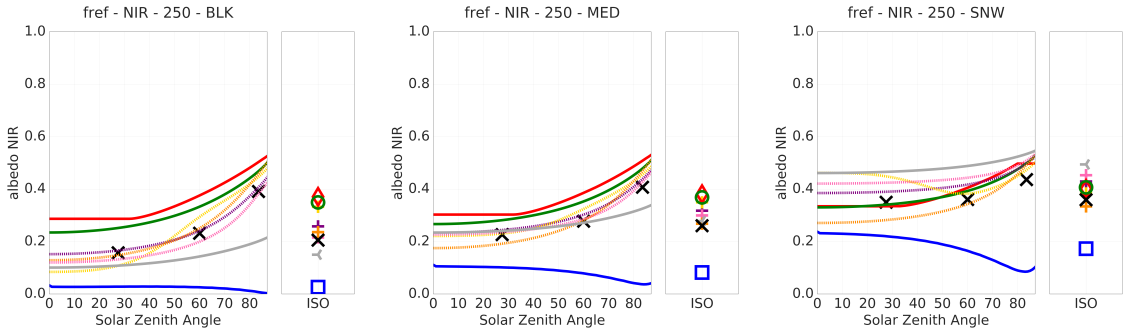

(c) Dense

Figure 4.8: Intercomparison of zenith profile of fraction of direct, and diffuse (ISO) reflected NIR (700-3000 nm) calculated with 3 different models (two-stream, MAESPA, and GORT), 4 clumping indices applied into the two-stream scheme (Nilson (1971), Kucharik et al. (1999), Pinty et al. (2006), and Ni-Meister et al. (2010)), a parameterisation scheme commonly used in LSMs based on the vegetation cover of a gridbox (Veg$_{frac}$), and the RAMI4PILPS reference values obtained with a 3D Monte Carlo ray-tracing model, raytran.

especially over the dense canopy. In the NIR spectrum, GORT presented a persistent underestimation in reflectance, for both illumination conditions, and GORT was not able to reproduce the increasing curve of NIR reflectance over all evaluated cases either.

The Veg_{frac} correction slightly underestimates PAR and NIR reflectances over a black soil for all canopy densities, but it is not able to reproduce the reference values for large Sun zenith angles (83.5°). For a medium reflective soil background, this parameterisation scheme overestimates canopy albedo in up to 5% over a dense canopy associated with large Sun zenith angle. Over snow, its overestimation can be up to 40% over a dense canopy in the PAR spectral region. For the NIR spectrum, the Veg_{frac} correction shows a good agreement with the reference values for a medium reflective soil background, but underestimates it for a black soil, and overestimates it over snow.

As for PAR absorption, Pinty's and Nilson's clumping indices showed a very good agreement with the RAMI4PILPS reference values for PAR reflectance over snow. Their major differences are associated with the medium canopy density over snow, where the presence of the term b in the structure factor (Eq. 3.14) seems to better represent the RAMI4PILPS reference values.

Figure 4.7 indicates that, overall, the structure factor parameterisation scheme consistently showed a better agreement with the RAMI4PILPS reference values than any other approach under direct (for Sun zenith angles from 0 to 90°), and diffuse illumination conditions.

4.5 Evaluating vegetation structural effects in the two-stream scheme: vertical profile

This section explores the vertical impacts of canopy structure on shortwave radiation partitioning using different radiative transfer approaches. Vegetation structure mainly affects the way shortwave radiation is vertically distributed in a vegetation canopy from the top to the bottom. It is expected that the major impacts on photosynthesis are due to the shortwave radiation distribution along the vertical axis through canopy height, described as LAI increments in the two-stream approximation.

The main goals of this section are: first, to estimate the impact of different clumping indices on vertical PAR direct transmittance; and second, to evaluate the impacts on

vertical PAR partitioning calculated by the modified two-stream scheme using different clumping indices.

4.5.1 Transmittance

The models used in this comparison of vertical PAR transmittance were: the two-stream scheme, the modified two-stream scheme with 4 different clumping indices, the Veg_{frac} parameterisation, and the vertical 3D models, MAESPA and GORT. The bottom of canopy reference values from the RAMI4PILPS experiment of transmittance were obtained through the energy conservation law:

$$T(\theta) = \frac{1 - fAPAR(\theta) - \alpha_{PAR}(\theta)}{(1 - \alpha_{soil})} \tag{4.5}$$

where T(θ) is the total transmittance, fAPAR(θ) is the fraction absorbed PAR, $\alpha_{PAR}(\theta)$ is the PAR canopy albedo, and α_{soil} is the background soil albedo in the PAR spectral region. For this experiment, only the medium soil reflectance was used, where $\alpha_{soil} = 0.12$.

In the PAR waveband total transmittance (T(θ)) is roughly equal to direct transmittance ($\text{P}_{gap}(\theta)$) because multiple scattering in this part of the electromagnetic spectrum is very small, consequently it is assumed in here that total transmittance is approximately equal to direct transmittance.

Figure 4.9 shows the vertical profiles of transmittance. The major difference between the models are found at the bottom of the canopy, as optical depth increases. The two-stream scheme underestimates direct transmittance of all the other approaches along the vertical axis. Over the sparse case in the zenith angle of 83.5°, the two-stream scheme shows up to 30% less direct transmittance than the reference model.

The spread between the results of the 3D models increases with canopy density, however: the maximum spread is up to 15% over the dense canopy in 60.0°, which is much less than the differences caused by the default two-stream scheme. The use of a clumping index in the two-stream scheme improves the total vertical distribution of transmittance, as it makes the results of the modified two-stream scheme closer to the 3D models, which take canopy structure into account.

By comparing Pinty's parameterisation scheme with Nilson's parameterisation scheme

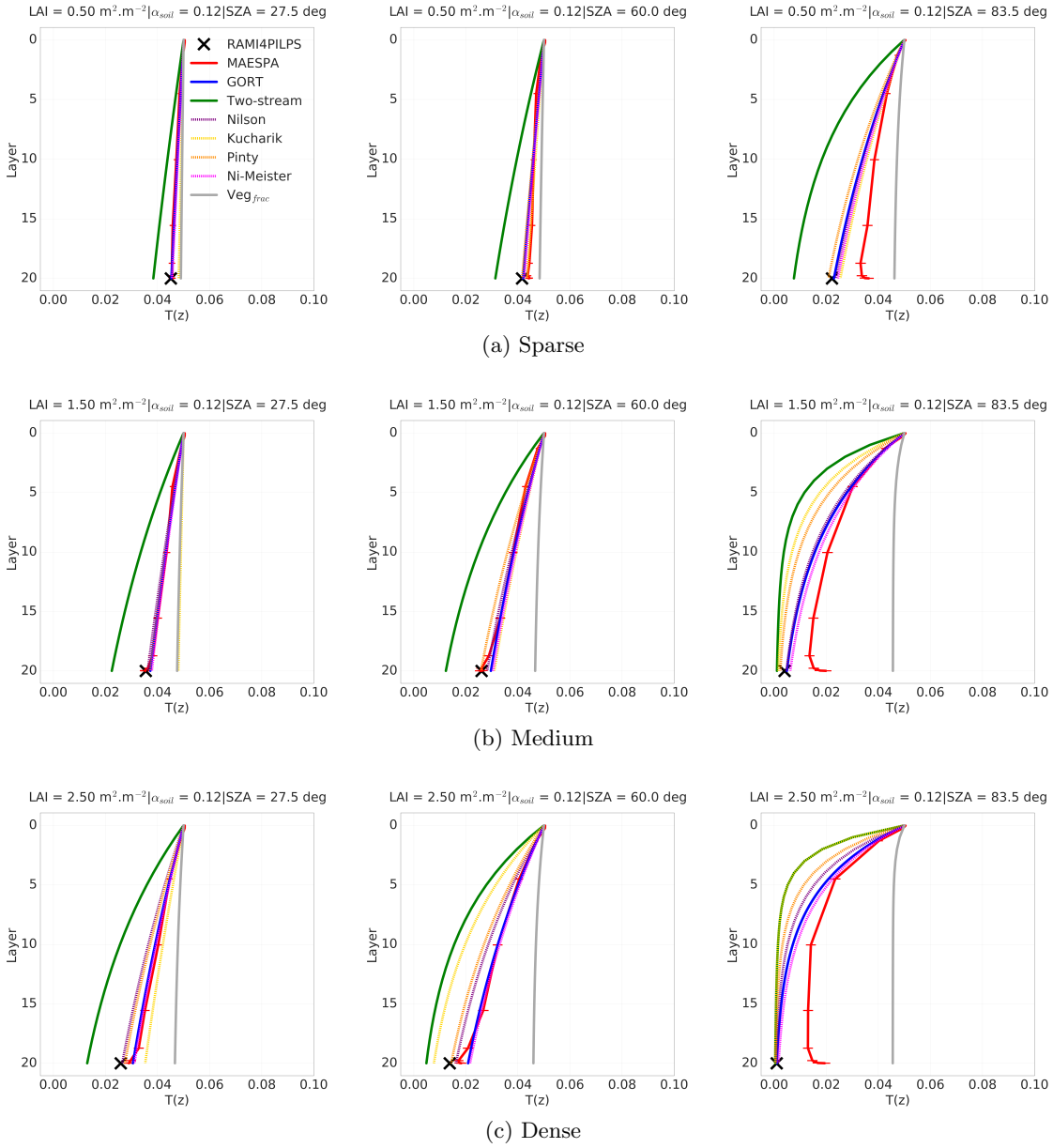

Figure 4.9: Vertical profile of PAR total transmittance (T(z)) comparing the two-stream scheme, 4 clumping indices used in the modified two-stream, Veg_{frac} parameterisation, and the 3D models, MAESPA and GORT, for the RAMI4PILPS canopy scenes. The RAMI4PILPS reference values for the bottom of the canopy are showed for comparison. $\alpha_{soil} = 0.12$. The horizontal bars in red associated with MAESPA output represent the 95% CI of the average.

it is possible to determine the impact of the b parameter (Eq. 3.14) on the vertical distribution of shortwave radiation as well. Their differences are a maximum of 10% for the medium canopy density case at 60.0°, and at half way through the canopy in 83.5°. The presence of a clumping index that varies with zenith angle allows less shortwave radiation

to go through the canopy for elevated Sun zenith angles because less clumping gives a higher optical depth. However, their differences are much smaller than the differences between the two-stream scheme and the 3D radiative transfer models.

In general, larger amounts of total incident PAR are often associated with smaller Sun zenith angles and so it is usually more important for photosynthesis to obtain good estimates of fAPAR over these smaller angles, because photosynthesis is related to the total amount of absorbed PAR (Eq. 3.21).

In this section, the values of PAR transmittance generated with the modified two-stream scheme with the minimised clumping indices, especially the structure factor (Pinty et al., 2006) agreed well with more complex 3D models over the vertical dimension, for small and intermediate solar zenith angles. For larger solar zenith angles, the parameterisation approximates the results of transmittance to the ones generated by 3D models, and decreases the discrepancies between the 1D and the 3D schemes.

4.5.2 Absorptance

Figure 4.10 shows the vertical profile of absorptance for the two-stream scheme and the parameterised two-stream scheme with clumping indices of Nilson (1971), Kucharik et al. (1999), Pinty et al. (2006), and Ni-Meister et al. (2010), as well as the Veg_{frac} parameterisation scheme (Sec. 3.3.6). The results shown refer only to the snow case of the RAMI4PILPS scenes, because the major differences in vertical fAPAR profiles between different approaches are given over high soil reflectance ($\alpha_{soil} = 0.96$) since more shortwave radiation is reflected upwards isotropically and can be absorbed by the canopy. Plots over the other two canopy reflectances roughly present the same behaviour.

The addition of a clumping index into the two-stream scheme results in a decrease in PAR absorption at the top of the canopy and an increase of PAR absorption at the bottom canopy, except over the sparse case for angles 27.5° and 60.0°. Note that the fAPAR values on the x-axis have a different range for different canopy densities, once a denser canopy presents higher values for PAR absorption.

The effect of soil albedo is mostly perceived when the value of soil albedo is high (α_{soil} = 0.96), and the zenith angle of the incident radiation is small (SZA = 27.5°), because at nadir the optical path length is shortest.

For the sparse canopy, the clumping indices reduce the total amount of fAPAR in

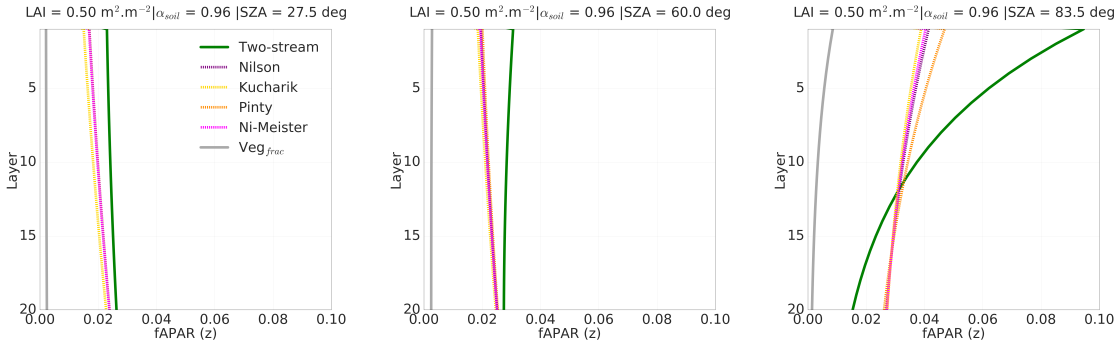

(a) Sparse

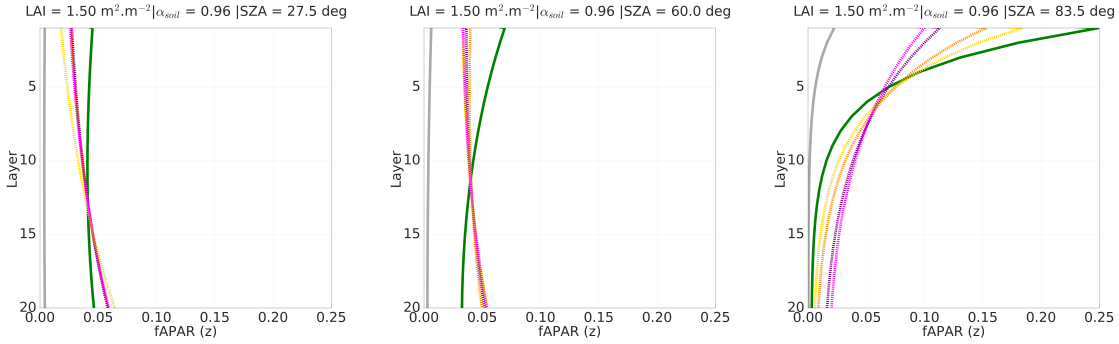

(b) Medium

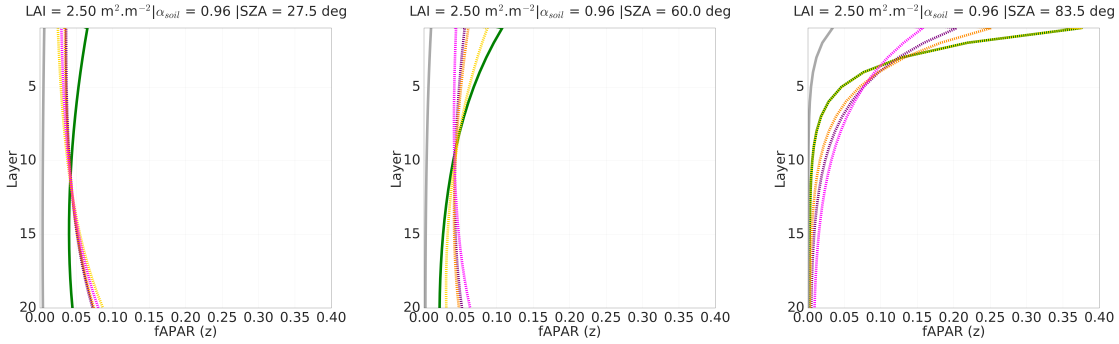

(c) Dense

Figure 4.10: Comparison of absorptance in the two-stream scheme; 4 clumping indices used in the modified two-stream; and Veg_{frac} parameterisation, vertical distribution of fraction of PAR absorption in the RAMI4PILPS scenes over snow ($\alpha_{soil} = 0.96$). The vertical axis is given in layers of equal increment of LAI according to the the two-stream scheme.

about half of the one obtained by the default two-stream scheme, and they distribute the absorption more homogeneously over the vertical canopy. Over a bright soil, the fAPAR at the bottom of the canopy is relatively larger than at the top because of scattering effects from the underneath background. This effect has also been shown by Pinty et al.

(2006) who affirms that, for low vegetation density conditions, fAPAR is rather small and so the differences between the 1D and the 3D model remains limited given a non-bright background.

For the medium and dense canopies the clumping indices have a double effect on the vertical profile of fAPAR: first, it reduces the total amount of PAR absorption at the top layers; second, it increases the PAR absorption at the bottom of the canopy, especially when associated with brighter soil backgrounds.

Over a high soil reflectance, the fAPAR at the bottom of the canopy, obtained with the parameterised two-stream scheme, is more than twice as large as the one calculated by the default two-stream scheme for the dense canopy, and about of 1.5 times larger than in the medium canopy. This effect is observed throughout all Sun zenith angles, and it gets more prominent the larger the zenith angle gets.

4.6 Summary of Findings

In order to study the effect of vegetation canopy structure on shortwave radiation partitioning and the ability of the two-stream scheme to reproduce the results of more detailed schemes, three 3D radiative transfer models were used over a number of hypothetical scenarios described in Table 3.1. Four clumping indices developed for the purpose of considering architectural effects in 1D radiative transfer models were evaluated. The results for shortwave radiation partitioning of different clumping schemes implemented in a modified version of the two-stream scheme (Sec. 3.3.1) were then explored over solar zenith and vertical profiles, and their results were compared with reference values obtained in a benchmarking experiment for radiative transfer in heterogeneous vegetation canopies, the RAMI4PILPS (Widlowski et al., 2011).

The evaluation of shortwave radiation partitioning indicated that canopy architectural features seem to have a large impact on the way shortwave radiation propagates and interacts with plants. These results are consistent with previous studies on vegetation clumping (Chen et al., 2008), which have indicated a strong impact of structure, horizontally and vertically.

The key findings of this chapter are summarised in bullet points below:

1. LAI modulated by the G-function is often used as the only way to describe the

optical depth of a vegetation canopy in current radiative transfer models, without differences between sparse and dense canopies. An evaluation developed in Section 4.2 highlighted the limitations associated with the use of a single variable to characterise canopy spatial heterogeneity. To neglect canopy spatial heterogeneity in radiative transfer models can lead to overestimations of up to 300% in PAR absorption, and underestimations up to 100% in PAR reflectance over sparse canopies for the evaluated scenes.

2. Several authors attempted to characterise canopy heterogeneity in radiative transfer schemes by including an extra variable to modulate the optical depth of the vegetation canopy, the 'clumping index' (Nilson, 1971; Kucharik et al., 1999; Pinty et al., 2006; Ni-Meister et al., 2010). These indices were implemented in a two-stream scheme, and tested against the RAMI4PILPS reference values for shortwave radiative partitioning in vegetation canopies in Section 4.4. The clumping indices of Nilson (1971) and Pinty et al. (2006) showed fewer discrepancies for absorption, reflectance, and transmittance than the Ni-Meister et al. (2010) and Kucharik et al. (1999) indices in comparison with 3D Monte Carlo ray-tracing simulations, and other more accurate 3D radiative transfer models (MAESPA and GORT). The inclusion of a zenith-varying clumping index in the modified two-stream scheme showed the best agreement with the reference values among all the clumping indices.

3. The two-stream scheme with clumping indices was tested vertically against 3D radiative transfer schemes in Section 4.5. The results obtained from the analysis indicates that considering structurally heterogeneous vegetation in the two-stream scheme has an impact on the representation of shortwave radiation distribution along the canopy height, mainly by reducing absorption at the top, and increasing absorption at the bottom layers of the canopy.

Although these conclusions are in agreement with key conclusions of former studies (Pinty et al., 2006; Loew et al., 2014), there are still a number of differences that have been found since these results were first published. Furthermore, the minimised clumping indices, especially the ones from Nilson (1971) and Pinty et al. (2006) seemed to have a vertical impact on PAR absorption, which presented a better agreement with 3D radiative transfer schemes than other evaluated indices. It is recommended to make use of minimised

values of clumping indices other than empirical or semi-empirical relationships, because the former present better performance than the latter. Of course, this is only possible when data is available for the minimisation process. Also, MAESPA may not be conserving energy, which is highlighted in the evaluations shortwave radiation partitioning over snow. These results open up a new possibility of coupling the presented parameterisation schemes with other parts of land surface models, which depend on radiative processes, such as photosynthesis.

Chapter 5:

Deriving Vegetation Architectural Parameters from Observed Data

5.1 Introduction

The main goal of this chapter is to investigate to what extent it is possible to retrieve the required parameters of two different vegetation structure parameterisations applied to the two-stream radiative transfer scheme, based on two different clumping indices, i.e., the ones based on Nilson (1971) and Pinty et al. (2006). These were previously presented and evaluated in other chapters but now directly derived from fieldwork observations via digital hemispherical photography (DHP). The experiments described in this chapter make use of fieldwork observations of gap fraction ($P_{gap}(\theta)$) in order to parameterise the two-stream radiative transfer scheme and the MAESPA 3D radiative transfer model over real study sites.

This chapter evaluates the clumping parameterisation schemes already tested in Chapter 4 and verifies whether or not the parameters are also applicable to real scenarios. Moreover, the experiments presented here demonstrate under what conditions different parameterisation schemes of vegetation canopy structure in radiative transfer schemes are applicable to real forest canopies, and which one of the two clumping indices are the most appropriate for use within different study sites.

The main research questions addressed by this Chapter are:

1. to what extent is it possible to retrieve the required parameters of a Sun zenith

varying clumping index from digital hemispherical photographs?

2. is it possible to accurately derive the clumping indices from structural data sets, e.g., derived from LiDAR data or dendrometry?

3. Moreover, how accurately is it possible to predict GPP by making use of a LSM parameterised with observed parameters?

In Section 5.2 a brief explanation of how the direct transmittance was derived from DHPs is given. P_{gap} databases were available for few study sites, e.g., for the BOREAS sites, but for all the other sites the data were in their raw form as DHPs. The DHPs were pre-processed via the Otsu's threshold method (Otsu, 1979) using the CIMES-FISHEYE software (Walter, 2012). Section 5.2 establishes all the estimated values of P_{gap} together for all study sites describing the period when the data were collected. Also a description of how the LAI values were obtained is presented because LAI and P_{gap} are both used in the Beer's law equation to obtain the clumping indices; it is important to highlight that LAI was not obtained directly from P_{gap} in order to avoid circularity. The zenith profiles of P_{gap} were then estimated through DHPs, while the LAI values were estimated with different methods, e.g., litterfall traps or LAI-2000 canopy analyser.

In Section 5.3 two study sites had their vegetation structure recreated virtually within the MAESPA 3D model in order to calculate direct transmittance and compare it with observations. This second part has two main purposes: the first one is to determine whether or not one type of structural measurement could be used in the absence of the other one, i.e., in the absence of DHPs, is it equivalent to have only structural data derived from other sources, for example LiDAR data? This section verifies whether P_{gap} zenith profiles derived from DHPs are comparable to 3D modelling calculations. Secondly, if the observed data agrees with the modelled radiation partitioning, especially transmittance, it indicates that absorptance calculated with the MAESPA model could represent a useful estimate for real study sites in nature. Comparing fAPAR from MAESPA with the ones generated by the two-stream scheme with the structural parameterisation can be used as a validation tool of the clumping indices obtained in the field.

In Section 5.4 the clumping indices are derived from the P_{gap} zenith profiles and statistical values. For instance, RMSE, AIC, and BIC of the fits are calculated in order to address the question of whether or not considering clumping index variations with Sun

zenith angle is important to describe the forest canopy direct transmittance. This section also evaluates which one of the two indices is the best one to describe the observed P_{gap} zenith curves.

Finally, Section 5.5 shows a comparison between flux tower and modelled GPP via three different methods calculated with the full JULES v4.6 model: i) default two-stream scheme, ii) two-stream scheme with clumping index (Nilson, 1971), and iii) two-stream scheme with structure factor (Pinty et al., 2006).

In Section 5.6.2 a brief discussion of the observed changes in modelled GPP based on the analysis of the Farquhar photosynthesis limiting regimes in JULES is presented.

5.2 Estimating direct transmittance from DHPs

The zenith profile of direct transmittance was derived from DHPs for 12 study sites in the Northern hemisphere over four PFTs, i.e., Deciduous Broadleaf Forest, Evergreen Needleleaf, Mixed Forest, and Woody Savannah, following the IGBP classification (Loveland and Belward, 1997) with more details described in Table 5.2. The locations of the 12 sites are presented in Figure 5.1 and a detailed description of the study sites is presented in Section 3.6.

Table 5.1: Study sites categorised by plant functional type (PFT)*, country, latitude and longitude, climate, and dominant tree species. P_{gap} column indicates the derivation method: DHP for digital hemispherical photographs; and 3D refers to the 3D tree based model MAESPA. Year indicates the period when DHPs were collected.

PFT	Country	Site	Latitude	Longitude	Climate	Species	$P_{gap}(\theta)$	Year	Reference
	Canada	NSA-OBS	55.880° N	98.481° W	Boreal	Black Spruce	DHP	1994	Sellers (1997)
	Canada	NSA-OJP	55.928° N	98.624° W	Boreal	Jack Pine	DHP	1994	Sellers (1997)
ENF	Canada	NSA-YJP	55.896° N	98.287° W	Boreal	Jack Pine	DHP	1994	Sellers (1997)
	Canada	SSA-OBS	53.987° N	105.118° W	Boreal	Black Spruce	DHP	1994	Sellers (1997)
	Canada	SSA-OJP	53.916° N	104.692° W	Boreal	Jack Pine	DHP	1994	Sellers (1997)
	Canada	SSA-YJP	53.876° N	104.645° W	Boreal	Jack Pine	DHP	1994	Sellers (1997)
	USA	US-Me2	44.452° N	121.557° W	Temperate Mediterranean	Ponderosa Pine	DHP	2006	De Kauwe et al. (2011); Thomas et al. (2009)
	USA	US-Me4	53.876° N	104.645° W	Temperate Mediterranean	Ponderosa Pine	DHP	2006	De Kauwe et al. (2011); Law et al. (2001b)
	USA	US-Ha2	42.539° N	72.178° W	Continental	Hemlock	DHP	2015	Hadley and Schedlbauer (2002)
MF	UK	Alice Holt	51.117° N	0.850° W	Temperate oceanic	Oak Woodland	DHP	2015	Wilkinson et al. (2012)
DBF	Canada	SSA-OA	53.876° N	104.645° W	Boreal	Aspen	DHP 3D modelling	1994	Chen et al. (1997)
WSA	USA	US-Ton	38.432° N	120.966° W	Mediterranean	Blue Oak	DHP 3D modelling	2008	Ryu et al. (2012)

* **ENF:** Evergreen Needleleaf **MF:** Mixed Forest **DBF:** Deciduous Broadleaf Forest **WSA:** Woody-Savannah.

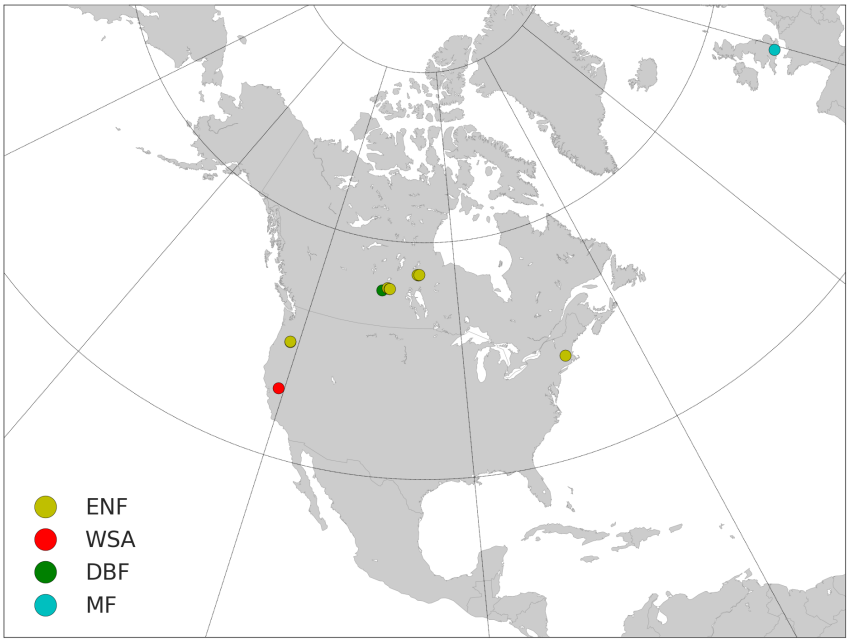

Figure 5.1: The coloured circles represent study sites spread over the Northern Hemisphere, mainly over North America. Different colours represent different PFTs: **ENF:** Evergreen Needle-leaf. **WSA:** Woody Savannah. **DBF:** Deciduous Broadleaf Forest. **MF:** Mixed Forest.

For the BOREAS sites P_{gap} data were already available in the dataset '**BOREAS TE-23 Canopy Architecture and Spectral Data from Hemispherical photos**' (Rich et al., 1999), and more information about experimental design and software used for DHPs post-processing can be found in Chen et al. (1997). For all the other study sites the DHPs were in the format of raw images and in order to keep consistency during the P_{gap} derivation process for all the other sites, the direct transmittance was obtained in the closest way possible to the one used for the BOREAS sites.

The DHPs were automatically thresholded via the Otsu's method (Otsu, 1979) with a *Python* script, where the images were reduced from grey level to a binary image. This method assumes that the image contains two classes of pixels following a bi-modal histogram, i.e., foreground pixels representing the vegetation and background pixels representing the sky. Then it calculates the optimum threshold separating the two classes. More details on DHPs pre-processing can be found in Section 3.6.2.

The binary form of the images were then divided into 5° zenith intervals, from 0° to 90° giving a total of 18 equally divided intervals. The azimuth angles were also divided into 18 parts of 20° each. The last 3 points of the zenith profile were excluded from the

statistical analysis performed later on in this chapter, hence a total of 15 points were used to represent the zenith profile of direct transmittance from 0 to 75 degrees. The P_{gap} zenith curve from each DHP is represented in Figure 5.2 by a coloured line and the average is represented by the central thick black line with the 95% confidence interval of the mean represented by vertical bars.

Note that overall sites with higher LAI present lower values of direct transmittance because LAI is one of the major factors controlling the shape of the P_{gap} zenith curves but not the only one, therefore study sites with same LAI can present distinct direct transmittance zenith profiles (see Sec. 4.2). A good example is presented in Figure 5.2d and Figure 5.2j corresponding to an old jack pine site in Canada and a ponderosa pine site in Oregon, USA, respectively. Both study sites are classified as evergreen needleleaf vegetation with the same average LAI (2.25 $m^2.m^{-2}$), although their P_{gap} average curves are substantially different.

Direct transmittance is related to a number of different factors, such as leaf orientation and vegetation structure, which are not completely represented by LAI alone, as discussed in Section 4.2. Mature sites usually present higher LAI and smaller P_{gap} curves than younger sites, as it can be noticed when comparing NSA-OJP (old jack pine) and NSA-YJP (young jack pine) (Fig. 5.2d and Fig. 5.2e), SSA-OBS (old black spruce) and SSA-YBS (young black spruce) (Fig. 5.2g and Fig. 5.2h), and US-Me4 (mature ponderosa pine) and US-Me2 (intermediate ponderosa pine) (Fig. 5.2k and Fig. 5.2j). As a forest grows old, the trees not only become taller but also display more branches in multiple directions, which creates a more structurally complex vegetation. As a result the direct transmittance decreases as LAI increases with time (Law et al., 2001a).

P_{gap} usually decreases with zenith angle among all sites except in Alice Holt, UK, where direct transmittance reaches an optimum value in the middle of the zenith profile. This behaviour indicates that this forest presents more vegetation optical depth overhead than at intermediate angles, which can be partly explained by the presence of clearings (Benham et al., 2012).

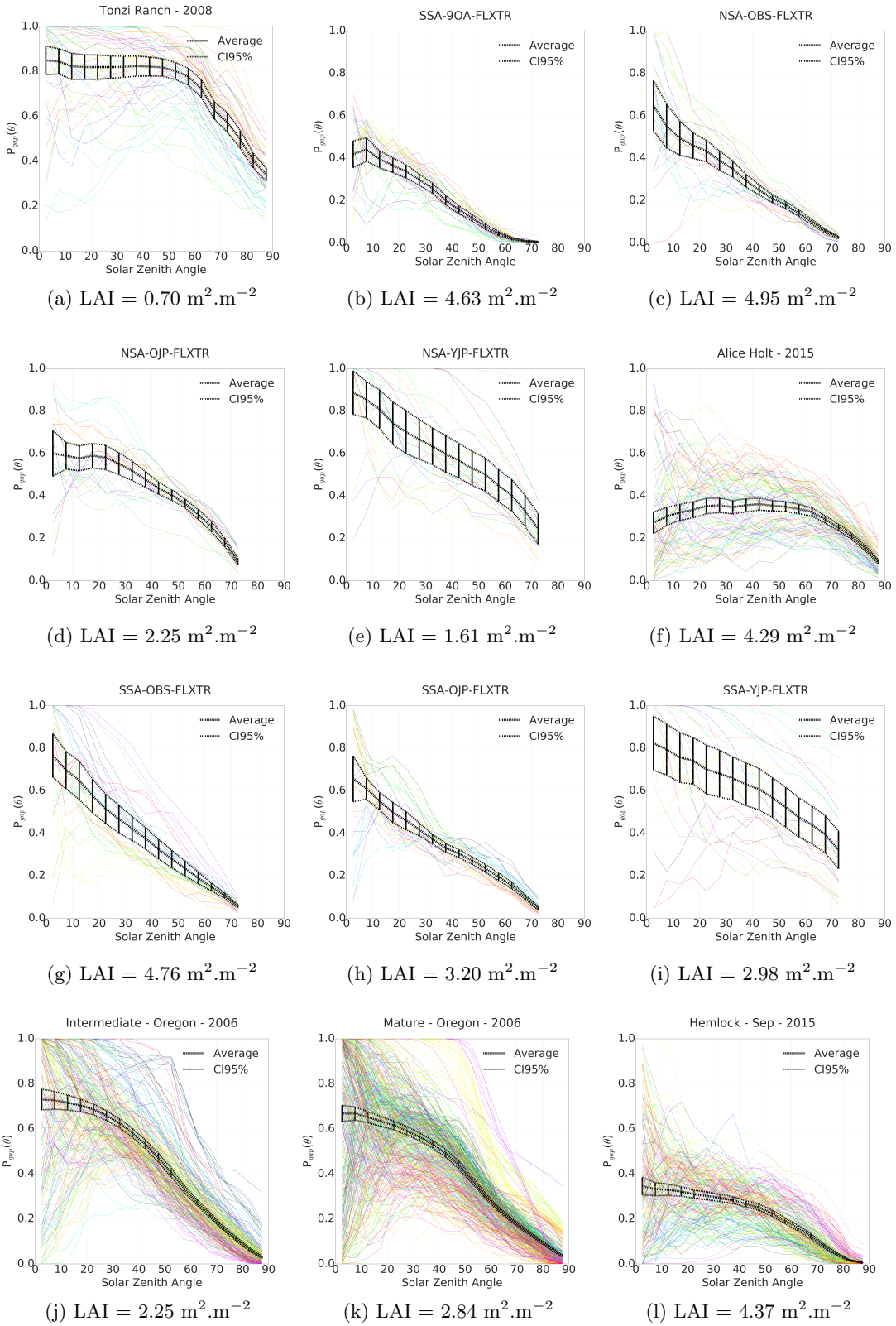

(a) LAI = 0.70 $m^2.m^{-2}$ (b) LAI = 4.63 $m^2.m^{-2}$ (c) LAI = 4.95 $m^2.m^{-2}$

(d) LAI = 2.25 $m^2.m^{-2}$ (e) LAI = 1.61 $m^2.m^{-2}$ (f) LAI = 4.29 $m^2.m^{-2}$

(g) LAI = 4.76 $m^2.m^{-2}$ (h) LAI = 3.20 $m^2.m^{-2}$ (i) LAI = 2.98 $m^2.m^{-2}$

(j) LAI = 2.25 $m^2.m^{-2}$ (k) LAI = 2.84 $m^2.m^{-2}$ (l) LAI = 4.37 $m^2.m^{-2}$

Figure 5.2: $P_{gap}(\theta)$ derived from DHPs for 12 study sites described in Table 5.2. Coloured lines represent individual DHPs and the black line represents the mean. Vertical bars represent the 95% CI of the mean.

5.3 Comparison between modelled and observed direct transmittance

For two substantially different study sites, i.e, an old Aspen forest site in Canada (SSA-OA) and a blue oak savannah in California (US-Ton), the measured P_{gap} from DHPs is compared with the one calculated by the MAESPA model and the two-stream scheme. These two specific sites were selected because they have detailed structural data available, and present different canopy structures and LAI values.

For the old aspen site, the BOREAS TE-23 team (Rich et al., 1999) collected data in order to characterise and interpret information on canopy architecture at the BOREAS tower flux sites. The 300 m^2 mapped plot was used to characterise the forested surrounding of the flux tower. Detailed measurement of the mapped plot includes: i) stand characteristics (tree location, density, and basal area); ii) DBH of all trees in the designed area; and iii) detailed geometric measures of a subset of trees (height and crown dimensions) (Rich and Fournier, 1999). For any missing values the average of the available values was considered. The plot is shown in Figure 5.3a.

It can be seen that the structural representation of the old aspen forest canopy (trees are represented by green circles) is a partial representation of the canopy, 70 m away from the flux tower (represented by a red triangle). The DHPs were acquired along a straight line from the flux tower crossing the mapped plot area, represented by red circles. The BOREAS team assumed that the structural data collected in the mapped plot was representative of the flux tower footprint (Chen et al., 1997).

For the savannah site in California, USA, the structural data were directly derived by Chen et al. (2006) from LiDAR data acquired in 2006 in a 1000 m $\times$ 1000 m plot around the flux tower. As well as DHPs were acquired in August, 2008, in a 300 m $\times$ 300 m plot around the flux tower, subdivided in a 30 m $\times$ 30 m grid. The camera used to take the photographs was in manual mode, with fish-eye lens, fixed with centrally weighted exposure, and high quality JPEG format pictures were acquired (Ryu et al., 2010). Figure 5.3b shows a representation of the mapped plot, where green circles represent the tree trunk centres and red circles represent the places where the DHPs were acquired. The flux tower is represented by the red triangle in the centre of the plot.

Figure 5.3c and Figure 5.3d show a structural representation in 3D of both areas

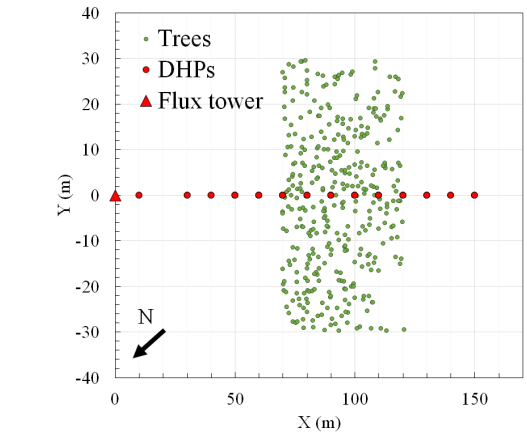

(a) SSA-OA

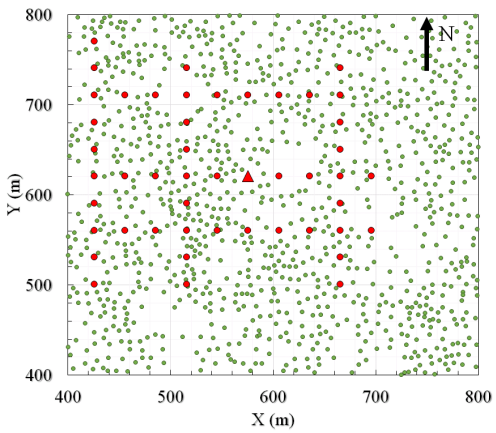

(b) US-Ton

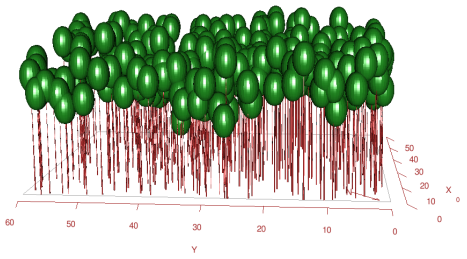

(c) SSA-OA

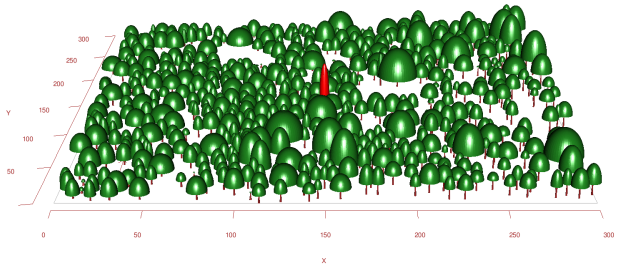

(d) US-Ton

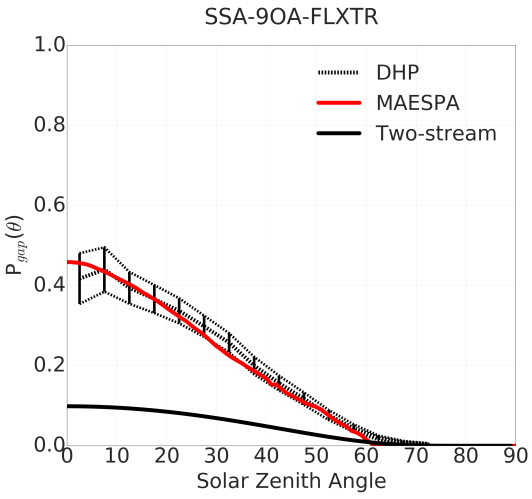

(e) SSA-OA

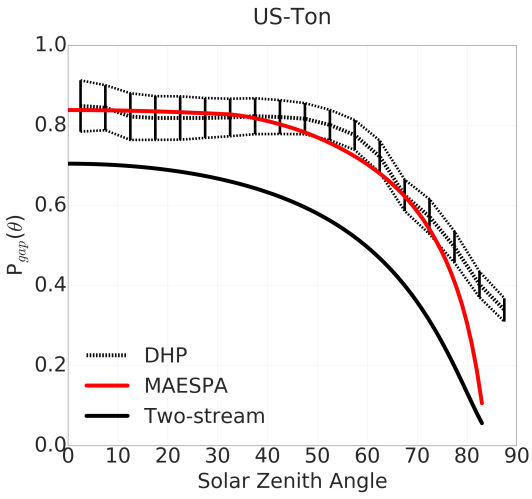

(f) US-Ton

Figure 5.3: Map plot of **(a.)** an old aspen site in Canada (SSA-OA: 53.88 N,104.65 W), and **(b.)** blue oak grassland in California, USA (US-Ton: 38.43 N, 120.97 W); 3D representation of forest canopies in MAESPA created with the *R* package *Maeswrap* for **(c.)** SSA-OA and **(d.)** US-Ton; and direct transmittance zenith profile calculated with the MAESPA model, the two-stream scheme, and measured through DHPs for **(e.)** SSA-OA and **(f.)** US-Ton. The vertical bars represent the 95% CI of the mean.

recreated with the *R* package *Maeswrap* (Duursma, 2015), where the red element in the centre of Figure 5.3d represents the flux tower. The shape of tree crowns in the old aspen site is an ellipsoid, while in the blue oak savannah the shape of the crowns was set to half-ellipsoids in order to represent the tree shape as close as possible to reality. The impact of considering an ellipsoid or a half-ellipsoid for the evaluated cases with MAESPA on direct transmittance is negligible. The structural data is available over a much larger area over the savannah site, although only the central 300 m × 300 m area was used in this study to ensure that the DHPs and the LiDAR data were representing vegetation canopy structure over the same area. The footprint of the flux tower in Tonzi Ranch is mostly represented by the surrounding 300 m × 300 m area under typical micrometeorological conditions (Baldocchi, 2006).

Given two different study sites the questions to be answered in this sections are:

1. how does the P_{gap} calculated with MAESPA compare with the one derived from DHPs?

2. how does the direct transmittance calculated with the two-stream scheme compare with other methods?

In order to obtain the direct transmittance from MAESPA the same type of black canopy approximation already described in Section 4.3.2 was used here, where the leaf reflectance and transmittance values were set to zero, as well as soil albedo. After that, P_{gap} is calculated as described in Eq. 4.3. In Figure 5.3e and Figure 5.3f the red lines represent the P_{gap} from MAESPA and the dashed black lines represent the P_{gap} derived from DHPs.

There is a good agreement between direct transmittance derived from DHPs and the one modelled by MAESPA for both sites. For the old aspen site especially, until about 20 degrees the modelled P_{gap} is very close to the average, while for the other part of the curve the calculated P_{gap} underestimates the average but is within the lower limit of the 95% confidence interval, which means the model roughly underestimates the observed P_{gap} but still within the 95% confidence interval. However, most attention should be given to how the shape of both curves agrees, and how P_{gap} goes to zero for 60 degrees zenith angle. This old aspen forest has a high LAI value (LAI = 4.63 $m^2.m^{-2}$) and it is a quite dense area with 356 trees in a 50 m × 60 m area plot. The results from the two-stream scheme,

however, underestimate both curves by up to 0.30 in P_{gap} at zero degrees zenith angle, and it is not able to reproduce the shape of the other curves either. This implies it could lead to discrepancies in fAPAR and albedo estimates as well.

The blue oak savannah is a much sparser canopy with 604 trees in a 300 × 300 m^2 area with lower LAI (LAI = 0.70 $m^2.m^{-2}$) but the agreement between the calculated P_{gap} and the one derived from observations is still close. For this study site the two-stream scheme also underestimates the direct transmittance but not as much as for the old aspen site, because transmittance is exponentially proportional to LAI, so it is expected that the uncertainty also would grow with LAI. The underestimation of P_{gap} via two-stream scheme is in the order of 0.10 for zero degrees Sun zenith angle. The shapes of direct transmittance with zenith angle are similar between MAESPA and DHPs until about 80 degrees but after that MAESPA underestimates the values obtained through DHPs. Figure 5.2a shows all P_{gap} curves for Tonzi Ranch and it is possible to note that at high zenith angles the spread between the P_{gap} curves is quite significant in comparison with Figure 5.2b, and even though the MAESPA model disagrees with the observation, only values up to 75 degrees are considered in the statistical analysis in this chapter. In other words, P_{gap} curves present a well behaved convergence towards high zenith angles for the old aspen site, while that is not observed for the savannah site. It is also important to highlight that the canopy representation in MAESPA is finite and limited to the size of the plotted area, while in nature the forest canopy extends over a much larger area.

Based on these evaluations over two sites with distinct values of LAI it possible to provide an accurate value of direct transmittance from 3D radiative transfer modelling with the MAESPA model parameterised with different types of structural data, i.e., manual dendrometry measurements and/or LiDAR data. This result suggests that in the absence of DHPs or any other way to measure gap probability, MAESPA could be parameterised with structural data in order to estimate the direct transmittance. However, as discussed in Section 4.4.1, MAESPA presents large underestimation of PAR absorptance over canopies with snow on the soil, as well as MAESPA is not able to accurately calculate PAR reflectance for all the evaluated cases as discussed in Section 4.4.2. Therefore, MAESPA should be used carefully, avoiding scenarios with large values of soil and/or leaf reflectance.

5.4 Deriving clumping indices from observed data

The main goal of this section is to derive the relevant parameters for both parameterisation schemes, i.e., the clumping index (Ω) from Nilson (1971) and both parameters (a and b) for the structure factor ($\zeta(\mu)$) from Pinty et al. (2006), by inverting the adapted Beer's law equation against direct transmittance obtained from DHPs for 12 study sites in order to answer the question of whether or not the inclusion of a zenith-dependent structural parameterisation presents a better agreement between the modelled and the observed data of gap probability derived from DHPs.

An example of fitting is shown in Figure 5.4 for the same two sites evaluated in Section 5.3 but the same evaluation was performed for all the others sites and the results are summarised in Table 5.2. The LAI for both sites was estimated from different sources that not DHPs in order to avoid circularity, as previously mentioned. For the old aspen site the LAI was obtained through LAI-2000, while for the blue oak savannah site the LAI was obtained from multiple sources described in Ryu et al. (2010).

The parameters were isolated through two different methodologies:

1. to obtain the clumping index from Nilson (1971) Eq. 3.10 was inverted as:

$$-\ln(P_{gap}) \cdot G(\mu)^{-1} \cdot LAI^{-1} = \Omega \cdot \frac{1}{\mu} \tag{5.1}$$

   A linear fit with one free parameter, i.e., with the line forced to cross zero against 15 data points of direct transmittance obtained from DHPs. Aho et al. (2014) found that for ecological publications from 1993 to 2013, the two most popular measures of models parsimony were the Akaike information criterion (AIC; Akaike (1973)) and the Bayesian information criterion (BIC; Schwarz (1978)). The AIC and BIC are statistical variables that represent how accurately a model fits the data, and the lower their values are, the better the evaluated model. The correlation coefficient (r), RMSE, AIC, and BIC were calculated for the fit and are presented in Figure 5.4a for two sites.

2. to obtain the structure factor parameters from Pinty et al. (2006) Eq. 2.5 with $\Omega(\theta)$ given by Eq. 3.14 was inverted as:

$$-\ln(P_{gap}) \cdot \mu \cdot G(\mu)^{-1} \cdot LAI^{-1} = a + b \cdot (1 - \mu) \tag{5.2}$$

A linear fit with two free parameters was then adjusted against the same 15 data points of direct transmittance obtained through DHPs. The correlation coefficient, RMSE, AIC, and BIC were also calculate for the second fit.

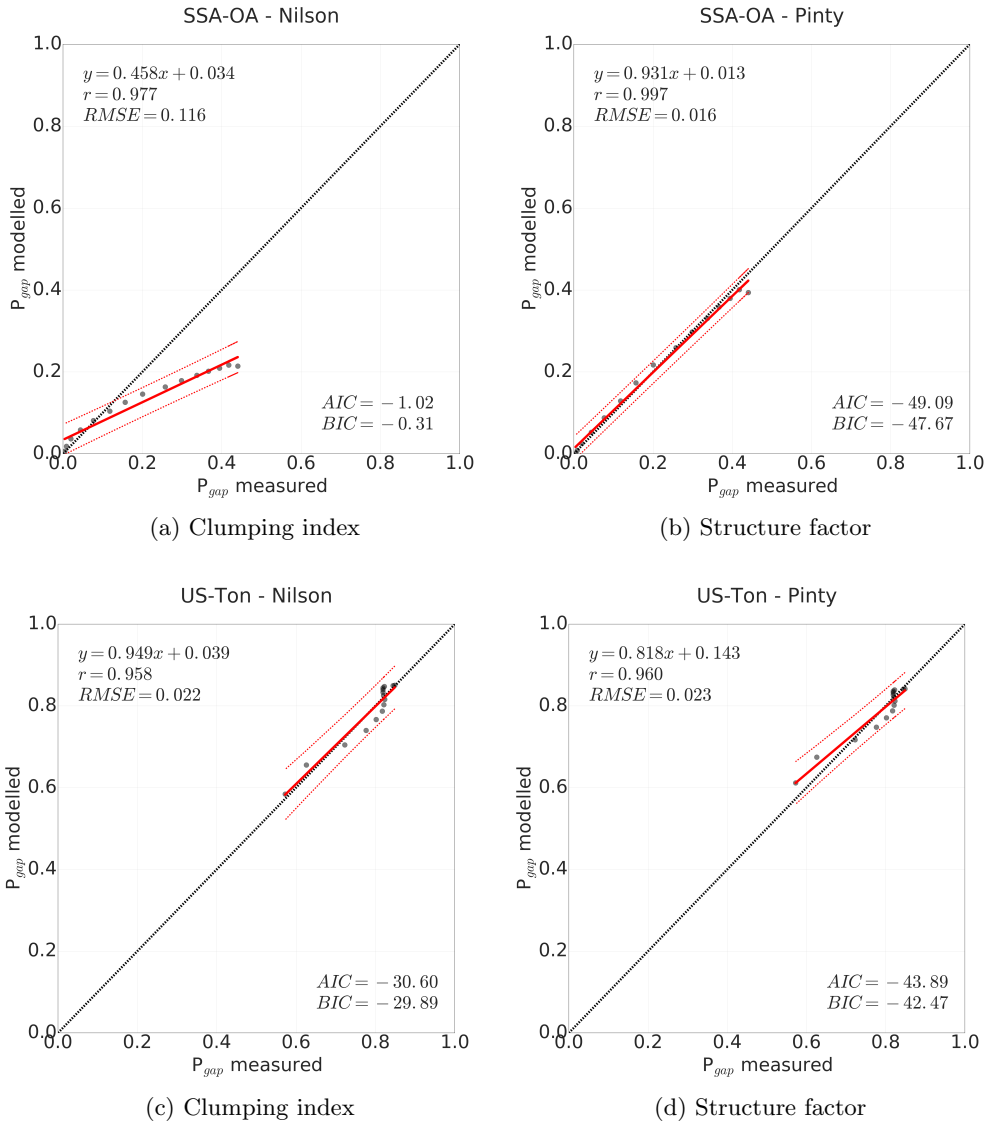

(a) Clumping index

(b) Structure factor

(c) Clumping index

(d) Structure factor

Figure 5.4: Old aspen site in Canada (SSA-OA: 53.88 N,104.65 W) with LAI = 4.63 $m^2.m^{-2}$ for **(a.)** clumping index (Ω) from Nilson (1971), and **(b.)** structure factor ($\zeta(\mu)$) from Pinty et al. (2006); and blue oak savannah in California, USA (US-Ton: 38.43 N, 120.97 W) with LAI = 0.70 $m^2.m^{-2}$ for **(c.)** clumping index (Ω), and **(d.)** structure factor ($\zeta(\mu)$).

The results for all sites are summarised in Table 5.2. All values presented in Table 5.2 are statistically significant with *p-value* smaller than 0.05, except for the b parameter of the structure factor for the blue oak savannah in California (US-Ton) as indicated. The RMSE

associated with the fit of the clumping index is always larger than the RMSE associated with the fit of the structure factor (Fig. 5.5a), which indicates that varying clumping with Sun zenith angle gives a better description of direct transmittance throughout the day than having a fixed single value of clumping. However, a possible question arising from the comparison between these two parameterisation schemes is related to the number of free parameters, and it can be thought that a parameterisation scheme with two free coefficients will always fit the observed data better than a parameterisation scheme with only one, referred to as overfitting in statistics and machine learning. In order to avoid overfitting, it is necessary to use additional statistical tools that penalise overly complex models.

Both parameters AIC and BIC obtained for the structure factor fit with Equation 5.2 are smaller than the ones obtained for the clumping index for all evaluated cases (Fig. 5.5b), meaning that the structure factor accounts for architectural heterogeneity on the zenith variation of direct transmittance more accurately than the associated clumping index.

Table 5.2: Summary of statistical evaluations. Values between parentheses indicate the lower and upper 95% confidence interval, respectively.

Study site	LAI	Index	Value (95% CI)	AIC	BIC	r	RMSE
NSA-OBS	4.95 $m^2.m^{-2}$	Ω	0.408 (0.372,0.444)	-23.01	-22.30	0.945	0.105
		$\zeta(\mu)$	a =0.280(0.242,0.318); b =0.310(0.199,0.421)	-48.76	-47.34	0.965	0.048
NSA-OJP	2.25 $m^2.m^{-2}$	Ω	0.563(0.529,0.597)	-24.34	-23.63	0.997	0.045
		$\zeta(\mu)$	a =0.456(0.441,0.471); b =0.235(0.191,0.279)	-76.73	-75.32	0.998	0.010
NSA-YJP	1.61 $m^2.m^{-2}$	Ω	0.491(0.440,0.543)	-12.27	-11.56	0.938	0.087
		$\zeta(\mu)$	a =0.321(0.243,0.398); b =0.427(0.203,0.651)	-27.67	-26.25	0.952	0.054
SSA-OBS	4.76 $m^2.m^{-2}$	Ω	0.336(0.300,0.372)	-23.03	-22.33	0.927	0.128
		$\zeta(\mu)$	a =0.211(0.166,0.256); b =0.312(0.181,0.443)	-43.74	-42.32	0.955	0.063
SSA-OJP	3.20 $m^2.m^{-2}$	Ω	0.531(0.490,0.571)	-19.64	-18.64	0.943	0.088
		$\zeta(\mu)$	a =0.395(0.339,0.452); b =0.331(0.167,0.495)	-37.07	-35.65	0.958	0.050
SSA-YJP	2.98 $m^2.m^{-2}$	Ω	0.236(0.220,0.252)	-47.16	-46.45	0.958	0.048
		$\zeta(\mu)$	a =0.194(0.166,0.221); b =0.116(0.037,0.196)	-58.86	-57.44	0.966	0.037
US-Me2	2.25 $m^2.m^{-2}$	Ω	0.460(0.413,0.507)	-14.89	-14.19	0.984	0.086
		$\zeta(\mu)$	a =0.292(0.264,0.319); b = 0.400(0.320,0.479)	-58.69	-57.27	0.994	0.020
US-Me4	2.84 $m^2.m^{-2}$	Ω	0.395(0.366,0.423)	-29.90	-29.19	0.986	0.059
		$\zeta(\mu)$	a=0.300(0.277,0.323); b = 0.233(0.167,0.299)	-64.66	-63.24	0.994	0.019
US-Ha2	4.37 $m^2.m^{-2}$	Ω	0.404(0.373,0.434)	-28.24	-27.53	0.996	0.053
		$\zeta(\mu)$	a =0.504(0.498,0.509); b =-0.219(-0.236,-0.203)	-106.55	-105.13	0.998	0.005
Alice Holt	4.29 $m^2.m^{-2}$	Ω	0.293(0.230,0.356)	-6.08	-5.37	0.341	0.141
		$\zeta(\mu)$	a =0.519(0.488,0.549); b =-0.517(-0.604,-0.429)	-55.91	-54.49	0.500	0.032
SSA-OA	4.63 $m^2.m^{-2}$	Ω	0.660(0.585,0.734)	-1.07	-0.31	0.977	0.116
		$\zeta(\mu)$	a =0.394(0.356,0.432); b =0.627(0.517,0.736)	-49.09	-47.67	0.997	0.016
US-Ton	0.70 $m^2.m^{-2}$	Ω	0.462(0.434,0.490)	-30.60	-29.89	0.958	0.022
		$\zeta(\mu)$	a =0.492(0.447,0.537); b* =-0.097(-0.230,0.031)	-43.89	-42.47	0.960	0.023

*$p\text{-}value = 0.123$. All other $p\text{-}values < 0.05$.

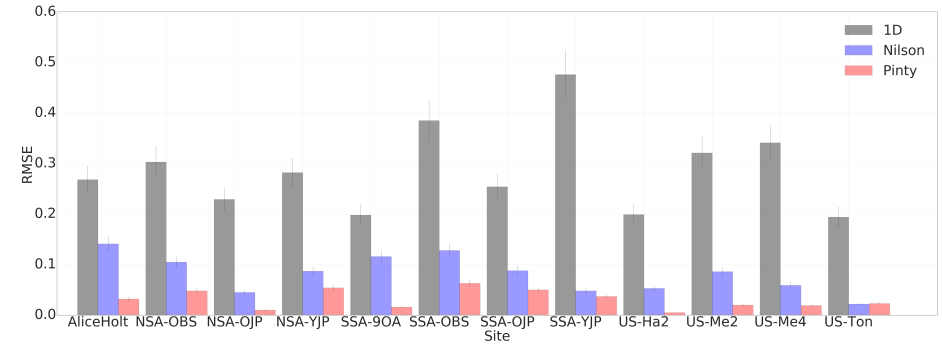

(a) RMSE

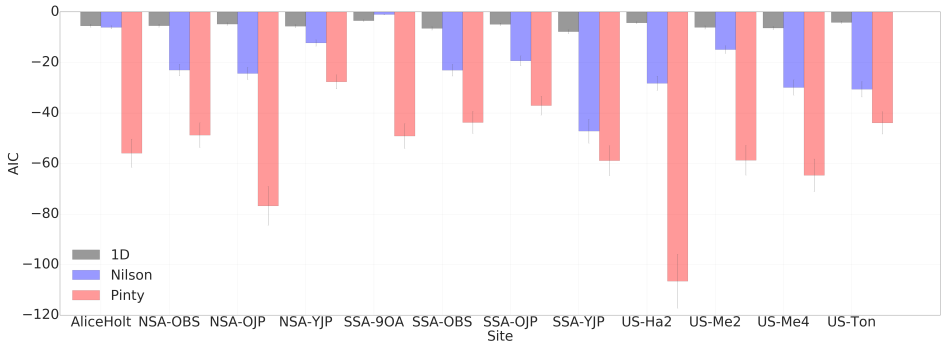

(b) AIC

Figure 5.5: Comparison of **(a.)** RMSE and **(b.)** AIC between Beer's law (1D), clumping index (Nilson), and structure factor (Pinty) for all 12 study sites.

5.5 The impact of structural parameterisations on GPP at site level

For the same two sites evaluated in Section 5.3, the two-stream scheme in JULES v4.6 and its modified versions with clumping indices were driven with measured meteorological and spectral data. For the old aspen site, spectral data was taken from the '**TE-08 spectral leaf**' database (Spencer and Rock, 1999), while soil albedo was taken from Betts and Ball (1997); and the spectral data for the blue oak savannah is described in Kobayashi et al. (2012).

The model was run for both sites in two distinct periods: i) for the old aspen site the model was run for a period of 13 days, from 11^{th} to 24^{th} July, 1996. This period was selected based on meteorological and GPP data availability. The DHPs were taken during Summer 1994, while the models were evaluated during Summer 1996, but, because

canopy structure does not change substantially in two years, unless some extraordinary event happens (e.g., fire, extreme winds, land use change), it was assumed that the old aspen canopy structure remained unchanged between Summer 1994 and 1996. Also, the relatively short period of analysis was preferred in order to keep consistency within Sun zenith angular variability and meteorological drivers; ii) for the blue oak savannah the model runs were performed from 1^{st} to 14^{th} August, 2008, and the DHPs were acquired on 6^{th} and 7^{th} August, 2008.

The meteorological and flux data were downloaded from the AMERIFLUX webpage (`http://ameriflux.lbl.gov`), and the variables used to drive the model were: shortwave incident radiation, longwave incident radiation, liquid and frozen precipitation, surface temperature at 2 m, wind speed at 10 m, surface pressure, specific moisture, and incident diffuse shortwave radiation. The canopy radiation transfer was calculated accordingly to the multilayer two-stream scheme with the addition of sunfleck penetration following Dai et al. (2004) and implemented by Mercado et al. (2007) (can_rad_mod = 5). For the savannah site the diffuse radiation was directly obtained from the Vaira ranch, which is about 2 km away from the flux tower in Tonzi ranch. For the old aspen site, the diffuse radiation was estimated through an empirical formula presented in Erbs et al. (1982), modified and validated by Black et al. (1991). This formula was derived based on data obtained in the same latitudinal band near Vancouver, Canada, and therefore it is considered to be applicable to the old aspen study site. The hydraulic soil characteristics for both sites were also prescribed in the models based on observations. The LAI was prescribed as the same one used for obtaining the structural parameters in Section 5.4.

The full JULES v4.6 was run for the same amount of time (13 days) for both study sites with three different experimental set ups: i) the default two-stream scheme with sunfleck penetration (**JULES**), ii) the parametrised version of two-stream scheme with clumping index (Ω), and iii) with the structure factor ($\zeta(\mu)$). The resulting fAPAR curves are shown in Figure 5.6a and Figure 5.6b and GPP curves are presented in Figure 5.6c and Figure 5.6d. The fAPAR curves are not smooth because of the presence of diffuse radiation in the calculations.

For the old aspen site, the differences in fAPAR are limited to 0.15, especially when associated with lower Sun zenith angles, i.e., for the beginning and end of the solar day. Both fAPAR curves calculated with the parameterised two-stream present a lower fAPAR

than the default version of the two-stream scheme, which is expected once the total LAI is being scaled by a parameter lower than one. It is also important to note that the fAPAR obtained through the two-stream scheme with the structure factor parameterisation is the lowest at 12 noon local time. The middle of the day is associated with small values of Sun zenith angle, and the path length through the canopy is shorter for small Sun zenith angles. Towards the sunrise and sunset times of the day the structure factor is larger because the Sun zenith angle is higher, and the b parameter is positive in this site, i.e., b = 0.627(0.517,0.736). In MAESPA calculations, 5 random trees at the centre of the plot were directly irradiated and all the other trees were used for shadowing. For small Sun zenith angles the fAPAR from two-stream with structure factor agrees with the MAESPA model but for high Sun zenith angles MAESPA presents numerical instability and shows unrealistic values of fAPAR ($>$ 1.0).

For Tonzi ranch, the difference between the default two-stream and the parameterised versions is significant (up to 0.20) and that is because LAI is relatively small (LAI = 0.70 $m^2.m^{-2}$). Impacts on fAPAR calculations via the two-stream scheme are more significant for smaller values of LAI, because the amount of absorbed radiation grows exponentially with LAI towards saturation, i.e., a constant plateau. For Tonzi ranch the structure factor presents a small negative value of b (b = -0.097(-0.230,0.031)), and the term a of the structure factor and the clumping index are within the same confidence interval, i.e., a = 0.492(0.447,0.537) and Ω = 0.462(0.434,0.490). The differences in fAPAR calculated with the two-stream parameterised with clumping index and the one parameterised with structure factor are negligible. Both curves agree with fAPAR from MAESPA for the greatest part of the day, except for the extremity of the solar day.

Although the fAPAR obtained for the old aspen site with the two-stream scheme parameterised with structure factor was the smallest one, the GPP obtained through this parameterisation scheme was the largest one. Both structural parameterisations are actually increasing the model's LUE because the bottom layers of the old aspen site are mostly light limited through the day (Fig. 5.8a), and that is because this specific site presents a relatively high value of LAI. Taking vegetation structure into account when calculating shortwave radiative transfer is in reality allowing more shortwave radiation to reach further layers at the bottom of the vegetation canopy, which makes the model photosynthesise more. This behaviour increases even more when a structure factor that

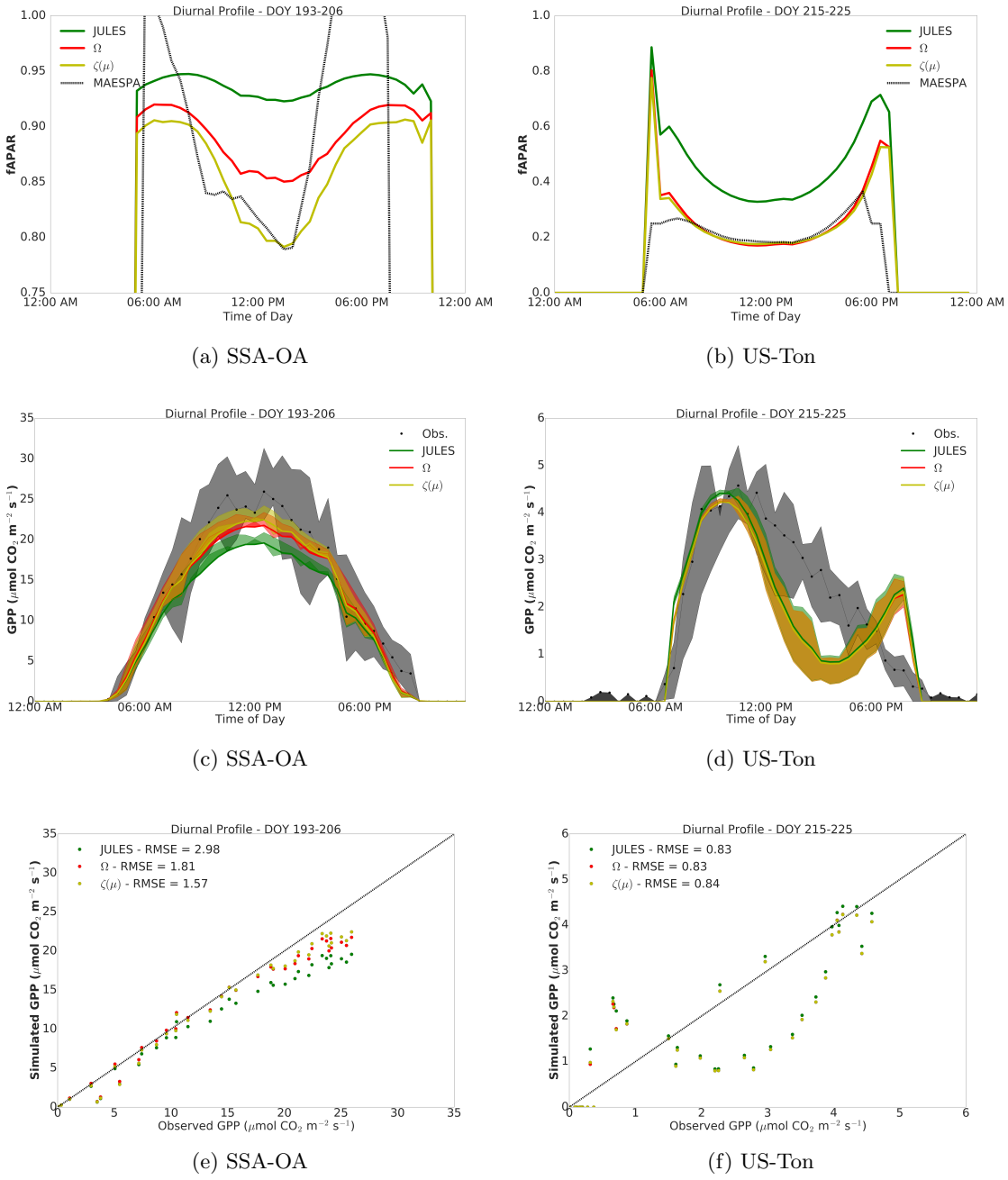

(a) SSA-OA (b) US-Ton

(c) SSA-OA (d) US-Ton

(e) SSA-OA (f) US-Ton

Figure 5.6: **(a.)** and **(b.)** fAPAR; **(c.)** and **(d.)** GPP vs. local time; and **(e.)** and **(f.)** modelled and flux tower GPP correlation for an old aspen site in Canada (SSA-OA) and a blue oak savannah site in California (US-Ton), respectively. The shaded areas represent the 25% and 75% quartiles of the average.

varies with Sun zenith angle is considered.

The comparison between flux tower and modelled GPP indicates that considering architectural canopy heterogeneity on the radiative transfer scheme in JULES improves the model prediction for the evaluated period in the old aspen site. The results are confirmed by the RMSE values going from 2.91 μmol.CO_2.m^{-2}.s^{-1} for the default two-stream scheme in JULES v4.6 to 1.75 μmol.CO_2.m^{-2}.s^{-1} when the clumping index parameterisation scheme is applied, and 1.57 μmol.CO_2.m^{-2}.s^{-1} when the structure factor parameterisation scheme is used. This is a site located at a high Northern latitude (53.629 N) with bottom layers of the vegetation mostly limited by light according to the Farquhar model.

For Tonzi ranch there are three key findings: first, in the early morning (06:00 AM to 09:00 AM local time) the agreement between the flux tower and modelled GPP within all experimental set ups is relatively high, and even though the difference in fAPAR between the schemes is up to 0.20, the difference in calculated GPP is small; second, the Tonzi ranch is a savannah site with considerable water limitation and in the middle of the day (09:00 AM to 03:00 PM) the surface temperature and vapour pressure deficit (VPD) increase substantially, which are conditions associated with a more carbon limiting regime in the Farquhar model (Fig. 5.8b) because the trees close the stomata and reduce total photosynthesis in order to avoid potential water losses. Both, flux tower and modelled GPP, decrease during this period but the calculated one decreases under a higher rate than the one derived from flux tower eddy covariance measurements, which highlights a potential misrepresentation of the stomata inertia by JULES over a savannah site; third, GPP from the model responds positively to the decay on temperature and VPD, with an increase at the very end of the solar day. However, this behaviour is not observed in the flux tower GPP, whose again presents a natural inertia on the stomata positioning.

Water limited sites are mostly under a carbon limiting regime, therefore changes in the radiative transfer scheme are not as impacting on carbon assimilation as other factors could be. This site is a good example of whether considering structural heterogeneity through a parameterisation applied to the radiative transfer scheme could be highly impacting, mainly because this woody savannah site is sparse, and changes in fAPAR due to structure are quite significant (Fig. 5.6b). In reality, however, considering architectural heterogeneity when estimating GPP is not as impacting once light is not the limiting regime of photosynthesis according to the Farquhar model for this study site (Fig. 5.8b).

The RMSE values for the different model representations are roughly the same for this savannah site (≈ 0.83 μmol.CO_2.m^{-2}.s^{-1}) and smaller than the ones presented for the old aspen site, mainly because the total flux tower GPP in the boreal site is five times larger than the GPP in Tonzi ranch, the same order of difference in LAI.

5.6 Evaluating impacts of structural parameterisations on photosynthesis limiting regimes at site level

5.6.1 Isolating the impacting factors of structural parameterisation schemes on photosynthesis

As discussed in Section 3.3.1 and Section 3.5, a number of different factors can affect photosynthesis calculated by the Farquhar model and the two-stream scheme within JULES including: i) differences in the nature of light, i.e., whether incident radiation is in a diffuse or direct form; ii) soil albedo; iii) the spectral properties of the leaves, and, to a further extent; iv) the vertical profile of leaf nitrogen concentration, which affects values of V_{cmax} and, therefore, modifies carbon and transport limiting rates (see Eq. 3.20 and Eq. 3.22).

In order to evaluate the impact of structural parameterisation schemes on JULES GPP and their interactions with other factors affecting photosynthesis, five seperate runs were performed with JULES for both study sites, i.e., an old aspen site in Canada (SSA-OA) and a blue oak savannah site in California (US-Ton), following different model setups at a time according to each one of the cases described below:

i. Case 1: all incident shortwave radiation is direct, soil reflectance is zero, leaf reflectance and transmittance are zero, and the vertical profile of leaf nitrogen concentration is constant and equal to the top leaf nitrogen concentration (n_0 in Eq. 3.24) in kg N [kg C]$^{-1}$.

ii. Case 2: all incident shortwave radiation is direct, soil reflectance is zero, leaf reflectance and transmittance are zero, and the vertical profile of leaf nitrogen concentration varies with canopy layers according to Eq. 3.24.

iii. Case 3: all incident shortwave radiation is direct, soil reflectance is zero, leaf reflectance and transmittance are set to measured values, and the vertical profile of leaf nitrogen concentration varies with canopy layers according to Eq. 3.24.

iv. Case 4: all incident shortwave radiation is direct, soil reflectance is set to a measured value, leaf reflectance and transmittance are set to measured values, and the vertical profile of leaf nitrogen concentration varies with canopy layers according to Eq. 3.24.

v. Case 5: incident shortwave radiation is given in terms of direct and diffuse proportions from measurements, soil reflectance is set to a measured value, leaf reflectance and transmittance are set to measured values, and the vertical profile of leaf nitrogen concentration varies with canopy layers according to Eq. 3.24.

For each one of the five cases, experiments with JULES were performed for the same period described in Section 5.5 without clumping and with both parameterisation schemes, i.e., the clumping index and the structure factor. The differences in GPP between the modified JULES with both parameterisation schemes and the non-clumped version were summed over the vertical canopy across 10 layers and throughout the entire Sun zenith angular interval (from 0° to 90° in intervals of 6°) for each study site. Results are shown in Figure 5.7 with associated deviations indicated by black error bars. The associated deviations for each scenario were calculated following the mean squared deviation (MSD):

$$MSD = \frac{1}{n \cdot nSZA} \sum_{i=1}^{n} \sum_{\theta=0^\circ}^{SZA} |GPP_{clump}(i,\theta) - GPP_{non-clump}(i,\theta)|^2 \tag{5.3}$$

where n is the number of canopy layers, i.e., $n = 10$, $nSZA$ is the number of Sun zenith angle intervals used in the experiment, i.e., $nSZA = 15$, and SZA is the maximum Sun zenith angle (90°). GPP_{clump} is GPP calculated by JULES with each one of the two parameterisation schemes, i.e., clumping index and structure factor, and $\text{GPP}_{non-clump}$ is GPP calculated by the original version of JULES.

Case 1 is equivalent to a complete black canopy with black soil and black leaves, as well as totally direct incident shortwave radiation and a constant vertical profile of leaf nitrogen content. This constant value of nitrogen is giving by the first canopy layer at the top of the canopy, which is dependent on PFT and the photosynthesis pathway, C3 or C4. Both structural parameterisation schemes in both sites present the maximum impact on GPP enhancement in comparison to the default version of JULES. This behaviour can be explained by the presence of more productive bottom layers with higher nitrogen content receiving more shortwave radiation due to the consideration of canopy spatial heterogeneity. The summed difference of GPP throughout the vertical canopy over the

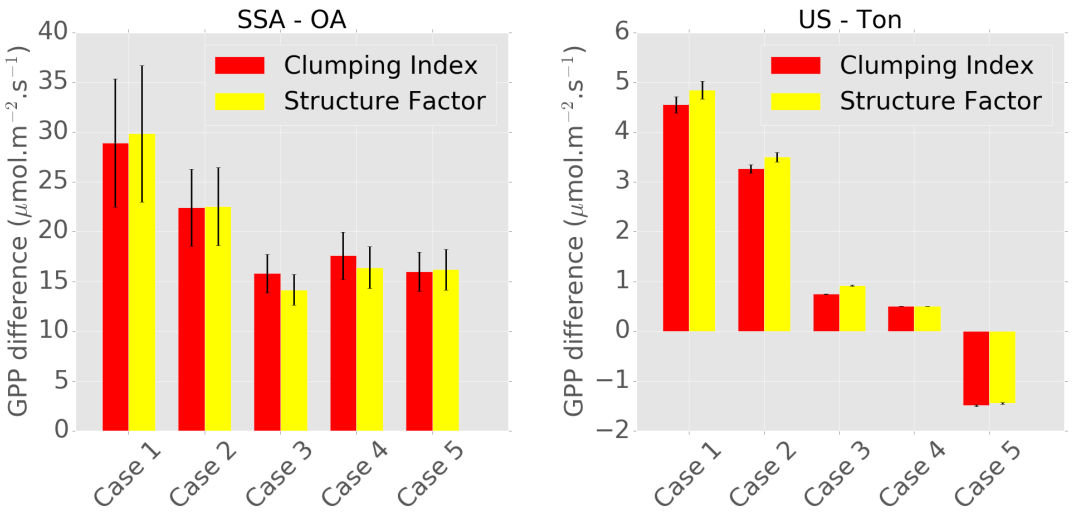

(a) SSA-OA

(b) US-Ton

Figure 5.7: Total difference in GPP between the modified JULES with both clumping indices, clumping index and structure factor, and the default non-clumped version summed across 10 vertical layers and throughout the Sun zenith angular interval for **(a.)** SSA-OA and **(b.)** US-Ton. Associated deviations are shown as black error bars and represent the mean squared deviation (MSD) obtained through Eq. 5.3.

whole Sun zenith interval in the old aspen site is roughly 5 times larger than in the savannah site because of much higher LAI values in the former site.

In case 2, leaf nitrogen concentration follows an exponential decay throughout the vertical axis towards the bottom given by Eq. 3.24. As a results, the most productive layers are located at the top of the canopy in comparison to the bottom layers. Smaller differences in GPP in case 2 compared to case 1 relates to less productive bottom canopy layers, and so, the impact of structural parameterisation schemes decreases.

In case 3, scattering processes reflect part of the shortwave radiation isotropically upwards and downwards, and because of the isotropic nature of diffuse light, there is a total reduction on the effect of canopy spatial heterogeneity on GPP enhancement. In general, heterogeneous structure has a lower impact on GPP enhancement in the present of isotropic radiation. This behaviour can be seen in both sites represented in Figure 5.7.

In case 4, with the addition of a reflective soil underneath the vegetation canopy, the impacts of heterogenous structure on JULES GPP behave differently in each study site. For the old aspen site in Canada, the difference in GPP increases when observed values of soil reflectance are used in JULES because part of the incident shortwave radiation in the

soil is reflected upwards and has the possibility of re-interact with the vegetation canopy equally in all directions. The soil behaves as a Lambertian surface that isotropically scatters shortwave radiation. In this case, canopy structure interacts with the shortwave radiation going upwards from the bottom of the canopy, and in the dense old aspen site, the difference in GPP enhancement is larger when soil reflectance is considered. This behaviour, however, is not observed in the Savannah site in California, because the later is so sparse that radiation reflected upwards has a small chance to re-interact with the canopy. Adding soil reflectance in a site with high LAI values results in larger impacts of structure in GPP than in sites with low LAI values.

Finally, in case 5, the measured proportion of incident diffuse shortwave radiation is considered. It is possible to verify that for the old aspen site the difference in GPP between the homogeneous and the heterogeneous canopy structures shows a slight decrease, while in the savannah site, there is an inversion of sign of GPP difference, which means that adding a structural parameterisation scheme has a negative impact on GPP. Most observed incident shortwave radiation was direct during the evaluated period in SSA-OA, which explains a small difference in GPP difference. In US-Ton, the very sparse character of the site associated with a low LAI value results in a large part of the soil being exposed to shortwave radiation, and so, a large part of the radiation is reflected backwards leaving the canopy without being absorbed, which explains the reduction on photosynthetic rate. However, this is the only case in which GPP difference is negative.

It is possible to notice that in each case, from 1 to 5, GPP differences decrease, which means that adding a varying nitrogen vertical profile and the spectral properties of leaves and soil acts in order to minimise the effect of canopy structure itself on GPP calculation. However, diffuse radiation shows a different impact on GPP difference when adding canopy structure. Figure 4.5 shows an intercomparison of zenith profile fraction of direct and diffuse absorbed PAR calculated with the two-stream scheme and different structure parameterisation schemes, and it illustrates the different impacts of direct and diffuse light on fAPAR dependent on canopy density. In all evaluated cases, considering structure decreases total fAPAR. However, considering structure in a dense canopy under diffuse light has a lower impact on fAPAR compared to a case under direct light, e.g., Figure 4.5a (SNW) shows a decrease of 0.20 in fAPAR with direct light and a decrease of 0.10 in fAPAR with diffuse light. Conversely, considering structure in a sparse canopy under

diffuse light has a higher impact on fAPAR compared to a case under direct light, e.g., Figure 4.5c (SNW) shows a decrease of 0.25 in fAPAR with direct light and a decrease of 0.35 in fAPAR with diffuse light. The only negative case is an example of a very specific site with low LAI and sparse vegetation.

The magnitude of the impact of GPP is relative to the other effects but always larger than the impact of each effect separately. For instance in SSA-OA, GPP differences due to structural parameterisation schemes vary from 14.2 μmol.CO_2.m^{-2}.s^{-1} (case 3 structure factor) to 29.8 μmol.CO_2.m^{-2}.s^{-1} (case 1 structure factor), but GPP differences between the cases themselves, one at a time, vary: 7.3 μmol.CO_2.m^{-2}.s^{-1} from case 1 to case 2, 8.4 μmol.CO_2.m^{-2}.s^{-1} from case 2 to case 3, -2.2 μmol.CO_2.m^{-2}.s^{-1} from case 3 to case 4, and 0.2 μmol.CO_2.m^{-2}.s^{-1} from case 4 to case 5, for the structure factor parameterisation scheme. In US-Ton, GPP differences due to structural parameterisation schemes vary from -1.5 μmol.CO_2.m^{-2}.s^{-1} (case 5 clumping index) to 4.8 μmol.CO_2.m^{-2}.s^{-1} (case 1 structure factor), but GPP differences between the cases, one at a time, vary: 1.3 μmol.CO_2.m^{-2}.s^{-1} from case 1 to case 2, 2.6 μmol.CO_2.m^{-2}.s^{-1} from case 2 to case 3, 0.4 μmol.CO_2.m^{-2}.s^{-1} from case 3 to case 4, and 1.9 μmol.CO_2.m^{-2}.s^{-1} from case 4 to case 5, for the structure factor parameterisation scheme. Through this experiment, it is possible to show that structure parameterisation schemes have an impact on GPP independently of the vertical nitrogen profile or the spectral properties of vegetation and soil described in JULES, even though these other factors alter the amount of impacted GPP, the structural parameterisation schemes cause a more significant impact on GPP.

5.6.2 The impact of structural parameterisations on photosynthesis limiting regimes

The photosynthesis limiting regimes according to the Farquhar model (Farquhar et al., 1980) were vertically derived from JULES for the same two sites by calculating the potential photosynthesis in each one of the three limiting regimes, i.e., carbon (▲), light (•), and electron export (+), and selecting the minimum value as the actual limiting regime. Figure 5.8a shows the vertical zenith profile of GPP in μmol.CO_2.m^{-2}.s^{-1} and the photosynthesis limiting regimes obtained from JULES v4.6. The vertical GPP values and the vertical photosynthesis limiting regime were averaged through the day and are presented in a zenith profile.

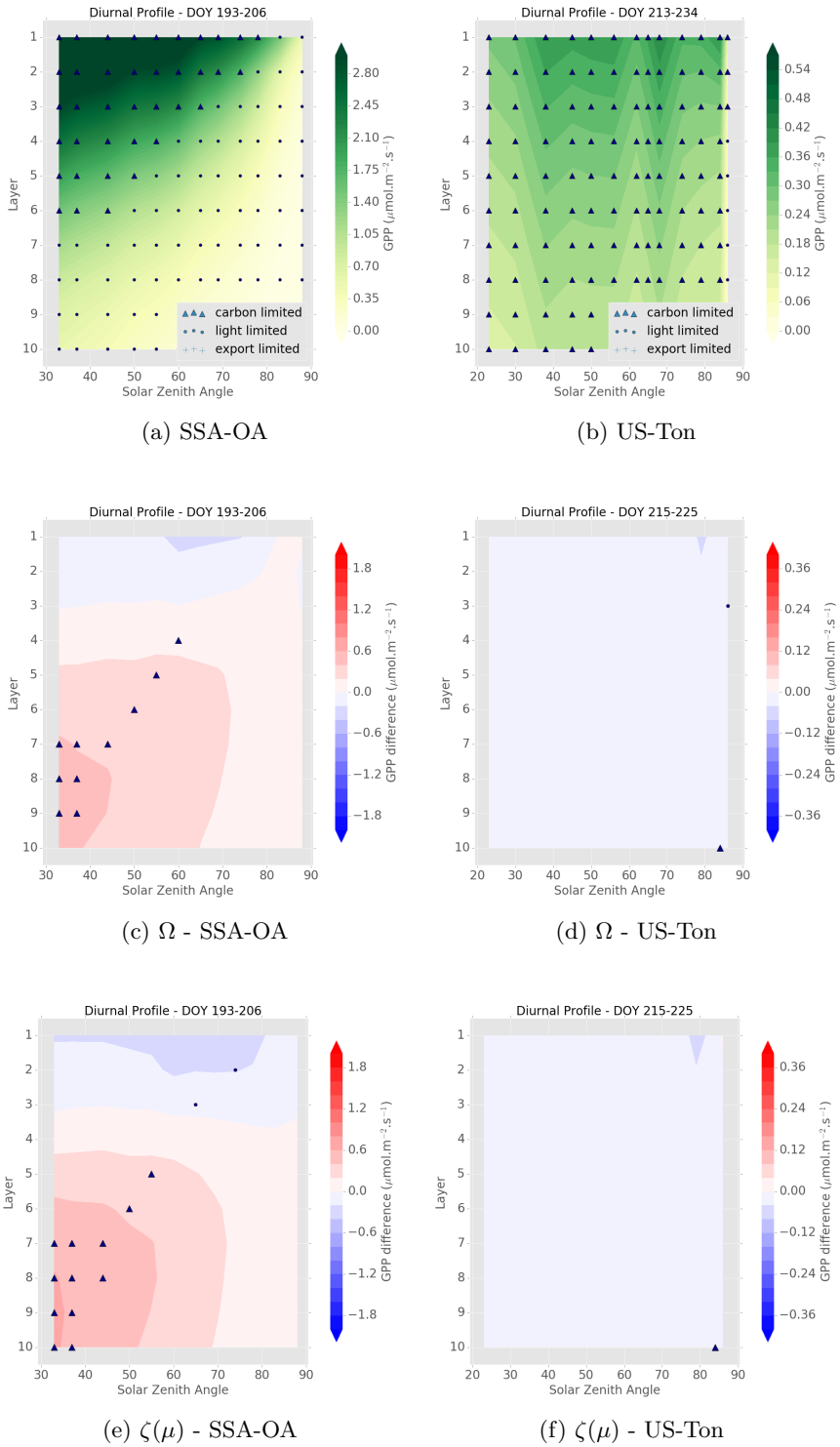

(a) SSA-OA (b) US-Ton

(c) Ω - SSA-OA (d) Ω - US-Ton

(e) $\zeta(\mu)$ - SSA-OA (f) $\zeta(\mu)$ - US-Ton

Figure 5.8: **(a.)** and **(b.)** vertical zenith profile of photosynthesis limiting regimes in JULES; **(c.)** and **(d.)** GPP difference between the modified two-stream with clumping index (Ω) minus the non-clump version; and **(e.)** and **(f.)** GPP difference between the modified two-stream with structure factor ($\zeta(\mu)$) minus the non-clump version. Symbols represented in figures from **(c.)** to **(f.)** indicate difference in photosynthesis limiting between model set ups, i.e., carbon (▲), light (•), and electron export (+).

The most productive layers in the old aspen site are located at the top of the canopy under smaller values of Sun zenith angles, i.e., when there is more shortwave radiation available. Carbon limiting regime is associated with higher values of GPP, and light limiting regime is associated with smaller values of GPP for larger Sun zenith angles and deeper layers of the canopy. There is no evident dependence between GPP and Sun zenith angle for the blue oak savannah site in California, although it is possible to observe more GPP on upper layers of the canopy related to higher nitrogen concentration (Mercado et al., 2007).

Accounting for vegetation canopy architecture through the addition of a structural parameterisation in the two-stream scheme in JULES had a major impact on the photosynthesis limiting regime over the old aspen site throughout the vertical zenith profile. The positive difference in GPP comes mainly from the bottom layers, that are now limited by carbon instead of being limited by light, and the positive difference in GPP is associated with smaller values of Sun zenith angle. The structure factor parameterisation scheme switches the photosynthesis limiting regimes of the last four layers of the canopy for angles smaller than 40° for the old aspen site, while the clumping index affects layers 7 to 9 but does not affect the very bottom layer. This change in photosynthesis limiting regime can be perceived by a higher value of GPP obtained through the structure factor parameterisation scheme in the middle of the day (Fig. 5.6). The impacts on GPP or photosynthesis limiting regimes for the savannah site are neglgible.

5.7 Summary of Findings

This chapter investigated the impacts of two different vegetation structure parameterisations applied to the two-stream radiative transfer scheme with parameters derived from fieldwork observations of structure.

Section 5.2 was used to describe and obtain direct transmittance over all evaluated study sites. For sites with low LAI the direct transmittance was found to be higher, and the opposite for sites with higher LAI, as expected.

In Section 5.3, a model intercomparison exercise showed that in the absence of DHPs, 3D modelling with MAESPA is an accurate tool to obtain direct transmittance, demonstrating that it is possible to accurately derive clumping indices from multiple structural

datasets. As demonstrated in Chapter 4 for hypothetical scenarios and shown here for real forest canopies, the two-stream scheme underestimates direct transmittance.

In Section 5.4, for all study sites the correlation coefficient, RMSE, AIC, and BIC were obtained from the Beer's law fit to the observed data showing that the structure factor has a better performance to fit the P_{gap} data than the clumping index, which indicates the importance of considering a clumping index that varies with zenith angle to accurately determine the shortwave radiation partitioning in heterogeneous vegetation canopies.

Section 5.5 shows that the impact of a structural parameterisation on the two-stream scheme can be of the order of 0.15 in fAPAR when the LAI is high, and up to 0.20 when LAI is lower. Although total fAPAR is smaller when considering canopy architecture through the modification of the two-stream scheme, canopy structure allows more shortwave radiation to propagate into deeper layers in the forest canopy, increasing GPP by the model over sites where the bottom layers are under the light limiting regime of photosynthesis according to the Farquhar model. The agreement between flux tower and modelled GPP improves with structural parameterisations in the radiative transfer scheme.

A better agreement between modelled and flux tower GPP was only observed in a mostly light limited forest with high LAI located in a high latitude boreal zone. This result was not observed on a carbon limited savannah site, and even though the impact of the structure factor parameterisation on fAPAR was substantial, the actual impact on GPP was negligible.

Section 5.6.2 shows that vertical zenith distribution of GPP and photosynthesis limiting regimes according to the Farquhar model, and moreover the impact of considering vegetation canopy structure on the two-stream scheme. The photosynthesis limiting regime of the old aspen boreal site changed when vegetation architecture was taken into account. The interpretation of the modified version of JULES is that canopy architecture has a positive effect on GPP generated by bottom layers, and a negative impact on upper layers, with the net effect on photosynthesis being positive. Over a savannah site with lower LAI and sparser canopy density, the bottom layers were mostly limited by carbon and considering vegetation structure had a negligible effect on modelled GPP.

The improvement on GPP predictions via land surface modelling was dependent on the characteristics of the vertical distribution of photosynthesis limiting regimes of each one of the evaluated sites, indicating that the variation of clumping index with Sun zenith angle

is more important over denser sites with higher LAI, and ultimately limited to locations where light limitation overcomes the other limiting regimes.

Chapter 6:

The Impact of Vegetation Architecture on Global Photosynthesis

6.1 Introduction

The goals of this chapter are to investigate the impact of vegetation canopy architectural heterogeneity on global GPP and to determine the possible impacts that vegetation structure could have on the spatial distribution of the Farquhar limiting regimes throughout the globe.

Section 6.2 presents the methodology used in this chapter including a description of the JULES model setups and data sets. This section also presents the methodology used to rescale the MODIS derived global clumping index map (He et al., 2012) and the development of different maps based on PFTs. Section 6.2 also describes the MTE-FLUXNET data set (Jung et al., 2011), which was used for validation.

Section 6.4 presents a comparison between global GPP generated with the default JULES and the modified version of JULES, parameterised with a global clumping index map, JULES$_{clump}$. Both results are compared with the MTE-FLUXNET GPP data globally and regionally.

Finally, Section 6.5 presents a discussion on how the photosynthesis limiting regimes according to the Farquhar model (Farquhar et al., 1980) are distributed around the globe. The analysis performed in this section gives a spatial perspective of the distribution of the Farquhar limiting regimes around the world, and it demonstrates how the inclusion

of vegetation canopy architecture in the radiative transfer scheme in JULES impacts this distribution.

6.2 Global experiment setup

6.2.1 Model description and experimental design

For global simulations with the JULES model, version 4.6 was run offline at $0.5^\circ \times 0.5^\circ$ spatial resolution forced with the 3 hourly WATCH-Forcing-Data-ERA-Interim data set (Weedon et al., 2014) for the year of 2008. This year was chosen to be close to the date of production of the clumping map (2006) and for being an ENSO neutral year on average. The WFDEI data set contains the following meteorological variables: downward shortwave and longwave radiation fluxes ($W.m^{-2}$), rainfall rate ($kg.m^{-2}.s^{-1}$), snowfall rate ($kg.m^{-2}.s^{-1}$), 2 m temperature (K), 10 m wind speed ($m.s^{-1}$), surface pressure (Pa), and 2 m specific humidity ($kg.kg^{-1}$). The WFDEI data set has two precipitation products, one is corrected using either the Climate Research Unit (CRU) from the University of East Anglia, and the Global Precipitation Climatology Centre (GPCC) precipitation totals (Weedon et al., 2014), both precipitation products are referred to as WFDEI-CRU and WFDEI-GPCC, respectively. For this experiment the product WFDEI-CRU was used. The diffuse shortwave radiation was set to a constant value of 40% of the total downward shortwave radiation flux following Harper et al. (2016).

As previously described in Section 3.3.6, JULES grid boxes consist of a mixture of 9 surface types, where 5 are PFTs (broadleaf trees, needleleaf trees, C3 grasses, C4 grasses, and shrubs) and 4 are non-vegetated surface types (urban, inland water, bare soil, and ice). These 9 surface types are modelled as 9 tiles specified by PFT fractions for each model grid box at the global scale following the Global Land Cover Characterization database version 2.0 (Loveland et al., 2000) (see Fig. 6.7). The model was configured following the Met Office JULES Global Land 4.0 configuration (Walters et al., 2014) with the Harmonized World Soil Database version 1.0 data set (Nachtergaele et al., 2008), and the model of runoff production (TOPMODEL) following Clark and Gedney (2008). Prior to performing the global scale model simulations, the soil moisture and temperature were brought to equilibrium using a 5 year global spin-up by cycling 1 year of meteorological data (2008) with the leaf phenology model on updated every 10 days following Cox (2001)

and described in Clark et al. (2011).

JULES version 4.6 includes a canopy clumping index, which scales LAI within the canopy radiation scheme and represents variation within and across canopy structures (Williams et al., 2017). The canopy structure factor (can_struct_a_io) was added in version 4.6 of JULES with a default value of 1.0, which indicates a structurally homogeneous canopy. This new variable corresponds to the structure factor ($\zeta(\mu)$) in Pinty et al. (2006) except assumed not to vary with zenith angle, i.e., $b = 0$ in Eq. 3.14. The canopy structure factor has no impact on the radiative transfer in JULES if Beer's law is used (can_rad_mod = 1). The variable was originally implemented in JULES with a single value per PFT, and it was tested and evaluated over crops by Williams et al. (2017). The authors found that a clumping index between 0.5 and 0.8 would be consistent with the majority of the canopy structures evaluated in their study. In here, JULES was modified to include a clumping index not only per PFT, but per PFT per gridbox based on a global map of clumping index derived from MODIS and adapted from He et al. (2012).

6.2.2 MODIS derived clumping index

Satellite observations are a useful tool to estimate biogeophysical parameters from vegetation over very large areas, usually the whole globe. However, the resolution of these variables are limited to the satellite pixels, which are usually not directly comparable to measurements acquired *in situ*. In the case of the clumping index, Chen et al. (2005) used bidirectional reflectance distribution function (BRDF) of vegetated land surfaces to extract vegetation structural information globally, using multi-angular data from the POLDER instrument. However, the clumping index map presented by these authors has several limitations, such as low spatial resolution, topographic effects, and a lack of evaluation with field measurements.

Using BRDFs, He et al. (2012) derived a global clumping index map at 500 m resolution from MODIS, that was exclusively aggregated to PFT level at 0.5° with the GLC2000 data set (Bartholomé and Belward, 2005) for this study following Table 6.1. The GLC2000 data were also used in the production of the original clumping map and is hence consistent.

The total clumping index map is represented in Figure 6.1, where the resulting 5 maps of clumping index at 0.5° resolution were weighted following the Global Land Cover Characterization database version 2.0 (Loveland et al., 2000) (Fig. 6.7). Values closer to

1.0 indicate less clumped vegetation represented by hot colours in Figure 6.1, and more clumped vegetation is represented in green. The most clumped areas of the globe are the boreal forests and areas with sparser vegetation, while the least clumped areas of the globe are in the presence of grasses, e.g., over savannahs in Africa and crops in the USA and Asia.

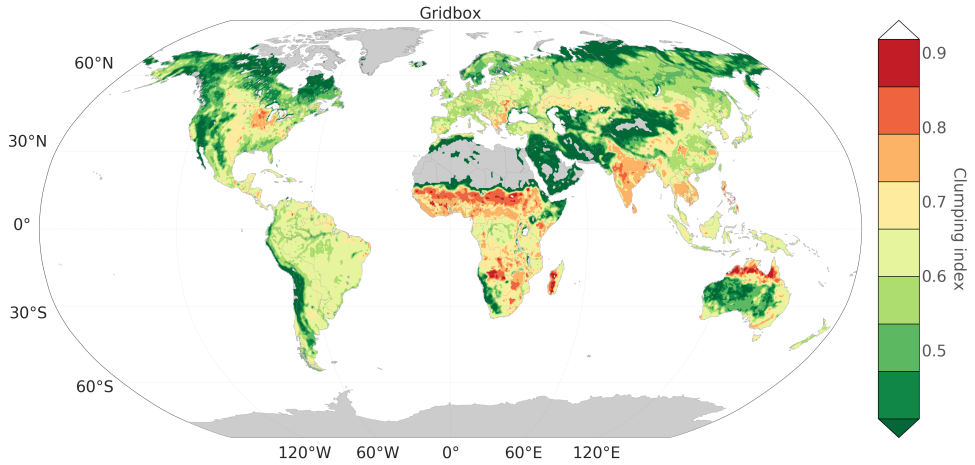

Figure 6.1: Global map of MODIS derived clumping index at 0.5° resolution for the year of 2006 for all PFTs adapted from He et al. (2012) according to GLC2000 land cover types following Table 6.1.

6.2.3 MTE-FLUXNET data set

The MTE-FLUXNET is a monthly global data product at 0.5° resolution upscaled from FLUXNET observations of energy, water, and CO_2 fluxes through a statistical method based on machine learning techniques called model tree ensembles (MTE) (Jung et al., 2011). In order to produce a MTE, the overall upscaling process goes through: i) quality control of the data used for training MTEs, ii) the actual MTE training for all the requested explanatory variables and fluxes at site level , and iii) application of the selected MTEs for global upscaling (Jung et al., 2011). The explanatory variables used for the development of the MTE-FLUXNET include flux tower observations, global satellite retrievals of fAPAR, and global climate fields (Anav et al., 2015); and they have been applied to generate global products of energy (H and LE) and carbon (NEE, GPP, and R_H) fluxes (Jung et al., 2009; Beer et al., 2010; Jung et al., 2011).

Table 6.1: GLC2000 land cover type to JULES PFTs used to generate global map of MODIS derived clumping index at 0.5° resolution for 2006 adapted from He et al. (2012).

GLC-2000 land cover	**JULES PFT**
Tree Cover, broadleaved, evergreen	Broadleaf trees
Tree Cover, broadleaved, deciduous, closed	Broadleaf trees
Tree Cover, broadleaved, deciduous, open	Broadleaf trees
Tree Cover, needleleaved, evergreen	Needleleaf trees
Tree Cover, needleleaved, deciduous	Needleleaf trees
Tree Cover, mixed leaf type	Broadleaf trees
Tree Cover, regularly flooded, fresh water	Broadleaf trees
Tree Cover, regularly flooded, saline water	Broadleaf trees
Mosaic: Tree cover / Other natural vegetation	Broadleaf trees
Tree Cover, burnt	Broadleaf trees
Shrub Cover, closed-open, evergreen	Shrubs
Shrub Cover, closed-open, deciduous	Shrubs
Herbaceous Cover, closed-open	C3 grasses
Sparse Herbaceous or sparse Shrub Cover	C3 grasses
Regularly flooded Shrub and/or Herbaceous Cover	C3 grasses
Cultivated and managed areas	C4 grasses
Mosaic: Cropland / Tree Cover / Other natural vegetation	C4 grasses
Mosaic: Cropland / Shrub or Grass Cover	C4 grasses
Bare Areas	*NA*
Water Bodies	*NA*
Snow and Ice	*NA*
Artificial surfaces and associated areas	*NA*
No data	*NA*

NA: Not applicable.

The MTE is trained against flux tower GPP estimates at site level using fAPAR from satellite observations and meteorological data as explanatory variables. Site level GPP estimates from 178 FLUXNET sites were processed following quality filtering and

partitioning of NEE into GPP and R_H based on Lasslop et al. (2010), and they were selected as target variables for the MTEs training. After that, global patterns of the target variables are estimated by using a combination of explanatory variables and trained MTEs (Jung et al., 2009, 2011). The MTE-GPP data product is currently available since 1982 but it is important to interpret the early very carefully since flux tower observations started roughly a decade after that, with a limited number of sites sparsely distributed mainly across North America and Europe. There is moreover a large uncertainty of the MTE-FLUXNET data products over regions with a limited amount of flux tower sites including most parts of Africa and South America, as well as Tropical and Northern Asia (Anav et al., 2015). In terms of MTE-GPP, Jung et al. (2011) assumes an average and constant value for atmospheric CO_2 concentration throughout the entire available temporal period 1982-2011 (Jung et al., 2011), which might have an impact on the estimated uncertainty since it does not take into account possible effects of CO_2 fertilisation and acclimation on global photosynthesis.

Jung et al. (2011) reported a global value of GPP of 119 $\pm$ 6 Pg C yr^1 for the 1982-2008, consistent with the estimate of 120 $\pm$ 8 Pg C yr^1 presented in latest IPCC AR5 (Ciais et al., 2013). However, the estimated uncertainty of MTE-GPP does not consider uncertainties related to the flux tower measurements, neither their gap-filling or partitioning, or other sources of uncertainty related to the fAPAR satellite product or meteorological data used as explanatory variables. The MTE-GPP uncertainty was simply quantified as the standard deviation of the ensemble mean of 25 different model trees (Slevin et al., 2016).

Despite all limitations associated with the MTE-GPP data product, it is nevertheless the best well known and established available global data set of GPP at 0.5° resolution because it is based on sensible algorithms and local eddy covariance derived GPP values.

6.3 The impact of vegetation canopy architecture on global fAPAR and PAR albedo

The first order impact of considering vegetation clumping in the radiative transfer scheme in JULES is related to fAPAR and PAR albedo, as described in detail in Chapter 4. Figure 6.2 and Figure 6.3 show the global maps of fAPAR and PAR albedo, respectively, for the default JULES, JULES with the implementation of the clumping index parameteri-

sation, and the differences between both results. As predicted by exercises performed in Section 4.4 and indicated in Figure 4.5 and Figure 4.7, fAPAR decreases across the entire globe after including canopy structural heterogeneity. Total canopy fAPAR is reduced, but more light is able to reach lower layers hence increasing the amount of light absorbed at the bottom of the canopy.

The average value of fAPAR for the globe in 2008 according to the default JULES is 0.607 ± 0.022 (95% confidence interval, Eq. 6.1). Applying the clumping index parameterisation scheme shifts the average value to 0.576 ± 0.021, or the equivalent of a total average decrease of 0.032 ± 0.002. Some locations of the Earth can present much larger differences in fAPAR, for instance the Southwest Canada and Northwest USA, Northeast Russia, as well as high altitudes such as the Himalayas and the Andes.

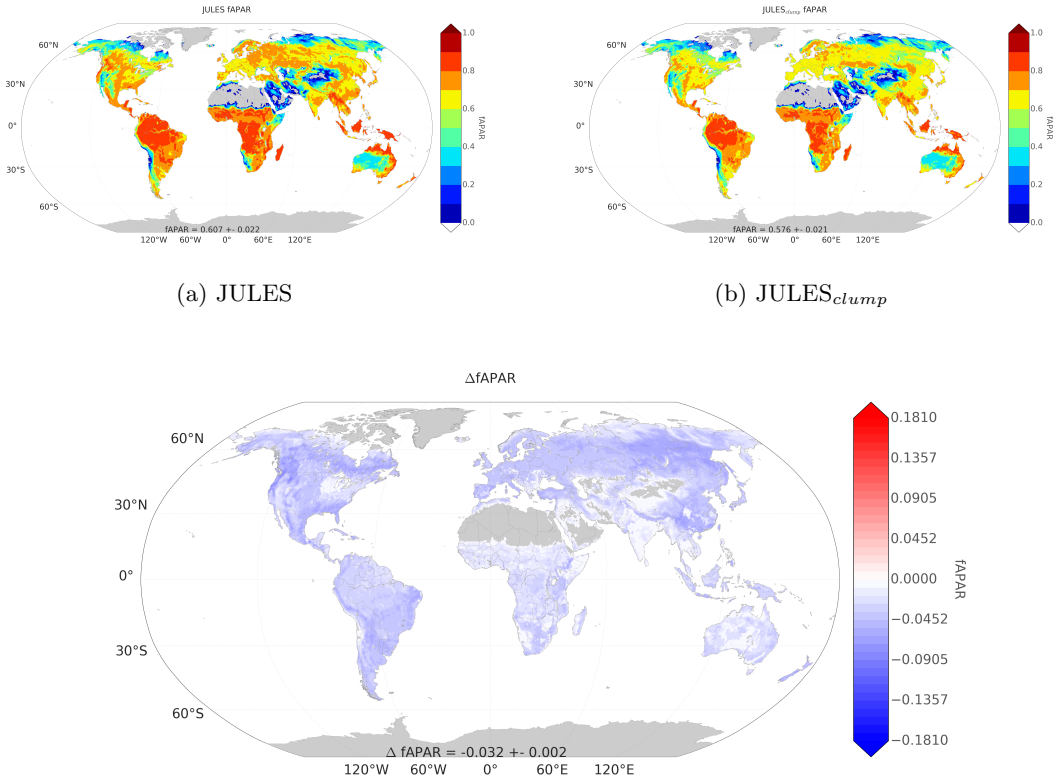

(a) JULES

(b) JULES$_{clump}$

(c) fAPAR difference (JULES$_{clump}$ - JULES)

Figure 6.2: Spatial distribution of total fAPAR for the year of 2008 according to **(a.)** the default JULES, and **(b.)** JULES with clumping; and **(c.)** the difference in fAPAR (JULES$_{clump}$ - JULES).

On the other hand, Figure 6.3 shows a total increase in PAR albedo across the entire

globe, almost to balance out the radiation, that in the new simulation with clumping, is not being absorbed by the canopy, but is being reflected to the atmosphere. The average value of PAR albedo for the globe in 2008 according to the default JULES is 0.247 ± 0.020. Applying the clumping index parameterisation scheme shifts the average value to 0.248 ± 0.020, or the equivalent of a total average decrease of 0.002. Some locations of the Earth present larger differences in PAR albedo: some parts of South Argentina and South Africa, areas of the Middle East, and Middle West USA. Still maximum increments in PAR albedo do not go over 0.02, which indicates that a major part of the radiation in the PAR spectrum is being transmitted to the soil rather than being reflected or absorbed.

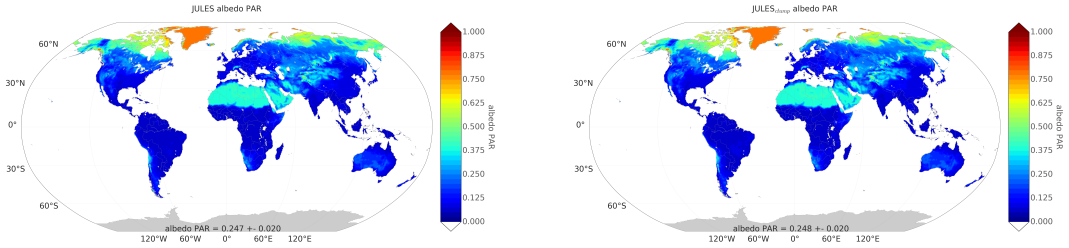

(a) JULES

(b) JULES$_{clump}$

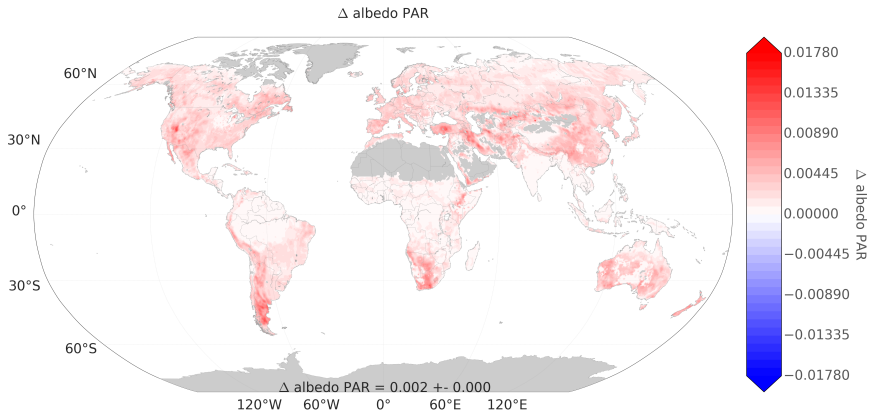

(c) PAR albedo difference (JULES$_{clump}$ - JULES)

Figure 6.3: Spatial distribution of total albedo for the year of 2008 according to **(a.)** the default JULES, and **(b.)** JULES with clumping; and **(c.)** the difference in PAR albedo (JULES$_{clump}$ - JULES).

6.4 The impact of vegetation canopy architecture on global GPP

The average global MTE-GPP for the year of 2008 is 133.76 ± 11.94 PgC (95% confidence interval) and its spatial distribution is represented in Figure 6.4a. For the same period the average global GPP calculated by JULES v4.6 was 115.24 ± 11.30 PgC (Figure 6.4b), and even though the spatial distribution of GPP estimated with JULES in this experiment follows the same patterns of the distribution attributed to MTE-GPP, JULES underestimated MTE-GPP by 18.52 PgC for the year of 2008.

Recent studies (Harper et al., 2016; Slevin et al., 2016) reported the opposite behaviour when comparing JULES-GPP and MTE-GPP. For example, Harper et al. (2016) reported a relatively high average global GPP calculated with JULES with 5 PFTs for the period 2000-2012, 135 PgC yr^{-1}, while MTE-GPP was estimated to be 121.76 PgC for the same period. Slevin et al. (2016) also reported a relatively high average global GPP with JULES in the order of 140 PgC yr^{-1} for the period 2000-2010, while MTE-GPP was found to be in the order of 130 PgC yr^{-1}. The most important difference between the study performed in this chapter and the one developed by Harper et al. (2016) is the value of maximum LAI, i.e., 5 $m^2.m^{-2}$ for broadleaf trees in the present study and 9 $m^2.m^{-2}$ in Harper et al. (2016), because the present one follows the GL4.0 configuration. Other important differences between this study and the one presented in Harper et al. (2016) are related to model resolution, i.e., Harper et al. (2016) used resolution N96 (1.875° longitude × 1.25° latitude), and the model was forced with observed annual average CO_2 (Dlugokencky and Tans, 2013), climate from the CRU-NCEP data set version 4 based on CRU T 3.2 (1901-2009) climate from the CRU-NCEP data set (N. Viovy, personal communication, 2013), and time-invariant fraction of agriculture in each grid cell (Hurtt et al., 2011). In the study performed by Harper et al. (2016), the authors modified JULES to account for 9 PFTs instead of the original 5, and although the proposed modifications improved global GPP, the authors reported underestimated GPP in a needleleaf site because the site is a plantation, where trees are evenly planted to optimize the incoming radiation, rather than a natural larch forest. In the study developed by Slevin et al. (2016), the authors have used the radiative transfer option in JULES that does not consider sunfleck penetration (can_rad_mod = 4), which is known to overestimate GPP.

Figure 6.5a shows the total spatial difference in GPP between JULES with clumping ($JULES_{clump}$) and the default version of JULES without clumping. It is possible to see that under the assumptions made in this experiment, vegetation clumping systematically increases carbon assimilation throughout the globe giving a total extra GPP of 5.53 ± 1.02 PgC for the year of 2008, where uncertainty is given by the 95% confidence interval. The strongest difference between the two model setups is found in the tropics (20°S - 20°N) with an extra GPP of 4.19 PgC, or 75% of the total extra GPP, followed by a bias of 1.14 PgC, or approximately 20% of the total extra GPP in the Northern Hemisphere (20°N - 90°N), and a bias of 0.30 PgC in the Southern Hemisphere (90°S - 20°S), which corresponds to approximately 5% of the total extra GPP.

As previously discussed in Chapter 4, the consideration of canopy structure in the two-stream radiative transfer scheme through the structure factor parameterisation has two main outcomes on fAPAR: first, it reduces the total amount of fAPAR, and second, it distributes the vertical fAPAR within the vegetation canopy, usually reducing the fAPAR at the top of the canopy and increasing it at the bottom. The exact impact of canopy structure on fAPAR depends on a series of different factors, such as LAI, Sun zenith angle, and spectral properties of vegetation and soil.

The evaluation of the impacts of vegetation canopy structure on fAPAR was extended to GPP in Chapter 5 where it was shown that, even though canopy architecture may have a strong impact on total fAPAR, the further impact on photosynthesis will only happen if the vegetation is under the light limited regime of the Farquhar model. The light limiting regime can be usually found in two different circumstances: first, when the Sun zenith angle is large, which can happen all over Earth at the sunrise and sunset, or more systematically over high latitudes; and second, at the bottom of dense vegetation canopies where the top layers will shade the bottom layers, common in wet and hot areas as much of the tropics are light limited.

In order to identify the vertical position where canopy clumping results in extra GPP, the difference in vertical zonal mean GPP between JULES with clumping and the default JULES is shown in Figure 6.6a. As already indicated in Figure 6.5a, the strongest bias in GPP between JULES with structure and without it can be found in the tropics. However, the extra GPP is not evenly distributed vertically. Figure 6.6a indicates the presence of a non-symmetrical dipole with opposite sign on vertical GPP throughout all latitudes where

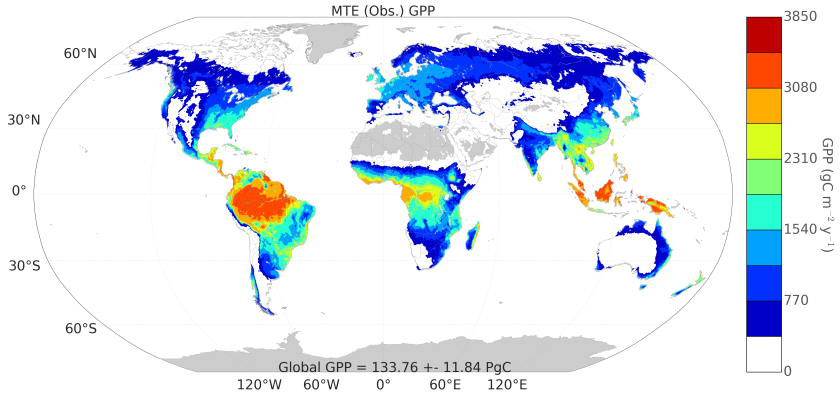

(a) MTE-GPP

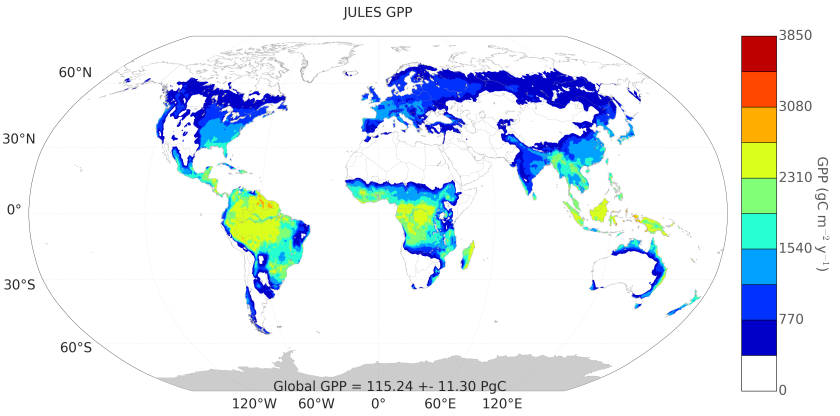

(b) JULES-GPP

Figure 6.4: Total average GPP for the year of 2008 derived from **(a.)** MTE-GPP; and **(b.)** JULES v4.6, global average values are indicated at the bottom of figures in PgC with the 95% confidence interval. Grey areas represent regions with no data.

the top 3 to 4 layers present a smaller absolute vertical GPP in JULES with structure, if compared to JULES without structure. Although the top layers of the canopy are more productive because they have higher V_{cmax} values (see Eq. 3.24), there is an overall increase in global GPP due to more light availability at the bottom of the canopies, where photosynthesis tends to be limited by light.

Figure 6.6b shows that the bottom of the canopy around the world presents a high relative difference in ΔGPP (>75%), especially in the tropics, and although the largest real contribution in ΔGPP comes from the bottom 60% to 90% of the canopy (Figure 6.6a), the relative change in ΔGPP is greater than 50% throughout all latitudes, at least at the

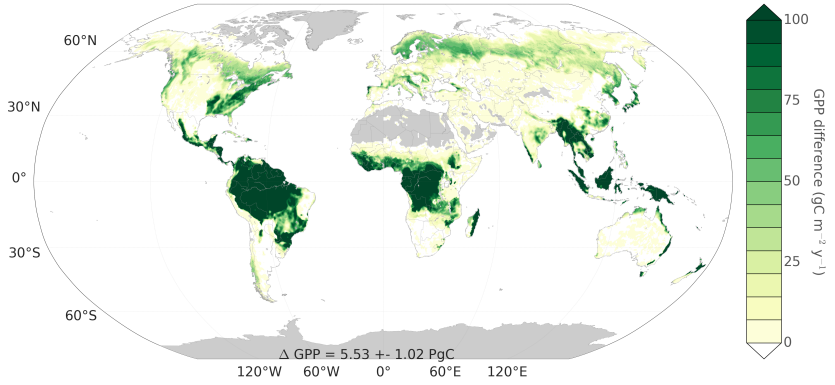

(a) GPP difference (JULES$_{clump}$ - JULES)

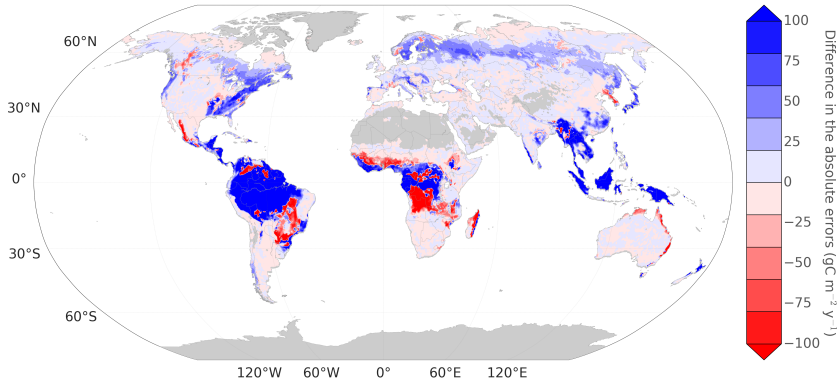

(b) Difference in the absolute deviation

Figure 6.5: **(a.)** Total difference in GPP between modified JULES and default JULES with global ΔGPP indicated in PgC; and **(b.)** the difference in the absolute GPP deviation between JULES and MTE, and JULES$_{clump}$ and MTE. Regions in blue indicate model improvement by addition of vegetation clumping.

very bottom of the canopy (around layers 9 and 10).

All three GPP zonal means of the products, MTE, JULES, and JULES$_{clump}$ are shown in Figure 6.6c. The GPP values were corrected by area in accordance to the latitude, and deserts were masked following the MTE-GPP product. In order to obtain the spatial uncertainty associated with the zonal mean, the temporal mean value of GPP for the year of 2008 is calculated, but the intra-annual variability associated with the temporal mean is not used in the calculation of uncertainty. Instead, the confidence interval of the zonal

mean is calculated as:

$$CI = \pm - \Phi\Big(\frac{1-C}{4}\Big)\frac{\sigma}{\sqrt{N}} \tag{6.1}$$

where σ is the standard deviation of the spatial mean, N is the population size, i.e., the numer of griboxes used in the calculation, Φ is the cumulative distribution function of the standard normal distribution, and C is the confidence level. Throughout the experiments performed in Chapter 6, $C = 95\%$ and exclusively based on the standard deviation of the spatial mean, which only represents the spatial variability of GPP.

Even though the MTE data set has an associated value of standard deviation for each grid box varying monthly, these values are simply a representation of uncertainty based on the standard deviation of the ensemble mean of 25 different model trees used to create the MTE data set (Slevin et al., 2016). In order to evaluate model variability in the zonal mean in a comparable way between runs performed with JULES and the MTE data set, the standard deviation ($\pm 1.\sigma$) of the zonal mean was considered as a measure of uncertainty instead of the 95% confidence interval, because the later was too large, and so, it was impossible to differentiate the area between uncertainties. It is well known that with the increasing frequency of extreme climate events and the increasing CO_2 concentration in the atmosphere, the seasonal and interannual variability of GPP are also projected to increase and impact the global carbon cycle (Zhang et al., 2016). However, the present study limits the evaluation of global GPP to one single year (i.e., 2008), which prevents the assessment of the uncertainty related to the interannual variability of GPP. Although only the spatial variability of the average global GPP is considered in this experiment, the main goal of this section is to perform a comparison of mean global GPP between two versions of JULES and the MTE data through space for one year, and so, the seasonal variability is not considered in the calculation of uncertainty. For longer analysis throughout time, the interannual variability of GPP should be taken into account in order to isolate the impact of structural parameterisation schemes in the model, as well as seasonal variability should be considered in order to evaluate the impact on the amplitude of GPP throughout the year between the standard JULES and the parameterised versions.

The mean of the GPP predicted by JULES without clumping is within the MTE-GPP spatial variability for most of the areas between 10°N and 45°N and 10°S and 30°S. The most important contribution of considering vegetation structure in JULES is noticed in the tropical equatorial area (between 10°S-10°N). The red line shows the GPP calculated

by JULES$_{clump}$ indicating that part of the deviation in GPP between the model and the observation is possibly due to a misrepresentation of canopy architecture in the radiative transfer calculations.

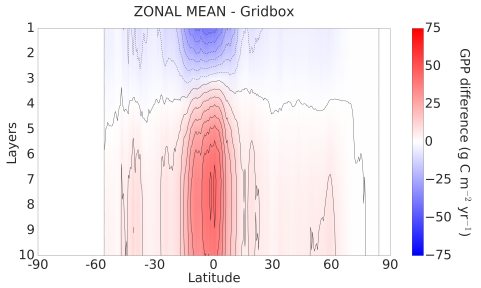

(a) Vertical profile of zonal mean absolute ΔGPP

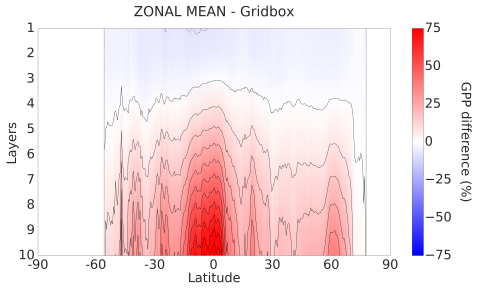

(b) Vertical profile of zonal mean relative ΔGPP

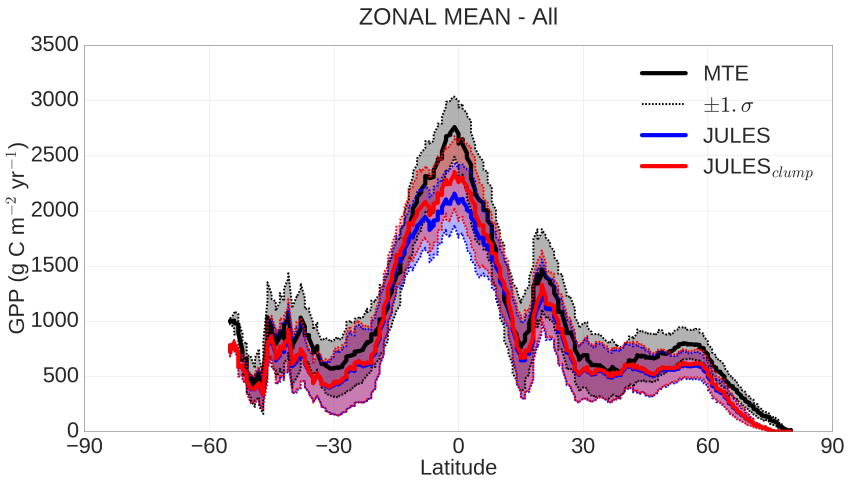

(c) GPP zonal mean

Figure 6.6: Zonal mean vertical profile of **(a.)** absolute and **(b.)** relative difference in GPP between JULES$_{clump}$ and JULES. Unbroken lines represent areas with same positive ΔGPP and dashed lines negative ΔGPP; **(c.)** Total GPP zonal mean of MTE, JULES$_{clump}$ (red), and JULES (blue). One standard deviation ($\pm 1.\sigma$) of the spatial zonal mean only for each GPP product averaged for the year of 2008 is represented by the filled areas.

Figure 6.5b shows the difference in GPP absolute deviation between JULES$_{clump}$ and MTE-FLUXNET, and JULES and MTE-FLUXNET, where regions in blue indicate an improvement towards the MTE data by the addition of vegetation clumping, and red areas indicate the opposite, i.e., JULES$_{clump}$ performs worse than JULES in comparison to the MTE-GPP product.

Tropical forests, the temperate forests in North America, and most of the boreal forests present a general improvement in GPP when considering vegetation clumping in the radiative transfer scheme in JULES, while the maximum additional GPP comes from the

tropical forests over Central and South America. On the one hand, the red areas associated with a worse GPP prediction when adding clumping can be found in the African and Brazilian savannahs, and sparser areas in the presence of grasses, especially C4 grasses (Fig. 6.7).

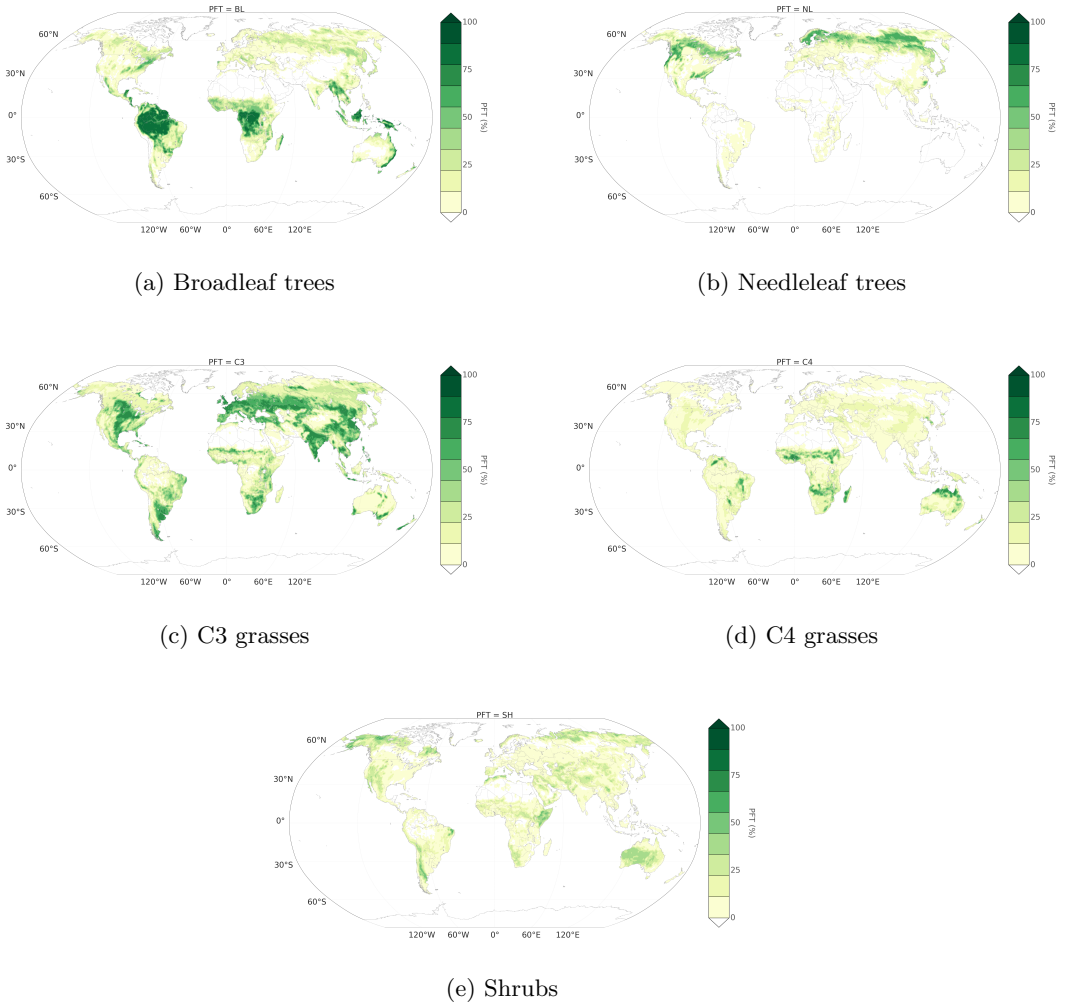

(a) Broadleaf trees

(b) Needleleaf trees

(c) C3 grasses

(d) C4 grasses

(e) Shrubs

Figure 6.7: PFTs global distribution acording to their fractions as represented in JULES.

On the other hand it is known that red areas present sparse vegetation dominated by C4 grasses and it might be that JULES does poorly in those regions because C4 pathway photosynthesis is more efficient than C3 pathway (Collatz et al., 1992; von Caemmerer and Furbank, 2003). C4 grasses were previously described as over-productive in JULES (Harper et al., 2016). However, it is also important to realise that the MTE-FLUXNET GPP data does not represent an absolute truth, and therefore results should be interpreted carefully because this behaviour might also be due to deficiencies on flux tower data on

those areas to generate the MTE-FLUXNET data product.

In order to further explore the impact of vegetation clumping on GPP over different regions on the planet, the globe was divided into 7 different boxes: three boxes in the tropics - Central and South America (20°S-20°N, 120°W-30°W), Africa (20°S-20°N, 20°W-60°E), and South and Southeast Asia (20°S-20°N, 65°E-180°E); three boxes in the Northern Hemisphere - North America (20°N-90°N, 180°W-25°W), Europe (20°N-90°N, 25°W-45°E), and Northern Asia (20°N-90°N, 45°E-180°E); and one in the Southern Hemisphere - Extratropical Southern Hemisphere (20°S-60°S, 180°W-180°E) (Figure 6.8a). The annual average area weighted GPP was calculated over each one of the 7 boxes for both model simulations (JULES and JULES$_{clump}$) and observation based GPP (MTE-FLUXNET) with error bars calculated as the weighted sum of the averaged standard deviation of the ensemble mean of the 25 best model trees associated with the MTE-GPP product for the year of 2008.

Figure 6.8b shows the average total area weighted GPP in PgC for each box for the MTE product (black circle with error bar, calculated as the weighted sum of the averaged standard deviation of the ensemble mean of the 25 best model trees associated with the MTE-GPP product), and the results for JULES (green) and JULES$_{clump}$ (red) as horizontal bars. In general JULES$_{clump}$ shows a higher GPP than the default JULES for all the evaluated areas with a larger absolute and relative impact over the boxes in the tropics, i.e., Central and South America, ΔGPP = 2.03 PgC, or 36.7% of the total extra GPP, followed by Africa, ΔGPP = 1.10 PgC, or 19.9% of the total extra GPP, and finally South and Southeast Asia, ΔGPP = 1.05 PgC, or 19.0% of the total extra GPP. Alone, the tropics are responsible for an extra 4.19 PgC per year by considering vegetation structure in the radiative transfer scheme in JULES (75.6% of the global ΔGPP).

The extratropics are responsible for the remaining 24.4% of extra GPP, whereas the Northern Hemisphere is where the most significant changes are found in the following order: Northern Asia, ΔGPP = 0.54 PgC, or 9.8% of the total extra GPP, followed by North America, ΔGPP = 0.39 PgC, or 7.1% of the total extra GPP, and Europe with ΔGPP = 0.17 PgC, or 3.2% of the total extra GPP. The extratopical Southern Hemisphere is responsible for 4.4% of the total extra GPP, represented by extra 0.24 PgC. Globally, the 5.53 PgC caused by the addition of vegetation clumping into the radiative transfer scheme in JULES is equivalent to an extra 4.8% in global GPP for the year of 2008.

Although for the majority of boxes JULES-GPP is within the error bars of the MTE product, JULES$_{clump}$ improves the estimates of GPP in comparison to the MTE values, except for Africa, where the error presents a switch in sign, i.e., while JULES-GPP underestimates MTE-GPP, JULES$_{clump}$ overestimates it. The most significant improvement is observed over Central and South America where the first prediction of GPP with the default JULES is too small if compared with MTE-GPP (outside the error bars). In these regions there is a significant improvement by the addition of vegetation structure resulting in the accumulated values of GPP falling within the observational uncertainty.

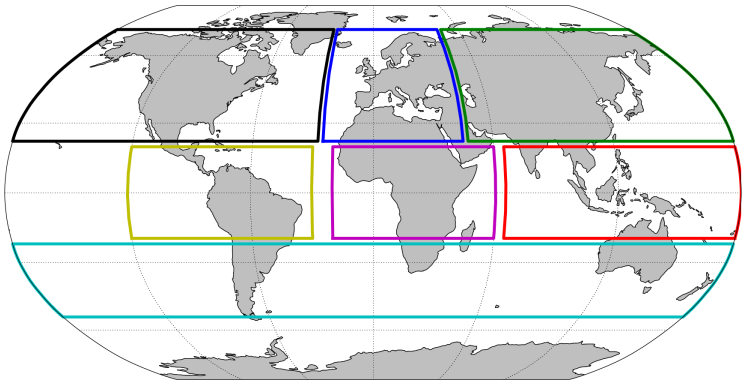

(a) Boxes

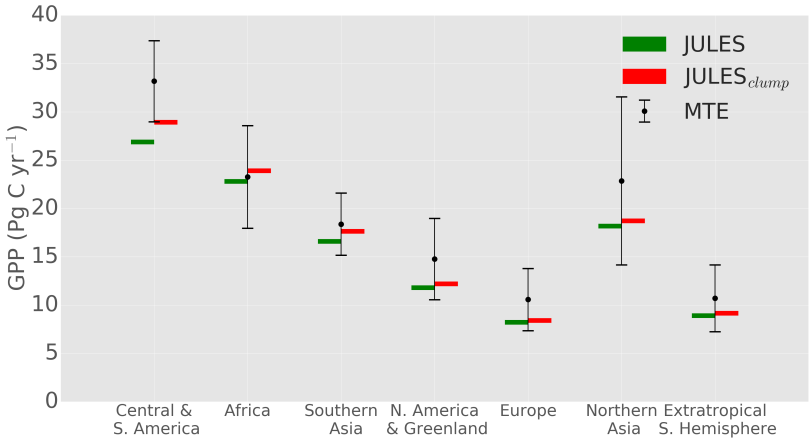

(b) Total GPP

Figure 6.8: **(a.)** Map showing the regions specified by boxes; **(b.)** Total (weighted sum over box area) model simulated (JULES and JULES$_{clump}$) and observation based (MTE) GPP fluxes for the year of 2008 at regional scales. Error bars indicate the weighted sum of the averaged standard deviation of the ensemble mean of the 25 best model trees associated with the MTE-GPP product.

6.5 The distribution of Farquhar limiting regimes around the globe

Previous studies have shown the geographic distribution of potential climatic constraints to global GPP derived from long-term climate statistics (Nemani et al., 2003), or these representations in LSMs (Anav et al., 2015), but there are no studies looking at the spatial-temporal distribution of the Farquhar limiting regimes of photosynthesis throughout the globe. As previously discussed in Section 6.4, the addition of vegetation structure in the radiative transfer scheme of a LSM impacted the total values of GPP throughout the planet, thus it might also impact the distribution of photosynthesis limiting regimes according to the Farquhar model. This section presents the results of a global evaluation of the distribution of photosynthetic limiting regimes according to the Farquhar model in JULES, and the impacts of considering vegetation canopy structure on the spatial distribution of these photosynthetic limiting regimes. Looking at the impacts of vegetation clumping on the distribution of photosynthesis limiting regimes throughout the globe is important to understand how different regions of the world, as well as the specific PFTs associated with them, have photosynthesis affected by the Farquhar limiting factors under a more accurate estimate of shortwave radiation partitioning within the vegetation canopy.

In order to calculate the vertically integrated limiting regime of photosynthesis (W_{int}) according to the Farquhar model, each one of the three assimilation limiting regimes (W_c,W_l,W_e) described in Section 3.5 were individually extracted from both JULES runs and the total minimum is calculated as the minimum value of the sum of each limiting regime throughout the vertical layers of the model as follows:

$$W_{int} = \min \left\{ \sum_{i=1}^{n} W_c, \sum_{i=1}^{n} W_l, \sum_{i=1}^{n} W_e \right\} \tag{6.2}$$

where n = 10 layers in JULES, W_c is the carbon limiting rate (Eq. 3.20), W_l is the light limiting rate (Eq. 3.21), and W_e is the export limiting rate (Eq. 3.22).

Figure 6.9a shows the vertically integrated limiting regime of photosynthesis according to the Farquhar model averaged for the year of 2008 for the non-clump JULES, and Figure 6.9b shows the same limiting regimes but for JULES with clumping. Both figures indicate that the tropics are mostly limited by light because temperature and humidity

are higher, with a few exceptions over drier areas, e.g., the West of the Andes in South America, the semi-arid ecoregion in Northeast Brazil, the Namib desert in Southwest Africa and parts of the Somali desert also in Africa, as well as in sparse regions of Australia. Mid-latitudes are partially limited by carbon, which indicates stronger dependence of photosynthesis on humidity and temperature, especially over drier areas, e.g., the far west in the USA, middle East, deep continental Asia, and tundra ecoregions in Northern Canada and Russia. Other parts of the Mid-latitudes, e.g., the Eastern USA and the boreal forest over Canada and North Europe and Asia, have photosynthesis mostly limited by light in the default version of JULES but the limiting regime changed to mostly carbon limited when vegetation canopy structure is considered through the inclusion of a global clumping map. Figure 6.9c indicates the vertically integrated limiting regime of photosynthesis according to the Farquhar model averaged for the year of 2008 for JULES with vegetation clumping but only for areas where both maps (Fig. 6.9a and Fig. 6.9b) are different. High latitudes are mostly limited by electron transport, which is an indication of photosynthesis mostly controlled by temperature. The export limitation is mostly found in regions with very low temperatures throughout the year, i.e., Northern Canada, Northern Europe, and Northern Asia.

In the default version of JULES for the integrated vertical limiting regimes averaged for the year of 2008, 60.9% of the gridboxes over the globe are light limited, 37.1% of them are carbon limited, and the remaining 2.0% are limited by electron export. When the global MODIS clumping index map (He et al., 2012) is included in the two-stream radiative transfer scheme in JULES, a shift of average Farquhar limiting regimes for photosynthesis is observed, where 45.9% of the gridboxes over the globe are now limited by light, 48.5% are carbon limited, and 5.6% are limited by electron transport.

The consideration of vegetation canopy structure on the radiative transfer scheme in JULES gives a different answer for the distribution of Farquhar limiting regimes of photosynthesis, with major impact in the Northern Hemisphere, especially over the boreal forests. Considering vegetation architecture in the radiative transfer of JULES predicts that less 14.9% of the gridboxes over the world that are not limited by light in comparison to the non-clump JULES run, 11.3% are limited by carbon, and 3.6% are limited by electron transport (Figure 6.9c).

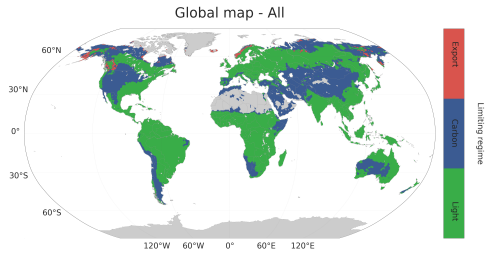

(a) JULES

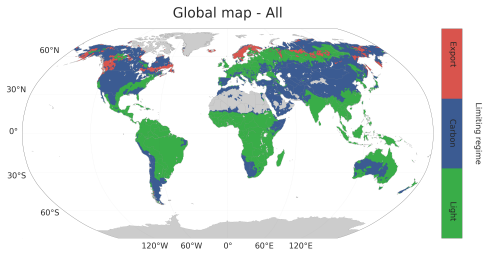

(b) JULES$_{clump}$

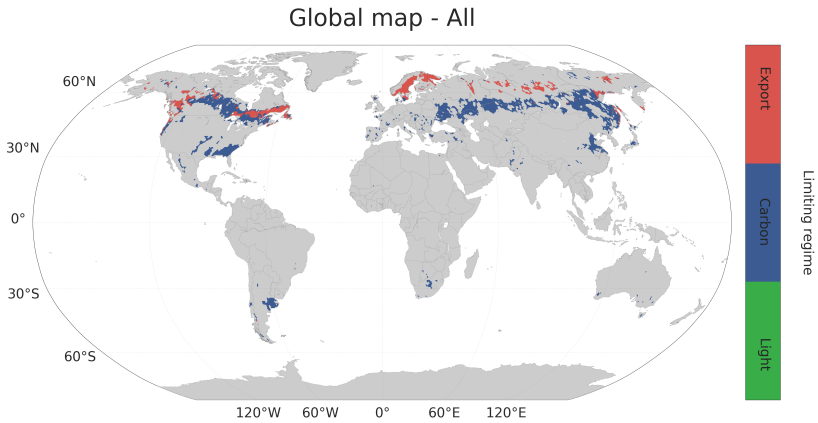

(c) JULES$_{clump}$ for areas that are different between a. and b.

Figure 6.9: Spatial distribution of the Farquhar limiting regimes of photosynthesis for the year of 2008 according to **(a.)** the default JULES, and **(b.)** JULES with clumping; **(c.)** regions where the limiting regimes changed from the default version to the version with clumping in JULES. The actual limiting regimes of difference are associated with the version considering canopy structure.

6.5.1 The vertical distribution of Farquhar limiting regimes

It is clear that the major differences on Farquhar limiting regimes because of canopy structure are located in the Northern Hemisphere, particularly over the boreal forest. However, it is not clear where these major changes in Farquhar limiting regimes are located vertically. In order to identify the vertical position of Farquhar limiting regimes, Figure 6.10a and Figure 6.10b show the vertical zonal mean of the Farquhar limiting regime of photosynthesis for the year of 2008 for JULES and JULES$_{clump}$, respectively.

Figure 6.10a and Figure 6.10b indicate that the top layers across the world are limited by carbon, as light is greatly available in that region of the canopy. The only exceptions are the latitudinal extremes in the Northern and Southern Hemispheres that are limited

by electron transport because those regions are cold throughout the year, and so, there is no vertical differences in the Farquhar limiting regimes. The major vertical changes are centred in 60° North at the last 30% of canopy layers, where the default JULES gives a dominant light limiting regime while JULES$_{clump}$ gives a constant vertical carbon limiting regime. The individual evaluation of vertical differences on Farquhar limiting regimes per PFT shows that this behaviour is majorly influenced by needleleaf trees located at 60° North.

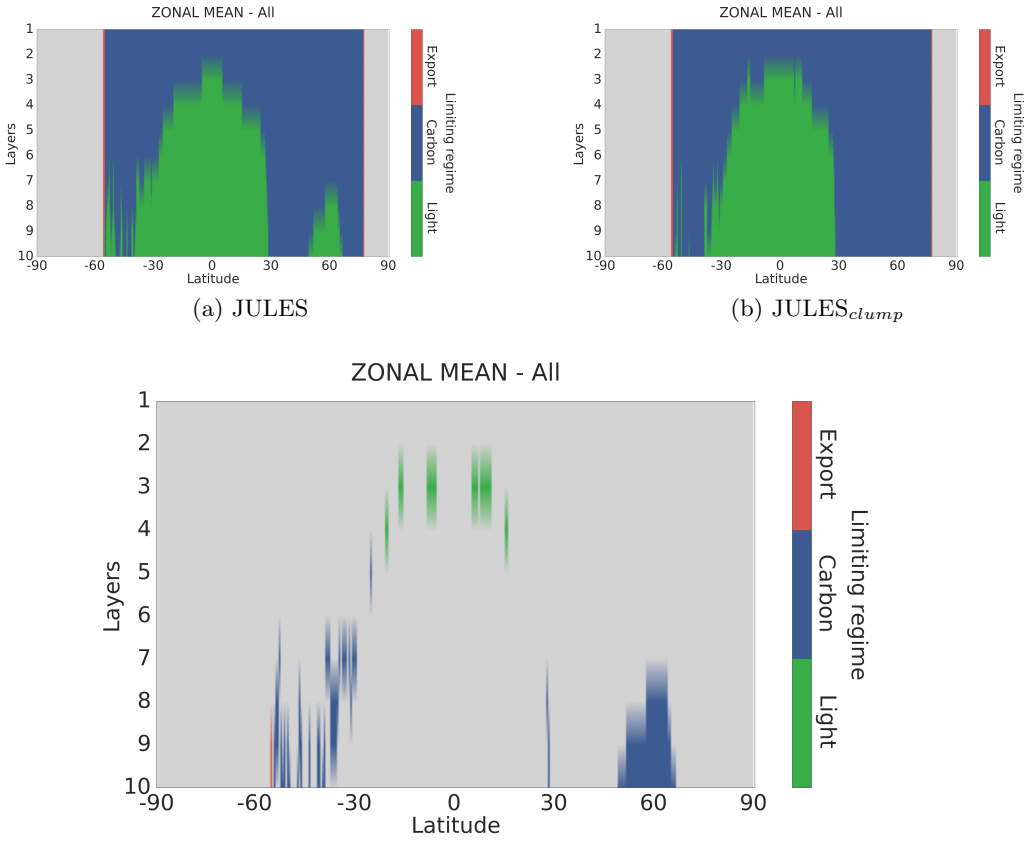

(a) JULES

(b) JULES$_{clump}$

(c) JULES$_{clump}$ for vertical regions that are different between a. and b.

Figure 6.10: Vertical distribution of the Farquhar limiting regimes of photosynthesis for the year of 2008 according to **(a.)** the default JULES, and **(b.)** JULES with clumping; **(c.)** vertical regions where the limiting regimes changed from the default version to the version with clumping in JULES. The actual limiting regimes of difference are associated with the version considering canopy structure.

Boreal forests must withstand very harsh conditions, which include long winters and short summers. These forests are located in high latitudes which means very high Sun zenith angles all over the year, which in terms means very limited amounts of total radiation. Therefore, tree species that inhabit boreal forests have adaptations that help

them to maximise photosynthesis under such a naturally light limited environment. Boreal forests are mostly dominated by needleleaf species and most of them are evergreen conifers, allowing these trees to begin photosynthesising early in the spring when temperatures are favourable, rather than wasting valuable resources to grow new leaves. These needled coniferous species also display more leaves per unit area than deciduous broadleaf species do. The needleleaf trees tend to be angled to the Sun, allowing them to use light for photosynthesis more efficiently, which is beneficial where cold temperatures already constrain carbon assimilation. Most conifers are cone-shaped, which allows branches and needles to receive more direct sunlight without shading other branches. Having a conical shape is especially useful for receiving sunlight that comes from a steep angle at these high boreal latitudes.

It is worth noting that tropical forests are adapted to light limiting conditions through the development of big leaves, for example. In a sense it is possible to make a comparison between the adaptations followed by forests in different regions on Earth to deal with photosynthesis limitation, among other limitations, such as reproductive reasons or adaptions to deal with predators. While forests in high latitudes present structure, forests in low latitudes present higher LAI values. Mid-latitude forests usually present mixed characteristics between tropical and boreal forests.

6.6 Summary of Findings

In order to study the effect of vegetation canopy structure on estimating global GPP and the impacts of structure on the spatial and vertical distribution of the Farquhar limiting regimes of photosynthesis, the JULES model v4.6 was parameterised with a global clumping map adapted from He et al. (2012). Global GPP generated with the default JULES and the modified JULES with clumping were compared with a product based on observations, i.e., MTE-GPP (Jung et al., 2011) across the globe for the year of 2008. The main results obtained from the first part of the experiment indicate a general underestimation in comparison to the MTE-FLUXNET global GPP by the non-clump JULES ($\approx$ 18.52 PgC) for the year of 2008. An overall increase of GPP when considering canopy structure is observed all over the world resulting in extra 5.53 $\pm$ 1.02 PgC in global GPP for the year of 2008 with a strong bias in the tropics ($\approx$ 75%), followed by a bias in the Northern Hemisphere ($\approx$ 20%), and a minor bias in the Southern Hemisphere ($\approx$ 5%).

The resulting extra GPP across the world can be explained by extra shortwave radiation reaching lower parts of the canopy around the globe, especially over the tropics in the presence of higher LAI. The bottom of the canopy is usually a light limited region that photosynthesises more when more radiation is allowed to penetrate deeper into the canopy, in a similar way that extra diffuse radiation penetrates dense canopies in a more efficient way. Even though the distribution of leaf nitrogen is not vertically homogeneous along the canopy, the non-symmetrical redistribution of light absorption, i.e., less radiation is absorbed at the top, and more radiation is absorbed at the bottom of the canopy, favours extra carbon assimilation by deeper canopy layers. Although a general improvement in GPP estimates was obtained by adding canopy structure in JULES, some regions of the world presented a larger bias when compared with the MTE-GPP product, especially over savannahs in Africa and South America, and over grasses-dominated surfaces throughout the globe. The most significant improvement was observed over Central and South America with an extra 2.03 PgC, after considering vegetation structure.

Regarding the distribution of Farquhar limiting regimes of photosynthesis, the addition of vegetation canopy structure caused a shift between light limited areas to carbon limited (+11.31%) and to export limited areas (+3.61%). The major differences on the Farquhar limiting regimes because of canopy structure are located in the Northern Hemisphere, particularly over the boreal forest.

Chapter 7:

Conclusions and Future Work

7.1 Introduction

This PhD thesis explored the broad context of radiative transfer schemes in LSMs, and more specifically, how the vegetation architecture impacts the shortwave radiation partitioning in vegetation canopies as well as how this affects the carbon assimilation calculated by these models.

The global relevance of this work is directly related to the improvement of transfer of radiation in LSMs that are treated very simply and still poorly represented, as discussed in the IPCC AR5 (Ciais et al., 2013) and in Section 1.5; therefore, the ability of LSMs to estimate the terrestrial carbon sink and its interannual variability is limited and uncertain now (Chen et al., 2012), and unreliable under future climate scenarios (Friedlingstein et al., 2006).

In addition, interannual climate variability plays a key role in the maintenance of some ecosystems, once plant growth is influenced by the climate. The seasonal and interannual variability of canopy structure and LAI are affected to a large extent by the climate itself, and so, feedback effects between vegetation and climate are also important to be understood, but they remain poorly explored. This work presented an evaluation of how the current method to calculate photosynthesis in LSMs is influenced by vegetation canopy structure, which indicates possible areas to be explored in order to improve scientific understanding on photosynthetic responses to climate change. Section 7.4 presents a number of questions in which this work is relevant and the directions to where these questions could be further explored.

7.2 Addressing research questions

7.2.1 Research question 1

1. *By using a 'clumping index', is it possible to make the 1D two-stream scheme match the shortwave radiation partitioning of more complex models that explicitly account for 3D structural variability of vegetation canopies?*

In order to answer this question, a model intercomparison exercise was performed. The approach used to address this question was: first, to use complex 3D radiative transfer models, i.e., MAESPA and GORT, and reference values obtained through the RAMI4PILPS experiment (Widlowski et al., 2001) over hypothetical canopy structural sets and to compare their behaviour with a 1D radiative transfer scheme, i.e., the two-stream scheme, and; second, to evaluate the differences between these two groups of radiative transfer schemes in terms of the shortwave radiation partitioning, specifically radiation absorptance and reflectance in two separate wavebands of the shortwave radiation spectrum.

The first result indicates that the 1D radiative transfer scheme usually overestimates shortwave radiation absorptance in comparison to schemes that take vegetation canopy architecture heterogeneity into account. The deviation between the 1D and the 3D cases gets more prominent the sparser the canopy gets. The opposite behaviour is true when analysing canopy reflectance: the 1D radiative transfer scheme usually underestimates canopy reflectance in comparison to the 3D models and the underestimation is higher the sparser the canopy gets. This result reinforces the need to take canopy structural variability into account in radiative transfer schemes commonly used in LSMs, otherwise using a 1D radiative transfer scheme could lead to errors of several orders of magnitude in fAPAR and albedo PAR, and therefore, ultimately affect predictions made by these models on carbon assimilation and radiative forcing.

The next step to address the first research question was to implement four parameterisation schemes into the two-stream scheme and make the 1D model behave more like 3D models, by modulating the vegetation canopy optical depth of the 1D turbid medium assumption. In order to test these parameterisation schemes, a number of heterogeneous canopy set ups, originally described in the RAMI4PILPS experiment were used.

Overall it was found that it is possible to make a 1D radiative transfer scheme reproduce

the shortwave radiation partitioning of a more complex 3D radiative transfer scheme over three canopy densities, over different Sun zenith angles, different illumination conditions, different soil brightness, and over two distinct spectral wavebands.

The structure factor parameterisation scheme (Pinty et al., 2006) consistently showed a better agreement to the RAMI4PILPS reference values of absorptance than other approaches under direct and diffuse illumination conditions for all evaluated scenarios, with particular attention to its performance over a brighter background, i.e., in the presence of snow. The clumping index of Nilson (1971) showed a good agreement with the reference values over the sparse case scenario for small Sun zenith angles ($< 30°$). However, it was not able to reproduce the complete behaviour of more complex models for absorption as canopy density increases for higher Sun zenith angles ($> 30°$), which indicates that considering a clumping index that varies with Sun zenith angle is important to match the results of 3D radiative transfer models more accurately.

Pinty's and Nilson's clumping indices agreed with the RAMI4PILPS reference values for PAR reflectance over snow with substantial differences associated with the medium canopy density over snow, where the presence of zenith variability of structure seems to better represent the RAMI4PILPS reference values. This effect is particularly relevant for the radiative partitioning treatment in boreal regions in the presence of snow, where the shadowing induced by sparse distributed plant structure diminishes surface albedo, in comparison to a closed-canopy/bare-snow scenario of identical cover fractions (Viterbo and Betts, 1999).

A second evaluation performed under the same scope of this research question was related to the vertical distribution of shortwave radiation absorptance within the vegetation canopy. This is especially important because in multi-layered LSMs the radiative transfer varies in the vertical direction and this has direct implications for photosynthesis, so it is necessary to understand not only what happens with the total canopy absorptance but also what happens with the vertical profile of shortwave radiation partitioning. The effect of different parameterisation schemes on the distribution of shortwave radiation was evaluated, and it is possible to observe two distinct behaviours. First, if the canopy has a low LAI (sparse case, LAI = 0.5 $m^2.m^{-2}$), the vertical profile of absorptance for this canopy presents an overall reduction, i.e., the 1D radiative transfer scheme with a structural parameter always gives a smaller value of absorptance throughout the entire

vertical direction. However, a second behaviour is observed by increasing canopy density, which is the case for the medium and dense canopy scenes in the RAMI4PILPS (LAI = 1.5 $m^2.m^{-2}$ and LAI = 2.5 $m^2.m^{-2}$, respectively), over all evaluated Sun zenith angles, there is a redistribution of energy in the vertical axis. At the top of the canopy, the clumping parameterisation schemes give less absorptance than the 1D radiative transfer scheme, while at the bottom of the canopy the parameterisation schemes actually give more shortwave absorptance than the 1D radiative transfer scheme.

The reason for this behaviour is that the clumping index simulates regions with gaps with no vegetated material. At the top of the canopy this would act in a sense of clumping together the upper leaves that were not clumped before the application of the parameterisation scheme, therefore at the top of the canopy there is a total reduction in shortwave radiation absorptance. On the other hand, the addition of gaps throughout the vegetation canopy allows more radiation to propagate vertically, reaching the bottom layers of the vegetation canopy, therefore, the bottom layers in all parameterised cases usually present higher shortwave radiation absorptance in comparison to the 1D scheme (see Fig. 4.10), except when the optical depth of the canopy is very small, i.e., they absorb less of the radiation incident on the layer, but more of the radiation incident on the canopy as a whole. Understanding this second phenomenon arising from the addition of clumping in a 1D radiative transfer scheme is very important to explain the results found in the following research questions.

7.2.2 Research question 2

2. *To what extent is it possible to retrieve the required parameters of a clumping index that varies with Sun zenith angle from digital hemispherical photographs?*

In order to address the second research question presented in this thesis, two analytical parameterisations schemes were evaluated: the clumping index (Nilson, 1971) described in Section 3.3.2 and the structure factor (Pinty et al., 2006) described in Section 3.3.4. These two parameterisation schemes were chosen in order to answer the question of whether or not considering Sun zenith variation in a structural parameter is important to: firstly, derive the parameter from fieldwork observations, and secondly, to evaluate to what extent this would impact other modules of LSMs, particularly carbon assimilation.

Fieldwork observations were used in Chapter 5 to address this question, mostly direct

transmittance derived from digital hemispherical photography. For 12 research sites, existing DHPs were acquired from other researchers and processed, and the zenith profile of direct transmittance was extracted from the observed data. It is possible to invert the gap probability equation (Eq. 2.5) and derive a single clumping index, or both parameters from the structure factor (Eq. 3.14) with zenith profile of direct transmittance.

A statistical evaluation of both parameterisation schemes against observed data through the evaluation of RMSE, r, AIC, and BIC indicate that for all the 12 evaluated study sites, the structure factor with Sun zenith variation fits better the observed data sets than its equivalent without zenith variability. The AIC and BIC are measures of the relative accuracy of statistical models for a given data set. For a number of models, AIC and BIC estimate the quality of each model, relative to each one of the other models. Therefore, AIC and BIC provide a means for model selection. A more detailed discussion on this topic can be found in Section 5.4. In summary, both parameters AIC and BIC obtained for the structure factor fit with Equation 5.2 are smaller than the ones obtained for the clumping index for all 12 study sites. This indicates that the structure factor accounts for architectural heterogeneity on the zenith variation of direct transmittance more accurately than the associated clumping index.

In order to determine which one of the two parameterisation schemes would make a 1D transfer scheme behave more closely to a 3D radiative transfer model a detailed study was performed over two flux tower sites with available structural data derived from dendrometry and LiDAR data. The structural data contained tree positioning, tree DBH, crown diameter and shape, tree height. It was possible to run a detailed 3D tree based radiative transfer model, MAESPA, for an old aspen boreal site in Canada and a blue oak savannah site in California, where the fAPAR was derived and compared with the 1D radiative transfer model and both of its modified parameterisation schemes, i.e., clumping index and structure factor.

The findings described in this section may be extended to other sites with LAI values going from 0.7 to 4.6 $m^2.m^{-2}$, and under different Farquhar limiting regimes. These findings are universal because of the characteristics of the two sites chosen for the analysis performed in here, i.e., they represent extreme cases of structurally heterogeneous forests under two different limiting regimes of photosynthesis. The results indicate that for a sparse forest site like the savannah in California, the 1D radiative transfer scheme over-

estimates PAR absorptance twice as much as the 3D radiative transfer scheme, and both parameterisation schemes improved fAPAR predictions by the 1D modified radiative transfer scheme without major differences between the Nilson's and Pinty's parameterisation schemes. Analysing the denser old aspen site in Canada, the 1D radiative transfer scheme also overestimated fAPAR, but not as much as in the savannah site because the LAI is as higher by 6.6 times and therefore fAPAR is higher over the Canadian site. However, there is a significant difference in fAPAR between the two parameterisation schemes because the structure factor that considers zenith angular variation presents better agreement with the 3D radiative transfer scheme than its peer clumping index.

Pinty's scheme is better for the old aspen boreal site but not for the blue oak savannah site because, in mathematical terms, the angular term of the structure factor $b = 0.627$ for the boreal site versus b = -0.097 for the savannah site. The zenith variation of clumping index does not matter much over the savannah site, and therefore the two parameterisation schemes behave closely for this sparse savannah site in California. A physical explanation for this effect is related to the direct transmittance for both sites. In the boreal BOREAS site, LAI is high (LAI = 4.63 $m^2.m^{-2}$) in comparison to the savannah site in Tonzi ranch, where LAI = 0.70 $m^2.m^{-2}$, which implies that in the savannah site the trees are so apart from each other that the effect of mutual shadowing does not impact the clumping index for different zenith angles. On the other hand, a denser canopy has a larger variation of structure with zenith angle and the structure factor is able to capture this variation, which is not the case for Nilson's parameterisation scheme.

7.2.3 Research question 3

3. *What are the impacts of clumping on photosynthesis calculated by the Farquhar model at site and global levels?*

The JULES model (Best et al., 2011; Clark et al., 2011) was used to test if the improvement in shortwave radiation partitioning also improves carbon assimilation calculated by the Farquhar model (Farquhar et al., 1980). The same two field sites described before (i.e., old aspen boreal site and blue oak savannah site) were studied, mainly because a complete evaluation of fAPAR was performed beforehand for these two sites, and it is clear that for both study sites the 1D and the 3D radiative transfer schemes present significant different values of fAPAR.

For the blue oak savannah site, where the differences in fAPAR between the 1D and the 3D radiative transfer model are quite significant (1D fAPAR is twice as large as the 3D case, see Fig. 5.6b), it is not possible to observe any significant change in GPP. The explanation for this particular behaviour over the savannah site is related to the limiting regime of photosynthesis at this site. For the evaluated period, the blue oak savannah site does not have photosynthesis limited by light but by other limiting factors, such as carbon limitation due to a smaller stomatal conductance. On the other hand, over the old aspen site in Canada, the implementation of both parameterisation schemes in the radiative transfer scheme of JULES actually improved GPP predictions in comparison to eddy covariance derived GPP. The impact of clumping over the old aspen site increased total GPP, even though it reduced total canopy absorptance of PAR.

The explanation of this effect is that with the addition of clumping, the bottom layers of the vegetation canopy get more shortwave radiation, and therefore, present higher values of absorptance with respect to the radiation incident on the top of the canopy. More absorptance of PAR is translated into greater photosynthesis in bottom layers, in which photosynthesis is mostly limited by light. A larger increment in canopy GPP was obtained when adding the structure factor, the parameterisation scheme that accounts for zenith variations, which indicates that a structural parameter that varies with Sun zenith angle can actually contribute to the increment of GPP over a light limited site, mainly because it takes into account the architectural heterogeneity variability throughout different zenith angles observed in diurnal and seasonal cycles.

Taking canopy structural variability into account in the radiative transfer scheme to correctly estimate absorptance, and coupling it with a photosynthesis model, can impact canopy GPP at site level dependent on the limiting regime of photosynthesis present in the evaluated ecosystem.

The JULES land surface model was also used to compare GPP for two different global runs with JULES: first, a default run without clumping, and second, a run with a unique value of clumping index per gridbox, per PFT. The importance of considering a variable clumping index per PFT and per gridbox throughout the globe is related to a dynamic variety of architectural arrangements that are not exclusively depend on plant biome, or PFT, but rather dependent on particular characteristics of plant canopies around the globe, which gives a much more realistic representation of canopy architecture. JULES

was also modified to output variables per vertical layer in the canopy. The results show the effect of canopy structure is to increase total GPP globally by 5.53 PgC yr^{-1} (for the year of 2008), which represents roughly 5% extra GPP in comparison to the model run without clumping.

From Chapter 4, the two observed effects of vegetation clumping on shortwave radiation partitioning were: firstly, to reduce total shortwave absorptance, and secondly, to redistribute the total canopy absorptance by decreasing absorptance at the top of the canopy and adding it at the bottom of the canopy. From results presented in Chapter 5, it is known that vertical redistribution of canopy shortwave absorptance might impact photosynthesis over light limited sites, but this might not have an impact at all over sites under other types of photosynthetic limiting regimes, i.e., carbon or export limitations. It is surprising though that throughout the entire world, even over regions of savannah, GPP increases when considering canopy architectural effects on shortwave radiation partitioning. Following an analysis presented in Chapter 6, where vertical zonal mean GPP was evaluated, it is possible to see that the same result observed at site level can be observed globally, i.e., a reduction of GPP at the top of the canopy, and an increment in GPP at the bottom of the canopy.

In order to validate global values of GPP, the MTE-FLUXNET GPP data set (Jung et al., 2011) was used. Overall, there is an improvement on GPP predictions globally for the evaluated year following the described model configurations. Improvements in GPP are more significant over tropical forests because photosynthesis in these biomes are mostly light limited, and tropical forests present higher LAI values, which intensifies light limitation in layers at the bottom of the canopy. GPP predictions got worse, however, over regions with grasses, e.g., savannah ecosystems in Africa, South America, and Northern Australia, as it can be verified by comparing PFTs spatial distribution over the world in Figure 6.7.

Another question that was addressed by Chapter 6 was the impact of vegetation clumping on the distribution of photosynthetic limiting regimes according to the photosynthesis model of Farquhar. It can be seen that the limiting regimes of photosynthesis in different canopy layers throughout the globe are mostly light limited because bottom layers are often shaded by layers at the top of the canopy.

7.3 Summary of Findings

In summary this thesis presented a number of parameterisation schemes of canopy architectural heterogeneity, which were implemented in a 1D radiative transfer scheme, the two-stream scheme (Sellers, 1985), by adding parameters referred to as clumping indices. Clumping indices modulate the optical depth of a 1D turbid medium representation of a vegetation canopy in order to account for spatial 3D variability, especially in the presence of gaps between tree crowns.

It was found that neglecting canopy spatial heterogeneity in radiative transfer models can lead to significant overestimates in PAR absorption and underestimates in PAR reflectance, especially over sparse canopies. A number of parameterisation schemes of canopy structure were implemented in the two-stream scheme by the inclusion of a variable that modulates the optical depth of the vegetation canopy. These indices were tested against reference values for shortwave radiative partitioning horizontally and vertically, and the clumping indices of Nilson (1971) and Pinty et al. (2006) showed the best results for absorption, reflectance, and transmittance than the other indices in comparison with more complex 3D radiative transfer models. A clumping index that varies with Sun zenith angle showed the best agreement with the RAMI4PILPS reference values among all the evaluated clumping indices. Considering vegetation structure in the two-stream scheme impacts shortwave radiation distribution along the vertical vegetation canopy reducing absorption at the top, and increasing it at the bottom layers.

The impacts of considering vegetation architecture in radiative transfer schemes in LSMs on photosynthesis were evaluated at site level with digital hemispherical photography and eddy covariance measurements, and at global level with satellite data and global modelling. It was found that GPP prediction by LSMs is dependent on the characteristics of the vertical distribution of photosynthesis limiting regimes, limited to locations where light limitation overcomes the other limiting regimes. It was also found that the variation of clumping index with Sun zenith angle is more important over denser sites with higher LAI than sparser sites with lower LAI. At global level, an overall increase of GPP was found when considering canopy structure all over the world resulting in extra 5.53 ± 1.02 $PgC.yr^{-1}$ in global GPP, with a strong signal in the tropics ($\approx 75\%$). A change in the Farquhar limiting regimes of photosynthesis was also found by considering canopy clumping, where 14.9% of the world moved from light limitation to other forms of photosynthesis

limiting regimes mainly over the boreal forest.

7.4 Questions arising

This thesis has demonstrated the impacts of considering vegetation canopy architecture in radiative transfer scheme of LSMs on shortwave radiation partitioning and carbon assimilation. However, many scientific opportunities for extending the scope of this thesis remain. This section presents some of these directions to further develop research in this field.

1. *Application of canopy structure parameterisation schemes into other modules of LSMs, e.g., water interception and momentum transfer.*

As previously discussed in Chapter 1, canopy architecture can impact other land surface processes, such as energy, water, and momentum transfer. Clumping indices could be applicable to other parts of LSMs to account for the impact of vegetation architecture on energy, water, and momentum transfer between the land surface and the atmosphere, as well as feedbacks generated by the inclusion of 3D structural variability.

2. *Generate a global map of clumping index that varies with time since the beginning of the MODIS time series based on the methodology of He et al. (2012) and Chen et al. (2005).*

The global clumping index map of He et al. (2012) is only available for the year of 2006, which limits long term model runs and the evaluation of the impact of vegetation clumping on global GPP for longer periods. A time varying global map of clumping index could not only be used for more evaluations of the impact of clumping on shortwave radiation partitioning in LSMs, but also give more insights on how global vegetation clumping changes with time and land use changes, for example.

3. *Evaluate the impacts of a clumping index that varies with Sun zenith angle following the structure factor proposed by Pinty et al. (2006) on photosynthesis calculated by LSMs.*

The global clumping index map of He et al. (2012) has a variable equivalent to the clumping index of Nilson (1971), which was described and evaluated in Chapter 3, Chapter 4, and Chapter 5 of this thesis; however, it was shown in Chapter 5 that considering a clumping index that varies with zenith angle, like the structure factor (Pinty et al., 2006), is important for some types of vegetation canopies, giving more accurate results when calculating fAPAR and GPP. Obtaining a global map of structure factor would be valuable to more accurately determine canopy shortwave absorptance, and a possible way to do that would be minimising the structure factor parameters a and b (Eq. 3.14) against satellite products of reflectance, such as BRDFs, for example.

4. *Evaluate ways to characterise and implement a dynamical architecture parameterisation into DGVMs in order to develop future global climate runs with a variable canopy structure.*

Several authors (Zhu et al., 2016; Keenan et al., 2016) proposed that the increase in atmospheric CO_2 is fertilising the land surface and increasing carbon assimilation by the plants. Plants use this extra carbon to grow leaves, stems, and branches, which means that canopy architecture will be directly impacted by this process. The development of process-based models of vegetation canopy growth is important to understand the extent to which tree growth is controlled by the supply of carbon from photosynthesis and the impact of shortwave radiation partitioning on its growth. Applying these models into DGVMs would allow scientists to perform future runs, which could improve the understanding on carbon assimilation, plant growth, and temporal evolution of canopy structure, as well as to help scientists to propose new hypothesis for plant architectural changes and their relation to environmental factors.

5. *Evaluate the impact of canopy structure on shortwave radiation partitioning in future scenarios with doubled atmospheric CO_2 concentration.*

In a similar experiment performed in Chapter 6 of this thesis, evaluate the impact of canopy structure on global GPP based on scenarios with doubled atmospheric CO_2 concentration in order to address the question of whether or not the importance of canopy structure on shortwave radiation partitioning would become more important in the future. There is a lack of studies considering changes in photosynthesis limitation for future

climates, but there are some (Keenan et al., 2016; Zhu et al., 2016) showing an expected increase in total photosynthesis due to the CO_2 fertilisation effect. Based on differences in photosynthesis limiting regimes presented in Figure 6.9 and Figure 6.10, the consideration of vegetation clumping could lead to a stronger CO_2 fertilisation effect, given more areas of the globe would become carbon limited other than light limited. However, more studies are needed in this direction.

6. *Evaluate the impact of long-term acclimation and how this has been artificially enveloped into model tuning.*

Calculated carbon uptake by LSMs assume a constant response of plant physiological processes to changes in CO_2 concentration, temperature, and the light environment. However, empirical evidence suggests that photosynthetic responses often vary with current environmental features, implying that plants may 'acclimate' to changes in environmental variables. Model tuning can artificially envelope long-term acclimation and reduce uncertainty in global GPP simulations, both for the present day and for the future. In principle, algorithms used in LSMs could be adopted to describe dynamics of acclimation by modifying the way plants respond to light availability and its impacts on photosynthetic rates and carbon fixation. However, deficiencies in our understanding of the underlying processes and lack of suitable data have prevented a quantitative treatment of photosynthesis acclimation responses in simulation studies of global carbon cycle, therefore, more studies are needed in this area.

7. *The model improvement described in this thesis needs to be thoroughly tested against other models, not just JULES, including more detailed 3D models (such as FLIGHT, for example).*

REFERENCES

Aho, K., D. Derryberry, and T. Peterson, 2014: Model selection for ecologists: the worldviews of AIC and BIC. *Ecology*, **95**, 631–636, doi:10.1890/13-1452.1.

Akaike, H., 1973: Information theory and an extension of the maximum likelihood principle. *Second International Symposium on Information Theory*, A. Kaido, ed., Budapest, Hungary, 267 – 281.

Albertson, J. D., G. G. Katul, and P. Wiberg, 2001: Relative importance of local and regional controls on coupled water, carbon, and energy fluxes. *Advances in Water Resources*, **24**, 1103–1118, doi:10.1016/S0309-1708(01)00042-2.

Alton, P. B., R. Ellis, S. O. Los, and P. R. North, 2007: Improved global simulations of gross primary product based on a separate and explicit treatment of diffuse and direct sunlight. *Journal of Geophysical Research: Atmospheres*, **112**, 1–12, doi:10.1029/2006JD008022.

Anav, A., P. Friedlingstein, C. Beer, P. Ciais, A. Harper, C. Jones, G. Murray-Tortarolo, D. Papale, N. C. Parazoo, P. Peylin, S. Piao, S. Sitch, N. Viovy, A. Wiltshire, and M. Zhao, 2015: Spatiotemporal patterns of terrestrial gross primary production: A review. *Reviews of Geophysics*, **53**, 785–818, doi:10.1002/2015RG000483.

Anav, A., P. Friedlingstein, M. Kidston, L. Bopp, P. Ciais, P. Cox, C. Jones, M. Jung, R. Myneni, and Z. Zhu, 2013: Evaluating the Land and Ocean Components of the Global Carbon Cycle in the CMIP5 Earth System Models. *Journal of Climate*, **26**, 6801–6843, doi:10.1175/JCLI-D-12-00417.1.

Anderson, M. C., J. M. Norman, W. P. Kustas, F. Li, J. H. Prueger, and J. R. Mecikalski, 2005: Effects of Vegetation Clumping on TwoSource Model Estimates of Surface Energy Fluxes from an Agricultural Landscape during SMACEX.

Andrieu, B. and H. Sinoquet, 1993: Evaluation of structure description requirements for predicting gap fraction of vegetation canopies.

Asner, G. P., J. M. O. Scurlock, and J. A. Hicke, 2003: Global synthesis of leaf area index observations: implications for ecological and remote sensing studies. *Global Ecology & Biogeography*, **12**, 191–205, doi:10.1046/j.1466-822X.2003.00026.x.

Aston, A., 1979: Rainfall interception by eight small trees. *Journal of Hydrology*, **42**, 383–396, doi:10.1016/0022-1694(79)90057-X.

Atwell, B., P. Kriedemann, and C. Turnbull, 1999: *Plants in Action: Adaptation in Nature, Performance in Cultivation*. Macmillan Education Australia.

Bai, K., J. Katz, and C. Meneveau, 2015: Turbulent Flow Structure Inside a Canopy with Complex Multi-Scale Elements. *Boundary-Layer Meteorology*, **155**, 435–457, doi:10.1007/s10546-015-0011-2.

Baldocchi, D., 2006: Measuring and Modeling Carbon, Water Vapor and Energy Exchange over Grassland and Tree/Grass Ecosystems. Technical report, University of California, Berkeley, California, USA.

Baldocchi, D., E. Falge, L. Gu, R. Olson, D. Hollinger, S. Running, P. Anthoni, C. Bernhofer, K. Davis, R. Evans, J. Fuentes, A. Goldstein, G. Katul, B. Law, X. Lee, Y. Malhi, T. Meyers, W. Munger, W. Oechel, U. K. T. Paw, K. Pilegaard, H. P. Schmid, R. Valentini, S. Verma, T. Vesala, K. Wilson, and S. Wofsy, 2001: FLUXNET: A New Tool to Study the Temporal and Spatial Variability of Ecosystem-Scale Carbon Dioxide, Water Vapor, and Energy Flux Densities. *Bulletin of the American Meteorological Society*, doi:10.1175/1520-0477(2001)082¡2415:FANTTS¿2.3.CO;2.

Baldocchi, D. D., K. B. Wilson, and L. Gu, 2002: How the environment, canopy structure and canopy physiological functioning influence carbon, water and energy fluxes of a temperate broad-leaved deciduous forest–an assessment with the biophysical model CANOAK. *Tree physiology*, **22**, 1065–1077.

Baldocchi, D. D., L. Xu, and N. Kiang, 2004: How plant functional-type, weather, seasonal drought, and soil physical properties alter water and energy fluxes of an oak-grass savanna and an annual grassland. *Agricultural and Forest Meteorology*, **123**, 13–39, doi:10.1016/j.agrformet.2003.11.006.

Ball, J., 1988: *An analysis of stomatal conductance*. Ph.D. thesis, Stanford University, 88 pp.

Barford, C. C., S. C. Wofsy, M. L. Goulden, J. W. Munger, E. H. Pyle, S. P. Urbanski, L. Hutyra, S. R. Saleska, D. Fitzjarrald, and K. Moore, 2001: Factors Controlling Long- and Short-Term Sequestration of Atmospheric CO2 in a Mid-latitude Forest. *Science*, **294**, 1688–1691, doi:10.1126/science.1062962.

Bartholomé, E. and A. S. Belward, 2005: GLC2000: a new approach to global land cover mapping from Earth observation data. *International Journal of Remote Sensing*, doi:10.1080/01431160412331291297.

Beer, C., M. Reichstein, E. Tomelleri, P. Ciais, M. Jung, N. Carvalhais, C. Rodenbeck, M. A. Arain, D. Baldocchi, G. B. Bonan, A. Bondeau, A. Cescatti, G. Lasslop, A. Lindroth, M. Lomas, S. Luyssaert, H. Margolis, K. W. Oleson, O. Roupsard, E. Veenendaal, N. Viovy, C. Williams, F. I. Woodward, and D. Papale, 2010: Terrestrial Gross Carbon Dioxide Uptake: Global Distribution and Covariation with Climate. *Science*, doi:10.1126/science.1184984.

Benham, S. E., E. I. Vanguelova, and R. M. Pitman, 2012: Short and long term changes in carbon, nitrogen and acidity in the forest soils under oak at the Alice Holt Environmental Change Network site. *Science of the Total Environment*, **421-422**, 82–93, doi:10.1016/j.scitotenv.2012.02.004.

Best, M., M. Pryor, D. Clark, G. Rooney, R. Essery, C. Menard, J. Edwards, M. Hendry, a. Porson, N. Gedney, L. Mercado, S. Sitch, E. Blyth, O. Boucher, P. Cox, C. Grimmond, and R. Harding, 2011: The Joint UK Land Environment Simulator (JULES), model description. Part 1: Energy and water fluxes. *Geoscientific Model Development*, **4**, 677–699.

Betts, A. K. and J. H. Ball, 1997: Albedo over the boreal forest. *Journal of Geophysical Research: Atmospheres*, **102**, 28901–28909, doi:10.1029/96JD03876.

Black, T. A., J.-M. Chen, X. Lee, and R. M. Sagar, 1991: Characteristics of shortwave and longwave irradiances under a Douglas-fir forest stand.

Bonan, G. B., 2008: Forests and climate change: forcings, feedbacks, and the climate benefits of forests. *Science (New York, N.Y.)*, **320**, 1444–1449, doi:10.1126/science.1155121.

— 2016: *Ecological Climatology: concepts and applications*. Cambridge University Press, Cambridge, United Kingdom, third edit edition, 754 pp.

Bussiere, F., F. Solmon, and A. Fouere, 2002: Implementation and evaluation of DROP, a model for the simulation of rainfall distribution below plants described in 3D. *AGRONOMIE*, doi:10.1051/agro:2001002.

Chen, J., P. Rich, S. Gower, J. Norman, and P. S, 1997: Leaf area index of boreal forests: Theory, techniques, and measurements. *Journal of Geophysical Research*, **102**, 29429, doi:10.1029/97JD01107.

Chen, J. M., 1996: Optically-based methods for measuring seasonal variation of leaf area index in boreal conifer stands. *Agricultural and Forest Meteorology*, **80**, 135–163, doi:10.1016/0168-1923(95)02291-0.

Chen, J. M. and T. A. Black, 1991: Measuring leaf area index of plant canopies with branch architecture. *Agricultural and Forest Meteorology*, doi:10.1016/0168-1923(91)90074-Z.

Chen, J. M. and T. a. Black, 1992: Defining leaf area index for non-flat leaves. *Plant, Cell and Environment*, **15**, 421–429.

Chen, J. M. and J. Cihlar, 1995: Plant canopy gap-size analysis theory for improving optical measurements of leaf-area index. *Applied optics*, **34**, 6211–6222.

Chen, J. M., C. H. Menges, and S. G. Leblanc, 2005: Global mapping of foliage clumping index using multi-angular satellite data. *Remote Sensing of Environment*, **97**, 447–457.

Chen, J. M., G. Mo, J. Pisek, J. Liu, F. Deng, M. Ishizawa, and D. Chan, 2012: Effects of foliage clumping on the estimation of global terrestrial gross primary productivity. *Global Biogeochemical Cycles*, **26**.

Chen, Q., D. Baldocchi, P. Gong, and T. Dawson, 2008: Modeling radiation and photosynthesis of a heterogeneous savanna woodland landscape with a hierarchy of model complexities. *Agricultural and Forest Meteorology*, **148**, 1005–1020.

Chen, Q., D. Baldocchi, P. Gong, and M. Kelly, 2006: Isolating Individual Trees in a Savanna Woodland Using Small Footprint Lidar Data. *Photogrammetric Engineering & Remote Sensing*, **72**, 923–932, doi:10.14358/PERS.72.8.923.

Ciais, P., C. Sabine, G. Bala, L. Bopp, V. Brovkin, J. Canadell, a. Chhabra, R. DeFries, J. Galloway, M. Heimann, C. Jones, C. L. Quéré, R. Myneni, S. Piao, and P. Thornton, 2013: Carbon and Other Biogeochemical Cycles. *Climate Change 2013 - The Physical Science Basis*, doi:10.1017/CBO9781107415324.015.

Clark, D., L. Mercado, S. Sitch, C. D. Jones, N. Gedney, M. Best, M. Pryor, G. Rooney, R. Essery, E. Blyth, R. Harding, C. Hutingford, and P. Cox, 2011: The Joint UK Land Environment Simulator (JULES), model description. Part 2: Carbon fluxes and vegetation dynamics. *Geoscientific Model Development*, **4**, 701–722, doi:10.5194/gmd-4-701-2011.

Clark, D. B. and N. Gedney, 2008: Representing the effects of subgrid variability of soil moisture on runoff generation in a Land surface model. *Journal of Geophysical Research Atmospheres*, doi:10.1029/2007JD008940.

Collatz, G., J. Ball, C. Grivet, and J. a. Berry, 1991: Physiological and environmental regulation of stomatal conductance, photosynthesis and transpiration: a model that includes a laminar boundary layer. *Agricultural and Forest Meteorology*, **54**, 107–136, doi:10.1016/0168-1923(91)90002-8.

Collatz, G. J., J. A. Berry, G. D. Farquhar, and J. Pierce, 1990: The relationship between the Rubisco reaction mechanism and models of photosynthesis. *Plant, Cell & Environment*, doi:10.1111/j.1365-3040.1990.tb01306.x.

Collatz, G. J., M. Ribas-Carbo, and J. a. Berry, 1992: Coupled photosynthesis-stomatal conductance model for leaves of C4 plants. *Australian Journal of Plant Physiology*, **19**, 519–539, doi:10.1071/PP9920519.

Cox, P., 2001: Description of the " TRIFFID " Dynamic Global Vegetation Model. *Hadley Centre technical note*, **24**, 1–17.

Cox, P. M., R. A. Betts, C. B. Bunton, R. L. H. Essery, P. R. Rowntree, and J. Smith, 1999: The impact of new land surface physics on the GCM simulation of climate and climate sensitivity. *Climate Dynamics*, **15**, 183–203, doi:10.1007/s003820050276.

Cox, P. M., R. a. Betts, C. D. Jones, S. a. Spall, and I. J. Totterdell, 2000: Acceleration of global warming due to carbon-cycle feedbacks in a coupled climate model. *Nature*, **408**, 184–187, doi:10.1038/35041539.

Dai, Y., R. Dickinson, and Y. Wang, 2004: A Two-Big-Leaf Model for Canopy Temperature , Photosynthesis , and Stomatal Conductance. *Journal of Climate*, **17**, 2281–2299, doi:10.1175/1520-0442(2004)017¡2281:ATMFCT¿2.0.CO;2.

De Kauwe, M. G., M. I. Disney, T. Quaife, P. Lewis, and M. Williams, 2011: An assessment of the MODIS collection 5 leaf area index product for a region of mixed coniferous forest. *Remote Sensing of Environment*, **115**, 767–780.

De Pury, D. G. G. and G. D. Farquhar, 1997: Simple scaling of photosynthesis from leaves to canopies without the errors of big-leaf models. *Plant, Cell and Environment*, **20**, 537–557.

Deardorff, J. W., 1978: Efficient prediction of ground surface temperature and moisture, with inclusion of a layer of vegetation. *Journal of Geophysical Research*, doi:10.1029/JC083iC04p01889.

Dickinson, R. E., 1983: Land Surface Processes and Climate-Surface Albedos and Energy Balance. *Advances in Geophysics*, **25**, 305–353, doi:10.1016/S0065-2687(08)60176-4.

Disney, M. I., P. Lewis, and P. R. J. North, 2000: Monte Carlo ray tracing in optical canopy reectance modelling. *Remote Sensing Reviews*, **18**, 163–196.

Dlugokencky, E. and P. Tans, 2013: http://www.esrl.noaa.gov/gmd/ccgg/trends.

Dutta, D., K. Wang, E. Lee, A. Goodwell, D. K. Woo, D. Wagner, and P. Kumar, 2017: Characterizing Vegetation Canopy Structure Using Airborne Remote Sensing Data. *IEEE Transactions on Geoscience and Remote Sensing*, **55**, 1160–1178, doi:10.1109/TGRS.2016.2620478.

Duursma, R., 2015: Maeswrap: Wrapper functions for MAESTRA/MAESPA.

Duursma, R. A. and B. E. Medlyn, 2012: MAESPA: A model to study interactions between water limitation, environmental drivers and vegetation function at tree and stand levels, with an example application to [CO2] x drought interactions. *Geoscientific Model Development*, **5**, 919–940.

Ellison, A., 2005: Light Environment in Hemlock Removal Experiment at Harvard Forest since 2004.

Erbs, D. G., S. A. Klein, and J. A. Duffie, 1982: Estimation of the diffuse radiation fraction for hourly, daily and monthly-average global radiation. *Solar Energy*, **28**, 293–302.

Farquhar, G. D., S. Caemmerer, and J. A. Berry, 1980: A biochemical model of photosynthetic CO2 assimilation in leaves of C3 species. *Planta*, **149**, 78–90, doi:10.1007/BF00386231.

Fournier, R. A., P. M. Rich, and R. Landry, 1997: Hierarchical characterization of canopy architecture for boreal forest.

Friedlingstein, P., P. Cox, R. Betts, L. Bopp, W. von Bloh, V. Brovkin, P. Cadule, S. Doney, M. Eby, I. Fung, G. Bala, J. John, C. Jones, F. Joos, T. Kato, M. Kawamiya, W. Knorr, K. Lindsay, H. D. Matthews, T. Raddatz, P. Rayner, C. Reick, E. Roeckner, K. G. Schnitzler, R. Schnur, K. Strassmann, A. J. Weaver, C. Yoshikawa, and N. Zeng, 2006: Climate-carbon cycle feedback analysis: Results from the C4MIP model intercomparison. *Journal of Climate*, doi:10.1175/JCLI3800.1.

Galmés, J., J. Flexas, A. J. Keys, J. Cifre, R. A. C. Mitchell, P. J. Madgwick, R. P. Haslam, H. Medrano, and M. A. J. Parry, 2005: Rubisco specificity factor tends to be larger in plant species from drier habitats and in species with persistent leaves. *Plant, Cell and Environment*, doi:10.1111/j.1365-3040.2005.01300.x.

Gastellu-Etchegorry, J. P., 2008: 3D modeling of satellite spectral images, radiation budget and energy budget of urban landscapes. *Meteorology and Atmospheric Physics*, **102**, 187–207, doi:10.1007/s00703-008-0344-1.

Gastellu-Etchegorry, J. P., V. Demarez, V. Pinel, and F. Zagolski, 1996: Modeling radiative transfer in heterogeneous 3-D vegetation canopies. doi:10.1016/0034-4257(95)00253-7.

Gastellu-Etchegorry, J. P., E. Martin, and F. Gascon, 2004: DART: a 3D model for simulating satellite images and studying surface radiation budget. *International Journal of Remote Sensing*, **25**, 73–96, doi:10.1080/0143116031000115166.

Gobron, N., B. Pinty, M. Verstraete, and Y. Govaerts, 1999: The MERIS Global Vegetation Index (MGVI): Description and preliminary application. *International Journal of Remote Sensing*, **20**, 1917–1927, doi:10.1080/014311699212542.

Godin, C., E. Costes, and H. Sinoquet, 2005: Plant architecture modelling: Virtual plants and complex systems. *Plant architecture and its manipulation*, C. G. N. Turnbull, ed., Blackwell Publishing Ltd, Oxford, chapter 9, 322.

Goll, D. S., V. Brovkin, B. R. Parida, C. H. Reick, J. Kattge, P. B. Reich, P. M. Van Bodegom, and Ü. Niinemets, 2012: Nutrient limitation reduces land carbon uptake in simulations with a model of combined carbon, nitrogen and phosphorus cycling. *Biogeosciences*, **9**, 3547–3569, doi:10.5194/bg-9-3547-2012.

Gonsamo, A. and P. Pellikka, 2009: The computation of foliage clumping index using hemispherical photography. *Agricultural and Forest Meteorology*, **149**, 1781–1787, doi:10.1016/j.agrformet.2009.06.001.

Goudriaan, J., 1977: *Crop Micrometeorology: a Simulation Study*. Pudoc, Wageningen, 249 pp.

Govaerts, Y. and M. M. Verstraete, 1995: Modeling the scattering of light in three-dimensional canopies: Contribution of a Monte Carlo ray tracing approach. *Combined Optical-Microwave Earth and Atmosphere Sensing - Conference Proceedings*, 31–34.

Govaerts, Y. M. and M. M. Verstraete, 1998: Raytran: A Monte Carlo ray-tracing model to compute light scattering in three-dimensional heterogeneous media. *IEEE Transactions on Geoscience and Remote Sensing*, **36**, 493–505, doi:10.1109/36.662732.

Grill, E. and H. Ziegler, 1998: A Plant's Dilemma. *Science*, **282**, 252–253, doi:10.1126/science.282.5387.252.

Hadley, J. L. and J. L. Schedlbauer, 2002: Carbon exchange of an old-growth eastern hemlock (Tsuga canadensis) forest in central New England. *Tree Physiology*, **22**, 1079–1092, doi:10.1093/treephys/22.15-16.1079.

Hall, F. G. and P. J. Sellers, 1995: First International Satellite Land Surface Climatology Project (ISLSCP) Field Experiment (FIFE) in 1995.

Hardiman, B., G. Bohrer, C. Gough, and P. Curtis, 2013: Canopy Structural Changes Following Widespread Mortality of Canopy Dominant Trees. *Forests*, **4**, 537–552, doi:10.3390/f4030537.

Hardy, J. P., R. E. Davis, R. Jordan, X. Li, C. Woodcock, W. Ni, and J. C. McKenzie, 1997: Snow ablation modeling at the stand scale in a boreal jack pine forest.

Harper, A. B., P. M. Cox, P. Friedlingstein, A. J. Wiltshire, C. D. Jones, S. Sitch, L. M. Mercado, M. Groenendijk, E. Robertson, J. Kattge, G. Bönisch, O. K. Atkin, M. Bahn, J. Cornelissen, U. Niinemets, V. Onipchenko, J. Peñuelas, L. Poorter, P. B. Reich, N. A. Soudzilovskaia, and P. Van Bodegom, 2016: Improved representation of plant functional types and physiology in the Joint UK Land Environment Simulator (JULES v4.2) using plant trait information. *Geoscientific Model Development*, **9**, 2415–2440.

Hartmann, D. J., A. M. G. Klein Tank, M. Rusticucci, L. V. Alexander, S. Brönnimann, Y. A.-R. Charabi, F. J. Dentener, E. J. Dlugokencky, D. R. Easterling, A. Kaplan, B. J. Soden, P. W. Thorne, M. Wild, and P. Zhai, 2013: Observations: Atmosphere and Surface. *Climate Change 2013: The Physical Science Basis. Contribution of Working Group I to the Fifth Assessment Report of the Intergovernmental Panel on Climate Change*, doi:10.1017/CBO9781107415324.008.

He, L., J. M. Chen, J. Pisek, C. B. Schaaf, and A. H. Strahler, 2012: Global clumping index map derived from the MODIS BRDF product. *Remote Sensing of Environment*, **119**, 118–130.

Higgins, P. A. T. and J. Harte, 2012: Carbon cycle uncertainty increases climate change risks and mitigation challenges. *Journal of Climate*, doi:10.1175/JCLI-D-12-00089.1.

Huntingford, C., R. A. Fisher, L. Mercado, B. B. B. Booth, S. Sitch, P. P. Harris, P. M. Cox, C. D. Jones, R. A. Betts, Y. Malhi, G. R. Harris, M. Collins, and P. Moorcroft, 2008: Towards quantifying uncertainty in predictions of Amazon 'dieback'. *Philosophical transactions of the Royal Society of London. Series B, Biological sciences*, **363**, 1857–64, doi:10.1098/rstb.2007.0028.

Hurtt, G. C., L. P. Chini, S. Frolking, R. A. Betts, J. Feddema, G. Fischer, J. P. Fisk, K. Hibbard, R. A. Houghton, A. Janetos, C. D. Jones, G. Kindermann, T. Kinoshita, K. Klein Goldewijk, K. Riahi, E. Shevliakova, S. Smith, E. Stehfest, A. Thomson, P. Thornton, D. P. van Vuuren, and Y. P. Wang, 2011: Harmonization of land-use scenarios for the period 1500-2100: 600 years of global gridded annual land-use transitions, wood harvest, and resulting secondary lands. *Climatic Change*, doi:10.1007/s10584-011-0153-2.

Jarvis, P. G., 1976: The Interpretation of the Variations in Leaf Water Potential and Stomatal Conductance Found in Canopies in the Field. *Philosophical Transactions of the Royal Society B: Biological Sciences*, doi:10.1098/rstb.1976.0035.

Jill Harrison, C., 2017: Development and genetics in the evolution of land plant body plans. *Philosophical Transactions of the Royal Society B: Biological Sciences*, **372**, 20150490, doi:10.1098/rstb.2015.0490.

Jogireddy, V., P. M. Cox, C. Huntingford, R. J. Harding, and L. Mercado., 2006: An improved description of canopy light interception for use in a GCM land-surface scheme: calibration and testing against carbon fluxes at a coniferous forest. *Hadley Centre Technical Note 63*, Hadley Centre, Met Office, Exeter, UK.

Jonckheere, I., S. Fleck, K. Nackaerts, B. Muys, P. Coppin, M. Weiss, and F. Baret, 2004: Review of methods for in situ leaf area index determination Part I. Theories, sensors and hemispherical photography.

Jung, M., M. Reichstein, and A. Bondeau, 2009: Towards global empirical upscaling of FLUXNET eddy covariance observations: validation of a model tree ensemble approach using a biosphere model. *Biogeosciences Discussions*, doi:10.5194/bgd-6-5271-2009.

Jung, M., M. Reichstein, H. A. Margolis, A. Cescatti, A. D. Richardson, M. A. Arain, A. Arneth, C. Bernhofer, D. Bonal, J. Chen, D. Gianelle, N. Gobron, G. Kiely, W. Kutsch, G. Lasslop, B. E. Law, A. Lindroth, L. Merbold, L. Montagnani, E. J. Moors, D. Papale, M. Sottocornola, F. Vaccari, and C. Williams, 2011: Global patterns of land-atmosphere fluxes of carbon dioxide, latent heat, and sensible heat derived from eddy covariance, satellite, and meteorological observations. *Journal of Geophysical Research: Biogeosciences*, doi:10.1029/2010JG001566.

Kampe, T. U., 2010: NEON: the first continental-scale ecological observatory with airborne remote sensing of vegetation canopy biochemistry and structure. *Journal of Applied Remote Sensing*, **4**, 043510, doi:10.1117/1.3361375.

Keenan, T., I. C. Prentice, J. G. Canadell, C. Williams, H. Wang, M. R. Raupach, and G. J. Collatz, 2016: Recent pause in the growth rate of atmospheric CO2 due to enhanced terrestrial carbon uptake. *Nature Communications*, doi:10.1038/ncomms13428.

Keller, M., A. Alencar, G. P. Asner, B. Braswell, M. Bustamante, E. Davidson, T. Feldpausch, E. Fernandes, M. Goulden, P. Kabat, B. Kruijt, F. Luizao, S. Miller, D. Markewitz, A. D. Nobre, C. a. Nobre, N. Priante Filho, H. da Rocha, P. Silva Dias, C. von Randow, and G. L. Vourlitis, 2004: Ecological Research in the Large-Scale Biosphere Atmosphere Experiment in Amazonia: Early Results. *Ecological Applications*, **14**, 3–16, doi:10.1890/03-6003.

Kelliher, F. M., R. Leuning, M. R. Raupach, and E. D. Schulze, 1995: Maximum conductances for evaporation from global vegetation types. *Agricultural and Forest Meteorology*, **73**, 1–16.

Kim, J., Q. Guo, D. D. Baldocchi, M. Y. Leclerc, L. Xu, and H. P. Schmid, 2006: Upscaling fluxes from tower to landscape: Overlaying flux footprints on high-resolution (IKONOS) images of vegetation cover. *Agricultural and Forest Meteorology*, doi:10.1016/j.agrformet.2004.11.015.

Knyazikhin, Y., J. Kranigk, R. B. Myneni, O. Panfyorov, and G. Gravenhorst, 1998: Influence of small-scale structure on radiative transfer and photosynthesis in vegetation canopies. **103**, 6133, doi:10.1029/97JD03380.

Kobayashi, H., D. D. Baldocchi, Y. Ryu, Q. Chen, S. Ma, J. L. Osuna, and S. L. Ustin, 2012: Modeling energy and carbon fluxes in a heterogeneous oak woodland: A three-dimensional approach. *Agricultural and Forest Meteorology*, **152**, 83–100.

Krinner, G., N. Viovy, N. de Noblet-Ducoudré, J. Ogée, J. Polcher, P. Friedlingstein, P. Ciais, S. Sitch, and I. C. Prentice, 2005: A dynamic global vegetation model for studies of the coupled atmosphere-biosphere system. *Global Biogeochemical Cycles*, **19**, doi:10.1029/2003GB002199.

Kucharik, C. J., J. M. Norman, and S. T. Gower, 1999: Characterization of radiation regimes in nonrandom forest canopies: theory, measurements, and a simplified modeling approach. *Tree Physiology*, **19**, 695–706.

Kucharik, C. J., J. M. Norman, L. M. Murdock, and S. T. Gower, 1997: Characterizing canopy nonrandomness with a multiband vegetation imager (MVI). *J. Geophys. Res.*, **102**, 29455–29473, doi:10.1029/97jd01175.

Kurz, W. A., C. C. Dymond, G. Stinson, G. J. Rampley, E. T. Neilson, A. L. Carroll, T. Ebata, and L. Safranyik, 2008: Mountain pine beetle and forest carbon feedback to climate change. *Nature*, doi:10.1038/nature06777.

Lasslop, G., M. Reichstein, D. Papale, A. Richardson, A. Arneth, A. Barr, P. Stoy, and G. Wohlfahrt, 2010: Separation of net ecosystem exchange into assimilation and respiration using a light response curve approach: Critical issues and global evaluation. *Global Change Biology*, doi:10.1111/j.1365-2486.2009.02041.x.

Law, B. E., a. Cescatti, and D. D. Baldocchi, 2001a: Leaf area distribution and radiative transfer in open-canopy forests: implications for mass and energy exchange. *Tree physiology*, **21**, 777–787.

Law, B. E., O. J. Sun, J. Campbell, S. Van Tuyl, and P. E. Thornton, 2003: Changes in carbon storage and fluxes in a chronosequence of ponderosa pine. *Global Change Biology*, doi:10.1046/j.1365-2486.2003.00624.x.

Law, B. E., P. E. Thornton, J. Irvine, P. M. Anthoni, and S. Van Tuyl, 2001b: Carbon storage and fluxes in ponderosa pine forests at different developmental stages. *Global Change Biology*, **7**, 755–777.

Lawrence, D. M., K. W. Oleson, M. G. Flanner, P. E. Thornton, S. C. Swenson, P. J. Lawrence, X. Zeng, Z.-L. Yang, S. Levis, K. Sakaguchi, G. B. Bonan, and A. G. Slater, 2011: Parameterization improvements and functional and structural advances in Version 4 of the Community Land Model. *Journal of Advances in Modeling Earth Systems*, **3**, n/a–n/a, doi:10.1029/2011MS00045.

Le Quéré, C., R. M. Andrew, J. G. Canadell, S. Sitch, J. Ivar Korsbakken, G. P. Peters, A. C. Manning, T. A. Boden, P. P. Tans, R. A. Houghton, R. F. Keeling, S. Alin, O. D. Andrews, P. Anthoni, L. Barbero, L. Bopp, F. Chevallier, L. P. Chini, P. Ciais, K. Currie, C. Delire, S. C. Doney, P. Friedlingstein, T. Gkritzalis, I. Harris, J. Hauck, V. Haverd, M. Hoppema, K. Klein Goldewijk, A. K. Jain, E. Kato, A. K??rtzinger, P. Landschützer, N. Lefévre, A. Lenton, S. Lienert, D. Lombardozzi, J. R. Melton, N. Metzl, F. Millero, P. M. S. Monteiro, D. R. Munro, J. E. M. S. Nabel, S. I. Nakaoka, K. O'Brien, A. Olsen, A. M. Omar, T. Ono, D. Pierrot, B. Poulter, C. Rödenbeck, J. Salisbury, U. Schuster, J. Schwinger, R. Séférian, I. Skjelvan, B. D. Stocker, A. J. Sutton, T. Takahashi, H. Tian, B. Tilbrook, I. T. Van Der Laan-Luijkx, G. R. Van Der Werf, N. Viovy, A. P. Walker, A. J. Wiltshire, and S. Zaehle, 2016: Global Carbon Budget 2016. *Earth System Science Data*, doi:10.5194/essd-8-605-2016.

Le Quéré, C., M. R. Raupach, J. G. Canadell, G. Marland et al., C. Le Quéré et al., C. Le Quéré et al., M. R. Raupach, J. G. Canadell, G. Marland, L. Bopp, P. Ciais, T. J. Conway, S. C. Doney, R. A. Feely, P. Foster, P. Friedlingstein, K. Gurney, R. A. Houghton, J. I. House, C. Huntingford, P. E. Levy, M. R. Lomas, J. Majkut, N. Metzl, J. P. Ometto, G. P. Peters, I. C. Prentice, J. T. Randerson, S. W. Running, J. L. Sarmiento, U. Schuster, S. Sitch, T. Takahashi, N. Viovy, G. R. van der Werf, and F. I. Woodward, 2009: Trends in the sources and sinks of carbon dioxide. *Nature Geoscience*, doi:10.1038/ngeo689.

LeBauer, D. S. and K. K. Treseder, 2008: Nitrogen limitation of net primary productivity in terrestrial ecosystems is globally distributed. *Ecology*, doi:10.1890/06-2057.1.

Leblanc, S., J. Chen, and M. Kwong, 2002: Tracing radiation and architecture of canopies. TRAC Manual. Version 2.1. 3. *Natural Resources Canada, Canada Centre for*, 1–25.

Leblanc, S. G., J. M. Chen, R. Fernandes, D. W. Deering, and A. Conley, 2005: Methodology comparison for canopy structure parameters extraction from digital hemispherical photography in boreal forests. *Agricultural and Forest Meteorology*, **129**, 187–207.

Leuning, R., F. M. Kelliher, D. G. G. de Pury, and E. D. Schulze, 1995: Leaf nitrogen, photosynthesis, conductance and transpiration: Scaling from leaves to canopies. *Plant, Cell and Environment*, **18**, 1183–1200.

Li, X., A. H. Strahler, and C. E. Woodcock, 1995: Hybrid geometric optical-radiative transfer approach for modeling albedo and directional reflectance of discontinuous canopies. *IEEE Transactions on Geoscience and Remote Sensing*, **33**, 466–480.

Loew, A., P. M. Van Bodegom, J. L. Widlowski, J. Otto, T. Quaife, B. Pinty, and T. Raddatz, 2014: Do we (need to) care about canopy radiation schemes in DGVMs? Caveats and potential impacts. *Biogeosciences*, **11**, 1873–1897.

Loveland, T. R. and A. S. Belward, 1997: The IGBP-DIS global 1 km land cover data set , DISCover : first results. *int. j. remote sensing*.

Loveland, T. R., B. C. Reed, J. F. Brown, D. O. Ohlen, Z. Zhu, L. Yang, and J. W. Merchant, 2000: Development of a global land cover characteristics database and IGBP DISCover from 1 km AVHRR data. *International Journal of Remote Sensing*, doi:10.1080/014311600210191.

Lynch, P., 2008: The origins of computer weather prediction and climate modeling. *Journal of Computational Physics*, **227**, 3431–3444.

Ma, S., D. D. Baldocchi, L. Xu, and T. Hehn, 2007: Inter-annual variability in carbon dioxide exchange of an oak/grass savanna and open grassland in California. *Agricultural and Forest Meteorology*, **147**, 157–171.

Manabe, S., 1969: Climate and the ocean circulation 1. The atmospheric circulation and the hydrology of the earths surface. *Monthly Weather Review*, **97**, 739–774.

Marcolla, B., A. Pitacco, and A. Cescatti, 2003: Canopy architecture and turbulence structure in a coniferous forest. *Boundary-Layer Meteorology*, doi:10.1023/A:1023027709805.

Mcmurtrie, R. E. and Y. P. Wang, 1993: Mathematical-Models of the Photosynthetic Response of Tree Stands to Rising Co2 Concentrations and Temperatures. *Plant Cell and Environment*, **16**, 1–13.

Meador, W. E. and W. R. Weaver, 1980: Two-stream approximation to radiative transfer in planetary atmospheres: a unified description of existing methods and a new improvement. *Journal of the Atmospheric Sciences*, **37**, 630–643, doi:http://dx.doi.org/10.1175/1520-0469(1980)037¡0630:TSATRT¿2.0.CO;2.

Medlyn, B., 2004: A MAESTRO retrospective. *Forests at the Land-Atmosphere Interface*, M. Mencuccini, J. Grace, J. B. Moncrieff, and K. McNaughton, eds., CAB International, volume 53, chapter 8, 105–121.

Medlyn, B. E., 1998: Physiological basis of the light use efficiency model. *Tree physiology*, doi:10.1093/treephys/18.3.167.

Medlyn, B. E., D. A. Pepper, A. P. O'Grady, and H. Keith, 2007: Linking leaf and tree water use with an individual-tree model. *Tree Physiology*, **27**, 1687–1699, doi:10.1093/treephys/27.12.1687.

Mercado, L. M., C. Huntingford, J. H. C. Gash, P. M. Cox, and V. Jogireddy, 2007: Improving the representation of radiation interception and photosynthesis for climate model applications. *Tellus, Series B: Chemical and Physical Meteorology*, **59**, 553–565, doi:10.1111/j.1600-0889.2007.00256.x.

Monsi, M. and T. Saeki, 1953: Uber den Lichtfaktor in den Pflanzengesellschaften und seine Bedeutung fur die Stoffproduktion. *Jpn J Bot*, **14**, 22–52.

Monteith, J. L. and M. H. Unsworth, 1990a: *Principles of environmental physics*, volume 10. 177–178 pp.

— 1990b: Principles of environmental physics, 2nd Edition. *Edward Arnold, London*.

Myhre, G., D. Shindell, F.-M. Bréon, W. Collins, J. Fuglestvedt, J. Huang, D. Koch, J.-F. Lamarque, D. Lee, B. Mendoza, T. Nakajima, A. Robock, G. Stephens, T. Takemura, and H. Zhang, 2013: Anthropogenic and Natural Radiative Forcing. *Climate Change 2013: The Physical Science Basis. Contribution of Working Group I to the Fifth Assessment Report of the Intergovernmental Panel on Climate Change*, doi:10.1017/CBO9781107415324.018.

Myneni, R. B., S. Hoffman, Y. Knyazikhin, J. L. Privette, J. Glassy, Y. Tian, Y. Wang, X. Song, Y. Zhang, G. R. Smith, a. Lotsch, M. Friedl, J. T. Morisette, P. Votava, R. R. Nemani, and S. W. Running, 2002: Global products of vegetation leaf area and fraction absorbed PAR from year one of MODIS data. *Remote Sensing of Environment*, **83**, 214–231, doi:10.1016/S0034-4257(02)00074-3.

Myneni, R. B., C. D. Keeling, C. J. Tucker, G. Asrar, and R. R. Nemani, 1997: Increased plant growth in the northern high latitudes from 1981 to 1991.

Myneni, R. B., J. Ross, and G. Asrar, 1989: A review on the theory of photon transport in leaf canopies. *Agricultural and Forest Meteorology*, **45**, 1–153, doi:10.1016/0168-1923(89)90002-6.

Nachtergaele, F., H. van Velthuizen, L. Verelst, N. Batjes, K. Dijkshoorn, V. van Engelen, G. Fischer, A. Jones, L. Montanarella, M. Petri, S. Prieler, E. Teixeira, D. Wiberg, and X. Shi, 2008: Harmonized World Soil Database (version 1.0).

Nelder, J. a. and R. Mead, 1964: A simplex method for function minimization. *The Computer Journal*, **7**, 308–313, doi:10.1093/comjnl/7.4.308.

Nemani, R. R., C. D. Keeling, H. Hashimoto, W. M. Jolly, S. C. Piper, C. J. Tucker, R. B. Myneni, and S. W. Running, 2003: Climate-Driven Increases in Global Terrestrial Net Primary Production from 1982 to 1999. *Science*, doi:10.1126/science.1082750.

Ni, W., X. Li, C. E. Woodcock, M. R. Caetano, and A. H. Strahler, 1999: An analytical hybrid GORT model for bidirectional reflectance over discontinuous plant canopies. *IEEE Transactions on Geoscience and Remote Sensing*, **37**, 987–999.

Ni, W. and C. E. Woodcock, 2000: Effect of canopy structure and the presence of snow on the albedo of boreal conifer forests. *Journal of Geophysical Research*, **105**, 11879, doi:10.1029/1999JD901158.

Ni, W. G., X. W. Li, C. E. Woodcock, J. L. Roujean, and R. E. Davis, 1997: Transmission of solar radiation in boreal conifer forests: Measurements and models. *Journal of Geophysical Research-Atmospheres*, **102**, 29555–29566.

Ni-Meister, W., W. Yang, and N. Y. Kiang, 2010: A clumped-foliage canopy radiative transfer model for a global dynamic terrestrial ecosystem model. I: Theory. *Agricultural and Forest Meteorology*, **150**, 881–894.

Nilson, T., 1971: A theoretical analysis of the frequency of gaps in plant stands. *Agricultural Meteorology*, **8**, 25–38, doi:10.1016/0002-1571(71)90092-6.

— 1999: Inversion of gap frequency data in forest stands. *Agricultural And Forest Meteorology*, **98-9**, 437–448, doi:10.1016/S0168-1923(99)00114-8.

Norman, J. and J. Welles, 1983: Radiative transfer in an array of canopies. *Agronomy Journal*, **75**, 481–488.

Norman, J. M., 1979: Modeling the complete crop canopy. *Modification of the Aerial Environment of Plants*, B. Barfield and J. Gerber, eds., Am. Soc. Agric. Eng. Monogr. No. 2, ASAE, chapter 3.6, 249–277.

— 1982: *Biometeorology in Integrated Pest Management*. Academic Press, 502 pp.

— 1993: Scaling processed between leaf and canopy levels. *Scaling Physiological Processes: Leaf to Globe*, J. R. Ehleringer and C. B. Field, eds., Academic Press, San Diego, 41–76.

Norman, J. M. and G. S. Campbell, 1989: Canopy structure. *Plant Physiological Ecology: Field Methods and Instrumentation*, 301–325.

Norman, J. M. and P. G. Jarvis, 1974: Photosynthesis in Sitka spruce (Picea sitchensis (Bong.) Carr.). III. Measurements of canopy structure and interception of radiation. *Journal of Applied Ecology*, doi:10.2307/2402028.

— 1975: Photosynthesis in Sitka spruce (Picea sitchensis (Bong.) Carr.): V. Radiation penetration theory and a test case. *Journal of Applied Ecology*, doi:10.2307/2402094.

North, P. R., 1996: Three-dimensional forest light interaction model using a Monte Carlo method. *Geoscience and Remote Sensing, IEEE Transactions on*, **34**, 946–956, doi:10.1109/36.508411.

Otsu, N., 1979: Threshold selection method from grey-level histograms. *IEEE Trans Syst Man Cybern*, **SMC-9**, 62–66, doi:10.1109/TSMC.1979.4310076.

Pan, Y., R. A. Birdsey, J. Fang, R. Houghton, P. E. Kauppi, W. A. Kurz, O. L. Phillips, A. Shvidenko, S. L. Lewis, J. G. Canadell, P. Ciais, R. B. Jackson, S. W. Pacala, A. D. McGuire, S. Piao, A. Rautiainen, S. Sitch, and D. Hayes, 2011: A large and persistent carbon sink in the world's forests. *Science (New York, N.Y.)*, doi:10.1126/science.1201609.

Pearcy, R. W., H. Muraoka, and F. Valladares, 2005: Crown architecture in sun and shade environments: Assessing function and trade-offs with a three-dimensional simulation model. doi:10.1111/j.1469-8137.2005.01328.x.

Pearcy, R. W. and W. A. Pfitsch, 1991: Influence of sunflecks on the δ13 C of Adenocaulon bicolor plants occurring in contrasting forest understory microsites. *Oecologia*, doi:10.1007/BF00318310.

Pinnington, E. M., E. Casella, S. L. Dance, A. S. Lawless, J. I. Morison, N. K. Nichols, M. Wilkinson, and T. L. Quaife, 2016: Investigating the role of prior and observation error correlations in improving a model forecast of forest carbon balance using Four-dimensional Variational data assimilation. *Agricultural and Forest Meteorology*, doi:10.1016/j.agrformet.2016.07.006.

Pinnington, E. M., E. Casella, S. L. Dance, A. S. Lawless, J. I. L. Morison, N. K. Nichols, M. Wilkinson, and T. L. Quaife, 2017: Understanding the effect of disturbance from selective felling on the carbon dynamics of a managed woodland by combining observations with model predictions. *Journal of Geophysical Research: Biogeosciences*, **122**, 886–902, doi:10.1002/2017JG003760.

Pinty, B., N. Gobron, J.-l. Widlowski, S. A. W. Gerstl, M. M. Verstraete, M. Antunes, C. Bacour, F. Gascon, J.-P. Gastellu, N. Goel, S. Jacquemoud, P. North, W. Qin, and R. Thompson, 2001: Radiation transfer model intercomparison (RAMI) exercise. *Journal of Geophysical Research: Atmospheres*, **106**, 11937–11956, doi:10.1029/2000JD900493.

Pinty, B., N. Gobron, J. L. Widlowski, T. Lavergne, and M. M. Verstraete, 2004: Synergy between 1-D and 3-D radiation transfer models to retrieve vegetation canopy properties from remote sensing data. *Journal of Geophysical Research D: Atmospheres*, **109**.

Pinty, B., T. Lavergne, R. E. Dickinson, J. L. Widlowski, N. Gobron, and M. M. Verstraete, 2006: Simplifying the interaction of land surfaces with radiation for relating remote sensing products to climate models. *Journal of Geophysical Research: Atmospheres*, **111**.

Pisek, J., J. M. Chen, R. Lacaze, O. Sonnentag, and K. Alikas, 2010: Expanding global mapping of the foliage clumping index with multi-angular POLDER three measurements: Evaluation and topographic compensation. *ISPRS Journal of Photogrammetry and Remote Sensing*, **65**, 341–346, doi:10.1016/j.isprsjprs.2010.03.002.

Pisek, J., A. Govind, S. K. Arndt, D. Hocking, T. J. Wardlaw, H. Fang, G. Matteucci, and B. Longdoz, 2015: Intercomparison of clumping index estimates from POLDER, MODIS, and MISR satellite data over reference sites. *ISPRS Journal of Photogrammetry and Remote Sensing*, **101**, 47–56, doi:10.1016/j.isprsjprs.2014.11.004.

Pisek, J. and a. J. Oliphant, 2013: A note on the height variation of foliage clumping: comparison with remote sensing retrievals. *Remote Sensing Letters*, **4**, 400–408, doi:10.1080/2150704x.2012.742212.

Pitman, A. J., 2003: The evolution of, and revolution in, land surface schemes designed for climate models. *International Journal of Climatology*, doi:10.1002/joc.893.

Porcar-Castell, A. and S. Palmroth, 2012: Modelling photosynthesis in highly dynamic environments: the case of sunflecks. *Tree Physiology*, **32**, 1062–1065, doi:10.1093/treephys/tps085.

Prentice, I. C., X. Liang, B. E. Medlyn, and Y. P. Wang, 2015: Reliable, robust and realistic: The three R's of next-generation land-surface modelling. *Atmospheric Chemistry and Physics*, doi:10.5194/acp-15-5987-2015.

Pronk, J., 2002: The Amsterdam Declaration on Global Change. 207–208.

Quaife, T., P. Lewis, M. De Kauwe, M. Williams, B. E. Law, M. Disney, and P. Bowyer, 2008: Assimilating canopy reflectance data into an ecosystem model with an Ensemble Kalman Filter. *Remote Sensing of Environment*, **112**, 1347–1364.

Räisäenen, P., 2002: Two-stream approximations revisited: A new improvement and tests with GCM data. *Quarterly Journal of the Royal Meteorological Society*, **128**, 2397–2416, doi:10.1256/qj.01.161.

Reichstein, M., E. Falge, D. Baldocchi, D. Papale, M. Aubinet, P. Berbigier, C. Bernhofer, N. Buchmann, T. Gilmanov, A. Granier, T. Grünwald, K. Havránková, H. Ilvesniemi, D. Janous, A. Knohl, T. Laurila, A. Lohila, D. Loustau, G. Matteucci, T. Meyers, F. Miglietta, J. M. Ourcival, J. Pumpanen, S. Rambal, E. Rotenberg, M. Sanz, J. Tenhunen, G. Seufert, F. Vaccari, T. Vesala, D. Yakir, and R. Valentini, 2005: On the separation of net ecosystem exchange into assimilation and ecosystem respiration: Review and improved algorithm. doi:10.1111/j.1365-2486.2005.001002.x.

Rich, P., J. Chen, S. Sulatycki, R. Vashisht, and W. Wachspress, 1995: Calculation of leaf area index and other canopy indices from gap fraction: a manual for the LAICAL software.

Rich, P. and R. Fournier, 1999: Data, BOREAS TE-23 Map Plot. doi:http://dx.doi.org/10.3334/ORNLDAAC/359.

Rich, P. M., 1989: A Manual for Analysis of Hemispherical Canopy Photography. Technical report, Los Alamos National Laboratory.

— 1990: Characterizing plant canopies with hemispherical photographs. *Remote Sensing Reviews*, **5**, 13–29, doi:10.1080/02757259009532119.

Rich, P. M., F. G. Hall, and A. Papagno, 1999: BOREAS TE-23 Canopy Architecture and Spectral Data from Hemispherical Photographs.

Ridler, S. and T. Calvard, 1978: Picture Thresholding Using an Iterative Selection Method. *IEEE Transactions on Systems, Man, and Cybernetics*, **8**, 630–632, doi:10.1109/TSMC.1978.4310039.

Roden, J. S. and R. W. Pearcy, 1993: Photosynthetic gas exchange response of poplars to steady-state and dynamic light environments. *Oecologia*, doi:10.1007/BF00317673.

Ross, J., 1981: *The radiation regime and architecture of plant stands*. Junk, Boston, 391 pp.

Ryu, Y., O. Sonnentag, T. Nilson, R. Vargas, H. Kobayashi, R. Wenk, and D. D. Baldocchi, 2010: How to quantify tree leaf area index in an open savanna ecosystem: A multi-instrument and multi-model approach. *Agricultural and Forest Meteorology*, **150**, 63–76, doi:10.1016/j.agrformet.2009.08.007.

Ryu, Y., J. Verfaillie, C. Macfarlane, H. Kobayashi, O. Sonnentag, R. Vargas, S. Ma, and D. D. Baldocchi, 2012: Continuous observation of tree leaf area index at ecosystem scale using upward-pointing digital cameras. *Remote Sensing of Environment*, **126**, 116–125.

Saint-Jean, S., M. Chelle, and L. Huber, 2004: Modelling water transfer by rain-splash in a 3D canopy using Monte Carlo integration. *Agricultural and Forest Meteorology*, doi:10.1016/j.agrformet.2003.08.034.

Sarlikioti, V., P. H. B. De Visser, and L. F. M. Marcelis, 2011: Exploring the spatial distribution of light interception and photosynthesis of canopies by means of a functionalstructural plant model. *Annals of Botany*, doi:10.1093/aob/mcr006.

Schaaf, C. B., F. Gao, A. H. Strahler, W. Lucht, X. Li, T. Tsang, N. C. Strugnell, X. Zhang, Y. Jin, J.-P. Muller, P. Lewis, M. Barnsley, P. Hobson, M. Disney, G. Roberts, M. Dunderdale, C. Doll, R. P. D'Entremont, B. Hu, S. Liang, J. L. Privette, and D. Roy, 2002: First operational BRDF, albedo nadir reflectance products from MODIS. *Remote Sensing of Environment*, **83**, 135–148, doi:10.1016/S0034-4257(02)00091-3.

Scheffer, M., M. Holmgren, V. Brovkin, and M. Claussen, 2005: Synergy between small- And large-scale feedbacks of vegetation on the water cycle. *Global Change Biology*, **11**, 1003–1012, doi:10.1111/j.1365-2486.2005.00962.x.

Schulze, E., F. M. Kelliher, C. Korner, J. Lloyd, and R. Leuning, 1994: Relationships among Maximum Stomatal Conductance, Ecosystem Surface Conductance, Carbon Assimilation Rate, and Plant Nitrogen Nutrition: A Global Ecology Scaling Exercise.

Schwarz, G., 1978: Estimating the Dimension of a Model. *The Annals of Statistics*, **6**, 461–464, doi:10.1214/aos/1176344136.

Schwarz, P. A., B. E. Law, M. Williams, J. Irvine, M. Kurpius, and D. Moore, 2004: Climatic versus biotic constraints on carbon and water fluxes in seasonally drought-affected ponderosa pine ecosystems. *Global Biogeochemical Cycles*, doi:10.1029/2004GB002234.

Seidl, R., W. Rammer, and K. Blennow, 2014: Simulating wind disturbance impacts on forest landscapes: Tree-level heterogeneity matters. *Environmental Modelling & Software*, **51**, 1–11, doi:10.1016/j.envsoft.2013.09.018.

Sellers, P., 1985: Canopy reflectance, photosynthesis and transpiration. *International Journal of Remote Sensing*, **6**, 1335–1372, doi:10.1080/01431168508948283.

Sellers, P., J. Berry, G. Collatz, C. Field, and F. Hall, 1992: Canopy reflectance, photosynthesis, and transpiration. III. A reanalysis using improved leaf models and a new canopy integration scheme. *Remote Sensing of Environment*, **42**, 187–216, doi:10.1016/0034-4257(92)90102-P.

Sellers, P. J., 1997: Modeling the Exchanges of Energy, Water, and Carbon Between Continents and the Atmosphere. *Science*, **275**, 502–509, doi:10.1126/science.275.5299.502.

Sellers, P. J., D. a. Randall, G. J. Collatz, J. a. Berry, C. B. Field, D. a. Dazlich, C. Zhang, G. D. Collelo, and L. Bounoua, 1996: A revised land surface parameterization (SiB2) for atmospheric GCMs. Part I: Model formulation. **9**, 676–705, doi:10.1175/1520-0442(1996)009¡0676:ARLSPF¿2.0.CO;2.

Sinclair, T. R., 2006: A reminder of the limitations in using Beer's Law to estimate daily radiation interception by vegetation.

Sitch, S., P. M. Cox, W. J. Collins, and C. Huntingford, 2007: Indirect radiative forcing of climate change through ozone effects on the land-carbon sink. *Nature*, doi:10.1038/nature06059.

Sitch, S., C. Huntingford, N. Gedney, P. E. Levy, M. Lomas, S. L. Piao, R. Betts, P. Ciais, P. Cox, P. Friedlingstein, C. D. Jones, I. C. Prentice, and F. I. Woodward, 2008: Evaluation of the terrestrial carbon cycle, future plant geography and climate-carbon cycle feedbacks using five Dynamic Global Vegetation Models (DGVMs). *Global Change Biology*, doi:10.1111/j.1365-2486.2008.01626.x.

Slevin, D., S. F. B. Tett, J.-F. Exbrayat, A. A. Bloom, and M. Williams, 2016: Global Evaluation of Gross Primary Productivity in the JULES Land Surface Model. *Geoscientific Model Development Discussions*, doi:10.5194/gmd-2016-214.

Song, C., G. Katul, R. Oren, L. E. Band, C. L. Tague, P. C. Stoy, and H. R. McCarthy, 2009: Energy, water, and carbon fluxes in a loblolly pine stand: Results from uniform and gappy canopy models with comparisons to eddy flux data. *Journal of Geophysical Research: Biogeosciences*, **114**, 1–18, doi:10.1029/2009JG000951.

Spencer, S. and B. N. Rock, 1999: BOREAS TE-08 Aspen Bark Spectral Reflectance Data.

Thomas, C. K., B. E. Law, J. Irvine, J. G. Martin, J. C. Pettijohn, and K. J. Davis, 2009: Seasonal hydrology explains interannual and seasonal variation in carbon and water exchange in a semiarid mature ponderosa pine forest in central Oregon. *Journal of Geophysical Research: Biogeosciences*, **114**.

Todd-Brown, K. E. O., F. M. Hopkins, S. N. Kivlin, J. M. Talbot, and S. D. Allison, 2012: A framework for representing microbial decomposition in coupled climate models.

Van Bodegom, P. M., J. C. Douma, J. P. M. Witte, J. C. Ordoñez, R. P. Bartholomeus, and R. Aerts, 2012: Going beyond limitations of plant functional types when predicting global ecosystem-atmosphere fluxes: Exploring the merits of traits-based approaches.

Viterbo, P. and A. K. Betts, 1999: Impact on ECMWF forecasts of changes to the albedo of the boreal forests in the presence of snow. *Journal Of Geophysical Research-Atmospheres*, **104**, 27803–27810.

von Caemmerer, S. and R. T. Furbank, 2003: The C4 pathway: an efficient CO2 pump. *Photosynthesis Research*, **77**, 191–207, doi:10.1023/A:1025830019591.

Walter, J.-M., 2012: CIMES-FISHEYE 20092015 HEMISPHERICAL PHOTOGRAPHY OF FOREST CANOPIES.

Walters, D. N., K. D. Williams, I. A. Boutle, A. C. Bushell, J. M. Edwards, P. R. Field, A. P. Lock, C. J. Morcrette, R. A. Stratton, J. M. Wilkinson, M. R. Willett, N. Bellouin, A. Bodas-Salcedo, M. E. Brooks, D. Copsey, P. D. Earnshaw, S. C. Hardiman, C. M. Harris, R. C. Levine, C. Maclachlan, J. C. Manners, G. M. Martin, S. F. Milton, M. D. Palmer, M. J. Roberts, J. M. Rodríguez, W. J. Tennant, and P. L. Vidale, 2014: The Met Office Unified Model Global Atmosphere 4.0 and JULES Global Land 4.0 configurations. *Geoscientific Model Development*, **7**, 361–386.

Wang, W. M., Z. L. Li, and H. B. Su, 2007: Comparison of leaf angle distribution functions: Effects on extinction coefficient and fraction of sunlit foliage. *Agricultural and Forest Meteorology*, **143**, 106–122, doi:10.1016/j.agrformet.2006.12.003.

Wang, Y. and P. Jarvis, 1990: Description and validation of an array model MAESTRO.

Wang, Y. P., 2003: A comparison of three different canopy radiation models commonly used in plant modelling. *Functional Plant Biology*, **30**, 143–152, doi:10.1071/FP02117.

Wang, Y. P., A. Rey, and P. G. Jarvis, 1998: Carbon balance of young birch trees grown in ambient and elevated atmospheric CO2 concentrations. *Global Change Biology*, **4**, 797–807.

Watson, D. J., 1937: The estimation of leaf area in field crops. *The Journal of Agricultural Science*, **27**, 474, doi:10.1017/S002185960005173X.

Weedon, G. P., G. Balsamo, N. Bellouin, S. Gomes, M. J. Best, and P. Viterbo, 2014: The WFDEI meteorological forcing data set: WATCH Forcing data methodology applied to ERA-Interim reanalysis data. *Water Resources Research*, **50**, 7505–7514.

Widlowski, J. L., B. Pinty, M. Clerici, Y. Dai, M. De Kauwe, K. De Ridder, A. Kallel, H. Kobayashi, T. Lavergne, W. Ni-Meister, A. Olchev, T. Quaife, S. Wang, W. Yang, Y. Yang, and H. Yuan, 2011: RAMI4PILPS: An intercomparison of formulations for the partitioning of solar radiation in land surface models. *Journal of Geophysical Research G: Biogeosciences*, **116**.

Widlowski, J. L., B. Pinty, N. Gobron, and M. M. Verstraete, 2001: Detection and characterization of boreal coniferous forests from remote sensing data. *Journal of Geophysical Research-Atmospheres*, **106**, 33405–33419, doi:Doi 10.1029/2000jd000276.

Widlowski, J.-l., B. Pinty, N. Gobron, M. M. Verstraete, D. J. Diner, and a. B. Davis, 2004: Canopy Structure Parameters Derived From Multi-Angular Remote Sensing Data for Terrestrial Carbon Studies. *Climatic Change*, **67**, 403–415, doi:10.1007/s10584-004-3566-3.

Widlowski, J. L., B. Pinty, T. Lavergne, M. M. Verstraete, and N. Gobron, 2005: Using 1-D models to interpret the reflectance anisotropy of 3-D canopy targets: Issues and caveats. *IEEE Transactions on Geoscience and Remote Sensing*, doi:10.1109/TGRS.2005.853718.

Widlowski, J. L., B. Pinty, M. Lopatka, C. Atzberger, D. Buzica, M. Chelle, M. Disney, J. P. Gastellu-Etchegorry, M. Gerboles, N. Gobron, E. Grau, H. Huang, A. Kallel, H. Kobayashi, P. E. Lewis, W. Qin, M. Schlerf, J. Stuckens, and D. Xie, 2013: The fourth radiation transfer model intercomparison (RAMI-IV): Proficiency testing of canopy reflectance models with ISO-13528. *Journal of Geophysical Research D: Atmospheres*, **118**, 6869–6890.

Widlowski, J. L., M. Robustelli, M. Disney, J. P. Gastellu-Etchegorry, T. Lavergne, P. Lewis, P. R. J. North, B. Pinty, R. Thompson, and M. M. Verstraete, 2008: The RAMI On-line Model Checker (ROMC): A web-based benchmarking facility for canopy reflectance models. *Remote Sensing of Environment*, doi:10.1016/j.rse.2007.07.016.

Widlowski, J. L., M. Taberner, B. Pinty, V. Bruniquel-Pinel, M. Disney, R. Fernandes, J. P. Gastellu-Etchegorry, N. Gobron, A. Kuusk, T. Lavergne, S. Leblanc, P. E. Lewis, E. Martin, M. Mõttus, P. R. J. North, W. Qin, M. Robustelli, N. Rochdi, R. Ruiloba, C. Soler, R. Thompson, W. Verhoef, M. M. Verstraete, and D. Xie, 2007: Third Radiation Transfer Model Intercomparison (RAMI) exercise: Documenting progress in canopy reflectance models. *Journal of Geophysical Research: Atmospheres*, **112**, 1–28, doi:10.1029/2006JD007821.

Wild, M., D. Folini, C. Schär, N. Loeb, E. G. Dutton, and G. König-Langlo, 2013: The global energy balance from a surface perspective. *Climate Dynamics*, doi:10.1007/s00382-012-1569-8.

Wilkinson, M., E. L. Eaton, M. S. J. Broadmeadow, and J. I. L. Morison, 2012: Inter-annual variation of carbon uptake by a plantation oak woodland in south-eastern England. *Biogeosciences*, **9**, 5373–5389, doi:10.5194/bg-9-5373-2012.

Williams, K., J. Gornall, A. Harper, A. Wiltshire, D. Hemming, T. Quaife, T. Arkebauer, and D. Scoby, 2017: Evaluation of JULES-crop performance against site observations of irrigated maize from Mead, Nebraska. *Geoscientific Model Development*, **10**, 1291–1320, doi:10.5194/gmd-10-1291-2017.

Williams, M., E. B. Rastetter, D. N. Fernandes, M. L. Goulde, S. C. Wofsy, G. R. Shaver, J. M. Melillo, J. W. Munger, S.-M. Fan, and K. J. Nadelhoffer, 1996: Modelling the soil-plant-atmosphere continuum in a Quercus-Acer stand at Harvard Forest: the regulation of stomatal conductance by light, nitrogen and soil/plant hydraulic properties. *Plant, Cell and Environment*, doi:10.1111/j.1365-3040.1996.tb00456.x.

Williams, M., P. A. Schwarz, B. E. Law, J. Irvine, and M. R. Kurpius, 2005: An improved analysis of forest carbon dynamics using data assimilation. *Global Change Biology*, doi:10.1111/j.1365-2486.2004.00891.x.

Woodward, F. I., 1987: *Climate and Plant Distribution*, volume 154. Cambridge University Press, 174 pp.

Yang, R., M. A. Friedl, and W. Ni, 2001: Parameterization of shortwave radiation fluxes for nonuniform vegetation canopies in land surface models. *Journal of Geophysical Research*, **106**, 14275, doi:10.1029/2001JD900180.

Yang, R. Q. and M. A. Friedl, 2003: Modeling the effects of three-dimensional vegetation structure on surface radiation and energy balance in boreal forests. *Journal of Geophysical Research-Atmospheres*, **108**, doi:10.1029/2002jd003109.

Zhang, Y., X. Xiao, L. Guanter, S. Zhou, P. Ciais, J. Joiner, S. Sitch, X. Wu, J. Nabel, J. Dong, E. Kato, A. K. Jain, A. Wiltshire, and B. D. Stocker, 2016: Precipitation and carbon-water coupling jointly control the interannual variability of global land gross primary production. *Scientific Reports*, doi:10.1038/srep39748.

Zhu, Z., S. Piao, R. B. Myneni, M. Huang, Z. Zeng, J. G. Canadell, P. Ciais, S. Sitch, P. Friedlingstein, A. Arneth, R. Liu, J. Mao, Y. Pan, S. Peng, J. Peñuelas, and B. Poulter, 2016: Greening of the Earth and its drivers. *Nature Climate Change*, doi:10.1038/NCLIMATE3004.